Systematic Design of Slow Light Waveguides

Wang, Fengwen

Publication date:
2012

Document Version
Publisher's PDF, also known as Version of record

Systematic Design of Slow Light Waveguides

PhD Thesis

$$(EIv'')''=q-\rho A\ddot{v}$$

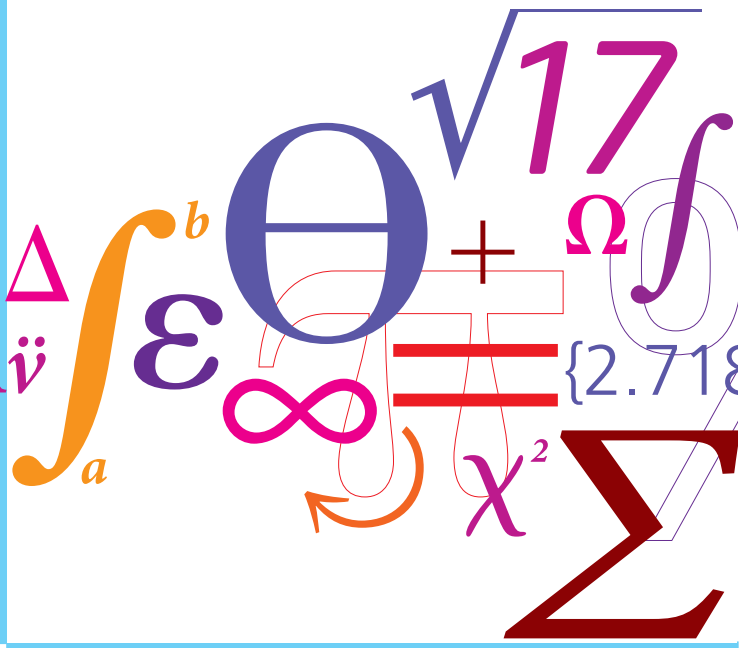

Fengwen Wang
DCAMM Special Report No. S145
August 2012

DTU Mechanical Engineering
Department of Mechanical Engineering

Systematic design of slow light waveguides

by

Fengwen Wang

DEPT. OF MECHANICAL ENGINEERING
Solid Mechanics

TECHNICAL UNIVERSITY OF DENMARK

Title of the thesis:
Systematic design of slow light waveguides

Ph.D. student:
Fengwen Wang
E-mail: fwan@mek.dtu.dk

Supervisors:
Jakob Søndergaard Jensen
E-mail: jsj@mek.dtu.dk

Ole Sigmund
E-mail: sigmund@mek.dtu.dk

Jesper Mørk
E-mail: jesm@fotonik.dtu.dk

Address:
Department of Mechanical Engineering, Solid Mechanics
Technical University of Denmark
Nils Koppels Allé, Building 404, 2800 Kgs. Lyngby, Denmark

Preface

This thesis is submitted in partial fulfillment of the requirements for obtaining the degree of Ph.D. in mechanical engineering at the Technical University of Denmark (DTU). The Ph.D. project was funded by the Villum Kann Rasmussen(VKR) Centre of Excellence via NAnophotonics for TErabit Communications (NATEC), and carried out at the Department of Mechanical Engineering, Solid Mechanics, at DTU in the period September 1st 2009 – August 31st 2012. Supervisors on the project were Associate Professor Dr. techn. Jakob Søndergaard Jensen (DTU Mechanical Engineering), Professor Dr. techn. Ole Sigmund (DTU Mechanical Engineering) and Professor Dr. techn. Jesper Mørk (DTU Photonics Engineering).

First and foremost, I would express my sincere gratitude to my three supervisors for offering me a wonderful opportunity to learn nano-photonics at DTU, and for their invaluable suggestions and inspiring support during the project.

Special thanks are given to Professor Dr. techn. Niels Asger Mortensen from the Department of Photonics Engineering for his professional suggestions during the last part of the project and for providing me the fundamental understanding of photonics through "Modern Photonics" course.

I am grateful to my colleagues in NATEC Group: Lars Hagedorn Frandsen, Sara Ek, Minhao Pu and Kresten Yvind. Their valuable inputs from the experimental aspect are indispensable for the project.

I wish to thank my colleagues in TopOpt Group and at the section of Solid Mechanics for creating a cheerful and inspiring working environment and in particular Boyan Stefanov Lazarov, Yuriy Elesin, Niels Aage, Casper Schousboe Andreasen and Jacob Andkjær for the helpful discussions. I am also thankful to Krister Svanberg at Royal Institute of Technology, Sweden for the permission to use the MMA-code.

Last but not the least, many thanks to my husband, Qixiao Huang, for his endless love and unyielding support and to my family for their support and understanding.

Kgs. Lyngby, August 31st 2012.

Fengwen Wang

Resumé

Lys kan udbrede sig meget langsommere i fotoniske krystalbølgeledere og plasmoniske bølgeledere end i vakuum. Langsom lysudbredelse i bølgeledere giver store muligheder inden for f.eks. terabit kommunikationssystemer. Desværre udviser de en række uheldige egenskaber såsom kraftig signal omformning og et højt udbredelsestab. Desuden er disse bølgeledere meget følsomme over for unøjagtigheder i fremstillingsprocessen. Formålet med denne afhandling er at afhjælpe disse svagheder ved hjælp af systematiske designmetoder baseret på topologioptimering af materialefordelingen i bølgelederne.

For at afhjælpe signalforvrængninger i bølgeledere, udvikles en optimeringsformulering til at tilpasse hældningen på dispersionskurven. Et robust design opnås ved at inkludere forskellige fremstillingsprocesser i optimeringen. Både fri-og fast-topologi (f.eks. cirkulære huller) optimerede bølgeledere kan opnås ved brug af to forskellige parametriseringer. En detaljeret sammenligning viser, at båndbredden kan forøges signifikant ved at tillade uregelmæssige geometrier i bølgelederne.

En optimeringsformulering præsenteres med henblik på at mindske udbredelsestab i de fotoniske krystalbølgeledere. Denne tilgang bliver anvendt til at designe fri topologi bølgeledere. Numeriske resultater illustrerer, at langsomt lys i de optimerede bølgeledere har et signifikant mindre udbredelsestab og samtidig holder en konstant båndbredde.

Den udviklede optimeringsformulering anvendes yderligere til at designe metal-dielektrisk-metal plasmoniske bølgeledere. Det vises, at de optimerede bølgeledere muliggør dispersionsløs langsom lysudbredelse. Yderligere undersøgelser viser, at tabet i metal kan kompenseres ved at integrere aktive medier i den optimerede bølgeleder, uden at det medfører yderligere signalforvrængninger.

Abstract

Light can propagate much slower in photonic crystal waveguides and plasmonic waveguides than in vacuum. Slow light propagation in waveguides shows broad prospects in the terabit communication systems. However, it causes severe signal distortions and displays large propagation loss. Moreover it is vulnerable to manufacturing disorders. This thesis aims to design novel waveguides to alleviate signal distortions and propagation loss using optimization methodologies, and to explore the design robustness with respect to manufacturing imperfections.

To alleviate the signal distortions in waveguides, an optimization formulation is presented to tailor the slope of the dispersion curve. The design robustness is enforced by considering different manufacturing realizations in the optimization procedure. Both free- and fixed-topology (circular-hole based) slow light photonic crystal waveguides are obtained using two different parameterizations. Detailed comparisons show that the bandwidth of slow light propagation can be significantly enhanced by allowing irregular geometries in the waveguides.

To mitigate the propagation loss due to scattering in the photonic crystal waveguides, an optimization problem is formulated to minimize the average propagation loss of the designed modes. The presented approach is employed to design a free-topology slow light waveguide. Numerical result illustrates that slow light propagation in the optimized waveguide displays significantly suppressed propagation loss while keeping the same bandwidth.

The first optimization formulation is further employed to design slow light metal-dielectric-metal plasmonic waveguides. It is shown that dispersionless slow light propagation is achieved in the optimized plasmonic waveguide. Further study reveals that the loss in metal can be compensated by integrating gain media in the optimized waveguide, while keeping negligible signal distortions.

Publications

The following publications are part of the thesis

[P1] J. Grgić, J. R. Ott, F. Wang, O. Sigmund, A. P. Jauho, J. Mørk and N. A. Mortensen, Fundamental limitations to gain enhancement in periodic media and waveguides, *Physical Review Letters*, **108**, 183903, 2012.

[P2] F. Wang, B. S. Lazarov and O. Sigmund, On projection methods, convergence and robust formulations in topology optimization, *Structural and Multidisciplinary Optimization*, **43**, 767–784, 2011.

[P3] F. Wang, J. S. Jensen and O. Sigmund, Robust topology optimization of photonic crystal waveguides with tailored dispersion properties, *Journal of the Optical Society of America B*, **28**, 387–397, 2011.

[P4] F. Wang, J. S. Jensen and O. Sigmund, High-performance slow light photonic crystal waveguides with topology optimized or circular-hole based material layouts, *Photonics and Nanostructures: Fundamentals and Applications*, http://dx.doi.org/10.1016/j.photonics.2012.04.004, 2012, (In press).

[P5] F. Wang, J. S. Jensen, J. Mørk and O. Sigmund, Systematic design of loss engineered slow light waveguides, (Submitted for publication).

[P6] F. Wang, J. S. Jensen, B. S. Lazarov, N. A. Mortensen and O. Sigmund, Systematic design of plasmonic slow light waveguides with tailored dispersion, (To be submitted).

Contents

Chapter 1
Introduction

The recent developments of nanotechnology have provided new possibilities for controlling and manipulating light propagation to achieve desirable functionalities for different applications. In particular, the advent of photonic crystal waveguides (PhCWs) and plasmonic waveguides has provided promising platforms for controlling the fundamental photonic properties, such as slow light propagation. The strong field enhancement in slow light effects has enabled various potential applications in connection with the miniaturized and integrated optical circuit. However, slow light propagation in both types of waveguides is accompanied by severe group velocity dispersion (GVD) and large propagation loss induced by scatterings and/or material loss, which restrict the potential application scope of slow light devices. Moreover, manufacturing imperfections, e.g. surface roughness, introduce significant influence on the device performances and can degrade the desirable functionalities. This thesis aims to develop systematic design approaches for slow light waveguides to alleviate the GVD and/or suppress propagation loss using topology optimization, and to further enhance the design robustness with respect to the manufacturing imperfections.

1.1 Photonic crystal waveguides

Photonic crystals (PhCs) are periodic media, where the dielectric constant is modulated in a periodical pattern with a lattice constant on the order of the operation wavelength, i.e. sub-micron range for the optical domain. The high contrast of the dielectric constants in PhCs leads to the destructive interference of light propagation within certain wavelengths and results in photonic band gap effects. Among different types of PhCs, the PhC slabs, which are composed of a two-dimensional (2D) PhC membrane surrounded by low index claddings, have recently been investigated energetically. This reason is that the PhC slabs can be fabricated using the existing fabrication techniques (Loncar et al., 2000; Letartre et al., 2001; Loncar et al., 2002; Baba et al., 2002), such as electron beam lithography and thin-layer formation. A line defect in PhCs facilitates light propagation along the line defect within the band gaps of PhCs, and generates waveguides, known as PhCWs (see in Fig. 1.1).

The principle characteristics of PhCs and PhCWs manifest themselves in their band structures, i.e. the relations between the propagation frequency (ω) and the wavenumber (k). The band structure maps out all the propagating modes in the structure. It can be obtained by the eigensolutions of Maxwell's equations in the periodic unit cell or supercell along the irreducible Brillouin zone (Brillouin, 1953). The periodic unit cell is defined as the smallest repetitive unit in the structures

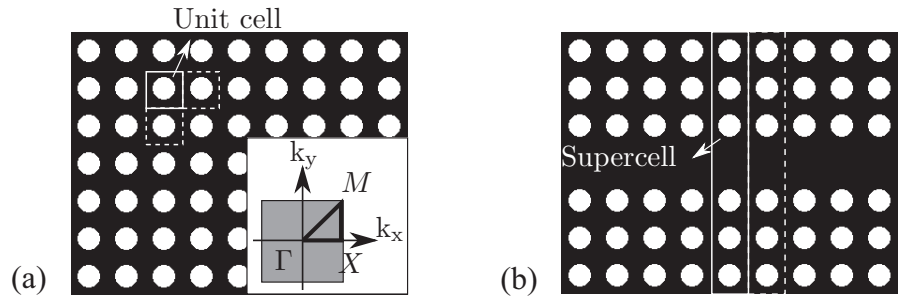

Figure 1.1 (a) Photonic crystal. Black and white regions represent dielectric material and air, respectively. In the subset, the gray region shows the irreducible Brillouin zone for a general 2D unit cell, and the triangle ΓXM shows the one for this case. (b) Photonic crystal waveguide.

as shown in Fig. 1.1 (a), and the periodic supercell is defined as the smallest repetitive unit along the waveguide direction as illustrated in Fig. 1.1 (b). The irreducible Brillouin zone is defined as the smallest wavenumber space to construct band structures, according to the symmetries of unit cells or supercells, see the subset in Fig. 1.1 (a).

Light can propagate much slower in PhCWs than in vacuum, displaying slow light phenomenon. Due to the spatial compressions of the light pulse when coupled into PhCWs, the field intensity is strongly enhanced in the slow light modes, which is favorable in various applications, e.g. for tunable delays (Krauss, 2008; Baba, 2008), optical switches (Beggs et al., 2008), nonlinear optics (McMillan et al., 2006; Corcoran et al., 2009) and mode-locked lasers (Heuck et al., 2010). Two main challenges encountered by slow light in PhCWs are the high group velocity dispersion (GVD), i.e. the strong dependence of group velocity on frequency, and the large propagation loss. The high GVD results in severe signal distortions and restricts the available slow light bandwidth (Engelen et al., 2006), while the large propagation loss limits the effective propagation length of signals.

To alleviate signal distortions, several approaches have been proposed addressing the high GVD in PhCWs, including dispersion compensation in the coupled photonic crystal waveguides (Mori and Baba, 2004; Mori et al., 2007; Kawasaki et al., 2007), and dispersion curve engineering. The dispersion curve engineering is realized by changing the radii and locations of air holes guided by physical intuition (Frandsen et al., 2006; Li et al., 2008; Hao et al., 2010; Schulz et al., 2010; Liang et al., 2011) and by redistributing dielectric material using topology optimization (Stainko and Sigmund, 2007).

Even though slow light propagation in PhCWs is intrinsically lossless under the light line, they experience extrinsic losses due to the manufacturing imperfections. The manufacturing disorders, i.e. variation of vertical wall and surface roughness, cause significant out-of-plane radiation (Benisty et al., 2000; Ferrini et al., 2003; Andreani and Gerace, 2007) and back-scattering (Hughes et al., 2005; Kuramochi

et al., 2005; Patterson et al., 2009; O'Faolain et al., 2010; Patterson and Hughes, 2010). Recently, Petrov et al. (2009), O'Faolain et al. (2010) and Baron et al. (2011) have demonstrated that the propagation loss varies in different PhCWs due to the different field intensity on the interfaces between air and dielectric material. These very first studies have opened up a new prospect in the loss engineering of slow light waveguides.

1.2 Plasmonic waveguides

The level of the integration and minimization of PhCW devices is circumscribed by the diffraction limit of light in dielectric materials (Gramotnev and Bozhevolnyi, 2010). One feasible way to circumvent the diffraction limit and to localize light into a region as small as few nanometers is to use plasmonic waveguides. Plasmonic waveguides, consisting of metal and isolators/dielectric materials, can facilitate surface plasmon propagation, which is highly localized at the interface between metal and surrounding materials (Maier, 2007). This remarkable capability provides unique prospects of plasmonic waveguides in the integrated optical circuit (Barnes et al., 2003; Anker et al., 2008; Ebbesen et al., 2008; Berini and De Leon, 2012).

Among diverse plasmonic waveguides, the metal-dielectric-metal (MDM) plasmonic waveguides are of particular interest, due to their capability to support surface plasmon propagation over a very wide frequency range (Economou, 1969) and to integrate gain media for loss compensation (Govyadinov and Podolskiy, 2006; Yu et al., 2008). Lately, plasmonic slow light, displaying characteristics of both slow light effects and surface plasmons, has been demonstrated in various MDM plasmonic waveguide configurations with coupled resonators, utilizing a plasmonic analogue of electromagnetically induced transparency (EIT). It has been shown by Huang et al. (2011) that the dispersion curves of the MDM plasmonic waveguides can be tailored by changing the side-coupled resonators to reduce GVD. To mitigate the propagation loss induced by metallic components, the incorporation of gain media has been anticipated to be an efficient approach in various MDM plasmonic waveguides for different applications (Govyadinov and Podolskiy, 2006; Yu et al., 2008; Noginov et al., 2008; De Leon and Berini, 2009).

1.3 Topology optimization

Topology optimization was intentionally introduced to serve as a systematic approach to perform mechanical structural design by Bendsøe and Kikuchi (1988) through redistributing materials in the structures. The structures are updated by an iterative optimization algorithm based on sensitivity analysis. An elaborate overview of the theory, method and corresponding applications of topology optimization can be found in the monograph from Bendsøe and Sigmund (2003).

In the last decade, topology optimization has been successfully employed in var-

ious fields. Fluidic components have been designed using topology optimization, including flow inverters, flow switches (Gersborg-Hansen et al., 2005), micro fluidic devices (Andreasen et al., 2009; Kreissl et al., 2010). In the elastic wave propagation problems, phononic band gap structures and materials have been designed by Sigmund and Jensen (2003) and Halkjaer et al. (2006). Acoustic devices, including acoustic horns (Wadbro and Berggren, 2006), the devices for acoustic-structure interaction problems (Yoon et al., 2007) and sound barriers (Duhring et al., 2008) have been achieved using topology optimization.

Simultaneously, topology optimization has been employed to design optical devices covering microwave and telecom frequencies. In the microwave regime, subwavelength antennas have been obtained by Kiziltas et al. (2003), Aage et al. (2010), Erentok and Sigmund (2011). In the telecom frequency regime, nano-scale components in the integrated optical circuit have been designed, to enhance transmissions (Jensen and Sigmund, 2004), to realize optical splitters (Borel et al., 2005), slow light effects (Stainko and Sigmund, 2007; Matzen et al., 2011) and optical switches (Elesin et al., 2012). Moreover, optical cloaking has been achieved by the topology optimized structures (Andkjaer and Sigmund, 2011; Andkjaer et al., 2012). A comprehensive review on the applications of topology optimization in optical devices has been done by Jensen and Sigmund (2011).

Two of the main challenges encountered in topology design procedure were the mesh-dependency of results and the appearance of checkerboards, where the solid and void elements appear in a checkerboard like fashion. Different numerical techniques have been developed to tackle these two issues, e.g. perimeter control from Haber et al. (1996), sensitivity filtering from Sigmund (1997) and density filtering from Bourdin (2001), Bruns and Tortorelli (2001). A summary on this topic has been done by Sigmund (2007). One of the remaining challenges encountered by the optimized components is the design robustness with respect to manufacturing imperfections. Sigmund (2009) has proposed the concept of robust topology optimization, where the design robustness of the optimized components has been enhanced through considering different manufacturing processes in the optimization procedure.

1.4 Structure of the thesis

This thesis addresses the dispersion and loss engineering in the PhCWs and dispersion engineering in the MDM plasmonic waveguides by topology optimization, and further explores the robust topology optimization to enhance the design robustness. It presents an overview of the main results. The detailed descriptions can be found in the papers [P1]–[P6].

Chapter 2 is dedicated to the band structure calculations for periodic media. The finite element formulations for the band structure calculations are derived in the frequency domain. Part of the chapter summarizes [P1].

Chapter 3 explores the robust topology optimization by mimicking different design realizations using a threshold projection. The robust topology optimization is formulated as a worst case optimization considering different design realizations, and further evaluated by designing a compliant inverter. This chapter is a summary of [P2].

Chapter 4 studies dispersion engineering in PhCWs by formulating it as an optimization problem. The robust fixed- and free-topology waveguides are systematically designed and compared in order to highlight the corresponding capabilities and limitations, based on two different parameterizations. This chapter summarizes [P3] and [P4].

Chapter 5 is devoted to the loss engineering problem of slow light PhCWs. Loss mechanisms are analyzed by studying the characteristics of slow light modes in different PhCWs, where scattering loss is represented by an effective edge-related dissipation. The loss engineering is realized by minimizing the average propagation loss of the designed slow light modes, and demonstrated by designing free-topology loss engineered waveguides. This chapter is a summary of [P5].

In Chapter 6, the dispersion engineering formulation is employed to systematically design slow light MDM plasmonic waveguides by parameterizing the supercell with a set of superellipses. Also the loss compensation of the designed slow light propagation is further investigated by integrating gain media. This chapter is a summary of [P6].

Chapter 7 sums up the thesis and gives perspectives for the further work.

Chapter 2
Band structure calculations

The band structures describe the relations between the angular frequency and the wavevector of the modes which can propagate in the periodic structures, and consist of several dispersion curves. The band structures allow the survey of all the propagation scenarios in the structures. Using the Bloch–Floquet theorem, which states that the propagation behavior in a periodic structure is governed by a periodic envelope function multiplied by a plane wave, the band structure can be obtained by solving an eigenvalue problem of Maxwell's equations in the periodic cell.

In this chapter, the numerical formulations for band structure calculations are derived from the governing equations of time-harmonic electromagnetic waves using the finite element method (FEM). It is shown how the material loss and material gain affect the performance of PhCWs based on the band structure calculations, and how to adapt the band structure calculations to obtain the band structures of plasmonic waveguides. Part of this chapter is a summary of the paper [P1].

2.1 Maxwell's equations

Light can be described as an electromagnetic wave phenomenon consisting of an electric field and a magnetic field. The electric and magnetic fields oscillate perpendicular to each other and transfer energy obeying Ampere's and Faraday's laws. Within the classic theory, all the electromagnetic waves are governed by the Maxwell's equation systems, found in 1865 by Maxwell combining Ampere's, Faraday's and Gauss' laws. In a medium without free electric charges or currents, the Maxwell's equations take the following form (Maxwell, 1891)

$$\nabla \times \mathbf{H} = \varepsilon \frac{\partial \mathbf{E}}{\partial t} \tag{2.1}$$

$$\nabla \times \mathbf{E} = -\mu \frac{\partial \mathbf{H}}{\partial t} \tag{2.2}$$

$$\nabla \cdot \varepsilon \mathbf{E} = 0 \tag{2.3}$$

$$\nabla \cdot \mu \mathbf{H} = 0 \tag{2.4}$$

where $\mathbf{E} = \mathbf{E}(\mathbf{r}, t)$ and $\mathbf{H} = \mathbf{H}(\mathbf{r}, t)$ denote the time-varying electric and magnetic fields, respectively, with $\mathbf{r} = (x, y, z)$ representing the spatial location vector and t being time, ε and μ represent the material permittivity and the material permeability. In this thesis, the light propagation is restricted to mixed non-magnetic media, hence, the material permittivity is a function of position, given by $\varepsilon = \varepsilon_r(\mathbf{r})\,\varepsilon_0$, where $\varepsilon_0 \approx 8.8542 \times 10^{-12}$ F/m is the vacuum permittivity and ε_r is the relative

permittivity, and the material permeability is given by $\mu = \mu_r \mu_0$ with $\mu_r = 1$ and $\mu_0 = 4\pi \times 10^{-7}$ H/m being the vacuum permeability. The light speed in vacuum is defined as $c = 1/\sqrt{\varepsilon_0 \mu_0}$.

The Maxwell's equations can be converted into a second-order differential equation of the magnetic field, $\mathbf{H}$, by eliminating the electric field, $\mathbf{E}$. By assuming time harmonic field quantities of $\mathbf{H}(\mathbf{r}, t) = \mathbf{H}(\mathbf{r}) e^{-i\omega t}$ and $\mathbf{E}(\mathbf{r}, t) = \mathbf{E}(\mathbf{r}) e^{-i\omega t}$, Eqs. (2.1)– (2.4) yield the Maxwell's equations in the frequency domain as

$$\nabla \cdot \left(\frac{1}{\varepsilon_r(\mathbf{r})} \nabla \mathbf{H}(\mathbf{r}) \right) + \left(\frac{\omega}{c} \right)^2 \mathbf{H}(\mathbf{r}) = 0 \tag{2.5}$$

where the electric field is recovered by $\mathbf{E}(\mathbf{r}) = i/(\omega \varepsilon_0 \varepsilon_r(\mathbf{r})) \nabla \times \mathbf{H}(\mathbf{r})$.

Following the same procedure, the Maxwell's equations can also be solved using the electric field, given by

$$\nabla^2 \mathbf{E}(\mathbf{r}) + \left(\frac{\omega}{c} \right)^2 \varepsilon_r(\mathbf{r}) \mathbf{E}(\mathbf{r}) = 0 \tag{2.6}$$

here, the magnetic field is found via $\mathbf{H}(\mathbf{r}) = -i/(\omega \mu_0) \nabla \times \mathbf{E}(\mathbf{r})$.

The energy flow transfered in the electromagnetic wave is governed by the time average of the Poynting vector, defined by $\langle \mathbf{S} \rangle = \frac{1}{2} \Re \left(\mathbf{E} \times \overline{\mathbf{H}} \right)$ with $\Re(\cdot)$ denoting the real part and $\overline{(\cdot)}$ denoting the complex conjugate.

This thesis focuses on the wave propagation in two dimensional (2D) structures with an infinite extension in the third direction, say z direction. The wave propagation in 2D structures is classified into two distinct polarizations, H_z polarization with (E_x, E_y, H_z) as unknowns and E_z polarization with (H_x, H_y, E_z) as unknowns. In both polarizations, the out-of-plane field quantities are governed by the scalar Helmholtz equation as

$$\nabla \cdot \left(\frac{1}{\varepsilon_r(\mathbf{r})} \nabla H_z(\mathbf{r}) \right) + \left(\frac{\omega}{c} \right)^2 H_z(\mathbf{r}) = 0 \tag{2.7}$$

or

$$\nabla^2 E_z(\mathbf{r}) + \left(\frac{\omega}{c} \right)^2 \varepsilon_r(\mathbf{r}) E_z(\mathbf{r}) = 0 \tag{2.8}$$

For simplicity, this thesis only concerns the H_z polarization. However, the approaches presented in this thesis can also be employed in the E_z polarization.

2.2 Band structure calculations

In a period medium, $\varepsilon_r(\mathbf{r}) = \varepsilon_r(\mathbf{r} + \mathbf{a})$ with $\mathbf{a}$ as the periodic vector, the magnetic field, H_z, is characterized by a wave vector $\mathbf{k}$ following the Bloch–Floquet theorem, given by $H_z = U e^{i(\mathbf{k} \cdot \mathbf{r})}$. The quantity U is the periodic envelope function satisfying

$$\begin{aligned} (\nabla + i\mathbf{k}) \cdot \varepsilon_r^{-1} (\nabla + i\mathbf{k}) U + (\omega/c)^2 U = 0 \\ U(\mathbf{r}) = U(\mathbf{r} + \mathbf{a}) \end{aligned} \tag{2.9}$$

The band structure of the periodic medium is comprised of the eigenstates governed by Eq. (2.9) for all possible wave vectors $\mathbf{k}$, given as frequency versus wave vector. According to the periodicity and symmetry of the periodic unit cell, one can compute the eigenstates along the irreducible Brillouin zone only (Brillouin, 1953). The band structure projects the propagation modes in the periodic structure in the order of increasing frequency.

Following the finite element discretization procedure (Cook et al., 2002), Eq. (2.9) results in the following eigenvalue equation,

$$\left(\mathbf{K}_0 - \omega^2\mathbf{M}\right)\mathbf{u} + \mathbf{K}_1 k\mathbf{u} + \mathbf{K}_2 k^2\mathbf{u} = 0 \tag{2.10}$$

where $\mathbf{u}$ is the nodal value vector of U. The element-wise quantities in Eq. (2.10) can be expressed by

$$\begin{aligned}
\mathbf{K}_0 &= \sum_e \varepsilon_r^{-1} \int_e \left(\frac{\partial \mathbf{N}^T}{\partial x}\frac{\partial \mathbf{N}}{\partial x} + \frac{\partial \mathbf{N}^T}{\partial y}\frac{\partial \mathbf{N}}{\partial y} \right) dV \\
\mathbf{M} &= \sum_e 1/c^2 \int_e \left(\mathbf{N}^T\mathbf{N}\right) dV \\
\mathbf{K}_1 &= \sum_e \varepsilon_r^{-1} i \int_e \left(\mathbf{N}^T\frac{\partial \mathbf{N}}{\partial x} - \frac{\partial \mathbf{N}^T}{\partial x}\mathbf{N} \right) dV \\
\mathbf{K}_2 &= \sum_e \varepsilon_r^{-1} \int_e \left(\mathbf{N}^T\mathbf{N}\right) dV
\end{aligned} \tag{2.11}$$

with k as the wavenumber along x direction, and $\mathbf{N}$ being the standard finite element shape functions, which can be found in many references (Cook et al., 2002; Jin, 2002; Jin and Riley, 2009). In this thesis, bilinear rectangular elements are utilized.

Eq. (2.10) can be solved either for eignefrequencies (ω) for a given wavenumber (k), named as $\omega(k)$-formulation, or for eigen wavenumbers (k) for a given frequency (ω), named as $k(\omega)$-formulation. In a dispersive medium, where the material properties are dependent on frequency, the $\omega(k)$-formulation results in a nonlinear eigenvalue problem and calls for an expensive iterative algorithm. In contrast to the $\omega(k)$-formulation, material dispersion does not induce any difference in the $k(\omega)$-formulation. Moreover, the spatial propagation loss can be evaluated directly when considering loss in the system, such as material loss. The comparisons between the $k(\omega)$-formulation and the $\omega(k)$-formulation have been elaborated by Huang et al. (2004).

2.2.1 $\omega(k)$-formulation

In order to construct the band structure of a periodic medium, Eq. (2.10) is solved for eigenfrequencies, ω, for each possible wave vector, i.e. $\omega(k)$-formulation. For a unit cell in Fig. 2.1 (a), the irreducible Brillouin zone is illustrated by the triangle

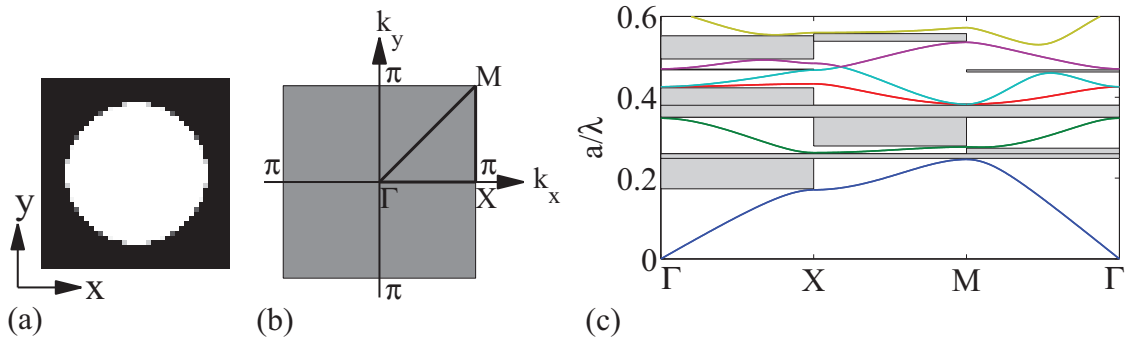

Figure 2.1 (a) Periodic unit cell consisting of Si in the black region and air in the white region. (b) Irreducible Brillouin zone. The gray area indicates the wave vectors to be searched for a general 2D unit cell, and the triangle ΓXM indicates the wave vectors for a square symmetrical unit cell. (c) Band structure calculated using the $\omega\,(k)$-formulation. The light gray regions represent the band gaps.

(ΓXM) in Fig. 2.1 (b). The band structure in this case is composed of the eigenfrequencies associated with the wave vectors along the edges, i.e. $\mathbf{k} = [k,\ 0]$ along Γ–X, $\mathbf{k} = [\pi,\ k]$ along X–M and $\mathbf{k} = [\pi - k,\ \pi - k]$ along M–Γ for $\forall k \in [0, \pi]$. Fig. 2.1 (c) depicts the band structure of the unit cell consisting of Silicon (Si) (black region) and air (white region), where a is the lattice constant and $\lambda = 2\pi c/\omega$ is the wavelength of guided modes. Two complete band gaps are observed between the first and second bands and the second and third bands, where propagation is prevented in all the directions. Several partial band gaps show in certain directions, such as the one between the fifth and sixth bands along Γ–X and the one between the second and third bands along X–M. All the band gaps and the partial band gaps are indicated by the light gray regions in Fig. 2.1 (c).

2.2.2 $k(\omega)$-formulation

In the $k\,(\omega)$-formulation, Eq. (2.10) can be solved for eigen wavenumbers, k, for a given frequency, ω, by reformulating the equation as (Davanco et al., 2007; Engstroem et al., 2009; Schmidt and Kappeler, 2010)

$$(\mathbf{K}_l - k\mathbf{M}_l)\,\mathbf{v} = \mathbf{0} \tag{2.12}$$

with

$$\mathbf{K}_l = \begin{bmatrix} -\mathbf{K}_1 & -(\mathbf{K}_0 - \omega^2\mathbf{M}) \\ \mathbf{I} & \mathbf{0} \end{bmatrix}, \quad \mathbf{M}_l = \begin{bmatrix} \mathbf{K}_2 & \mathbf{0} \\ \mathbf{0} & \mathbf{I} \end{bmatrix}, \quad \mathbf{v} = \begin{bmatrix} k\mathbf{u} \\ \mathbf{u} \end{bmatrix} \tag{2.13}$$

The eigen wavenumbers in Eq. (2.12) are complex valued, with the real part, $\Re(k)$, denoting the wavenumber and the imaginary part, $\Im(k)$, representing the propagation loss, i.e. the exponential spatial attenuation of the propagation.

Different to the $\omega(k)$-formulation, the eigenmodes in the $k(\omega)$-formulation are classified into two categories according to their propagation characteristics: guided

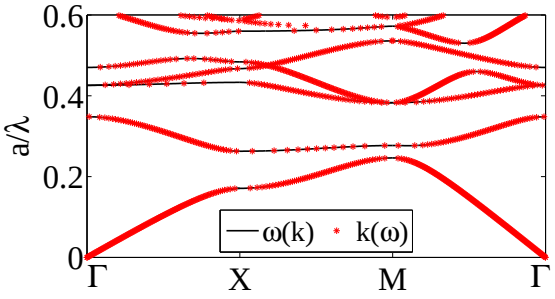

Figure 2.2 Band structures calculated using the $\omega\,(k)$-formulation and the $k(\omega)$-formulation. The lines and asterisks represent the band structures obtained from the $\omega\,(k)$-formulation and the $k(\omega)$-formulation, respectively.

modes and evanescent modes connecting the inflection points in different bands. The evanescent modes attenuate exponentially in the structure. The guided and evanescent modes can be easily identified due to the big difference on the propagation loss. Band structures calculated by the $k(\omega)$-formulation and by the $\omega(k)$-formulation coincide with each other, as illustrated in Fig. 2.2.

2.2.3 Influence of material loss/gain on the performance of PhCWs [P1]

Photonic crystal waveguides (PhCWs) facilitate light propagation within the band gaps of PhCs. The gap-guided modes are highly confined at the line defect with a small penetration into PhC claddings. Assuming an infinite periodic extension normal to the waveguide direction, the band structure of a PhCW is obtained using periodic boundary conditions in the periodic supercell of the waveguide. It should be pointed out that the perfectly matched layers (PMLs) proposed by Berenger (1994), can also be adopted to truncate the open boundary normal to the waveguide direction in the $k(\omega)$-formulation. There is no significant difference in the band structures using the periodic boundary condition and PMLs when considering sufficient PhC claddings normal to the waveguide direction. In this thesis, the periodic boundary condition is employed normal to the waveguide direction in the band structure calculations of PhCWs.

Based on the band structure, the speed of a guided mode is described by the group velocity v_g, defined by the slope of the dispersion curve,

$$v_g = \frac{c}{n_g} = \Re\left(\frac{\partial\omega}{\partial k}\right) \tag{2.14}$$

here n_g is the group index of the guided mode. When n_g increases, the propagation of the guided mode is slowed down with $v_g << c$. The phase rate of the guided mode is defined as the phase velocity, given as $v_p = \omega/k$. Fig. 2.3 graphically illustrates how the phase and group velocities of the guided mode at $(\omega_0,\ k_0)$ can be deduced from the dispersion curve.

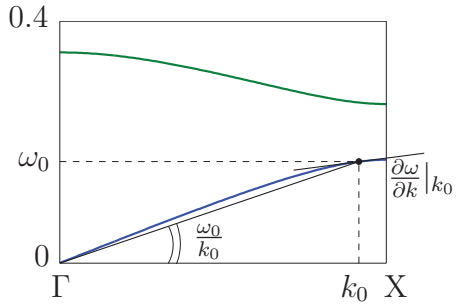

Figure 2.3 Illustration of the phase and group velocities of the guided mode at (ω_0, k_0).

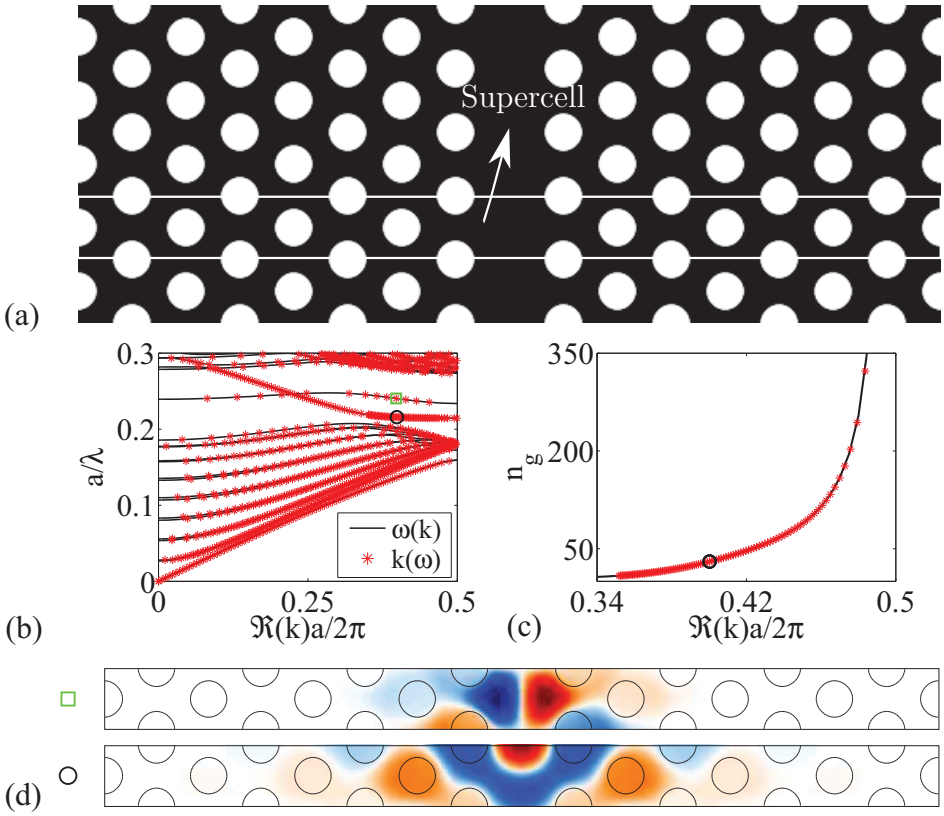

Figure 2.4 (a) Photonic crystal waveguide with triangular patterned air holes in Si. The white rectangle shows the periodic supercell. (b) Band structure. (c) Group index plot of the even band indicated by a circle in (b). (d) Modal profiles of the guided modes marked in (b).

Fig. 2.4 (b) shows the band structure of a lossless PhCW ($\varepsilon_r = (n + in'')^2$ where $n'' = 0$) with triangular patterned air holes of $r = 0.3a$ in Si shown in Fig. 2.4 (a). There are two guided bands within the band gap of the corresponding PhC, i.e. one even band, where the guided modes display symmetrical modal profiles along the waveguide direction, and one odd band, where the guided modes show

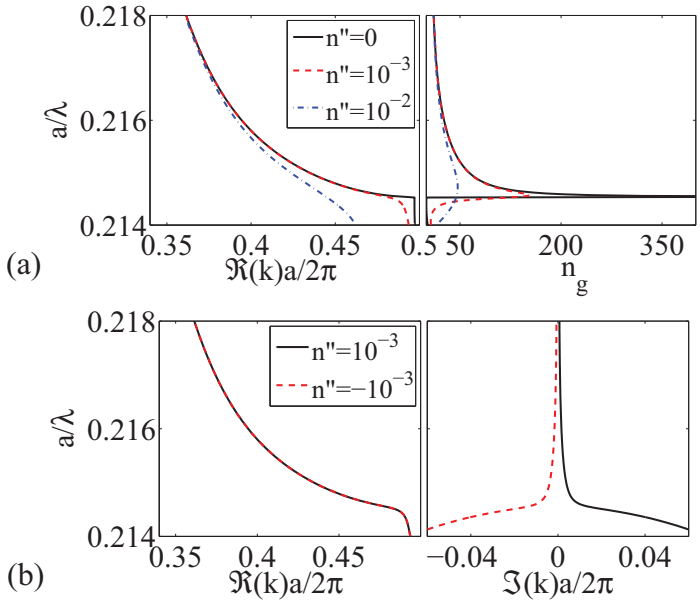

Figure 2.5 (a) Influence of material loss on the performance of waveguides. Left panel: Guided band. Right panel: Group index plot. The solid, dashed and dash-dot lines represent the guided bands in the waveguides considering material loss of $n'' = 0$, $n'' = 10^{-3}$ and $n'' = 10^{-2}$, respectively. (b) Performance of waveguides considering material gain and loss. Left panel: Guided band. Right panel: Propagation characteristic. The solid and dashed lines show the characteristics of the guided bands in the waveguides with material loss and with the same amount of material gain, respectively.

asymmetrical modal profiles, as illustrated in Fig. 2.4 (d). This thesis focuses on the even band, since it displays higher field confinement for a same group index and larger wavenumber range for slow light propagation than the odd band. Fig. 2.4 (c) shows that the group index of the even-guided mode increases sharply when approaching the band edge, correspondingly, the even mode is dramatically slowed down.

While ideal PhCWs can bring light to stop, the experimental demonstrations of slow light propagation in PhCWs stay around $n_g \propto 10^2$, despite tremendous fabrication effects (Notomi et al., 2001; Schulz et al., 2010). The limitation of the achievable group index in the PhCWs has been attributed to the structural imperfections, absorptions and other loss mechanisms. Pedersen et al. (2008) and Grgic et al. (2010) have quantitatively explained this phenomenon using a perturbation theory, where a small imaginary part has been added in the dielectric function to represent loss in the PhCWs.

In the following, the achievable group index in PhCWs is studied in the presence of material loss, using the $k(\omega)$-formulation. Fig. 2.5 (a) depicts the influence of material loss ($n'' > 0$) on the performance of the waveguide. It is noted that the material loss causes the even band to deviate from a parabolic shape as in the

lossless case when approaching the band edge and hence restricts the achievable group index. Moreover, it is observed that a redshift in the band is induced by material loss, i.e. the wavelength of the guided modes increases as material loss rises. Fig. 2.5 (b) shows that the guided modes become leaky with $\Im(k) > 0$, in the presence of material loss. It is seen that the propagation loss increases as the group index increases due to the large modal profiles associated with high group indices.

Since loss is an inherent part of any passive devices, integration of gain material in the passive devices has received special attentions for various applications, e.g. for loss compensation in the lossy metamaterial (Stockman, 2011) and plasmonic nanostructures (Berini and De Leon, 2012), and for active nanophotonic devices (Matsuo et al., 2010). It is anticipated that gain in the periodic medium is effectively enhanced by a factor of the group index associated with the passive structure, by assuming that material gain will not induce any influence on the dispersion relations of the structure.

However, material gain in the PhCWs acts same as material loss in terms of dispersion curve. as shown in Fig. 2.5 (b). The saturation of the achievable group index is also observed in the presence of material gain ($n'' < 0$). This conclusion can be deduced from Eq. (2.10), because the eigen wavenumbers for the active waveguides are the conjugates of the ones for the waveguides with the same amount of dissipation. The trade-off between material gain and slow light effects leads to a saturation of gain enhancement in active waveguides. Further details consult [P1].

The finite achievable group index can be explained by the amplitude mismatch in multiple scattered light induced by material loss/gain. The amplitude mismatch results in an interference pattern and causes the group index to stay finite (Krauss, 2007).

2.2.4 Band structure of plasmonic waveguides

The band structure calculations of plasmonic waveguides are difficult issues due to the material dispersion in metal. By employing PMLs to truncate the open boundary normal to the waveguide direction, the presented $k(\omega)$-formulation can be employed to calculate the band structures of plasmonic waveguides. The computational model is sketched in Fig. 2.6 (a) with the waveguide direction along the longitudinal direction.

In order to evaluate the feasibility and accuracy of the $k(\omega)$-formulation in the band structure calculations of plasmonic waveguides, the band structure of a single interface waveguide, consisting of Silver (Ag) and air, is calculated. Here the permittivity of Ag is modeled by the Drude-Lorentz model presented by Johnson and Christy (1972). The band structure of such a waveguide follows an analytical formulation as (Maier, 2007).

$$k = \omega \sqrt{\varepsilon_{\text{air}} \varepsilon_{\text{Ag}} / \left(\varepsilon_{\text{air}} + \varepsilon_{\text{Ag}}\right)} \tag{2.15}$$

Due to the introduction of PMLs, many evanescent modes localized in the PMLs

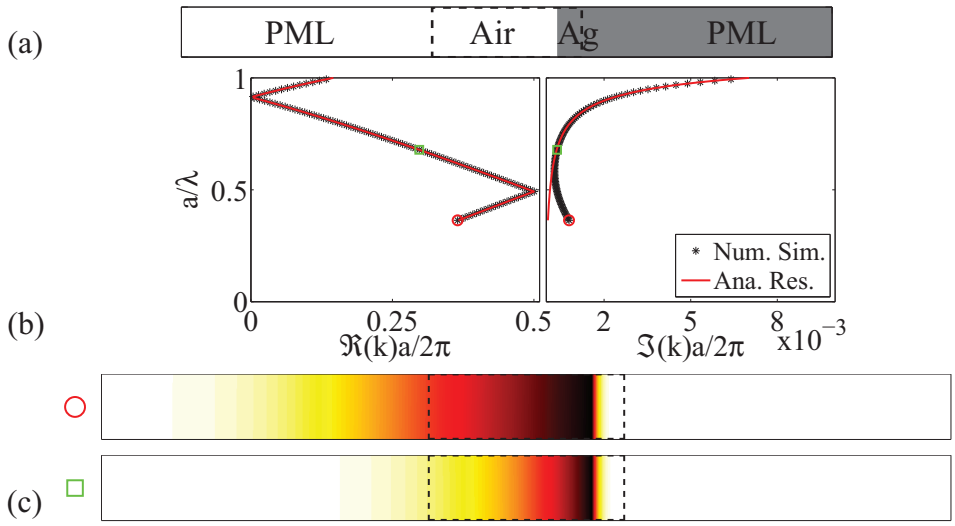

Figure 2.6 (a) Illustration of computational domain. The dashed rectangle shows the supercell consisting of Ag and air. (b) Propagation characteristics of the guided modes. The asterisks depict the band structure and corresponding propagation losses from the numerical simulation, and the lines represent the ones from the analytical calculations. (c) Field intensity of the guided modes marked in (b).

can be detected. However, the guided modes can be identified according to the characteristics of surface modes, i.e. high localization at the interface. Fig. 2.6 (b) shows the band structures obtained from the analytical calculation represented by the solid lines and the numerical simulation in asterisks.

The band folds back due to the periodic boundary condition in the waveguide direction, and it is noted that the band structure obtained from the numerical simulation agrees with the analytical one. However, big deviations are observed in the propagation loss of the guided modes at high wavelengths. The field intensities in Fig. 2.6 (c) demonstrate that the inaccuracy on the propagation loss is induced by the severe penetration of the eigenmode into the PMLs. Hence it can be resolved by enlarging the computational domain normal to the waveguide direction. Nevertheless, there is no observable difference in the propagation loss of the highly confined modes between these two different calculations.

Chapter 3
Robust topology optimization formulations [P2]

Topology optimization is applied to find an optimized material distribution regarding two or more different types of materials, in a prescribed design domain, Ω_D, such that the response of the structure is optimized in terms of a prescribed objective in the output domain, Ω_O, as illustrated in Fig. 3.1.

By allowing topological changes in the design domains, topology optimization exhibits great potentials serving as a systematic design approach over its counterparts, sizing optimization, where the size of the structural components can be modified, and shape optimization, where the shapes of the structural boundaries can be altered. One challenge encountered by topology optimization is the design robustness of the topology optimized structures. The fine tuned topology optimized structures are vulnerable to manufacturing errors. Manufacturing imperfections, such as under- or over-etching processes, may degrade or even discard the optimized functionalities. In particular, slow light propagation in the PhCWs is very sensitive to small variations in the structural geometry.

This chapter addresses the design robustness of the optimized structures with respect to manufacturing imperfections. A robust topology optimization formulation is presented to enhance the design robustness by considering under-, ideal- and over-etching processes in the optimization procedure as in the study of Sigmund (2009). The proposed approach is evaluated by designing a compliant inverter. This chapter presents the main result from the paper [P2].

3.1 Parameterizations of structures

This thesis considers designs consisting of two materials, such as air and solid material. Based on the finite element discretization, an element-wise quantity $\overline{\rho}_e \in [0,\ 1]$

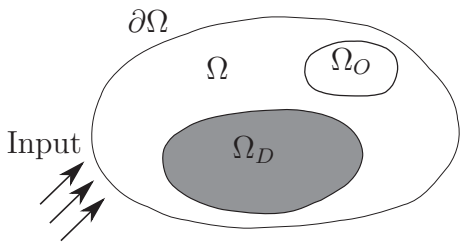

Figure 3.1 Illustration of the design domain in topology optimization. The material distribution in the design domain Ω_D is iteratively updated to achieve an optimized objective in the output domain Ω_O.

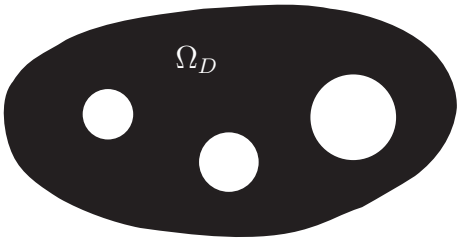

Figure 3.2 Illustration of the material mask overlay strategy. The regions within circles are air, and the region outside is solid material.

is introduced to control the material properties in element e in the design domain, where the material in the element e is solid material when $\overline{\rho}_e = 1$ and air when $\overline{\rho}_e = 0$. The material property of element e is interpolated using the solid isotropic material with penalization (SIMP) model (Bendsøe and Sigmund, 1999), stated as

$$A_e = A_1 + \overline{\rho}_e^p \left(A_2 - A_1\right) \tag{3.1}$$

here A_1 and A_2 are material properties for air and the solid material, and p is an exponential factor utilized to penalize the intermediate value between 0 and 1. In the optimization procedure, the quantity $\overline{\rho}_e$ is allowed to take an intermediate value between 0 and 1. But in the final design, a pure 0 and 1 solution is pursued, which is corresponding to the well defined material properties.

In this thesis, the element-wise quantity, $\overline{\rho}_e$, is obtained using two different parameterization methods, i.e. the density approach in the topology optimization (Bendsøe and Sigmund, 2003) and the material mask overlay strategy (MMOS) shown in Fig. 3.2 (Saxena, 2011).

3.1.1 Density approach

In the density approach, an element-wise design variable, ρ_e, is assigned to element e. The element-wise quantity $\overline{\rho}_e$ can be obtained from the design variables in various methods (Sigmund, 2007). This thesis employs a threshold projection since it can be easily integrated with the robust topology optimization formulation presented by Sigmund (2009). The threshold projection is given by (Xu et al., 2010),

$$\overline{\rho}_e = \begin{cases} \eta \left\{ \exp\left[-\beta\left(1 - \frac{\widetilde{\rho}_e}{\eta}\right)\right] - \left(1 - \frac{\widetilde{\rho}_e}{\eta}\right)\exp\left(-\beta\right)\right\}, & 0 \le \widetilde{\rho}_e \le \eta \\ (1-\eta)\left[1 - \exp\left(-\beta\frac{\widetilde{\rho}_e - \eta}{1-\eta}\right) + \frac{\widetilde{\rho}_e - \eta}{1-\eta}\exp\left(-\beta\right)\right] + \eta, & \eta < \widetilde{\rho}_e \le 1 \end{cases} \tag{3.2}$$

where $\eta \in [0,\ 1]$ is the threshold, β is the regularization parameter and $\widetilde{\rho}_e$ is the filtered density of element e, calculated by

$$\widetilde{\rho}_e = \frac{\sum\limits_{j \in Ne} w\left(\mathbf{r}_j\right) v_j \rho_j}{\sum\limits_{j \in Ne} w\left(\mathbf{r}_j\right) v_j}. \tag{3.3}$$

here ρ_j is the design variable in element j, $\mathbf{r}_j = (x_j,\ y_j)$ and v_j is the centroid and the volume of element j, N_e is the neighborhood of element e within a certain filter radius r specified by $N_e = \{j \mid \|\mathbf{r}_j - \mathbf{r}_e\| \leq r\}$, and $w(\mathbf{r}_j)$ is the weight factor of element j, obtained by $w(\mathbf{r}_j) = r - \|\mathbf{r}_j - \mathbf{r}_e\|$.

Alternatively, the threshold projection can be written in a simpler form as

$$\overline{\rho}_e = \frac{\tanh(\beta\eta) + \tanh(\beta(\widetilde{\rho}_e - \eta))}{\tanh(\beta\eta) + \tanh(\beta(1-\eta))}. \tag{3.4}$$

These two threshold projections behave similarly in the optimization procedure.

3.1.2 Material mask overlay strategy

The geometry of the design can also be described by a set of circles using the MMOS, where the regions within the circles are occupied by air and the regions outside are occupied by the solid material, as illustrated in Fig. 3.2. The elemental quantity $\overline{\rho}_e$ of element e at the location $\mathbf{r}_e = (x_e,\ y_e)$ generated from the ith circle is calculated using a regularized Heaviside function,

$$H(\mathbf{r}_e, \mathbf{y}_i, r_i) = \frac{1}{1 + \exp\left(-\beta\left(\frac{\|\mathbf{r}_e - \mathbf{y}_i\|^2}{r_i^2} - 1\right)\right)} \tag{3.5}$$

where $\mathbf{y}_i = (x_i,\ y_i)$ and r_i are the location and radius of the ith circle and β is the regularization parameter. The final quantity $\overline{\rho}_e$ of element e generated from all M circles is calculated by

$$\overline{\rho}_e = \prod_{i=1}^{M} H(\mathbf{r}_e, \mathbf{y}_i, r_i) \tag{3.6}$$

Both the locations and radii of the circles can be chosen as design variables in the MMOS.

3.2 Robust topology optimization formulations

3.2.1 Standard topology optimization and numerical procedures

Based on the parameterizations of structures, all the optimization problems considered in this thesis can be described using a general form, given by

$$\begin{array}{lll} \min\limits_{\mathbf{x}} & f(\overline{\boldsymbol{\rho}}, \mathbf{u}) & \text{Objective function} \\ s.t. & \mathbf{K}(\overline{\boldsymbol{\rho}})\,\mathbf{u} = \mathbf{b} & \text{State equations} \\ & f_i(\overline{\boldsymbol{\rho}}, \mathbf{u}) \leq 0 \quad \forall i \in [1, N] & \text{Constraints} \\ & \mathbf{a}_1 \leq \mathbf{x} \leq \mathbf{a}_2 & \text{Box constraints} \end{array} \tag{3.7}$$

where $\mathbf{x}$ is the design variable vector, i.e. the element-wise variables in the density approach, and the radii and locations of the circles in the MMOS, N is the number of constraints, $\mathbf{a}_1$ and $\mathbf{a}_2$ are the lower and upper bound vectors of the design variables.

The sensitivity of the objective and constraints with respect to design variables is calculated using adjoint sensitivity analysis (Bendsøe and Sigmund, 2003; Christensen and Klarbring, 2009) and the chain rule (Sigmund, 2007).

Based on the sensitivity analysis, the structure is iteratively updated using a gradient-based optimization algorithm, such as the method of moving asymptote (MMA) (Svanberg, 1987) and globally convergent version of method of moving asymptote (GCMMA) (Svanberg, 2001). Most of the employed methods are based on solving the convex approximations of the nonlinear problems. All the optimized designs in this thesis have been obtained using MMA, GCMMA or "Fmincon" in Matlab. The algorithms for individual subjects can be found in the relevant papers and will not be specified in the thesis.

In order to obtain a pure 0 and 1 design, a continuation scheme may be employed on the regularization parameter in Eqs. (3.2) and (3.4) as $\beta = \tau\beta$ with $\tau > 1$. The whole optimization procedure is briefly outlined as follows

1. Set the design domain and choose η for the density approach
2. Initialize the design variable vector $\mathbf{x}$
3. Compute the design realization ($\overline{\boldsymbol{\rho}}$) and solve the problems using FEM
4. Calculate objectives, constraints and corresponding sensitivities
5. Update the design variable vector $\mathbf{x}$ using the optimization algorithm
6. Update the regularization parameter using $\beta = \tau\beta$, for every mth iteration or when the stop criterion on change of design variables or objective is satisfied. m is a constant integer as $m = 40$ or $m = 50$.
7. Repeat steps 3 - 6 until the stop criterion is fulfilled and $\beta \geq \beta_{max}$

As a test case, a compliant inverter is optimized using the density approach, to maximize the negative lateral displacement (u_{out}) at the output port for a given input force ($f_{\text{in}} = 1$), see Fig. 3.3 (a). Only the bottom half part of the structure is modeled according to the structural symmetry. The input and output ports are modeled using springs with the stiffness coefficients of $k_{\text{in}} = 1$ and $k_{\text{out}} = 0.001$. The interpolated material property is Young's moduli with $A_2 = 1.0$ for the solid material and $A_1 = 10^{-9}$ for air, and the penalty parameter is set to be $p = 3$. The constraint in this problem is the volume fraction of the solid material, stated as $f \leq 30\%$. The design is discretized using 180×90 quadrilateral four-node elements, and the updating scheme of β is set to be $\beta = 2\beta$ with $\beta_{\text{max}} = 128$.

The optimized design is depicted in Fig. 3.3 (b). The optimized design is generated using a threshold of $\eta = 0.5$ with a filter radius of $r = \frac{7}{225}l$ represented by the dashed circle in Fig. 3.3 (b). The one or two nodes connected hinges are observed in the optimized design. A slight erosion due to manufacturing imperfections will disconnect the output port from the input port, hence discard the optimized performance completely. Therefore, the design robustness has to be enhanced in the optimization procedure to guarantee the performance of the fabricated structure under certain manufacturing imperfections.

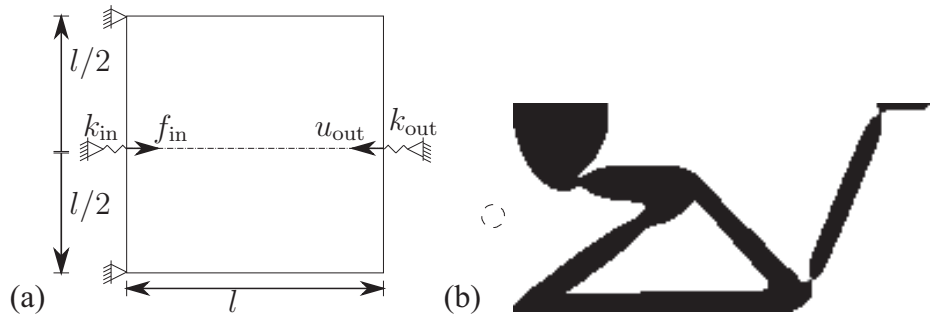

Figure 3.3 (a) Sketch of the compliant inverter problem. The objective is to maximize the displacement at the output port (u_{out}) for an input force f_{in}. (b) Standard topology optimized compliant inverter. The dashed circle shows the filter size.

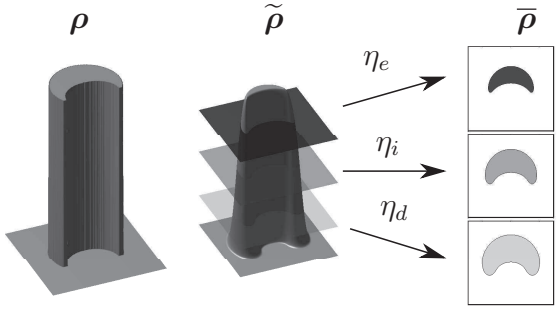

Figure 3.4 Illustration of the threshold projection for different fabrication processes.

3.2.2 Robust topology optimization

In an etching process, the fabricated samples obtained from under-, ideal- or over-etching process can be modeled by the threshold projection using different thresholds, i.e. η_d, η_i and η_e for the under-, ideal- and over-etching processes as illustrated in Fig. 3.4, or by a radius variation as $r_i - \Delta r$, r_i and $r_i + \Delta r$ in the MMOS. In order to take the manufacturing imperfections into account in the design procedure, the goal of the optimization problem is modified to optimize the performance of the worst case among the three different design realizations, such that the performance of the design with respect to the under- and over-etching processes can be ensured. The worst case optimization formulation is realized using a bound formulation, i.e. a new variable $f_{\max}$ is introduced to represent the maximum value of the objectives, stated as

$$\begin{array}{lll} \min\limits_{\mathbf{x}} & f_{\max} & \\ s.t. & f\left(\overline{\boldsymbol{\rho}}^q, \mathbf{u}\right) \leq f_{\max} & \text{Objective funtions} \\ & \mathbf{K}\left(\overline{\boldsymbol{\rho}}^q\right)\mathbf{u} = \mathbf{b} & \text{State equations} \\ & f_i\left(\overline{\boldsymbol{\rho}}^q, \mathbf{u}\right) \leq 0 \quad \forall i \in [1, N] & \text{Constraints} \\ & \mathbf{a}_1 \leq \mathbf{x} \leq \mathbf{a}_2 & \text{Box constraints} \end{array} \tag{3.8}$$

where $\overline{\boldsymbol{\rho}}^q$ denotes the three different realizations with $q \in [e,\ i,\ d]$.

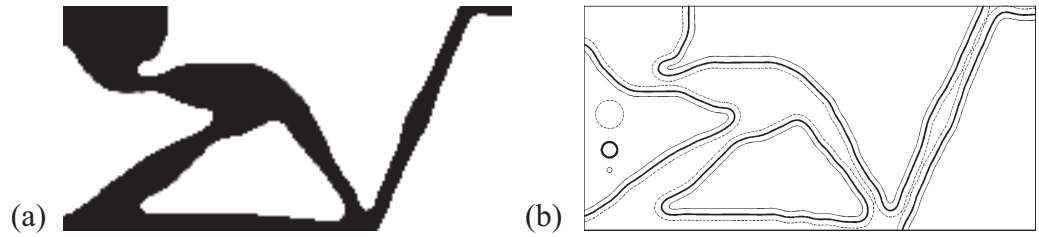

Figure 3.5 (a) Robust topology optimized compliant inverter. (b) Illustration of the different design realizations considered. The dashed circle denotes the filter size, the bold solid circle denotes the minimal length scale on the optimized design represented by the bold solid lines, and the solid circle denotes the manufacturing tolerance considered.

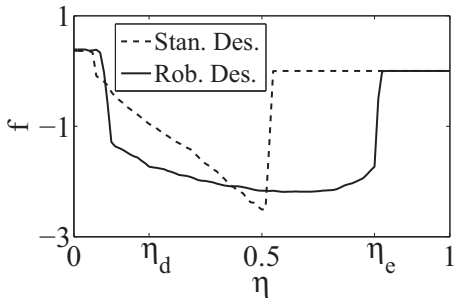

Figure 3.6 Performance of the different optimized designs under manufacturing imperfections. The dashed and solid lines show the standard and robust designs, respectively.

In the following part, the feasibility of the presented robust topology optimization is evaluated through designing the compliant inverter. The thresholds are chosen to be [0.2, 0.5, 0.8] with the identical resolution and filter radius as in the previous case. The final design is shown Fig. 3.5 (a). Compared to the standard topology optimized design shown in Fig. 3.3, no hinges can be observed in the robust topology optimized design. The three different design realizations are illustrated in Fig. 3.5 (b), where the bold solid lines denote the robust optimized design, i.e. the blueprint design for fabrications, the solid lines denote the dilated design realization from the under-etching process and the dotted lines denote the eroded design realization from the over-etching process. All the three design realizations possess the same topology, hence a minimal length scale can be observed in the blueprint design in both phases. The detailed discussions and calculations of the minimal length scale can be found in the paper [P2]. Moreover, an analytical calculation of the minimal length scale has been recently presented by Qian and Sigmund (2012).

In order to evaluate the design robustness with respect to manufacturing imperfections, 101 different design realizations generated by 101 uniformly distributed thresholds in the interval of $[0, 1]$ are calculated. Fig. 3.6 depicts the performances of the standard topology optimized design (dashed line) and the robust topology optimized design (solid line). As mentioned above, a slight erosion ruins the optimized

performance of the standard topology optimized design. In contrast, the robust design still exhibits a good performance under certain manufacturing imperfections. However, it is noted that the design robustness is enhanced at the expense of the objective, f, of the blueprint design ($\eta = 0.5$).

As shown in Fig. 3.6, the performance of the robust topology optimized compliant inverter varies smoothly with the manufacturing errors in the range of $[\eta_d,\ \eta_e]$, hence three design realizations are sufficient to ensure the performance of the optimized design. In case that the structural performance is more sensitive to the manufacturing errors, more design realizations should be taken into account to enforce the design robustness. To simplify the problem, this thesis assumes that there are uniform manufacturing errors in the fabricated structures. Beside the presented approach, the design robustness can also be enhanced using a stochastic robust formulation presented by Lazarov et al. (2011).

Chapter 4
Dispersion engineered slow light waveguides [P3] – [P4]

Slow light propagation effects prevail in PhCWs when approaching the band edge of PhCWs. However, the slow light propagation in PhCWs displays high group velocity dispersion (GVD), hence causing severe optical signal distortions and restricting operating bandwidth. Moreover, slow light propagation is sensitive to the structural geometry, and manufacturing errors, e.g. dilation and erosion, may degrade the prescribed slow light effects in the PhCWs. Although many studies have proposed different slow light PhCWs with tailored dispersion using trial-and-error methods, a systematic robust design approach is still highly desirable in the dispersion engineering of PhCWs, from the fabrication point of view.

This chapter employs the robust optimization formulation presented in the previous chapter to perform systematic dispersion engineering of PhCWs. Based on the two different parameterizations, the fixed- (circular-holed based) and free-topology slow light waveguides are designed for prescribed group indices, and the detailed comparisons highlight the corresponding capabilities and limitations. This chapter gives an overview of the work presented in the papers [P3] and [P4].

4.1 Optimization formulations for dispersion engineering

Previous studies (Frandsen et al., 2006; Li et al., 2008; Schulz et al., 2010) have shown that the dispersion curve of PhCWs can be tailored by altering the geometry of the periodic supercell. The goal in this chapter is to design slow light waveguides in a systematic manner by reformulating dispersion engineering in PhCWs as an optimization problem.

Based on the generalized interpolation formulation presented in Eq. (3.1), the elemental permittivity in Eq. (2.10) is interpolated as

$$1/\varepsilon_e = 1/\varepsilon_1 + \overline{\rho}_e \left(1/\varepsilon_2 - 1/\varepsilon_1\right) \tag{4.1}$$

where ε_e is the relative permittivity of element e, and ε_1 and ε_2 are the relative permittivity of air and the dielectric material considered.

Using the $\omega\left(k\right)$-formulation, the dispersion engineering in PhCWs is achieved by minimizing the errors between actual group index, n_g, and a prescribed group index, n_g^*, in a given wavenumber range,

$$\min_{\mathbf{x}} \quad \max_{q} \quad \max_{k_i} \quad f\left(\overline{\boldsymbol{\rho}}^q\right) = \left(n_g\left(\overline{\boldsymbol{\rho}}^q, k_i\right)/n_g^* - 1\right)^2 \tag{4.2}$$

here $k_i \in [k_1,\ k_2]$ is the designed wavenumber with $[k_1,\ k_2]$ denoting the designed wavenumber range, $\mathbf{x}$ denotes the design variable vector, and $\overline{\boldsymbol{\rho}}^q$ represents different design realizations from the manufacturing process. Both the density approach and the MMOS are employed here to design slow light waveguides with free- and fixed-topology, respectively. Since the locations of air holes can be controlled more accurately in the electron beam fabrication process than the radii (Schulz et al., 2010), the location misplacement is thus neglected in the optimization procedure. The different design realizations are generated using different thresholds of $\eta \in [\eta_1,\ \eta_2]$ in the density approach, or using a small radius variation of air holes Δr in the MMOS. In both methods, the ideal design realization corresponds to the blueprint design for fabrications.

Multiple guided modes at one designed frequency may cause intermodal scattering (Kuramochi et al., 2005), hence band separation constraints are implemented to push the bands below and above away from the designed band, stated as

$$\omega_{n-1}\left(\overline{\boldsymbol{\rho}}^q, k_{ii}\right) \leq a_1\ \min\left(\omega_n\left(\overline{\boldsymbol{\rho}}^q, k_i\right)\right), \quad \omega_{n+1}\left(\overline{\boldsymbol{\rho}}^q, k_{ii}\right) \geq a_2\ \max\left(\omega_n\left(\overline{\boldsymbol{\rho}}^q, k_i\right)\right) \tag{4.3}$$

here k_{ii} is the specified wavenumber in the range of $[0,\ \pi/a]$, n is the order of the designed band, a_1 and a_2 are the prescribed numbers defining how far the designed band is separated from the other bands.

In addition, isolated components, that are unfavorable for fabrications, may appear in the fine tuned free-topology designs. The isolated components in the supercell result in zero fundamental frequencies in a free structural vibration problem, hence can be circumvented by a fundamental frequency constraint. The corresponding details can be found in the paper [P3]. In the MMOS, the design connectivity is ensured by the bound constraints of radii. The sensitivity analysis of the objective and constraints has been presented in the papers [P3] and [P4].

4.2 Dispersion engineered slow light waveguides

In this section, the optimization formulation for dispersion engineering is evaluated by designing free- and fixed-topology slow light waveguides for $n_g^* = 80$. The initial design is chosen as a conventional waveguide shown in Fig. 2.4. The design domain in the density approach is set to the first three and a half rows of air holes adjacent to the waveguide core represented by the gray rectangle in Fig. 4.1 (a), and the design variables in the MMOS are the locations and radii of the first two rows of air holes adjacent to the waveguide core and the radius of the remaining air holes shown in Fig. 4.1 (b). The symmetry is enforced along the waveguide direction by setting the same design variables at the symmetrical locations. However, asymmetrical waveguides can also be engineered to support dispersionless slow light propagation (Ma and Jiang, 2008; Colman et al., 2012). The asymmetrical dispersion engineered waveguides can be achieved using the presented optimization formulation by eliminating the symmetrical condition along the waveguide direction.

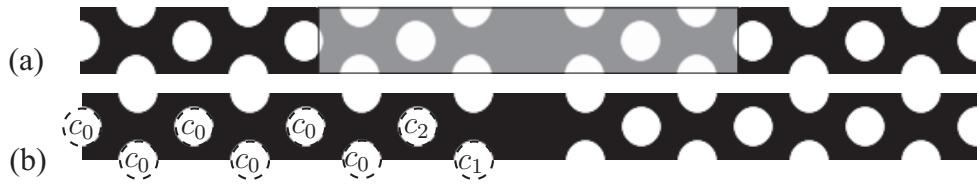

Figure 4.1 Design domains for different parameterizations. (a) Design domain in the density approach. (b) Design domain in the MMOS.

In the free-topology waveguides, the design robustness is realized by considering different design realizations generated by different thresholds of $\eta \in [0.35,\ 0.65]$ with a filter radius of $r = a/8$. This threshold interval is chosen to mimic an approximate etching variation of $\pm 0.02a$. For the fixed-topology waveguides, the design robustness is realized by considering different design realizations generated by small radius variations of $\Delta r \in [-0.02,\ 0.02]\, a$.

In order to systematically evaluate the free- and fixed-topology optimized slow light waveguides, this thesis employs the group index bandwidth product (GBP) and the GVD parameter as figures of merit. The GBP is used to represent the trade-off between high group index and large bandwidth, given as

$$GBP = \langle n_g \rangle \, \Delta\omega/\omega_0 = \langle n_g \rangle \, \Delta\lambda/\lambda_0 \tag{4.4}$$

here $\langle n_g \rangle$ is the average group index and $\Delta\omega$ ($\Delta\lambda$) is the bandwidth centered at ω_0 (λ_0) where the GVD is negligible. In practice, a relative group index error of $\pm 10\%$ is utilized to indicate the acceptable GVD region. The GVD parameter is defined to quantify the GVD, stated as

$$GVD = \frac{\partial^2 k}{\partial w^2} = -\frac{1}{v_g^3}\frac{\partial v_g}{\partial k} \tag{4.5}$$

4.2.1 Free-topology dispersion engineered waveguides

In the first example, a free-topology slow light waveguide is designed for $n_g^* = 80$ in a given wavenumber range $k_i \in [0.34,\ 0.36]\, 2\pi/a$. Following the optimization procedure in the previous chapter, three design realizations are firstly considered to enhance the design robustness as $\boldsymbol{\eta} = [0.35,\ 0.5,\ 0.65]$. The study in the paper [P3] has demonstrated that the design robustness of slow light waveguides for $n_g^* < 40$ can be enhanced by the 3-case robust optimization formulation. However, slow light propagation with a high group index of $n_g^* \geq 40$ is expected to be more sensitive to manufacturing imperfections because of large modal profiles associated with high group indices. Fig. 4.2 (a) shows the performance of the 3-case optimized design with respect to different manufacturing process mimicked by 101 uniformly distributed thresholds in the interval of $[0.35,\ 0.65]$. The asterisks represent group indices at 20 uniformly distributed wavenumbers in the designed wavenumber range

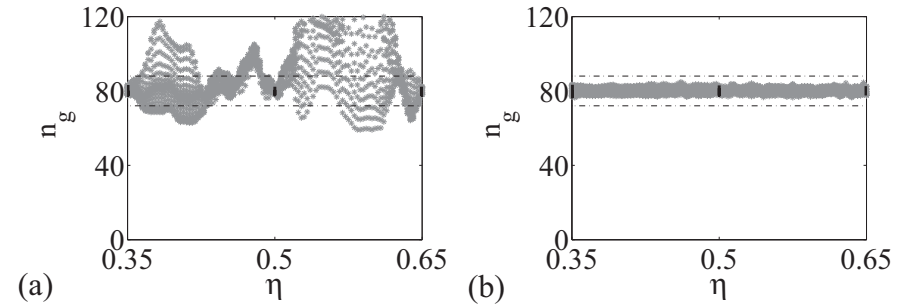

Figure 4.2 Performance of the optimized designs for $n_g^* = 80$ with respect to different manufacturing errors. (a) Performance of the 3-case robust design. The asterisks illustrate the performances of different design realizations in the designed wavenumber range, the solid lines display the performances of the three design realizations considered in the optimization procedure, and the dash-dot lines show the ±10% range. (b) Performance of the 51-case robust design.

for each design realization, while the solid lines represent the three considered design realizations. It is noted that three design realizations are not sufficient to ensure the design robustness for $n_g^* = 80$, albeit these three design realizations display promising performances. Hence, more design realizations have been considered in the paper [P4] to enhance the design robustness of the optimized waveguides for high group indices. 51 design realizations have been taken into account in the paper [P4] to enhance the design robustness of slow light waveguides. It is apparent that 51 design realizations are sufficient to ensure the robustness of the designed slow light waveguide with respect to the manufacturing errors considered here, as shown in Fig. 4.2 (b).

The detailed characteristics of the 51-case robust design are described in Fig. 4.3. Fig. 4.3 (b) illustrates the manufacturing errors considered in the optimization procedure with the bold lines representing the blueprint design, the dotted lines representing the eroded design realization for $\eta = 0.65$ and the solid lines denoting the dilated design realizations for $\eta = 0.35$. In contrast to the compliant inverter in the previous chapter, the different design realizations do not share the same topology in this case, hence no minimal length scale can be guaranteed for the blueprint design. Nevertheless, due to the design robustness, the length scale is not essential from the fabrication point of view (Lazarov et al., 2011). The detailed performances of the blueprint design are shown in Fig. 4.3 (c). Fig. 4.3 (d) shows the group indices of the different design realizations, where the gray region indicates the group index range from the 101 different design realizations and the solid line depicts the group index plot of the blueprint design. A small group index variation is observed in the blueprint design with respect to the prescribed group index represented by crosses. The blueprint design achieves a GBP of 0.49 centered at $\omega_0 = 0.2586\ 2\pi c/a$ with $\langle n_g \rangle = 80.29$. It is observed that the actual wavenumber range for the slow light propagation is larger than the prescribed one when the ±10% criterion is utilized.

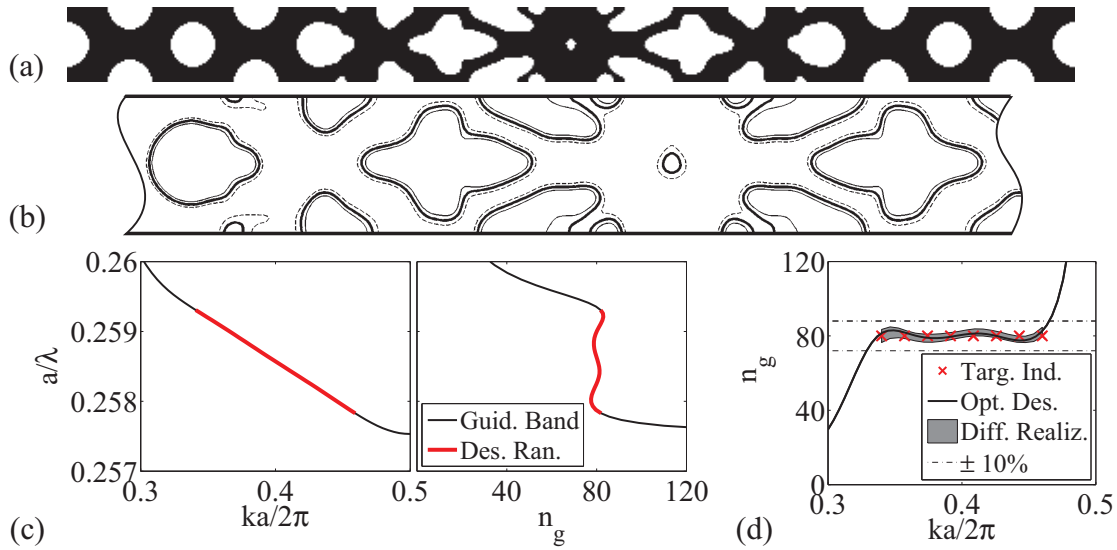

Figure 4.3 Characteristics of the free-topology robust design for $n_g^* = 80$. (a) Blueprint design. (b) Illustration of the manufacturing errors considered, the bold solid, dotted and solid lines show the contour plots of the blueprint design, the design realization of $\eta = 0.65$ and the design realization of $\eta = 0.35$, respectively. (c) Characteristics of the designed band in the blueprint design. The bold solid lines indicate the designed range. (d) Group index versus wavenumber. The gray region indicates the group index range of the 101 design realizations, the crosses display the prescribed target, the solid line denotes the performance of the blueprint design and the dash-dot lines illustrate the ±10% range.

It must be pointed out that the frequencies of the design modes shift upwards from the dilated design realization to the eroded design realization due to the volume fraction reduction of the dielectric material (Joannopoulos et al., 2008).

4.2.2 Fixed-topology dispersion engineered waveguides

A robust fixed-topology dispersion engineered waveguide is designed for $n_g^* = 80$ by considering 51 design realizations. Previous studies (Frandsen et al., 2006; Li et al., 2008; Schulz et al., 2010) have illustrated that the fixed-topology dispersion engineered waveguides exhibit a GBP around 0.3, hence the designed wavenumber range is narrowed to be $k_i \in [0.39,\ 0.45]\, 2\pi/a$ in this case.

The characteristics of the optimized fixed-topology slow light waveguide are depicted in Fig. 4.4. Fig. 4.4 (b) illustrates the manufacturing error considered, here it is slightly smaller than the one in the free-topology optimized design. The blueprint design achieves an average group index of $\langle n_g \rangle = 81.52$ with a GBP of 0.30 centered at $\omega_0 = 0.2150\ 2\pi c/a$ shown in Fig. 4.4 (c). It is noted that the group index variation of different design realizations (see Fig. 4.4 (d)) is slightly out of the range of ±10%. Nevertheless, the limited group index error ensures that signal distortions are restricted in the designed slow light PhCW.

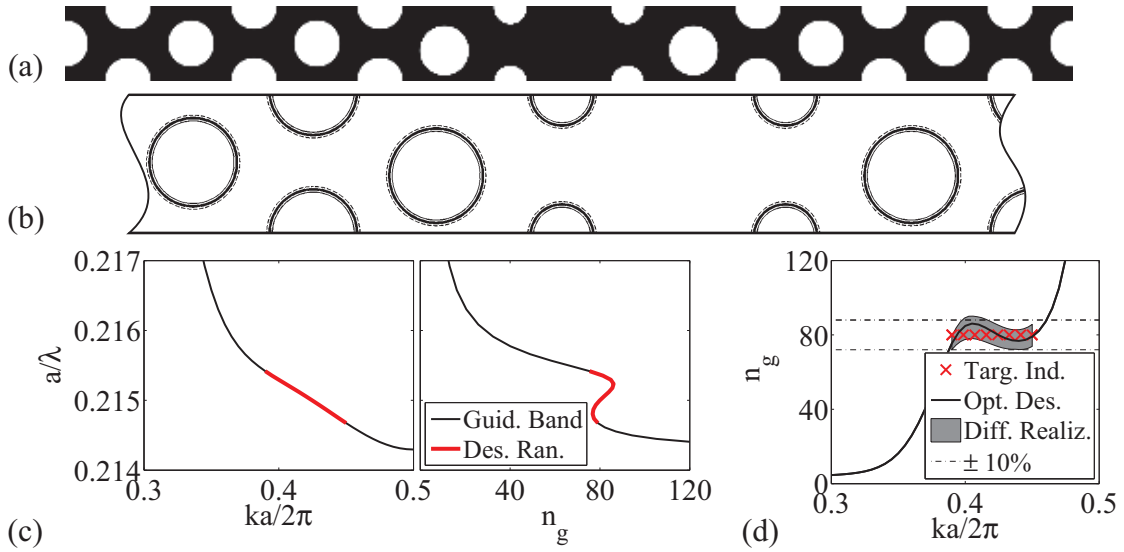

Figure 4.4 Characteristics of the fixed-topology robust design for $n_g^* = 80$. (a) Blueprint design. (b) Illustration of the manufacturing errors considered. (c) Characteristics of the designed band in the blueprint design. (d) Group index versus wavenumber.

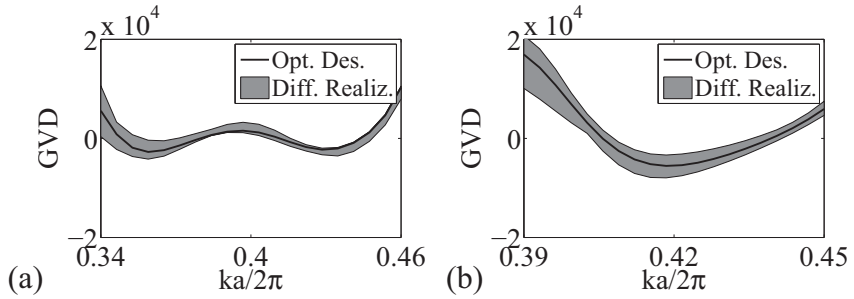

Figure 4.5 GVD comparison of the free- and fixed-topology robust designs. (a) GVD parameter of the free-topology robust design. The gray region indicating the GVD range of the 101 different design realizations. (b) GVD parameter of the fixed-topology robust design.

4.2.3 Comparisons and conclusions

The detailed studies on the free- and fixed-topology dispersion engineered waveguides show that the design robustness of the dispersion engineered waveguides has been enhanced by the robust optimization formulation, and that the GBP has been enlarged by a factor of 1.63 when allowing irregular topologies. Moreover, the GVD of the designed modes has been significantly suppressed in the free-topology waveguide, as shown in Fig. 4.5.

It need to be highlighted that, by using the systematic approach, other desirable functionalities beside the group index can be prescribed as constraints in the optimization formulations, e.g. high modal confinement and low field intensity in

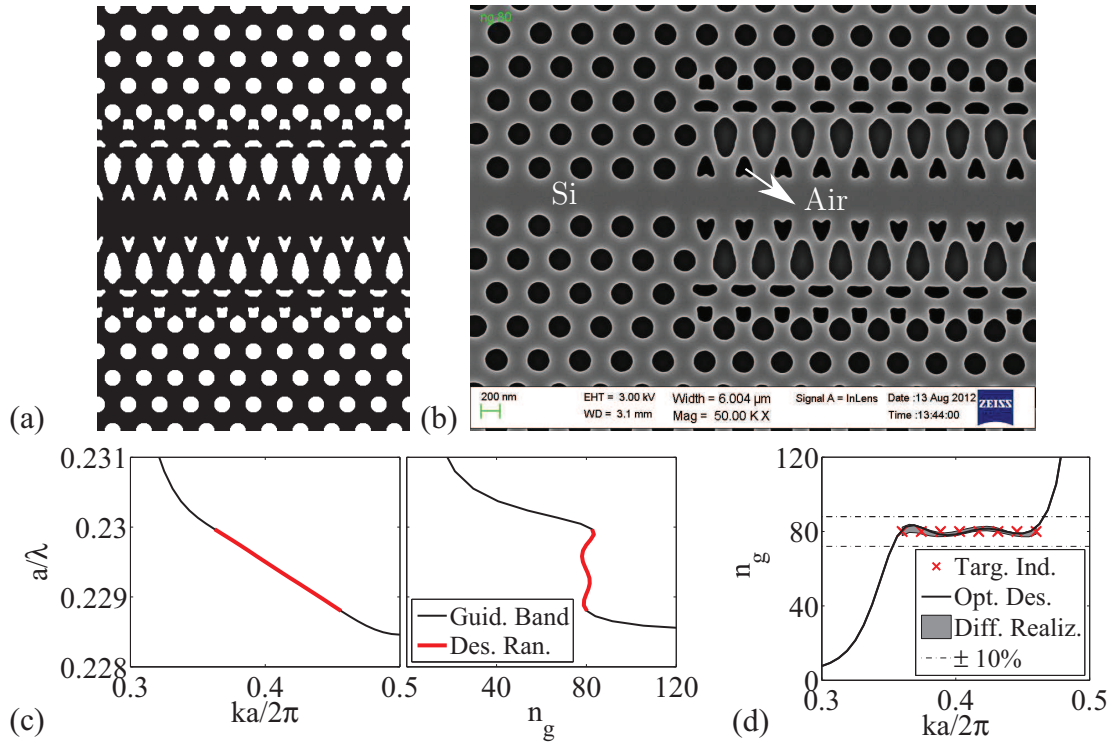

Figure 4.6 (a) Dispersion engineered slow light waveguide for $n_g^* = 80$ with high modal confinements. (b) Fabricated sample of the dispersion engineered waveguide. (c) Propagation characteristics of the designed band in the blueprint design. (d) Group index versus wavenumber.

the air holes. The corresponding details can be found in the paper [P4]. Beside the dispersion curve engineering presented in this thesis, slow light waveguides can also be systematically designed using a pulse delaying optimization scheme (Matzen et al., 2011).

Several robust dispersion engineered waveguides are fabricated in silicon-on-insulator (SOI) materials with a top silicon layer and a buried silicon dioxide layer in the Department of Photonic Engineering, Technical University of Denmark, and are going to be characterized. Fig 4.6 (b) shows a scanning electron micrograph (SEM) image of one fabricated sample for $n_g^* = 80$ with the left part as a coupling waveguide (White et al., 2008) [1]. Fig 4.6 (a) shows the corresponding blueprint waveguide. The blueprint waveguide facilitates slow light propagation with modal confinements bigger or equal to 0.4 at the waveguide core of $a \times \sqrt{3}/2a$. Fig. 4.6 (c) depicts the detailed propagation characteristics in the blueprint waveguide. Compared to the one in Fig. 4.3, the center frequency of the designed slow light propagation is pushed down using a center frequency constraint. The blueprint design supports

[1] All the SEM images of the fabricated sample are provided by Lars Hagedorn Frandsen in the Department of Photonic Engineering, Technical University of Denmark.

slow light propagation with $\langle n_g \rangle = 80.51$ centered at $\omega_0 = 0.2293\ 2\pi c/a$. The slow light propagation achieves a GBP of 0.44. The reduction of GBP in the case is attributed to a smaller prescribed wavenumber range of $k_i \in [0.36,\ 0.46]\, 2\pi/a$. The detailed comparisons between the blueprint waveguide and the fabricated sample illustrate that the free-topology optimized slow light waveguides can be fabricated using the current nanofabrication technology.

Chapter 5
Loss engineered slow light waveguides [P5]

Slow light propagation in PhCWs encounters large propagation loss due to manufacturing imperfections, in particular, the scattering loss at the interface between air and the dielectric material. Recent numerical and experimental studies from Petrov et al. (2009), O'Faolain et al. (2010) and Baron et al. (2011) have demonstrated that the propagation loss of slow light can be engineered through changing the field intensity available for scattering.

By assuming that propagation loss will be minimized if the optical intensity overlapping with hole edges is minimized, this chapter explores the use of a systematic method for designing waveguides with minimized propagation loss due to fabrication-related disorder effects. The scattering loss is represented using an edge-related loss and modeled by an imaginary part of the permittivity (Benisty et al., 2000; Ferrini et al., 2003, 2006). The propagation loss of the guided modes is directly evaluated using the $k(\omega)$-formulation. This chapter gives a brief summary on the paper [P5].

5.1 Optimization formulations for loss engineering

Backscattering induced by manufacturing imperfections has been reported to be the dominant loss mechanism in the slow light regime and has to be taken into account in the design procedure. In order to mimic the loss induced by surface roughness, a phenomenological approach presented by Benisty et al. (2000) and Ferrini et al. (2003, 2006) is adopted. The scattering loss is represented by an edge-related dissipation, i.e. an imaginary part of the permittivity.

Based on the threshold projection in Eq. (3.4), the interface between air and dielectric material can be described using a normalized quantity $\nu_e \in [0,\ 1]$, defined as the normalized derivative of the quantity, $\overline{\rho}_e$, with respect to the filtered density, $\widetilde{\rho}_e$,

$$\nu_e = 1 - \left(\tanh\left(\beta\left(\widetilde{\rho}_e - \eta\right)\right)\right)^2 \tag{5.1}$$

where the interface lies at $\nu_e > 0$. The final element-wise permittivity is now interpolated as

$$\varepsilon_e = \varepsilon_1 + \overline{\rho}_e\left(\varepsilon_2 - \varepsilon_1\right) + i{\nu_e}^p \varepsilon_0'' \tag{5.2}$$

with $p = 0.5$ and $\varepsilon_0'' = 0.1$. The value of $\varepsilon_0'' = 0.1$ is chosen to quantitatively evaluate the propagation loss in different designs for comparisons, and the magnitude does not affect neither the conclusions nor the designs presented in the following section.

It should be emphasized that a linear interpolation on the permittivity has been chosen to integrate the permittivity and the edge-related loss in a straightforward

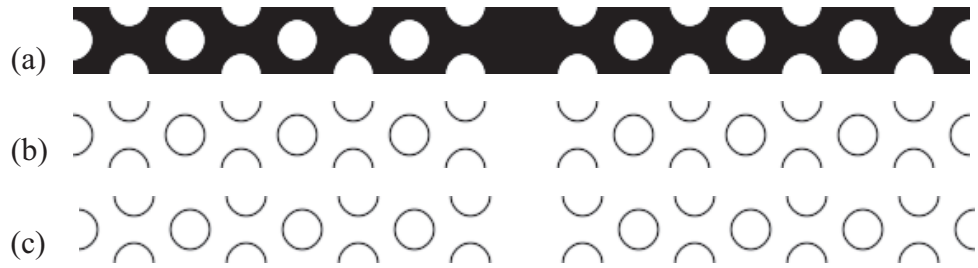

Figure 5.1 Illustration of the interface detection between air and dielectric material using two parameterizations. (a) Periodic supercell. (b) Normalized quantities $\boldsymbol{\nu}$ in the density approach. (c) Normalized quantities $\boldsymbol{\nu}$ in the MMOS.

manner. However, the interpolation scheme in the previous chapter can also be modified to include the edge-related dissipation.

As presented in the previous chapters, the element-wise quantities $\boldsymbol{\rho}$ are the design variables in the density approach. In order to employ the same edge-related loss scheme for both free- and fixed-topology waveguides, the element-wise quantities $\boldsymbol{\rho}$ are mapped using a set of circles in the MMOS, where ρ_e equals to zero when element e is within circles and ρ_e equals to one when e is outside of circles. Fig. 5.1 shows the interface detection using the normalized quantities $\boldsymbol{\nu}$ in the density approach and the MMOS. It's seen that the interfaces between air and dielectric material are accurately identified in both parameterizations.

Using the $k(\omega)$-formulation, the propagation loss of the guided modes can be directly evaluated, and loss engineering of slow light waveguides can be formulated as an optimization problem. The loss engineering can be realized by minimizing either the average propagation loss of the designed modes focusing on the average behavior, or by minimizing the maximal propagation loss of the designed modes emphasizing the largest propagation loss within the designed frequency range. Here, the first variant is employed and the optimization problem for the loss engineering is formulated as:

$$\begin{aligned} \min_{\mathbf{x}} \quad & f(\overline{\boldsymbol{\rho}}) = \sum_{\omega_i} \left(\Im\left(k\left(\overline{\boldsymbol{\rho}}, \omega_i\right)\right)\right) \\ s.t. \quad & \left(n_g\left(\overline{\boldsymbol{\rho}}, \omega_i\right)/n_g^* - 1\right)^2 < e_r^2 \\ & \left\langle n_g\left(\overline{\boldsymbol{\rho}}, \omega_i\right)\right\rangle \geq n_g^* \end{aligned}$$

where $\omega_i \in [\omega_1,\ \omega_2]$ is the designed frequency with $[\omega_1,\ \omega_2]$ being the designed frequency range, $0 \leq e_r \leq 1$ is the relative group index error, indicating the allowed GVD. The constraint on the average group index, $\langle n_g(\overline{\boldsymbol{\rho}}, \omega_i)\rangle$, is introduced to ensure that the average group index of the designed slow light propagation is equal to or bigger than the prescribed one.

In addition, band separation constraints have to be imposed to avoid the intermodal scattering. However, it is problematic to classify the bands in the order of increasing frequency in the $k(\omega)$-formulation. Thus, the bands below and above the designed band are calculated using the $\omega(k)$-formulation. The details of the

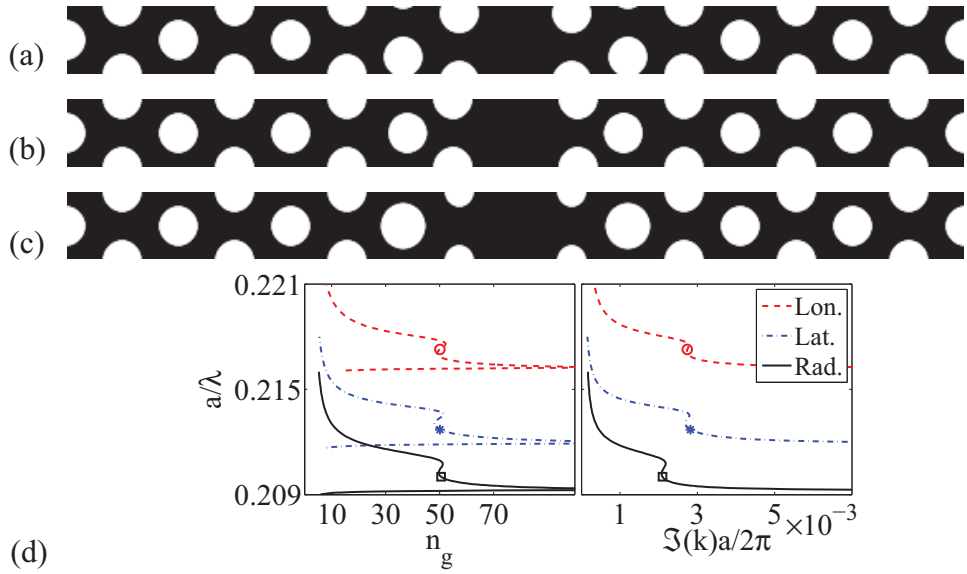

Figure 5.2 Fixed-topology dispersion engineered waveguides for $n_g^* = 50$. (a) Longitudinal location tuned waveguide. (b) Lateral location tuned waveguide. (c) Radius tuned waveguide. (d) Performance of different waveguides. Left panel: Group index plot. Right panel: Propagation loss. The dashed, dash-dot and solid lines represent the performances of the longitudinal location, lateral location and radius tuned waveguides, respectively. The markers indicate the slow light modes for further study.

band separation constraints have been stated in the previous chapter. The reader is referred to the paper [P5] for the detailed sensitivity analysis of the objective and constraints with respect to the design variables.

5.2 Loss engineered slow light waveguides

In this section, the loss mechanisms are firstly investigated by studying the propagation loss in different fixed-topology dispersion engineered waveguides with $n_g^* = 50$ obtained from longitudinal (along the waveguide direction), lateral (normal to the waveguide direction) location and radius tuning, respectively. Then, the loss engineering formulation is evaluated by designing free-topology loss engineered waveguides with an enlarged GBP.

Fig. 5.2 shows three fixed-topology slow light waveguides with $n_g^* = 50$. The detailed characteristics of the guided modes in these three different waveguides are described in Fig. 5.2 (d). These three slow light waveguides display equivalent performances in terms of group index, located at different frequency ranges. The frequency variations between the three waveguides are attributed to the difference in the permittivity and the modal profiles. For each waveguide, the propagation loss variation versus frequency coincides with the group index variation versus frequency. Thus, a high group index seems to be intrinsically linked to high propagation loss

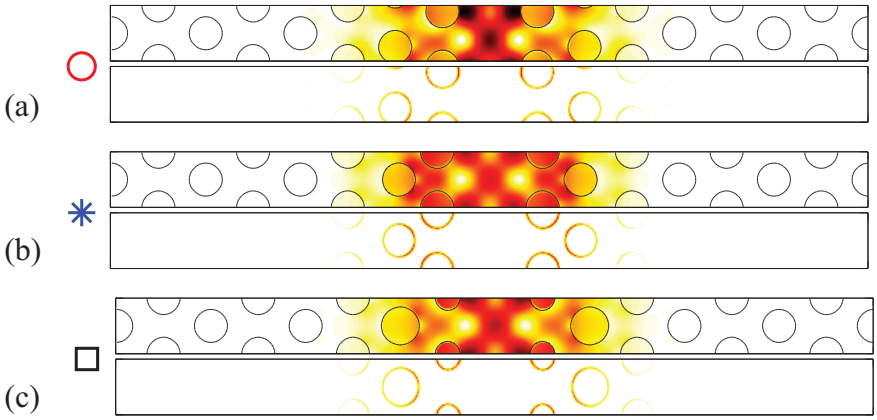

Figure 5.3 Energy density and dissipative energy density of slow light modes with $n_g = 50$ marked in Fig. 5.2 (d). (a) Longitudinal location tuned waveguide. Top: Energy density. Bottom: Dissipative energy density. (b) Lateral location tuned waveguide. (c) Radius tuned waveguide.

due to large modal profiles associated with high group indices. Among them, the radius tuned waveguide displays the smallest propagation loss.

In order to further study the loss mechanisms, the concept of the energy density, $\mathbf{I}_s$, and dissipative energy density, $\mathbf{I}_d$, presented by Nunes et al. (2011) are utilized, given by

$$\mathbf{I}_s = \frac{1}{2}\varepsilon_0\varepsilon_r' \left|\mathbf{E}\right|^2, \qquad \mathbf{I}_d = \frac{1}{2}\varepsilon_0\varepsilon_r'' \left|\mathbf{E}\right|^2 \tag{5.3}$$

here $\mathbf{E}$ is the electric field calculated by $\mathbf{E} = i/\left(\omega\varepsilon_0\varepsilon_r\right)\nabla \times \mathbf{H}$ with $\mathbf{H} = [0\ 0\ H_z]$, and $\varepsilon_r = \varepsilon_r' + i\varepsilon_r''$.

Fig. 5.3 shows the energy density and dissipative energy density of the slow light modes marked in Fig. 5.2 (d) with $n_g = 50$ in the three waveguides. Compared to the radius tuned waveguide, the longitudinal location tuned waveguide exhibits a stronger field intensity at the waveguide core due to a smaller waveguide core, which results in a larger energy dissipation on the interface of the first row of air holes. On the other hand, the stronger field intensity from the second row of air holes in the lateral location tuned waveguide causes a larger energy dissipation on the second row of air holes. Moreover, the radius tuned waveguide has the shortest interface among all the waveguides, which also results in a smaller fraction of field available for scattering at imperfections. The detailed studies on the energy density and dissipative energy density illustrate that the smallest propagation loss is found with the smallest fraction of field intensity involved in scattering at imperfections. This is in a good agreement with recent theoretical and experimental studies from Petrov et al. (2009) and O'Faolain et al. (2010).

GBP is crucial for the applications of slow light devices, thus, a free-topology loss engineered slow light waveguide with an enlarged GBP is designed in the following. The optimization is achieved in two steps. The dispersion engineering is, firstly,

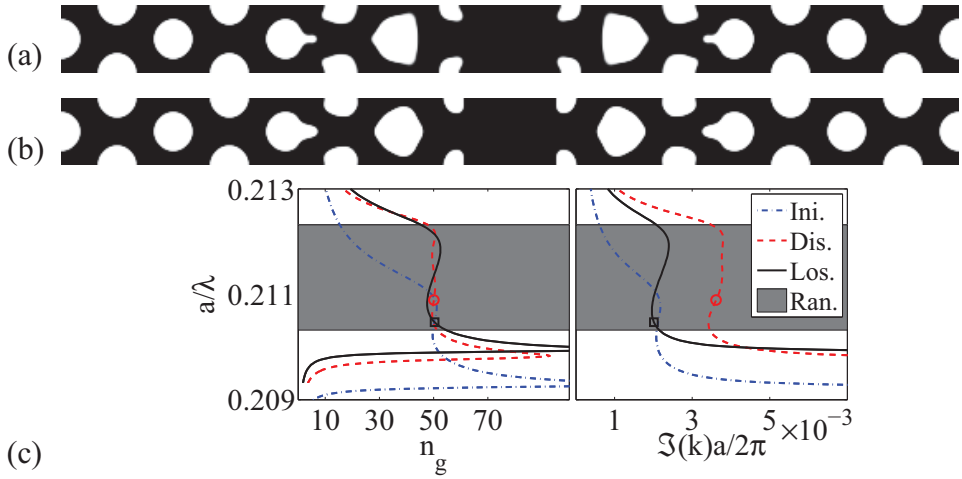

Figure 5.4 Free-topology optimized slow light waveguides with an enlarged GBP for n_g^*=50. (a) Free-topology dispersion engineered waveguide. (b) Free-topology loss engineered waveguide. (c) Group index and propagation loss of different waveguides. The dash-dot, dashed and solid lines represent the performances of the initial design, dispersion and loss engineered waveguides, respectively. The gray regions indicate the design range.

performed to enhance the GBP. Then, the loss engineering is performed to reduce the propagation loss of the designed slow light modes, with the dispersion engineered slow light waveguide as the initial design. The relative group index error is set to $e_r = 0.05$. Using the $k\,(\omega)$-formulation, dispersion engineering is realized by minimizing the errors between actual group index and a prescribed group index for a given frequency range. The design domain is as same as in the previous chapter. The design frequency range is set to be $\omega_i \in [0.2103,\ 0.2123]\,2\pi c/a$ for a GBP of 0.45 with the initial design as the radius tuned waveguide in Fig. 5.2 (c).

Fig. 5.4 shows the dispersion and loss engineered waveguides and corresponding performances in terms of group index and propagation loss. Compared to the radius tuned waveguide, both optimized waveguides achieve much larger GBP. However, the dispersion engineered waveguide encounters significantly higher propagation losses due to the sharp features in the waveguide (see Fig. 5.4 (a)) and the large modal size (see Fig. 5.5 (a)). A significant dissipative energy density can be observed on the third row of air holes in the dispersion engineered design. In contrast to the dispersion engineered slow light waveguide, the loss engineered slow light waveguide has a smooth interface between air and the dielectric material and the corresponding modal size is relatively small. Hence, the propagation loss has been significantly reduced in the loss engineered waveguide and is almost equivalent to the one in the radius tuned slow light waveguide.

The GBP and the average propagation loss in the designed frequency range ($\langle \Im\,(k) \rangle$) are utilized as figures of merit to systematically compare the performance of different waveguides. The detailed characteristics of the aforementioned waveg-

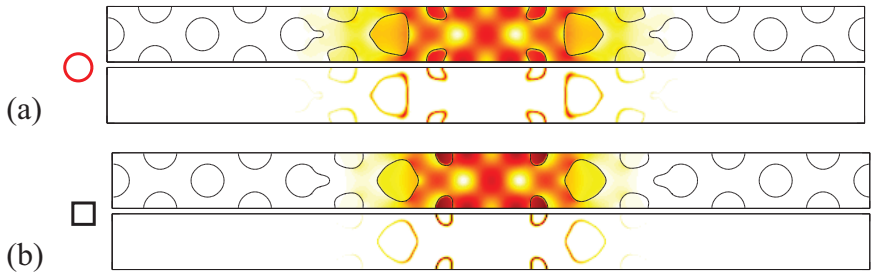

Figure 5.5 Energy density and dissipative energy density of slow light modes marked in Fig. 5.4 (c) with $n_g = 50$. (a) Dispersion engineered slow light waveguide. (b) Loss engineered slow light waveguide.

Des.	$\omega_0 a/2\pi c$	$\langle n_g \rangle$	GBP	$\langle \Im(k) \rangle\, a/2\pi$ (10^{-3})
Lon.	0.2172	50.54	0.29	2.78
Lat.	0.2131	49.77	0.31	2.75
Rad.	0.2104	50.50	0.33	2.12
Dis.	0.2111	50.27	0.50	3.62
Los.	0.2112	49.82	0.47	2.13

Table 5.1 Performance comparisons of different waveguides with $n_g^* = 50$. The first, second and third rows show the longitudinal (along the waveguide direction) location, lateral (normal to the waveguide direction) location and radius tuned waveguides, respectively. The forth and the fifth rows show the dispersion and loss engineered waveguides.

uides are summarized in Table 5.1. The GBP of the free-topology optimized waveguides has been improved by a factor of 1.42 or above, compared to the initial design. Furthermore, through loss engineering, the free-topology engineered slow light waveguide can achieve an equally good performance in terms of propagation loss as the radius tuned waveguide.

It must be highlighted that further comparisons between the fixed- and free-topology loss engineered waveguides for different group indices illustrate that the enhancement of GBP induces a small increase on the propagation loss in free-topology loss engineered waveguides with high prescribed group indices. The detailed studies can be found in the paper [P5].

Chapter 6
Dispersion engineered plasmonic waveguides [P6]

The MDM plasmonic waveguides with side-coupled resonators have been demonstrated to support plasmonic slow light propagation based on a plasmonic analogue of electromagnetically induced transparency (EIT). However, no systematic study has been performed for the MDM plasmonic waveguides to alleviate the high group velocity dispersion or large propagation loss undergone by plasmonic slow light propagation.

Based on the complex band structure calculations, this chapter studies the systematic dispersion engineering of periodic MDM plasmonic waveguides with side-coupled resonators presented by Huang et al. (2011), where the periodic supercell is parameterized by a set of superellipses. The loss compensation of the designed slow light propagation is further investigated by integrating material gain. This chapter gives a brief summary of the paper [P6].

6.1 Optimization problem of plasmonic waveguides

This chapter focuses on a planar MDM plasmonic waveguide, comprised of a periodic array of two stub resonators side-coupled to a MDM plamsonic waveguide, as sketched in Fig. 6.1 (a). The detailed structural parameters are as follows: the waveguide dielectric core is 60 nm and the side-coupled resonators have a total size of 60 nm × 330 nm with a downward shift of 50 nm along y direction. The dimension of the supercell is 300 nm × 1000 nm with the waveguide direction along x direction.

Inspired by the MMOS, this plasmonic waveguide can be parameterized using a set of superellipses, where the regions inside the superellipses are occupied by dielectric material and the regions outside are occupied by metal. Numerically, the elemental quantity, $\overline{\rho}_e$, projected using all the M superellipses is calculated by

$$\overline{\rho}_e = \prod_{i=1}^{M} H\left(\mathbf{r}_e, x_i, y_i, a_i, b_i, n_i\right) H\left(\mathbf{r}_e, x_i - a, y_i, a_i, b_i, n_i\right) H\left(\mathbf{r}_e, x_i + a, y_i, a_i, b_i, n_i\right) \tag{6.1}$$

with

$$H\left(\mathbf{r}_e, x_i, y_i, a_i, b_i, n_i\right) = \frac{1}{1 + \exp\left(-\beta\left(\frac{|x_i - x_e|^{n_i}}{a_i^{n_i}} + \frac{|y_i - y_e|^{n_i}}{b_i^{n_i}} - 1\right)\right)} \tag{6.2}$$

Here a is the lattice constant, $\mathbf{r}_e = (x_e,\ y_e)$ is the centroid of element e, $(x_i,\ y_i)$ is the center of the ith superellipse, a_i, b_i and n_i are the corresponding semi-diameters and curvature, β is the regularization parameter. Three periods of the superellipses,

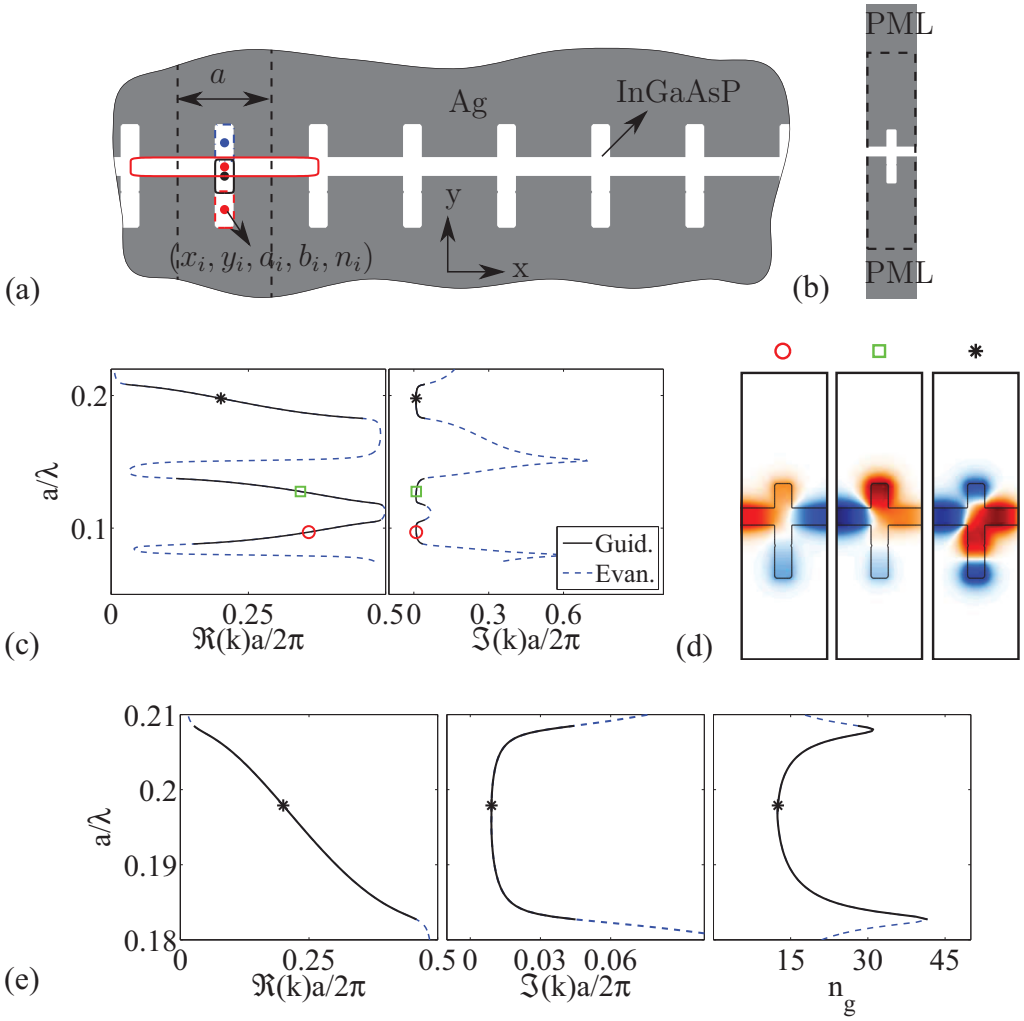

Figure 6.1 (a) Sketch of the parameterizations of a periodic MDM plasmonic waveguide consisting of Ag and InGaAsP. (b) Computational model of the periodic supercell. (c) Band structure of the MDM plasmonic waveguide. Left panel: Dispersion curve. Right panel: Propagation loss. The dashed and solid lines represent the evanescent and guided modes, respectively. (d) Modal profiles of the guided modes in the different bands marked in (c). (e) Detailed characteristics of the guided modes in the third band. Left panel: Dispersion curve. Middle panel: Propagation loss. Right panel: Group index plot.

stated as $H\left(x_i, y_i, a_i, b_i, n_i\right)$, $H\left(x_i - a, y_i, a_i, b_i, n_i\right)$ and $H\left(x_i + a, y_i, a_i, b_i, n_i\right)$, are utilized to ensure the waveguide periodicity along the waveguide direction.

The material property of element e is described by the elemental quantity, $\overline{\rho}_e$, as

$$\varepsilon_e = \varepsilon_{\mathrm{d}} + \overline{\rho}_e \left(\varepsilon_{\mathrm{m}} - \varepsilon_{\mathrm{d}}\right) \tag{6.3}$$

where ε_e is the relative permittivity of element e, ε_{d} is the relative permittivity of the dielectric material, and ε_{m} is the relative permittivity of the metal.

Here, one superellipse is employed to represent the dielectric waveguide core and three superellipses are employed to represent the coupled resonators as illustrated in Fig. 6.1 (a). It should be emphasized that four superellipses are chosen for an illustration purpose, and that more superellipses can be employed to parameterize the supercell. In this work, the material dispersion in InGaAsP is neglected and the corresponding relative permittivity is modeled as $\varepsilon_{\mathrm{d}} = 11.38$. The relative permittivity of Ag is modeled by the Drude-Lorentz model presented by Johnson and Christy (1972).

Fig. 6.1 (c) depicts the detailed performances of the MDM plasmonic waveguide, where the solid lines display the guided modes and the dashed lines represent the evanescent modes displaying large propagation loss. It is observed from the modal profiles in Fig. 6.1 (d) that the modes on the third band are higher order modes with one more node in the longitudinal direction, compared to the other two modes.

The third band corresponds to a wavelength range of $\lambda \in [1440,\ 1640]$ nm and is the focus of this work. The detailed propagation characteristics of the guided modes on the third band are described in Fig. 6.1 (e). The MDM plasmonic waveguide supports slow light propagation of $\langle n_g \rangle = 13$ over a bandwidth of $\Delta\lambda = 89$ nm, entering at $\lambda_0 = 1528$ nm. This corresponds to a GBP of 0.76. However, the slow light propagation displays relatively large propagation loss due to the energy dissipation in metal, as shown in the middle panel in Fig. 6.1 (e). In addition, the achievable group index in the waveguide is highly restricted by the material loss in metal.

The dispersion curve of the MDM plasmonic waveguide can be tailored by changing the geometry of the supercell. Numerically, the dispersion engineering in the MDM plasmonic waveguide can be formulated as an optimization problem as in the chapter 4, given by

$$\min_{\mathbf{x}} \quad f\left(\overline{\boldsymbol{\rho}}, \lambda_i\right) = \left(n_g\left(\overline{\boldsymbol{\rho}}, \lambda_i\right) / n_g^* - 1\right)^2 \tag{6.4}$$

where $\mathbf{x}$ denotes the design variable vector consisting of the locations, semi-diameters and curvatures of the superellipses, n_g^* represents the prescribed group index, $\lambda_i \in [\lambda_1,\ \lambda_2]$ is the prescribed wavelength with $[\lambda_1,\ \lambda_2]$ indicating the designed wavelength range.

To ensure that the designed modes are guided, a constraint is implemented to restrict the average propagation loss, $\langle \Im(k\left(\overline{\boldsymbol{\rho}}, \lambda_i\right))\rangle$, in the designed wavelength range. Moreover, additional constraints are implemented to force the designed modes away from the band edges. All the constraints are listed as follows

$$\langle \Im(k\left(\overline{\boldsymbol{\rho}}, \lambda_i\right))\rangle < a_{11}, \qquad \Re(k\left(\overline{\boldsymbol{\rho}}, \lambda_i\right)) > k_{11}, \qquad \Re(k\left(\overline{\boldsymbol{\rho}}, \lambda_i\right)) < k_{22} \tag{6.5}$$

where a_{11} is the constant number indicating the allowed average propagation loss, k_{11} and k_{22} are the constant numbers to ensure that the designed modes are away from the band edges.

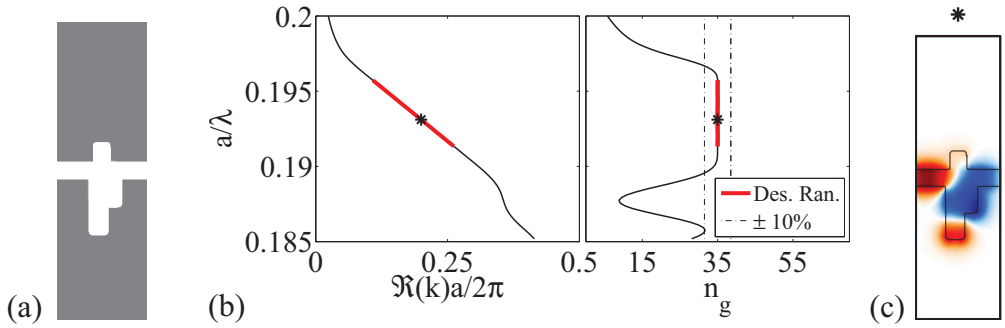

Figure 6.2 (a) Optimized MDM supercell. (b) Detailed characteristics of the designed plasmonic waveguide. Left penal: Dispersion curve. Right panel: Group index plot. The bold lines represent the designed wavelength range and the dash-dot lines show the ±10% range of the target group index. (c) Modal profile of the designed mode marked in (b).

ith	x_i (nm)	y_i (nm)	a_i (nm)	b_i (nm)	n_i
1	149.2	466.6	29.7	61.0	9.2
2	161.2	546.5	57.3	77.7	9.3
3	138.9	633.2	33.9	83.4	8.7

Table 6.1 Structural parameters of the optimized MDM plasmonic waveguide for $n_g^* = 35$.

6.2 Slow light MDM plasmonic waveguides

In this section, the aforementioned optimization formulation is employed to design a MDM plasmonic waveguide for $n_g^* = 35$ with a target wavelength range of $\lambda_i \in [1533,\ 1567]$ nm. The loss compensation of the designed slow light modes is further studied by integrating a gain medium. The design variables are chosen as the locations, semi-diameters and curvatures of the three superellipses employed to represent the side-coupled resonators.

Fig. 6.2 (a) shows the final optimized supercell, and the detailed parameters of the three designed superellipses are listed in Tab. 6.1. The propagation characteristics of the designed slow light modes are presented in Fig. 6.2 (b). A group index plateau is located at the prescribed group index of $n_g = 35$ over the designed wavelength range shown by the bold solid lines. Under the ±10% criterion, the optimized MDM plasmonic waveguide facilitates slow light propagation of $\langle n_g \rangle = 34.7$ over a bandwidth of $\Delta\lambda = 55$ nm centering $\lambda_0 = 1553$ nm. This corresponds to a GBP of 1.23.

It should be pointed out that the optimized design is a local minimum of the optimization problem, and that parameterizations using different number of superellipses may result in different designs. The details can be found in the paper [P6].

The energy dissipation in metal leads to decrease of the propagation length in MDM plasmonic waveguides, which limits the potential application scope of MDM

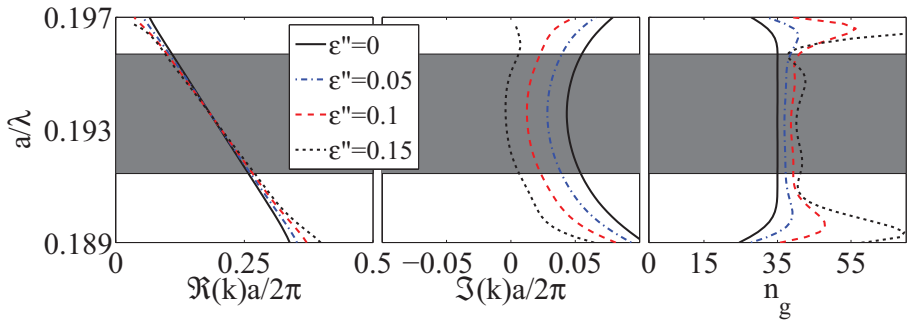

Figure 6.3 Detailed characteristics of the optimized slow light MDM plasmonic waveguide in the presence of the material gain. The gray regions indicate the designed wavelength range.

plasmonic waveguides. Incorporation of gain media has been demonstrated to be an efficient approach to compensate loss in various applications (Nezhad et al., 2004; Maier, 2006; Noginov et al., 2008; Yu et al., 2008). Below, the loss compensation in the dispersion engineered MDM plasmonic waveguide is studied, and the influence of the material gain on the signal distortions is investigated. To simplify the problem, this study assumes uniform gain in InGaAsP (Yu et al., 2008), and models the material gain by adding a small imaginary part, ε'', to the dielectric constant as $\varepsilon_{\mathrm{d}} = 11.38 - i\varepsilon''$, where the magnitude of ε'' depends on the pumping power.

Fig. 6.3 shows the detailed characteristics of the optimized MDM plasmonic waveguide in the presence of different amounts of material gain, where the gray regions indicate the designed wavelength range. It is noted that the propagation loss varies in the designed wavelength range. This is due to the field variations among different designed modes. The integration of a gain medium significantly suppresses or even cancels the propagation loss of the guided modes. The detailed observation shows that the designed modes are slightly amplified when considering a material gain of $\varepsilon'' = 0.15$, indicated by a negative $\Im(k)$. However, the incorporation of the gain medium upgrades the average group index of the designed slow light modes and induces a big group index variation. The group index variation increases monotonically as the material gain increases. The amplification of the group index variation is again explained by the field variations between the designed slow light modes.

Under the $\pm 10\%$ criterion, the performances of the gain-assisted MDM plasmonic waveguides are quantitively evaluated in terms of the GBP and the average propagation loss. Tab. 6.2 summarizes the detailed performances of the gain-assisted slow light plasmonic waveguide. It is seen that the average group index, $\langle n_g \rangle$, increases as the material gain rises, while the corresponding average propagation loss, $\langle \Im(k) \rangle$, reduces. When integrating a material gain of $\varepsilon'' = 0.15$, slow light propagation up to $\langle n_g \rangle = 40.9$ can be supported in the gain-assisted plasmonic waveguide. However, a small average propagation attenuation is observed in the slow light propagation.

ε''	λ_0 (nm)	$\langle n_g \rangle$	GBP	$\langle \Im(k) \rangle \, a/2\pi$
0	1553	34.7	1.23	0.05442
0.05	1554	37.7	1.44	0.04140
0.1	1554	39.7	1.16	0.01955
0.15	1553	40.9	1.16	0.00202

Table 6.2 Detailed performances of the gain-assisted slow light MDM plasmonic waveguide.

The propagation attenuation is induced by the slow light propagations located at the higher wavelengths out of the designed wavelength range, see Fig. 6.3. Larger material gain has to be added in order to fully compensate the propagation loss in the slow light propagation. All gain-assisted MDM plasmonic waveguides achieve a GBP of 1.16 or higher, which is at least 2.3 times of the one in the slow light PhCWs presented in the previous chapters.

Using the presented parameterization, other properties in the plasmonic MDM waveguides could also be improved by reformulating them as optimization problems. The propagation loss could be suppressed using the optimization formulation for loss engineering presented in the previous chapter. In addition, the gain enhancement could be further improved by maximizing the modal gain of the designed slow light modes when integrating gain media.

Chapter 7
Concluding remarks

7.1 Conclusions

This thesis presents the applications of the topology optimization method in designing novel slow light waveguides through redistributing materials in the periodic supercell, to alleviate signal distortions and propagation loss, and explores the robust topology optimization formulation to enhance the robustness of the optimized designs with respect to manufacturing imperfections.

The detailed characteristics of waveguides have been evaluated using band structure calculations. Both the $\omega\,(k)$-formulation, searching for eigenfrequencies for a given wave vector, and the $k\,(\omega)$-formulation, searching for eigen wavenumbers for a given frequency, have been employed to calculate the band structures of different waveguides using the finite element method. The latter variant has been utilized to tackle the material dispersion and to evaluate the propagation loss in waveguides induced by material loss and other loss mechanisms. Numerical studies have demonstrated that the achievable group index in waveguides is highly restricted by material loss/gain. Hence the gain enhancement is saturated as a result of the trade-off between slow light effects and material gain in the active waveguides.

In order to ensure the performance of fabricated samples under manufacturing imperfections, a robust topology optimization formulation has been formulated as a worst case optimization formulation considering different design realizations in the manufacturing process. The numerical test on the compliant inverter has shown that the design robustness can be enforced through the robust optimization formulation at a cost of the objective in the blueprint design.

Based on the band structure calculations, the dispersion engineering in PhCWs is formulated as an optimization problem and realized by minimizing the errors between actual group index and a target group index. Both robust free- and fixed-topology dispersion engineered slow light waveguides have been achieved by the presented approach using two different parameterizations. The detailed characteristics of these waveguides have illustrated that the design robustness is enforced in the slow light waveguides, and that the GBP of the slow light propagation is significantly enhanced by allowing irregular topologies in the waveguides.

Using the $k\,(\omega)$-formulation, the scattering loss in waveguides has been tackled by representing the scattering loss using an edge-related loss model. Numerical studies on the propagation loss of the slow light modes in different fixed-topology waveguides have shown that the propagation loss can be engineered by minimizing the field intensity available for scattering. The loss engineering in the slow light waveguides has been realized by minimizing the average propagation loss of the designed modes.

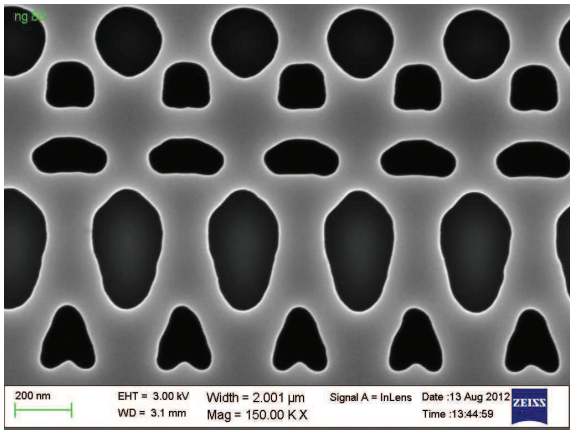

Figure 7.1 Illustration of the spatial non-periodic manufacturing imperfections in the fabricated sample.

The corresponding numerical example has illustrated that the propagation loss in the free-topology dispersion engineered waveguide can be significantly suppressed by the loss engineering optimization formulation while retaining the same GBP.

The presented dispersion engineering optimization formulation has been further employed to design slow light MDM plasmonic waveguides with side-coupled resonators. The dispersionless slow light MDM plasmonic waveguide has been achieved by parameterizing the supercell using a set of superellipses. The loss compensation of the designed slow light propagation has been investigated by integrating gain media. Numerical results have shown that the propagation loss in the slow light propagation can be compensated by gain media, and that the integration of gain media induces a bigger group index variation. All the gain-assisted optimized MDM plasmonic waveguides have achieved a GBP of 1.16 or above while keeping acceptable signal distortions.

7.2 Future work

In this work, the design robustness of the dispersion engineered PhCWs is enhanced using the periodic supercell, by assuming periodic manufacturing errors along the waveguide direction. However, the manufacturing imperfections in the fabricated samples show a non-periodic pattern, as illustrated in Fig. 7.1, the enlarged image of the fabricated sample of $n_g^* = 80$ in Fig. 4.6. Hence, from the application point of view, it is very important to evaluate the influence of the spatial non-periodic manufacturing imperfections on the slow light propagation in the dispersion engineered waveguides. Besides, it might be beneficial to design the robust dispersion engineered waveguides with respect to the spatial non-periodic manufacturing imperfections. Moreover, the non-periodic manufacturing disorders in the waveguides induce more complex loss mechanisms in the slow light propagation, hence loss en-

gineering considering the non-periodic manufacturing disorders is of high interest.

In the present study, all the optimized designs are obtained in the 2D planar waveguides. The additional dimension in 3D waveguides may induce extra signal distortions and cause additional out-of-plan radiation. To ensure the proper performance of the devices, optimization should be extended to 3D waveguides using the 2D planar waveguides as a starting point when computational power allows.

By assuming uniform material gain in dielectric material, this thesis preliminarily studies the loss compensation in the dispersion engineered MDM plasmonic waveguide. However, nonuniform gain distribution can be observed in the dielectric material due to position-dependent dipole lifetime and pump irradiance (De Leon and Berini, 2009). It is of high interest to include a more elaborate model of material gain to further investigate the loss compensation.

Last but not the least, experimental characteristics of the engineered waveguides are highly desirable for the applications and the development of the methodology.

References

Aage, N., Mortensen, N.A. and Sigmund, O. (2010). Topology optimization of metallic devices for microwave applications. *International Journal for Numerical Methods in Engineering*, 83(2):228–248.

Andkjaer, J., Mortensen, N.A. and Sigmund, O. (2012). Towards all-dielectric, polarization-independent optical cloaks. *Applied Physics Letters*, 100(10):101106.

Andkjaer, J. and Sigmund, O. (2011). Topology optimized low-contrast all-dielectric optical cloak. *Applied Physics Letters*, 98(2):021112.

Andreani, L.C. and Gerace, D. (2007). Light-matter interaction in photonic crystal slabs. *Physica Status Solidi B*, 244(10):3528–3539.

Andreasen, C.S., Gersborg, A.R. and Sigmund, O. (2009). Topology optimization of microfluidic mixers. *International Journal for Numerical Methods in Fluids*, 61(5):498–513.

Anker, J.N., Hall, W.P., Lyandres, O., Shah, N.C., Zhao, J. and Van Duyne, R.P. (2008). Biosensing with plasmonic nanosensors. *Nature Materials*, 7(6):442–453.

Baba, T. (2008). Slow light in photonic crystals. *Nature Photonics*, 2(8):465–473.

Baba, T., Motegi, A., Iwai, T., Fukaya, N., Watanabe, Y. and Sakai, A. (2002). Light propagation characteristics of straight single-line-defect waveguides in photonic crystal slabs fabricated into a silicon-on-insulator substrate. *IEEE Journal of Quantum Electronics*, 38(7):743–752.

Barnes, W.L., Dereux, A. and Ebbesen, T.W. (2003). Surface plasmon subwavelength optics. *Nature*, 424(6950):824–830.

Baron, A., Mazoyer, S., Smigaj, W. and Lalanne, P. (2011). Attenuation coefficient of single-mode periodic waveguides. *Physical Review Letters*, 107(15):153901.

Beggs, D.M., White, T.P., O'Faolain, L. and Krauss, T.F. (2008). Ultracompact and low-power optical switch based on silicon photonic crystals. *Optics Letters*, 33(2):147–149.

Bendsøe, M.P. and Kikuchi, N. (1988). Generating optimal topologies in structural design using a homogenization method. *Computer Methods in Applied Mechanics and Engineering*, 71(2):197–224.

Bendsøe, M.P. and Sigmund, O. (1999). Material interpolation schemes in topology optimization. *Archive of Applied Mechanics*, 69(9-10):635–654.

Bendsøe, M.P. and Sigmund, O. (2003). *Topology Optimization: Theory, Methods and Applications*. Springer, Berlin.

Benisty, H., Labilloy, D., Weisbuch, C., Smith, C.J.M., Krauss, T.F., Cassagne, D., Beraud, A. and Jouanin, C. (2000). Radiation losses of waveguide-based two-dimensional photonic crystals: Positive role of the substrate. *Applied Physics Letters*, 76(5):532–534.

Berenger, J.P. (1994). A perfectly matched layer for the absorption of electromagnetic-waves. *Journal of Computational Physics*, 114(2):185–200.

Berini, P. and De Leon, I. (2012). Surface plasmon-polariton amplifiers and lasers. *Nature Photonics*, 6(1):16–24.

Borel, P.I., Frandsen, L.H., Harpoth, A., Kristensen, M., Jensen, J.S. and Sigmund, O. (2005). Topology optimised broadband photonic crystal Y-splitter. *Electronics Letters*, 41(2):69–71.

Bourdin, B. (2001). Filters in topology optimization. *International Journal for Numerical Methods in Engineering*, 50(9):2143–2158.

Brillouin, L. (1953). *Wave Propagation in Periodic Structures: Electric Filters and Crystal Lattices*. Dover, New York.

Bruns, T.E. and Tortorelli, D.A. (2001). Topology optimization of non-linear elastic structures and compliant mechanisms. *Computer Methods in Applied Mechanics and Engineering*, 190(26-27):3443–3459.

Christensen, P.W. and Klarbring, A. (2009). *An Introduction to Structural Optimization*. Springer, [Dordrecht].

Colman, P., Combrié, S., Lehoucq, G. and De Rossi, A. (2012). Control of dispersion in photonic crystal waveguides using group symmetry theory. *Optics Express*, 20(12):13108–13114.

Cook, R., Malkus, D. and Plesha, M. (2002). *Concepts and Applications of Finite Element Analysis*. Wiley, New York, N.Y.

Corcoran, B., Monat, C., Grillet, C., Moss, D.J., Eggleton, B.J., White, T.P., O'Faolain, L. and Krauss, T.F. (2009). Green light emission in silicon through slow-light enhanced third-harmonic generation in photonic-crystal waveguides. *Nature Photonics*, 3(4):206–210.

Davanco, M., Urzhumov, Y. and Shvets, G. (2007). The complex Bloch bands of a 2D plasmonic crystal displaying isotropic negative refraction. *Optics Express*, 15(15):9681–9691.

De Leon, I. and Berini, P. (2009). Modeling surface plasmon-polariton gain in planar metallic structures. *Optics Express*, 17(22):20191–20202.

Duhring, M.B., Jensen, J.S. and Sigmund, O. (2008). Acoustic design by topology optimization. *Journal of Sound and Vibration*, 317(3-5):557–575.

Ebbesen, T.W., Genet, C. and Bozhevolnyi, S.I. (2008). Surface-plasmon circuitry. *Physics Today*, 61(5):44–50.

Economou, E.N. (1969). Surface plasmons in thin films. *Physical Review*, 182(2):539–554.

Elesin, Y., Lazarov, B.S., Jensen, J.S. and Sigmund, O. (2012). Design of robust and efficient photonic switches using topology optimization. *Photonics and Nanostructures: Fundamentals and Applications*, 10(1):153–165.

Engelen, R.J.P., Sugimoto, Y., Watanabe, Y., Korterik, J.P., Ikeda, N., van Hulst, N.F., Asakawa, K. and Kuipers, L. (2006). The effect of higher-order dispersion on slow light propagation in photonic crystal waveguides. *Optics Express*, 14(4):1658–1672.

Engstroem, C., Hafner, C. and Schmidt, K. (2009). Computations of lossy Bloch waves in two-dimensional photonic crystals. *Journal of Computational and Theoretical Nanoscience*, 6(3):775–783.

Erentok, A. and Sigmund, O. (2011). Topology optimization of sub-wavelength antennas. *IEEE Transactions on Antennas and Propagation*, 59(1):58–69.

Ferrini, R., Houdre, R., Benisty, H., Qiu, M. and Moosburger, J. (2003). Radiation losses in planar photonic crystals: two-dimensional representation of hole depth and shape by an imaginary dielectric constant. *Journal of the Optical Society of America B*, 20(3):469–478.

Ferrini, R., Leuenberger, D., Houdre, R., Benisty, H., Kamp, M. and Forchel, A. (2006). Disorder-induced losses in planar photonic crystals. *Optics Letters*, 31(10):1426–1428.

Frandsen, L.H., Lavrinenko, A.V., Fage-Pedersen, J. and Borel, P.I. (2006). Photonic crystal waveguides with semi-slow light and tailored dispersion properties. *Optics Express*, 14(20):9444–9450.

Gersborg-Hansen, A., Sigmund, O. and Haber, R.B. (2005). Topology optimization of channel flow problems. *Structural and Multidisciplinary Optimization*, 30(3):181–192.

Govyadinov, A.A. and Podolskiy, V.A. (2006). Gain-assisted slow to superluminal group velocity manipulation in nanowaveguides. *Physical Review Letters*, 97(22):223902.

Gramotnev, D.K. and Bozhevolnyi, S.I. (2010). Plasmonics beyond the diffraction limit. *Nature Photonics*, 4(2):83–91.

Grgic, J., Pedersen, J.G., Xiao, S. and Mortensen, N.A. (2010). Group index limitations in slow-light photonic crystals. *Photonics and Nanostructures: Fundamentals and Applications*, 8(2):56–61.

Haber, R.B., Jog, C.S. and Bendsøe, M.P. (1996). A new approach to variable-topology shape design using a constraint on perimeter. *Structural Optimization*, 11(1):1–12.

Halkjaer, S., Sigmund, O. and Jensen, J.S. (2006). Maximizing band gaps in plate structures. *Structural and Multidisciplinary Optimization*, 32(4):263–275.

Hao, R., Cassan, E., Kurt, H., Le Roux, X., Marris-Morini, D., Vivien, L., Wu, H.M., Zhou, Z.P. and Zhang, X.L. (2010). Novel slow light waveguide with controllable delay-bandwidth product and utra-low dispersion. *Optics Express*, 18(6):5942–5950.

Heuck, M., Blaaberg, S. and Mork, J. (2010). Theory of passively mode-locked photonic crystal semiconductor lasers. *Optics Express*, 18(17):18003–18014.

Huang, K.C., Lidorikis, E., Jiang, X.Y., Joannopoulos, J.D., Nelson, K.A., Bienstman, P. and Fan, S.H. (2004). Nature of lossy Bloch states in polaritonic photonic crystals. *Physical Review B*, 69(19):195111.

Huang, Y., Min, C.J. and Veronis, G. (2011). Subwavelength slow-light waveguides based on a plasmonic analogue of electromagnetically induced transparency. *Applied Physics Letters*, 99(14):143117.

Hughes, S., Ramunno, L., Young, J.F. and Sipe, J.E. (2005). Extrinsic optical scattering loss in photonic crystal waveguides: Role of fabrication disorder and photon group velocity. *Physical Review Letters*, 94(3):033903.

Jensen, J.S. and Sigmund, O. (2004). Systematic design of photonic crystal structures using topology optimization: Low-loss waveguide bends. *Applied Physics Letters*, 84(12):2022–2024.

Jensen, J.S. and Sigmund, O. (2011). Topology optimization for nano-photonics. *Laser & Photonics Reviews*, 5(2):308–321.

Jin, J. (2002). *The Finite Element Method in Electromagnetics*. Wiley, New York, N.Y.

Jin, J.M. and Riley, D.J. (2009). *Finite Element Analysis of Antennas and Arrays*. John Wiley & Sons IEEE Press, Hoboken, N.J.

Joannopoulos, J.D., Johnson, S.G., Winn, J.N. and Meade, R.D. (2008). *Photonic Crystals: Molding the Flow of Light*. Princeton University Press, Princeton.

Johnson, P.B. and Christy, R.W. (1972). Optical-constants of noble-metals. *Physical Review B*, 6(12):4370–4379.

Kawasaki, T., Mori, D. and Baba, T. (2007). Experimental observation of slow light in photonic crystal coupled waveguides. *Optics Express*, 15(16):10274–10281.

Kiziltas, G., Psychoudakis, D., Volakis, J.L. and Kikuchi, N. (2003). Topology design optimization of dielectric substrates for bandwidth improvement of a patch antenna. *IEEE Transactions on Antennas and Propagation*, 51(10):2732–2743.

Krauss, T.F. (2007). Slow light in photonic crystal waveguides. *Journal of Physics D*, 40(9):2666–2670.

Krauss, T.F. (2008). Why do we need slow light? *Nature Photonics*, 2(8):448–450.

Kreissl, S., Pingen, G., Evgrafov, A. and Maute, K. (2010). Topology optimization of flexible micro-fluidic devices. *Structural and Multidisciplinary Optimization*, 42(4):495–516.

Kuramochi, E., Notomi, M., Hughes, S., Shinya, A., Watanabe, T. and Ramunno, L. (2005). Disorder-induced scattering loss of line-defect waveguides in photonic crystal slabs. *Physical Review B*, 72(16):161318.

Lazarov, B.S., Schevenels, M. and Sigmund, O. (2011). Robust design of large-displacement compliant mechanisms. *Mechanical Sciences*, 2(2):175–182.

Letartre, X., Seassal, C., Grillet, C., Rojo-Romeo, P., Viktorovitch, P., d'Yerville, M.L., Cassagne, D. and Jouanin, C. (2001). Group velocity and propagation losses measurement in a single-line photonic-crystal waveguide on InP membranes. *Applied Physics Letters*, 79(15):2312–2314.

Li, J., White, T.P., O'Faolain, L., Gomez-Iglesias, A. and Krauss, T.F. (2008). Systematic design of flat band slow light in photonic crystal waveguides. *Optics Express*, 16(9):6227–6232.

Liang, J., Ren, L.Y., Yun, M.J., Han, X. and Wang, X.J. (2011). Wideband ultraflat slow light with large group index in a W1 photonic crystal waveguide. *Journal of Applied Physics*, 110(6):063103.

Loncar, M., Doll, T., Vuckovic, J. and Scherer, A. (2000). Design and fabrication of silicon photonic crystal optical waveguides. *Journal of Lightwave Technology*, 18(10):1402–1411.

Loncar, M., Nedeljkovic, D., Pearsall, T.P., Vuckovic, J., Scherer, A., Kuchinsky, S. and Allan, D.C. (2002). Experimental and theoretical confirmation of Bloch-mode light propagation in planar photonic crystal waveguides. *Applied Physics Letters*, 80(10):1689–1691.

Ma, J. and Jiang, C. (2008). Demonstration of ultraslow modes in asymmetric line-defect photonic crystal waveguides. *IEEE Photonics Technology Letters*, 20(13-16):1237–1239.

Maier, S.A. (2006). Gain-assisted propagation of electromagnetic energy in sub-wavelength surface plasmon polariton gap waveguides. *Optics Communications*, 258(2):295–299.

Maier, S.A. (2007). *Plasmonics: Fundamentals and Applications*. Springer, Bath.

Matsuo, S., Shinya, A., Kakitsuka, T., Nozaki, K., Segawa, T., Sato, T., Kawaguchi, Y. and Notomi, M. (2010). High-speed ultracompact buried heterostructure photonic-crystal laser with 13 FJ of energy consumed per bit transmitted. *Nature Photonics*, 4(9):648–654.

Matzen, R., Jensen, J.S. and Sigmund, O. (2011). Systematic design of slow-light photonic waveguides. *Journal of the Optical Society of America B*, 28(10):2374–2382.

Maxwell, J. (1891). *A Treatise on Electricity and Magnetism.* Dover, New York,N.Y.

McMillan, J.E., Yang, X.D., Panoiu, N.C., Osgood, R.M. and Wong, C.W. (2006). Enhanced stimulated raman scattering in slow-light photonic crystal waveguides. *Optics Letters*, 31(9):1235–1237.

Mori, D. and Baba, T. (2004). Dispersion-controlled optical group delay device by chirped photonic crystal waveguides. *Applied Physics Letters*, 85(7):1101–1103.

Mori, D., Kubo, S., Sasaki, H. and Baba, T. (2007). Experimental demonstration of wideband dispersion-compensated slow light by a chirped photonic crystal directional coupler. *Optics Express*, 15(9):5264–5270.

Nezhad, M.P., Tetz, K. and Fainman, Y. (2004). Gain assisted propagation of surface plasmon polaritons on planar metallic waveguides. *Optics Express*, 12(17):4072–4079.

Noginov, M.A., Podolskiy, V.A., Zhu, G., Mayy, M., Bahoura, M., Adegoke, J.A., Ritzo, B.A. and Reynolds, K. (2008). Compensation of loss in propagating surface plasmon polariton by gain in adjacent dielectric medium. *Optics Express*, 16(2):1385–1392.

Notomi, M., Yamada, K., Shinya, A., Takahashi, J., Takahashi, C. and Yokohama, I. (2001). Extremely large group-velocity dispersion of line-defect waveguides in photonic crystal slabs. *Physical Review Letters*, 87(25):253902.

Nunes, F.D., Vasconcelos, T.C., Bezerra, M. and Weiner, J. (2011). Electromagnetic energy density in dispersive and dissipative media. *Journal of the Optical Society of America B*, 28(6):1544–1552.

O'Faolain, L., Schulz, S.A., Beggs, D.M., White, T.P., Spasenovic, M., Kuipers, L., Morichetti, F., Melloni, A., Mazoyer, S., Hugonin, J.P., Lalanne, P. and Krauss, T.F. (2010). Loss engineered slow light waveguides. *Optics Express*, 18(26):27627–27638.

Patterson, M. and Hughes, S. (2010). Theory of disorder-induced coherent scattering and light localization in slow-light photonic crystal waveguides. *Journal of Optics*, 12(10):104013.

Patterson, M., Hughes, S., Schulz, S., Beggs, D.M., White, T.P., O'Faolain, L. and Krauss, T.F. (2009). Disorder-induced incoherent scattering losses in photonic crystal waveguides: Bloch mode reshaping, multiple scattering, and breakdown of the beer-lambert law. *Physical Review B*, 80(19):195305.

Pedersen, J.G., Xiao, S.S. and Mortensen, N.A. (2008). Limits of slow light in photonic crystals. *Physical Review B*, 78(15):153101.

Petrov, A., Krause, M. and Eich, M. (2009). Backscattering and disorder limits in slow light photonic crystal waveguides. *Optics Express*, 17(10):8676–8684.

Qian, X. and Sigmund, O. (2012). Robust topological design of electromechanical actuators. *(in review)*.

Saxena, A. (2011). Are circular shaped masks adequate in adaptive mask overlay topology synthesis method? *Journal of Mechanical Design*, 133(1):011001.

Schmidt, K. and Kappeler, R. (2010). Efficient computation of photonic crystal waveguide modes with dispersive material. *Optics Express*, 18(7):7307–7322.

Schulz, S.A., O'Faolain, L., Beggs, D.M., White, T.P., Melloni, A. and Krauss, T.F. (2010). Dispersion engineered slow light in photonic crystals: a comparison. *Journal of Optics*, 12(10):104004.

Sigmund, O. (1997). On the design of compliant mechanisms using topology optimization. *Mechanics of Structures and Machines*, 25(4):493–524.

Sigmund, O. (2007). Morphology-based black and white filters for topology optimization. *Structural and Multidisciplinary Optimization*, 33(4-5):401–424.

Sigmund, O. (2009). Manufacturing tolerant topology optimization. *Acta Mechanica Sinica*, 25:227–239.

Sigmund, O. and Jensen, J.S. (2003). Systematic design of phononic band-gap materials and structures by topology optimization. *Philosophical Transactions of the Royal Society of London Series A*, 361(1806):1001–1019.

Stainko, R. and Sigmund, O. (2007). Tailoring dispersion properties of photonic crystal waveguides by topology optimization. *Waves in Random and Complex Media*, 17(4):477–489.

Stockman, M.I. (2011). Spaser action, loss compensation, and stability in plasmonic systems with gain. *Physical Review Letters*, 106(15):156802.

Svanberg, K. (1987). The method of moving asymptotes: A new method for structural optimization. *International Journal for Numerical Methods in Engineering*, 24(2):359–373.

Svanberg, K. (2001). A class of globally convergent optimization methods based on conservative convex separable approximations. *SIAM Journal on Optimization*, 12(2):555–573.

Wadbro, E. and Berggren, M. (2006). Topology optimization of an acoustic horn. *Computer Methods in Applied Mechanics and Engineering*, 196(1-3):420–436.

White, T.P., Botten, L.C., de Sterke, C.M., Dossou, K.B. and McPhedran, R.C. (2008). Efficient slow-light coupling in a photonic crystal waveguide without transition region. *Optics Letters*, 33(22):2644–2646.

Xu, S.L., Cai, Y.W. and Cheng, G.D. (2010). Volume preserving nonlinear density filter based on heaviside functions. *Structural and Multidisciplinary Optimization*, 41(4):495–505.

Yoon, G.H., Jensen, J.S. and Sigmund, O. (2007). Topology optimization of acoustic-structure interaction problems using a mixed finite element formulation. *International Journal for Numerical Methods in Engineering*, 70(9):1049–1075.

Yu, Z.F., Veronis, G., Fan, S.H. and Brongersma, M.L. (2008). Gain-induced switching in metal-dielectric-metal plasmonic waveguides. *Applied Physics Letters*, 92(4):041117.

Appendix A
Errata [P2]

There are several errors in the publication [P2] regarding the minimal length scale in the intermediate design.

The labels of the longitudinal axis in Fig. 12, Fig. 20 and Fig. 21 were mistyped. The corrected ones are b/R, b_s/R and b_v/R respectively.

On page 780, all the ratios $b/2R$ should be b/R. In addition, $b = 0.092L$ should be corrected to $b = 0.046L$.

Publication [P1]

Fundamental limitations to gain enhancement in periodic media and waveguides

Fundamental Limitations to Gain Enhancement in Periodic Media and Waveguides

Jure Grgić,[1] Johan Raunkjær Ott,[1] Fengwen Wang,[2] Ole Sigmund,[2] Antti-Pekka Jauho,[3] Jesper Mørk,[1] and N. Asger Mortensen[1,*]

[1]DTU Fotonik, Department of Photonics Engineering, Technical University of Denmark, DK-2800 Kongens Lyngby, Denmark
[2]DTU Mekanik, Department of Mechanical Engineering, Solid Mechanics, Technical University of Denmark, DK-2800 Kongens Lyngby, Denmark
[3]DTU Nanotech, Department of Micro- and Nanotechnology, Technical University of Denmark, DK-2800 Kongens Lyngby, Denmark

(Received 21 November 2011; published 4 May 2012)

A common strategy to compensate for losses in optical nanostructures is to add gain material in the system. By exploiting slow-light effects it is expected that the gain may be enhanced beyond its bulk value. Here we show that this route cannot be followed uncritically: inclusion of gain inevitably modifies the underlying dispersion law, and thereby may degrade the slow-light properties underlying the device operation and the anticipated gain enhancement itself. This degradation is generic; we demonstrate it for three different systems of current interest (coupled-resonator optical waveguides, Bragg stacks, and photonic crystal waveguides). Nevertheless, a small amount of added gain may be beneficial.

DOI: 10.1103/PhysRevLett.108.183903 PACS numbers: 42.70.Qs, 41.20.Jb, 42.25.Bs, 78.67.−n

Light-matter interactions in periodic structures can be significantly enhanced in the presence of slow-light propagation. This paradigm has led to several important discoveries and demonstrations, including the enhancement of nonlinear effects [1–7], Purcell effects for light emission [8], light localization [9], as well as slow-light enhanced absorption and gain processes [10–14]. Loss is an inherent part of any passive optical material, and the inclusion of gain material is presently receiving widespread attention in many different situations, ranging from the fundamental interest in gain-compensation of inherently lossy metamaterials [15–18] and spasing in plasmonic nanostructures [19,20], to active nanophotonic devices such as low-threshold lasers [21] and miniaturized optical amplifiers. There is a common expectation that if a material with net gain g_0 is incorporated in a periodic medium, such as Bragg stacks, photonic crystals (PhC) or metamaterials, the gain will effectively be enhanced to $g_{\mathrm{eff}} \sim n_g^0 g_0$, where n_g^0 is the group index associated with the underlying dispersion relation $\omega_0(k)$ of the passive structure. In a device context the gain enhancement is anticipated to allow shrinking the structure by a factor equivalent to the group index, while maintaining the same output performance. However, this reasoning implicitly assumes that gain can be added without considering its impact on $\omega_0(k)$—an assumption that calls for a closer scrutiny.

In this Letter, we analyze the modification of the dispersion due to gain, and show that a large gain will eventually jeopardize the desired slow-light dispersion supported by the periodic system, thus suppressing the slow-light induced light-matter interaction enhancement anticipated in the first place. On the other hand, a small amount of material gain is shown to beneficial. Thus, importantly, devices employing quantum-dot gain material may display a superior performance.

Early investigations emphasized simple one-dimensional periodic media such as Bragg stacks in the context of slow-light enhanced gain and low-threshold band-edge lasing [22]. Likewise, the related phenomenon of slow-light enhanced absorption was proposed as a route to miniaturized Beer-Lambert sensing devices [11]. Slow-light enhancement thus appears to be a conceptual solution to a wide range of fundamental problems involving inherently weak light-matter interactions or technological challenges calling for miniaturization or enhanced performance. However, recent studies of linear absorption [23,24] suggest that n_g itself is also affected by the presence of loss. Likewise, the gain may also influence n_g [25] and analytical studies of coupled-resonator optical waveguides (CROW) show explicitly that the group index and attenuation have to be treated on an equal footing and in a self-consistent manner [26]. Here, we show that the same considerations apply to gain, and illustrate the general consequences with the aid of three examples. Recent studies on random scattering showed that fabrication disorder leads to a loss that increases with the group index [27,28]. This effect imposes another limitation to the degree of light slow-down that may be useful for the applications. However, in contrast, the effect investigated here is intrinsic, and will impede the performance even of a perfectly regular structure.

Coupled-resonator optical waveguide.—We consider first a CROW formed by a linear chain of identical and weakly coupled neighboring optical resonators (inset of Fig. 1). In the frequency range of interest the individual resonators support a single resonance at Ω and when coupled together they form a propagating mode with dispersion relation [29]

$$\omega(k) = \Omega(1 - ig_0)[1 - \gamma\cos(ka)]. \quad (1)$$

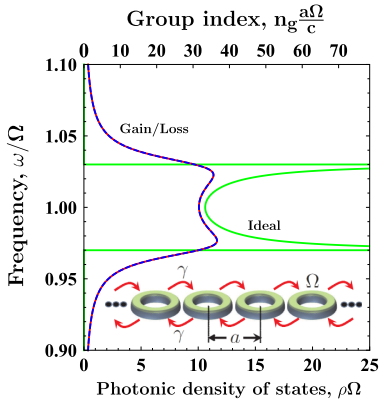

FIG. 1 (color online). Photonic density of states (per resonator) ρ (lower horizontal axis) and group index n_g (upper horizontal axis) versus frequency ω, for a CROW with $\gamma = 0.03$. For passive resonators with $g_0 = 0$, van Hove singularities appear at the band edges. For $g_0 = \pm 0.01$, gain or an equivalent loss cause a similar smearing of the singularities.

Here, a is the lattice constant while g_0 and γ are dimensionless parameters representing the material gain and the coupling, respectively. Our sign convention for the gain term is associated with an $\exp(i\omega t)$ time dependence, corresponding to a real-valued frequency relevant for the excitation by a cw laser source. Inverting Eq. (1) leads to a complex-valued Bloch vector $k(\omega) = k'(\omega) + ik''(\omega)$. The group velocity is computed from $v_g = (\partial k'/\partial\omega)^{-1}$. The photonic density of states (PDOS) is in general proportional to the inverse group velocity and in this particular example $\rho = a/(\pi v_g)$. In Fig. 1 we show the PDOS for a typical CROW, e.g., for a structure working at around the telecom wavelength, $\Omega \sim 10^{15}$ s^{-1}, the figure corresponds to a lattice constant of $a \sim 300$ nm. For the passive structure with $g_0 = 0$ the characteristic van Hove singularities at the lower and upper band edges are found. In the presence of damping ($g_0 < 0$) one expects a smearing of the PDOS and broadening of the singularities [26]. Intuitively, one might expect that loss compensation by addition of gain material will sharpen the PDOS features, but *a priori* it is not clear what net gain ($g_0 > 0$) will result in. However, with the dispersion relation (1) one can show that changing the sign of g_0 causes *no* changes in the PDOS, as is also evident from the plotted results (blue-dashed line). In the context of the intrinsic quality factor Q_0 of the resonators we note that $Q_0 = 1/(2|g_0|)$ [26], which in the present case corresponds to a $Q_0 = 500$. Since $n_g \propto \rho$ we conclude that both loss and gain will reduce the maximal achievable group index, in particular, near the band edges where the group index would otherwise diverge. For the lossy case this is easily understood in terms of multiple scattering, where even a small imaginary absorption coefficient will eventually cause a dephasing of the otherwise constructive interference leading to a standing-wave formation at the band edges. For gain the situation is very much the same; in this situation the multiply scattered wave components increase in amplitude and eventually prevent the perfect formation of a standing-wave solution. Mathematically, changing the sign of g_0 simply corresponds to a complex conjugation of $k(\omega)$, thus rendering the real part and the derived PDOS and group index invariant. This observation clearly illustrates a potential conflict for the anticipated slow-light enhancement of gain if a too high material gain is added. This effect is not special to the CROW as the following two examples demonstrate.

Bragg stack.—Next, we turn to a one-dimensional realization of a more complex PhC concept: the dielectric Bragg stack consisting of alternating layers of thickness a_1 and a_2, with dielectric constants ϵ_1 and ϵ_2, respectively (inset of Fig. 2). The dispersion relation is given by

$$\cos(ka) = \cos\left(\sqrt{\epsilon_1}a_1\frac{\omega}{c}\right)\cos\left(\sqrt{\epsilon_2}a_2\frac{\omega}{c}\right) - \frac{\epsilon_1+\epsilon_2}{2\sqrt{\epsilon_1}\sqrt{\epsilon_2}} \times \sin\left(\sqrt{\epsilon_1}a_1\frac{\omega}{c}\right)\sin\left(\sqrt{\epsilon_2}a_2\frac{\omega}{c}\right), \quad (2)$$

where $a = a_1 + a_2$ is the lattice constant and c is the speed of light in vacuum. The dielectric constants can be complex valued, allowing for analysis of both lossy and gain media [22,30]. The characteristic dispersion diagrams for Bragg stacks are readily derived from $k'(\omega)$. Here we examine the imaginary part $k''(\omega)$, central to our discussion of slow-light gain and loss enhancement. For simplicity, we assume that gain is added to both layers 1 and 2, so that all modes experience the same field overlap with the gain material. Relaxing this assumption will influence the different bands in a slightly different manner, but without changing the overall conclusions. Figure 2 shows a plot of k'' versus ω,

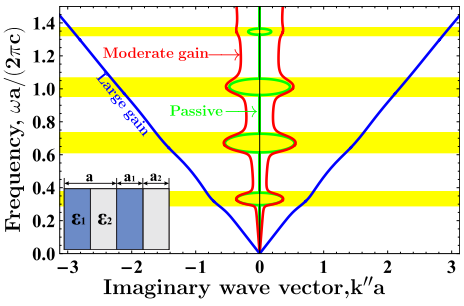

FIG. 2 (color online). Imaginary part of Bloch vector k'' versus frequency ω, for a Bragg stack with $a_2 = 2a_1$, $\epsilon_2' = 3$, and $\epsilon_1' = 1$ [31]. The passive structure (green line) exhibits clear band gaps (yellow shading), which are being smeared out for moderate gain or loss, $\epsilon'' = \pm 0.1$ (red line). Exaggerated large gain or loss ($\epsilon'' = \pm 1$) eventually removes the band-structure effects (blue line).

emphasizing both the positive and negative branches associated with backward and forward propagating branches in the usual k' versus ω dispersion diagram (not shown, however, see Ref. [31]). For the gainless material the imaginary part k'' is nonzero only inside the band gaps (shaded areas) while it vanishes inside the bands of free propagation. As the gain is moderately increased ($g_0 \sim 2000\ \mathrm{cm}^{-1}$ realizable, e.g., with GaAs, see [31]), a finite, enhanced gain develops inside the bands. Clearly, k'' remains finite near the band edges, in contrast to a diverging enhancement as predicted by a lowest-order perturbative treatment [11], where the backaction of material gain on the group index is neglected. For exaggerated larger values of g_0 there is no reminiscence of the band gaps: the structure effectively responds as a homogeneous material.

Photonic crystal waveguide.—As the final example, we consider PhC waveguide structures with a strong transverse guiding due to the presence of a periodic photonic crystal cladding (inset of Fig. 3). Firm light confinement and strong structural dispersion with high n_g [14,32,33] make such waveguides interesting candidates for compact photonic devices and for fundamental explorations of light-matter interactions [9,12]. Because of the need of a nonperturbative treatment, analytical progress is difficult and we proceed numerically with the aid of a finite-element method. We use a supercell approach with boundary conditions fulfilling Bloch-wave conditions with complex wave number k in the direction of the waveguide and simple periodic conditions in the transverse direction [34]. As in the Bragg stack example we model gain by adding a small imaginary part ϵ'' to the base material of the photonic crystal. For a specified real-valued frequency ω we find the associated complex k by diagonalizing a complex matrix eigenvalue problem. Mathematically, changing the sign of ϵ'' leads to the adjoint eigenvalue problem and thus the new eigenvalues are just the complex conjugates of the former. Physically, the group index and the PDOS thus remain unchanged when going from loss to a corresponding gain, while there of course is a change from a net loss to a net gain when inspecting the changes in k''.

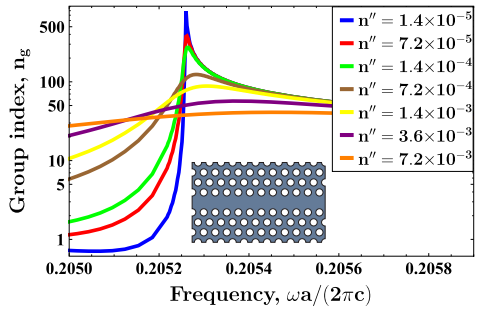

FIG. 3 (color online). Group index n_g versus frequency ω, for a photonic crystal semiconductor waveguide with varying gain $g_0 \propto n''$.

To make contact to practical nanophotonic applications, we parametrize the homogeneous material gain as $g_0 = 2(\omega/c)n''$, where $n = n' + in'' = \sqrt{\epsilon}$ is the complex refractive index of the material. For the specific simulations we consider a semiconductor planar PhC ($\epsilon' = 12.1$) with a triangular lattice of air holes, with lattice constant a and air-hole diameter $d = 0.5 \times a$. Light is localized to and guided along a so-called $W1$ defect waveguide formed by the removal of one row of air holes from the otherwise perfectly periodic structure. Gain in such structures can be realized by embedding layers of quantum wells or quantum dots, which are pumped externally to provide net gain. For simplicity we restrict ourselves to a two-dimensional representation; this does not alter our overall conclusions. This PhC is known to support a guided mode, displaying a low group velocity when k' approaches the Brillouin zone edge. In Fig. 3 we show the associated group index versus frequency. For the passive structure a clear divergence occurs around $\omega^* a/(2\pi c) = 0.205\,25$. As n'' is increased the divergence is smeared out and eventually the group index approaches a constant value well below 50 throughout the frequency range for n'' still as small as 7.2×10^{-3}. Quite surprisingly, increasing the n'' from 1.4×10^{-5} by roughly a factor 500 to 7.2×10^{-3} causes a *reduction* in the maximal group index from more than 500 to around 50. This shows that the addition of gain may reduce the anticipated group index, and as a consequence, also the desired slow-light enhancement of the gain.

Figure 4 shows the effective gain $g_{\mathrm{eff}} = 2k''$ (right-hand axis) versus g_0 evaluated at ω^* (where the propagation is initially slowest). Recalling the introductory discussion we anticipate an enhancement proportional to n_g for low gain and indeed $g_{\mathrm{eff}}a$ starts out with a big slope in the low-gain limit; i.e., gain is greatly enhanced. However, at the singularity $n_g(g_0) \propto g_0^{-1/2}$ [23], and consequently

$$g_{\mathrm{eff}}(g_0) \propto n_g(g_0) g_0 \propto g_0^{1/2}, \tag{3}$$

which is indeed supported by the full numerical data (circular data points) and the indicated square-root dependence (right-hand axis). The slow-light enhancement factor $\Gamma = g_{\mathrm{eff}}/g_0$ (left-hand axis) is correspondingly large for low g_0. Since ω^* is slightly detuned from the singularity a more detailed analysis yields $n_g \propto (\mathrm{const} + g_0)^{-1/2}$ [24] and consequently a deviation from the square-root dependence for small g_0 takes place (see inset). To make a connection with real gain materials, we consider an implementation at telecom frequencies with quantum dots as the active medium. Typically, g_0 is in the range of 10–45 cm^{-1} [35] corresponding to n'' in the range from 1.5×10^{-4} to 7.5×10^{-4}. The slow-light enhanced gain could then be as high as 1300–2835 cm^{-1}, corresponding to a gain enhancement extending from $\Gamma = 130$ down to

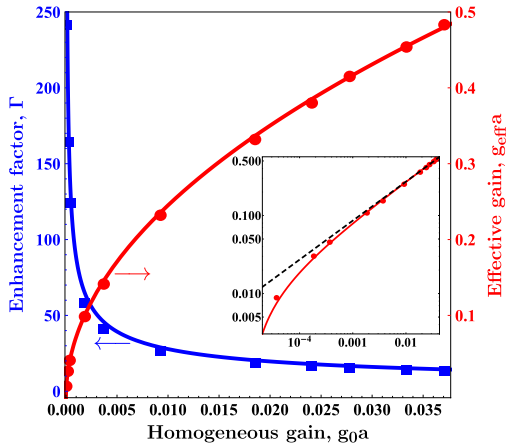

FIG. 4 (color online). Slow-light enhanced gain g_{eff} (right-hand axis) versus homogeneous gain g_0, evaluated at ω^* where the group index is initially maximal, see Fig. 3. The red solid line shows a fit to the anticipated square-root dependence, Eq. (3), while the inset (log-log scale) exhibits minor quantitative deviations from a strict square-root dependence (dashed black line) due to a slight detuning from the band-edge singularity, see discussion in text.

60 for the highest gain. This analysis implicitly assumes that the passive structure itself is ideal and with a diverging group index. However, disorder and imperfections will inevitably be present no matter the effort invested in the fabrication of the PhC. Ensemble averaging over disorder configurations will have the same overall effect on the PDOS as gain or absorption will have; singularities become smeared and the group index assumes a finite value. Clearly, such broadening cannot be compensated by the addition of gain and the achievable effective gain may turn out lower than the estimate given above.

Symmetry points and Brillouin zone edges.—Finally, we discuss our results in the context of Bloch-wave physics, inherent to the general class of periodic photonic metamaterials. From the Bloch condition, the dispersion relation $\omega(k')$ must necessarily be symmetric with respect to the zone edges (e.g., $k' = \pi/a$ for a Bragg stack). In the case of structures with zero gain (loss), this condition is met by $\partial\omega/\partial k' = 0$ at the zone edge, corresponding to a standing-wave pattern. However, in the presence of nonzero gain (loss), k is in general complex and the mode may even propagate inside the band gap region, albeit heavily damped. In this case, the symmetry condition is met by having two branches of solutions that extend across the band gap and with a degeneracy at the zone edge (i.e., crossing bands near the center of the band gap) and correspondingly the group index remains finite. Examples of such modes have been depicted in a number of recent works on lossy dielectric problems [25,26] and for damped plasmonic systems [34,36]. In an attempt to compensate the inherent loss of metamaterials, gain should thus be added with care; while modes seem unaffected under a lasing condition (zero net gain) the anticipated dispersion properties may be jeopardized in an amplifier setup if a too high net gain develops. We have focused on the regime of weak input signals, as appropriate to characterize the small-signal gain properties of an amplifier with no need to include saturation effects of the medium. Beyond this regime there would be a need for a self-consistent solution of the nonlinear light-matter coupling [16,17], possibly revealing new interesting findings when approaching the saturation regime.

In conclusion, adding gain to a periodically structured photonic material changes the dispersion properties and the slow-light enhanced gain in a complex manner. By both analytical examples and a numerical study we have illustrated how a large material gain degrades the slow-light properties supported by the corresponding passive structure, thereby eventually limiting the effective gain enhancement. Waveguide designs away from the band edge constitute an interesting case in the context of quantum-dot gain material. Here, the impact of gain is less detrimental and slow-light gain enhancement is possible with typical enhancement factors in the range from 60 to 130.

This work was financially supported by the Villum Kann Rasmussen Foundation (via the NATEC Center of Excellence), the EU FP7 project GOSPEL, and the FiDiPro program of Academy of Finland.

*asger@mailaps.org

[1] M. Soljačić, S. Johnson, S. Fan, M. Ibanescu, E. Ippen, and J. Joannopoulos, J. Opt. Soc. Am. B **19**, 2052 (2002).
[2] M. Soljačić and J. D. Joannopoulos, Nature Mater. **3**, 211 (2004).
[3] C. Monat, M. de Sterke, and B. J. Eggleton, J. Opt. **12**, 104003 (2010).
[4] B. Corcoran, C. Monat, C. Grillet, D. J. Moss, B. J. Eggleton, T. P. White, L. O'Faolain, and T. F. Krauss, Nature Photon. **3**, 206 (2009).
[5] P. Colman, C. Husko, S. Combrie, I. Sagnes, C. W. Wong, and A. De Rossi, Nature Photon. **4**, 862 (2010).
[6] M. Shinkawa, N. Ishikura, Y. Hama, K. Suzuki, and T. Baba, Opt. Express **19**, 22208 (2011).
[7] R. Boyd, J. Opt. Soc. Am. B **28**, A38 (2011).
[8] G. Lecamp, P. Lalanne, and J. P. Hugonin, Phys. Rev. Lett. **99**, 023902 (2007).
[9] L. Sapienza, H. Thyrrestrup, S. Stobbe, P. D. Garcia, S. Smolka, and P. Lodahl, Science **327**, 1352 (2010).
[10] T. Baba, Nature Photon. **2**, 465 (2008).
[11] N. A. Mortensen and S. Xiao, Appl. Phys. Lett. **90**, 141108 (2007).
[12] J. Mørk and T. R. Nielsen, Opt. Lett. **35**, 2834 (2010).
[13] K. Sakoda, Opt. Express **4**, 167 (1999).
[14] T. F. Krauss, J. Phys. D **40**, 2666 (2007).

[15] S. Xiao, V. P. Drachev, A. V. Kildishev, X. Ni, U. K. Chettiar, H.-K. Yuan, and V. M. Shalaev, Nature (London) **466**, 735 (2010).
[16] S. Wuestner, A. Pusch, K. L. Tsakmakidis, J. M. Hamm, and O. Hess, Phys. Rev. Lett. **105**, 127401 (2010).
[17] J. M. Hamm, S. Wuestner, K. L. Tsakmakidis, and O. Hess, Phys. Rev. Lett. **107**, 167405 (2011).
[18] M. I. Stockman, Phys. Rev. Lett. **106**, 156802 (2011).
[19] R. F. Oulton, V. J. Sorger, T. Zentgraf, R.-M. Ma, C. Gladden, L. Dai, G. Bartal, and X. Zhang, Nature (London) **461**, 629 (2009).
[20] M. A. Noginov, G. Zhu, A. M. Belgrave, R. Bakker, V. M. Shalaev, E. E. Narimanov, S. Stout, E. Herz, T. Suteewong, and U. Wiesner, Nature (London) **460**, 1110 (2009).
[21] S. Matsuo, A. Shinya, T. Kakitsuka, K. Nozaki, T. Segawa, T. Sato, Y. Kawaguchi, and M. Notomi, Nature Photon. **4**, 648 (2010).
[22] J. P. Dowling, M. Scalora, M. J. Bloemer, and C. M. Bowden, J. Appl. Phys. **75**, 1896 (1994).
[23] J. G. Pedersen, S. Xiao, and N. A. Mortensen, Phys. Rev. B **78**, 153101 (2008).
[24] J. Grgić, J. G. Pedersen, S. Xiao, and N. A. Mortensen, Photon. Nanostruct. **8**, 56 (2010).
[25] T. P. White and A. A. Sukhorukov, Phys. Rev. A **85**, 043819 (2012).
[26] J. Grgić, E. Campagnoli, S. Raza, P. Bassi, and N. A. Mortensen, Opt. Quantum Electron. **42**, 511 (2011).
[27] M. Patterson, S. Hughes, S. Combrié, N.-V.-Quynh Tran, A. De Rossi, R. Gabet, and Y. Jaouën, Phys. Rev. Lett. **102**, 253903 (2009).
[28] L. O'Faolain, S. A. Schulz, D. M. Beggs, T. P. White, M. Spasenović, L. Kuipers, F. Morichetti, A. Melloni, S. Mazoyer, J. P. Hugonin *et al.*, Opt. Express **18**, 27 627 (2010).
[29] F. Morichetti, C. Ferrari, A. Canciamilla, and A. Melloni, Laser Photon. Rev. **6**, 74 (2012).
[30] C. V. Shank, J. E. Bjorkholm, and H. Kogelnik, Appl. Phys. Lett. **18**, 395 (1971).
[31] See Supplemental Material at http://link.aps.org/supplemental/10.1103/PhysRevLett.108.183903 for an account of the full dispersion properties.
[32] Y. A. Vlasov, M. O'Boyle, H. F. Hamann, and S. J. Mcnab, Nature (London) **438**, 65 (2005).
[33] M. Notomi, K. Yamada, A. Shinya, J. Takahashi, C. Takahashi, and I. Yokohama, Phys. Rev. Lett. **87**, 253902 (2001).
[34] M. Davanco, Y. Urzhumov, and G. Shvets, Opt. Express **15**, 9681 (2007).
[35] T. Berg and J. Mørk, IEEE J. Quantum Electron. **40**, 1527 (2004).
[36] A. R. Davoyan, I. V. Shadrivov, S. I. Bozhevolnyi, and Y. S. Kivshar, J. Nanophoton. **4**, 043509 (2010).

Publication [P2]

On projection methods, convergence and robust formulations in topology optimization

Struct Multidisc Optim (2011) 43:767–784
DOI 10.1007/s00158-010-0602-y

RESEARCH PAPER

On projection methods, convergence and robust formulations in topology optimization

Fengwen Wang · Boyan Stefanov Lazarov · Ole Sigmund

Received: 10 August 2010 / Revised: 3 November 2010 / Accepted: 18 November 2010 / Published online: 24 December 2010

Abstract Mesh convergence and manufacturability of topology optimized designs have previously mainly been assured using density or sensitivity based filtering techniques. The drawback of these techniques has been gray transition regions between solid and void parts, but this problem has recently been alleviated using various projection methods. In this paper we show that simple projection methods do not ensure local mesh-convergence and propose a modified robust topology optimization formulation based on erosion, intermediate and dilation projections that ensures both global and local mesh-convergence.

Keywords Topology optimization · Robust design · Compliant mechanisms · Manufacturing constraints

1 Introduction

Topology optimization formulated as a density distribution problem has become immensely popular during the last two decades and has been applied to a wide range of application areas apart from the original mechanics problems (Bendsøe and Kikuchi 1988; Bendsøe and Sigmund 2004). By now, there exist a range of alternative topology optimization formulations, including phase field approaches, level-set methods and evolutionary approaches. Hitherto, however, the most popular and widely used approach has been the density approach where element or nodal density values are used as design variables. In order to ensure convergence with mesh refinement, methods can roughly be divided into three categories (cf. Sigmund and Petersson 1998): addition of constraints (e.g. gradient/perimeter control), reduction of the parameter space (e.g. coarser design mesh than analysis mesh), and application of filtering techniques. Of these, the latter have by far been the most popular. Filtering techniques originally comprised sensitivity filtering (Sigmund 1997) and density filtering approaches (Bruns and Tortorelli 2001; Bourdin 2001) and these two approaches have produced globally mesh-convergent designs that in many cases are fully satisfactory for practical purposes. The filters, however, inherently contain gray transitions regions between solid and void regions which in some cases hinder correct modeling of the underlying physics (as e.g. for electrostatic actuators (Yoon and Sigmund 2008)) since the boundaries are not well defined. Also, standard filtering techniques do not prevent the formation of one-node connected hinges in compliant mechanism design (see e.g. Sigmund 1997). Recently, a number of projection schemes that alleviate the gray transition problem have been proposed by Guest et al. (2004), Sigmund (2007), Xu et al. (2010) and Kawamoto et al. (2010) and combinations of the former two were suggested for a multi-projection strategy by Guest (2009) and a robust design formulation by Sigmund (2009).

Although there exist ways to ensure mesh-independence, we argue here that whereas these methods provide a global mesh-independence in the sense that the overall topology will converge with mesh-refinement (no new holes will be introduced), these methods will usually not ensure a local mesh-independence, i.e. they will not prevent small local

F. Wang · B. S. Lazarov (✉) · O. Sigmund
Department of Mechanical Engineering, Solid Mechanics, Technical University of Denmark, Niels Koppel's Allé, Building 404, 2800, Lyngby, Denmark
e-mail: bsl@mek.dtu.dk

F. Wang
e-mail: fwan@mek.dtu.dk

O. Sigmund
e-mail: sigmund@mek.dtu.dk

features e.g. in the form of hinges in compliant mechanisms and narrow gaps for electrostatic actuation problems. This observation is not restricted to density approaches but also includes level-set, phase-field and other alternative approaches. An example that demonstrates that the perimeter control method (Ambrosio and Buttazzo 1993; Haber et al. 1996) ensures global (topology level) but not local (minimum feature size level) convergence is shown in Fig. 1. As the authors see it, there are only very few papers that explicitly address the hinge or local convergence issues: that imposes a rather elaborate constraint (Poulsen 2003); that adds a quadratic energy functional to a level-set formulation and thereby imposes fixed feature size for both void and solid regions (apparently also preventing thick solid regions) (Luo et al. 2008); who proposes a multi-projection method (but with some gray scale issues) (Guest 2009) and that indirectly impose a fixed length scale using a robust formulation (although with some numerical artifacts) (Sigmund 2009).

The paper is composed as follows. In Section 2 we define the basic problem setting and propose a set of test problems (corresponding to those presented in Sigmund (2007) and Sigmund (2009) but with the addition of a thermal conduction problem from Bendsøe and Sigmund (2004) and Guest (2009)). In Section 3 we define the existing density projection schemes and in Section 4 we compare the schemes for the test set defined in Section 2. In Section 5 we propose a modified robust formulation that ensures local convergence, black and white solutions and manufacturing tolerant designs and demonstrate it on the test problems. In Section 6 we develop a framework for predicting length scales imposed by the robust formulation. The proposed robust formulation assumes connected structures and hence Section 7 discusses a problem where this assumption is violated. Section 8 demonstrates the proposed robust formulation combined with filtering based on the solution of partial differential equation (PDE) and Section 9 gives the conclusions.

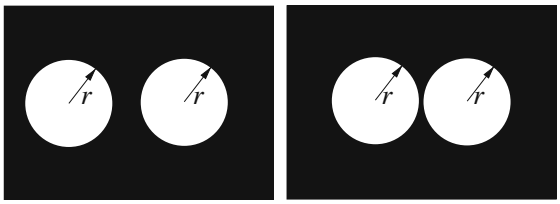

Fig. 1 Demonstration of global vs. local convergence using a perimeter constraint. The two topologies have the same internal perimeter ($P = 4\pi r$) and hence global convergence is achieved. However, the material bridge between the two holes can be infinitely small as seen in the figure (the width of one element) and hence no local mesh-convergence is ensured

2 Problems definition

The minimum compliance optimization problem is one of the most popular test cases for topology optimization procedures. Unfortunately due to its nice behavior (all sensitivities have same sign), some problems like one node connected hinges appearing in compliant mechanism design are disregarded. Therefore, the test set proposed here includes two compliant mechanism design problems and a heat conduction problem that provides strongly mesh-dependent solutions. Their common formulation is given as

$$\begin{aligned} \min_{\rho} &: f(\rho) = \mathbf{l}^{\mathsf{T}}\mathbf{u} \\ s.t. &: \mathbf{K}\mathbf{u} = \mathbf{f} \\ &: f_v(\rho) = \frac{\sum_{i\in\mathbb{N}_e} \tilde{\bar{\rho}}_i v_i}{V} \leq V^* \\ &: \mathbf{0} \leq \rho_i \leq \mathbf{1} \forall i \in \mathbb{N}_e \end{aligned} \tag{1}$$

where $\mathbf{K}$ is the tangent(stiffness) matrix of the physical problem obtained by finite element discretization, $\mathbf{u}$ and $\mathbf{f}$ are the solution and the input vectors to the system, $\mathbb{N}_e$ is the index set of all elements and $\tilde{\bar{\rho}}_i$ is the physical density associated with each design element. v_i is volume of element i, V is the total volume of the design domain and V^* is the allowed fraction of the total volume which can be occupied with material. The individual elements contributions to the tangent matrix $\mathbf{K}$ are calculated as $\mathbf{K}_i = E_i\mathbf{K}_0$ where $\mathbf{K}_0$ is the element stiffness matrix for unit stiffness/conductivity and E_i is the material stiffness/conductivity obtained by using the so-called solid isotropic material interpolation with penalization (SIMP) given as

$$E_i = E_{\min} + \tilde{\bar{\rho}}_i^p (E_0 - E_{\min}) \tag{2}$$

where E_0 is the stiffness/conductivity of the solid phase, p is the penalization power and $\tilde{\bar{\rho}}_i$ is the physical density of element i.

The vector $\mathbf{l}$ in (1) takes different values for the different test problems. For minimum compliance design (the conduction problem) $\mathbf{l} = \mathbf{f}$ and for the compliant mechanism design problems all values of $\mathbf{l}$ are zero except the element which corresponds to the output degree of freedom, which is set to one.

The sensitivity of the objective with respect to the physical design variables $\tilde{\bar{\rho}}_i$ can be calculated by adjoint sensitivity analysis and is given

$$\frac{\partial f}{\partial \tilde{\bar{\rho}}} = \boldsymbol{\lambda}^{\mathsf{T}} \frac{\mathrm{d}\mathbf{K}}{\mathrm{d}\tilde{\bar{\rho}}_i}\mathbf{u} \tag{3}$$

where $\boldsymbol{\lambda}$ is the adjoint vector determined from $\mathbf{K}\boldsymbol{\lambda} = -\mathbf{l}$. For the conduction problem $\boldsymbol{\lambda} = -\mathbf{u}$.

Sketches of the considered test examples are shown in Fig. 2. The first example considers a compliant inverter design problem drawn in Fig. 2a which was defined as a benchmark example for filtering schemes in Sigmund (2007). The objective is to maximize the displacement u_{out} in the negative direction, for applied force $f_{in} = 1$ and spring stiffness coefficients $k_{in} = 1$ and $k_{out} = 0.001$. The volume fraction is $V^* = 0.3$, and Young's moduli for the solid and the void phases are $E_0 = 1.0$ and $E_{\min} = 10^{-9}$, respectively. The second example is a heat conduction problem, where the objective is to transfer effectively heat generated in the design domain. The objective can be written as $f(\boldsymbol{\rho}) = \mathbf{f}^{\mathsf{T}}\mathbf{u}$. The conductivity of the solid is set to $E_0 = 1$, and the minimum conductivity for the void phase is $E_{\min} = 10^{-3}$. The loading is a distributed unit thermal load. The third example considers compliant gripper design, where the objective is to maximize the displacement u_{out} for applied force $f_{in} = 1$, and spring stiffness coefficients $k_{in} = 1$ and $k_{out} = 0.005$. The mechanical properties and the volume fraction are the same as for the compliant inverter. The penalization parameter in (2) is taken to be $p = 3$ for all of the presented examples.

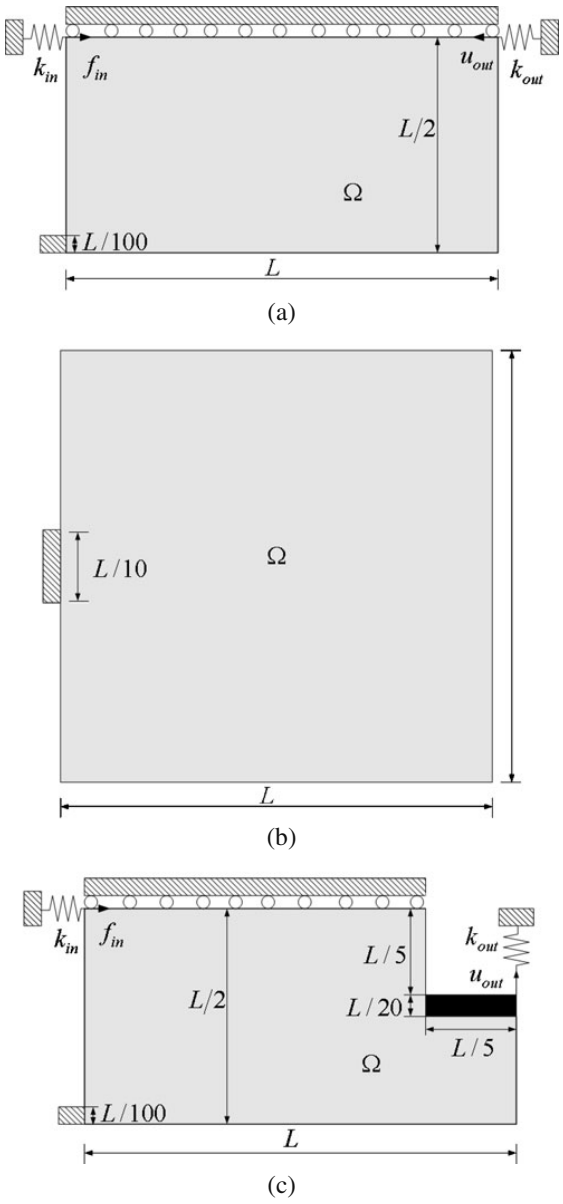

Fig. 2 **a** Design domain and boundary conditions for the compliant mechanism inverter. **b** Design domain and boundary conditions for the heat conduction problem. **c** Design domain and boundary conditions for the compliant mechanism gripper

3 Filtering

Setting the physical density in (1) to be equal to the design variable, i.e. $\bar{\tilde{\rho}}_i = \rho_i$, leads to a mesh dependent solution. Instead of obtaining a better description of the design by refining the finite element mesh, the topology optimization process might add thin details (small solid or void regions), comparable with the mesh size, and might converge to a design with completely different topology. Hence, the length scale in the obtained design becomes dependent on mesh size. Furthermore, for low order element discretization the design might suffer from the well known checkerboard pathology (Díaz and Sigmund 1995; Jog and Haber 1996). In order to avoid these problems the original design problem (1) needs to be regularized. Various techniques have been proposed in the literature (Bendsøe and Sigmund 2004; Sigmund and Petersson 1998). Here the mesh independent density filtering (Bruns and Tortorelli 2001; Bourdin 2001) is used as a basis to ensure existence of solutions. The main idea is to define the physical element density to be a weighted average of the neighboring design variables, where the neighborhood is defined by a circle in 2D or sphere in 3D with specified radius. Applying regularization to the original problem leads to gray transition regions with intermediate densities between 0 and 1. In many problems (e.g. compliance problems) the transition regions are not important and a simple contour plot will provide good interpretations for a final solid/void design. However, for problems with more complex physics and/or objective functions (like electrostatic actuators or compliant mechanisms) practical realizations of these designs are difficult and may provide wrong physical interpretations. Hence, projection techniques which project the filtered designs into 0/1 space have recently been proposed in the literature, e.g. Guest et al. (2004), Sigmund (2007), Xu et al.

(2010) and Kawamoto et al. (2010). In the following, the result from the density filter is denoted with $\tilde{\rho}_i$ and from the projection into 0/1 space with $\bar{\tilde{\rho}}_i$.

The filtered variable $\widetilde{\rho}_i$ for cell i is calculated as

$$\widetilde{\rho}_i = \frac{\sum_{j\in\mathbb{N}_{e,i}} w(\mathbf{x}_j) v_j \rho_j}{\sum_{j\in\mathbb{N}_{e,i}} w(\mathbf{x}_j) v_j} \tag{4}$$

where $\mathbb{N}_{e,i}$ is the neighborhood set of elements lying within the filter domain for element i, $w(\mathbf{x})$ is the weighting function defined as

$$w(\mathbf{x}_j) = R - |\mathbf{x}_j - \mathbf{x}_i| \tag{5}$$

with R the specified filter radius and, $\mathbf{x}_i$ and $\mathbf{x}_j$ contain the central coordinates of the design cells i and j respectively. The derivative of the filtered density $\widetilde{\rho}_i$ with respect to the design variables is calculated as

$$\frac{\partial \widetilde{\rho}_i}{\partial \rho_j} = \frac{w(\mathbf{x}_j) v_j}{\sum_{j\in\mathbb{N}_{e,i}} w(\mathbf{x}_j) v_j} \tag{6}$$

The 0/1 projection $\bar{\tilde{\rho}}_i$ is a function of the filtered density $\bar{\tilde{\rho}}_i(\widetilde{\rho}_i)$ and the sensitivities of the objective function (1) with respect to the original design variables are calculated by using the chain rule as follows

$$\frac{\partial f}{\partial \rho_j} = \sum_{i\in\mathbb{N}_{e,j}} \frac{\partial f}{\partial \bar{\tilde{\rho}}_i} \frac{\partial \bar{\tilde{\rho}}_i}{\partial \widetilde{\rho}_i} \frac{\partial \widetilde{\rho}_i}{\partial \rho_j} \tag{7}$$

3.1 Threshold projection

In this paper we will make use of the parametrized projection function suggested by Xu et al. (2010). This projection function is a generalization of the dilation and erosion projections suggested in Guest et al. (2004) and Sigmund (2007), respectively, and was introduced in order to alleviate bad convergence due to volume preservation issues. All filtered density values $\widetilde{\rho}_i$ above a threshold η are projected to 1 and the values below to 0. The projected physical density $\bar{\tilde{\rho}}_i$ is calculated by a smooth function controlled by a projection parameter β and given as

$$\bar{\tilde{\rho}}_i = \begin{cases} \eta\left[e^{-\beta(1-\widetilde{\rho}_i/\eta)} - (1-\widetilde{\rho}_i/\eta)e^{-\beta}\right] & 0 \le \widetilde{\rho}_i \le \eta \\ (1-\eta)\left[1 - e^{-\beta(\widetilde{\rho}_i-\eta)/(1-\eta)} \right. & \\ \qquad \left. + (\widetilde{\rho}_i-\eta)/(1-\eta)e^{-\beta}\right] + \eta & \eta < \widetilde{\rho}_i \le 1 \end{cases} \tag{8}$$

For $\eta = 0$, the projected value $\bar{\tilde{\rho}}_i$ is equal to the projected filtered value of $\widetilde{\rho}_i$ with the Heaviside step filter introduced by Guest et al. (2004), which ensures minimum length scale on the solid phase (a dilation operator). For $\eta = 1$, the threshold projection coincides with the modified Heaviside filter introduced in Sigmund (2007), which can provide minimum length scale on the void phase (an erosion operator). The studies in Xu et al. (2010) and Kawamoto et al. (2010) indeed shows that the convergence for η close to 0.5 is smooth compared with the previous projection methods and almost discrete designs are obtained for lower β values. However, as it is discussed and demonstrated later, a threshold projection with values of η between 0 and 1 does not enforce length scale on the 0/1 design even though length scale is introduced in the filtered design space by the density filter.

The expression for the threshold projection given by (8), can be replaced by a shorter and simpler expression based on the tanh function. The alternative can be written as

$$\bar{\tilde{\rho}}_i = \frac{\tanh(\beta\eta) + \tanh(\beta(\widetilde{\rho}_i - \eta))}{\tanh(\beta\eta) + \tanh(\beta(1-\eta))} \tag{9}$$

The alternative provides a faster way of computing the 0/1 projection, especially for vectorized computations as the conditional statement in (8) can be avoided. in the limit when $\beta \to \infty$ (9) delivers the same results as (8).

3.2 Multiple phase projections

In Guest (2009) multiple phase projections are proposed in order to ensure minimum length scale on both the solid and the void phases. Two independent design variables are introduced ρ_i^1 and ρ_i^0 to represent the solid and void phases respectively. 0/1 projections for both phases are obtained from (8) by setting $\eta = 0$

$$\bar{\tilde{\rho}}_i^0 = 1 - e^{-\beta\widetilde{\rho}_i^0} + \widetilde{\rho}_i^0 e^{-\beta} \tag{10}$$

$$\bar{\tilde{\rho}}_i^1 = 1 - e^{-\beta\widetilde{\rho}_i^1} + \widetilde{\rho}_i^1 e^{-\beta} \tag{11}$$

In the design the actual physical density is obtained as

$$\bar{\tilde{\rho}}_i = \frac{1}{2}\left(\left(1 - \bar{\tilde{\rho}}_i^0\right) + \bar{\tilde{\rho}}_i^1\right) \tag{12}$$

The multiple phase projection approach in principle provides length scale on both phases, however, our experience is that large gray areas with intermediate densities may appear if no extra measures are taken to penalize these regions strongly.

4 Filter comparison

The filters presented in Section 3 lead to different optimized designs. In order to compare their behavior, results for the compliant mechanism problem (Fig. 2a) and heat conduction problem (Fig. 2b) are presented in Figs. 3 and 4,

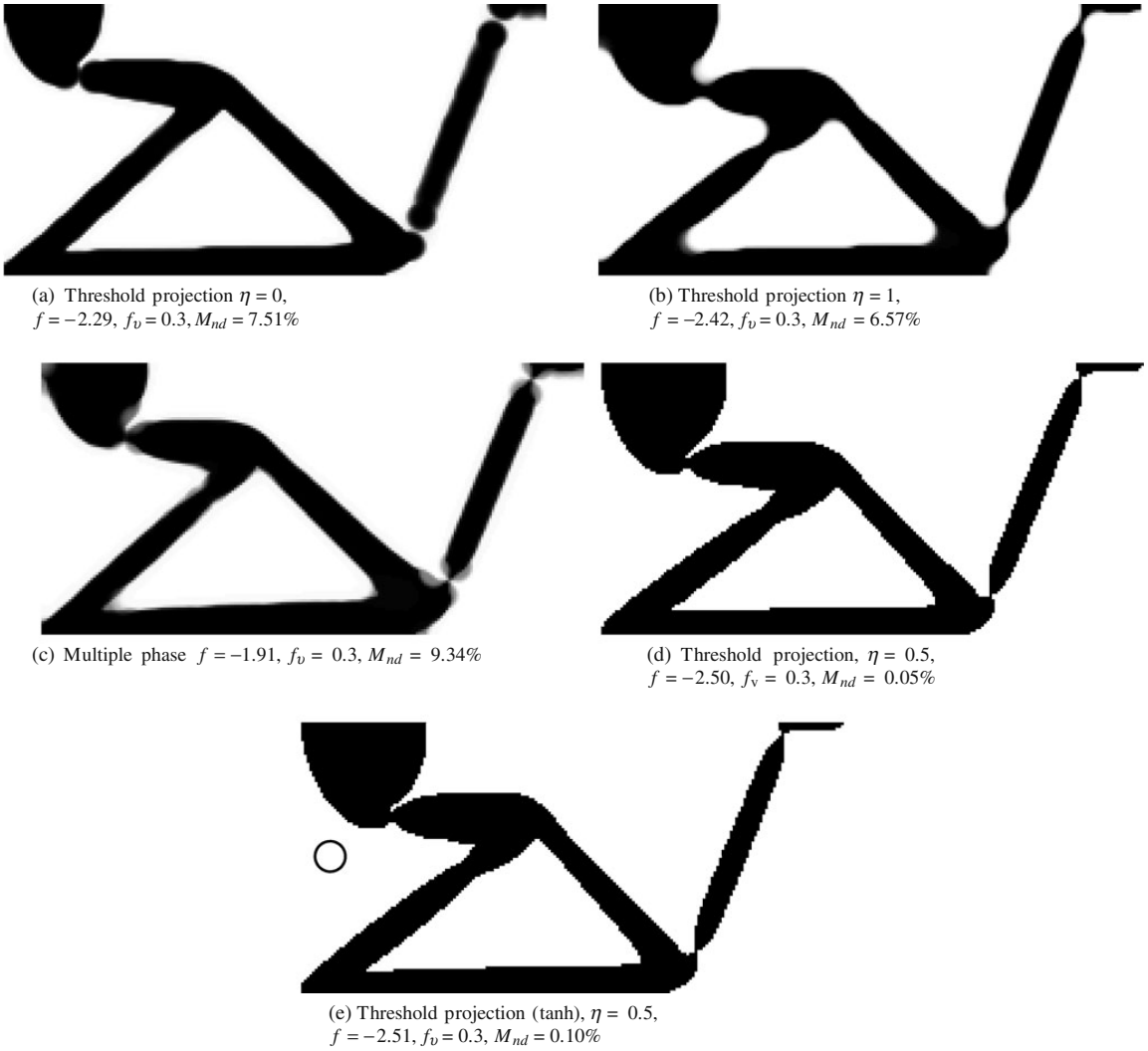

(a) Threshold projection $\eta = 0$, $f = -2.29$, $f_v = 0.3$, $M_{nd} = 7.51\%$

(b) Threshold projection $\eta = 1$, $f = -2.42$, $f_v = 0.3$, $M_{nd} = 6.57\%$

(c) Multiple phase $f = -1.91$, $f_v = 0.3$, $M_{nd} = 9.34\%$

(d) Threshold projection, $\eta = 0.5$, $f = -2.50$, $f_v = 0.3$, $M_{nd} = 0.05\%$

(e) Threshold projection (tanh), $\eta = 0.5$, $f = -2.51$, $f_v = 0.3$, $M_{nd} = 0.10\%$

Fig. 3 Topology optimization of compliant inverter based on different filters. The filter support is shown with *circle* in subfigure **e**

respectively. The filter radius for all designs is set to $R = 5.6L/200$. The value for the projection parameter in (8) is doubled every 50 topology optimization iterations or at convergence, with maximum set to $\beta_{\max} = 128$. The initial value is $\beta = 1$. The discreteness of the obtained designs is measured by a gray level indicator (Sigmund 2007)

$$M_{nd} = \frac{\sum_{i=1}^{n} 4\bar{\bar{\rho}}_i\left(1 - \bar{\bar{\rho}}_i\right)}{n} \times 100\% \tag{13}$$

If all elements have intermediate density, i.e. $\bar{\bar{\rho}}_i = 0.5$, the value of the indicator is 100%. If all elements have density 0 or 1 the value of the indicator is $M_{nd} = 0\%$.

4.1 Compliant mechanism design

Optimized topologies for the compliant inverter problem (Fig. 2a) using different filters are shown in Fig. 3. For most of the designs one or two-node connected hinges can be observed. Minimum length scale for the solid phase is ensured when $\eta = 0$ (Fig. 3a). In this case the void phase does not have any minimum length scale which is demonstrated by the sharp corners around the hinge. For $\eta = 1$ (Fig. 3b) the length scale is imposed on the void phase preventing the concentrated hinge but not the formation of a very thin hinge. In the multiple phase projection case (Fig. 3c), length scale is supposed to be imposed on both phases, however, the design consists of relatively large gray

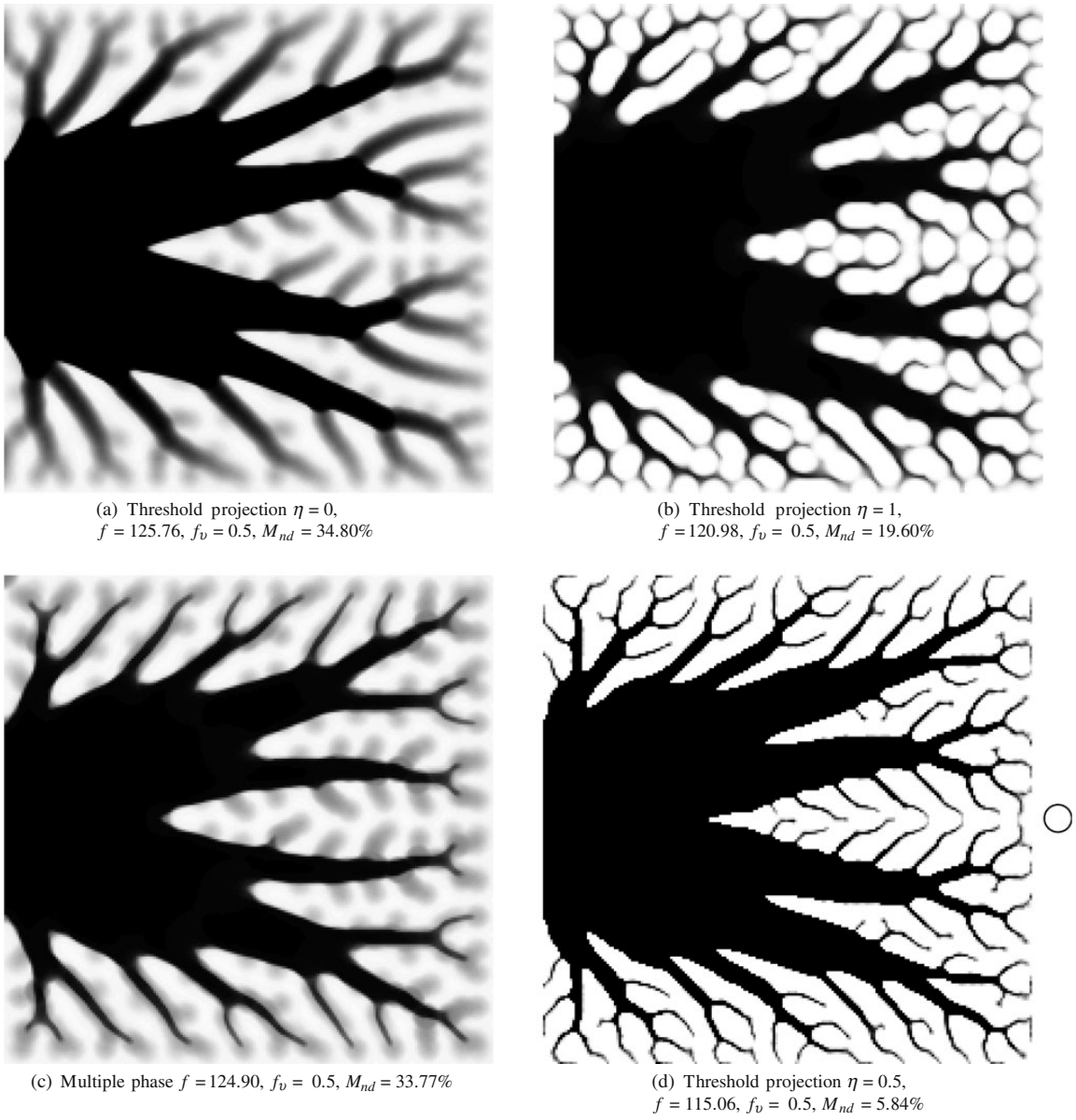

(a) Threshold projection $\eta = 0$, $f = 125.76$, $f_v = 0.5$, $M_{nd} = 34.80\%$

(b) Threshold projection $\eta = 1$, $f = 120.98$, $f_v = 0.5$, $M_{nd} = 19.60\%$

(c) Multiple phase $f = 124.90$, $f_v = 0.5$, $M_{nd} = 33.77\%$

(d) Threshold projection $\eta = 0.5$, $f = 115.06$, $f_v = 0.5$, $M_{nd} = 5.84\%$

Fig. 4 Topology optimization of heat conduction problem based on different filters. The filter support is shown with *circle* in subfigure **d**

areas which is confirmed by the value of M_{nd}. The designs obtained by the threshold projections (Fig. 3d and e) given by (8) and (9) (for $\eta = 0.5$) are practically indistinguishable with slightly higher gray level for the tanh projection. Localized hinges, however, exists in both designs. In conclusion, none of the 0/1 threshold projections can be said to provide satisfactory solutions for the compliant mechanism example and they all destroy the length scale imposed by the underlying density filter.

4.2 Heat conduction design

Optimized topologies for the heat conduction problem are shown in Fig. 4. Both the multiple phase projection and the threshold projection with $\eta = 0$ result in large gray areas. This problem may be avoided by increasing the penalization parameter p, however, this may cause other unwanted effects that may destabilize convergence and hence we prefer a scheme that works with the standard penalization

(i.e. $p = 3$). For $\eta = 1$ the solid phase of the design possesses many thin elements with widths much smaller than the utilized density filter radius. The threshold projection with $\eta = 0.5$ results in the best design in terms of contrast, however it shares the same features as the design for $\eta = 1$—very thin solid elements and sharp corners, which is a good indicator for the lack of local length scale in the design. The tanh projection is not shown as it results in a design very close to the one obtained with the projection given by (8).

4.3 Filter discussion

To further illustrate the lack of length-scale provision of the different projection methods we introduce a test design variable pattern in Fig. 5a. The test pattern consists of lines and circular elements with various thickness as well as a checkerboard region. The result from the density filtering of the test pattern, shown in Fig. 5b, contains large gray areas which is common for these type of filters. All designs obtained only with density filters have gray transition

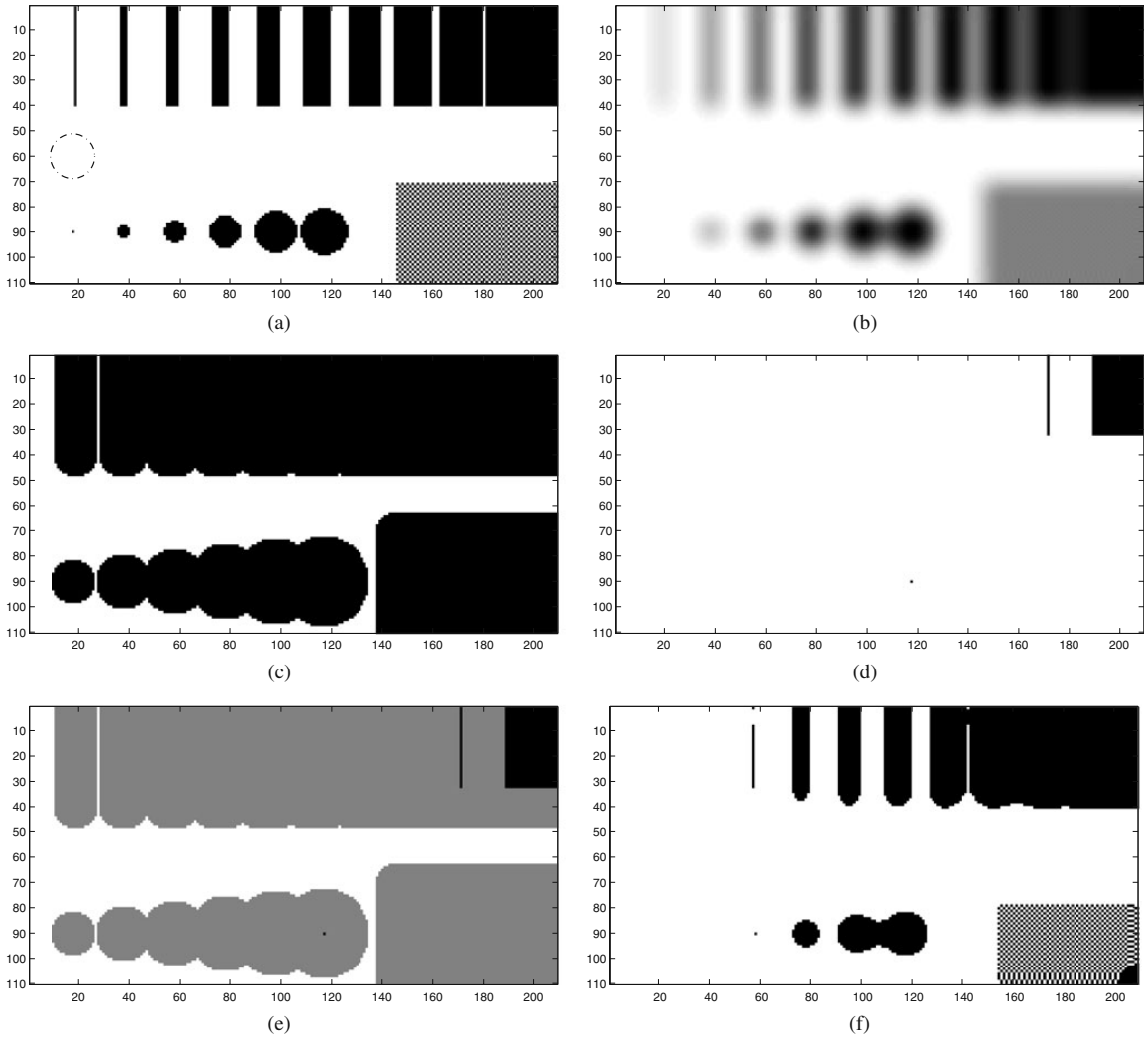

Fig. 5 **a** Design field, the dash-dot circle indicates the filter size. **b** Density distribution after density filter ($\widetilde{\rho}_i$). **c** Physical density distribution for $\eta = 0$. **d** Physical density distribution for $\eta = 1$. **e** Physical density distribution based on multiple phase projection. **f** Physical density distribution for $\eta = 0.5$

regions which depend on the filter radius. Larger filter radii result in larger gray areas. The threshold projections for $\eta = 0$ and $\eta = 1$ result in high contrast filtered designs, however in the first case sharp corners and thin void lines can be easily observed in the figure. In the second case thin solid lines can be observed as well, which indicates that no length scale is imposed on the void or the solid phases for $\eta = 0$ and $\eta = 1$, respectively. The multiple phase projection (Fig. 5e) results in large gray areas. The threshold projection with $\eta = 0.5$, shown in Fig. 5d results in a high contrast image with small features in both the solid and the void phases which indicates lack of length scale. Somewhat surprisingly the checkerboard pattern also survives the filtering process which pin points the shortcoming of this approach.

5 Modified robust topology optimization

In the previous section it can be clearly seen that simple threshold projections cannot provide local length scale control. Length scale can be ensured only on the solid or the void phases for $\eta = 0$ and $\eta = 1$, respectively. The imposed length scale relies on the fact that the filter has finite support domain. In Sigmund (2009) it has been demonstrated that reformulating the design problem as a robust problem that includes two projections, can avoid zero length hinges in the compliant mechanism design and therefore ensure local length scale control. Here the formulation is improved for numerical robustness to cover a larger class of problems. Estimation of the obtained length scale is shown as well.

5.1 Robust topology optimization

Following similar idea as in Sigmund (2009) dilated $\bar{\tilde{\rho}}^d$, intermediate $\bar{\tilde{\rho}}^i$ and eroded $\bar{\tilde{\rho}}^e$ designs can be formulated utilizing the threshold projection with thresholds η, 0.5 and $1-\eta$, respectively. For the three designs, the filtered field below the threshold is projected towards 0, and above the threshold towards 1, utilizing the threshold projection (8) as demonstrated in Fig. 6. The original design problem (1) is reformulated as a min/max problem

$$
\begin{aligned}
&\min_{\rho} : \max \quad \left(\mathbf{f}(\bar{\tilde{\rho}}^e(\rho)), \mathbf{f}(\bar{\tilde{\boldsymbol{\rho}}}^i(\rho)), \mathbf{f}(\bar{\tilde{\boldsymbol{\rho}}}^d(\rho))\right) \\
&s.t. : \mathbf{K}(\bar{\tilde{\rho}}^e)\mathbf{u}^e = \mathbf{f} \\
&\quad : \mathbf{K}(\bar{\tilde{\rho}}^i)\mathbf{u}^i = \mathbf{f} \\
&\quad : \mathbf{K}(\bar{\tilde{\rho}}^d)\mathbf{u}^d = \mathbf{f} \\
&\quad : f_v(\rho) = \frac{\sum_i \bar{\tilde{\rho}}_i^d v_i}{V} \le V_d^* \\
&\quad : 0 \le \rho \le 1
\end{aligned} \tag{14}
$$

where $\eta \le 0.5 \le 1-\eta$. The volume constraint is imposed on the dilated design. Every 20 iteration the volume fraction is updated so the volume of the intermediate design becomes equal to a prescribed value. Implementation of the robust formulation[1] requires the solution of three finite element problems. The sensitivities of the objective with respect to the design variables are calculated based on the three finite element solutions and utilizing the chain rule (7). The effect of the three projections is demonstrated in Fig. 6 for smooth linear transition of the filtered density from 0 to 1. If the obtained optimized designs $\bar{\tilde{\rho}}_e$, $\bar{\tilde{\rho}}_i$ and $\bar{\tilde{\rho}}_d$ have the same topology, the solid phase has elements with size decreasing from the dilated case to the eroded one and the void phase have elements with size increasing in the opposite way. Therefore the difference between the three designs defines manufacturing error bounds on both solid and void phases which ensure fulfillment of the min/max objective function (14).[2] The optimization process can be written in algorithmic form as follows.

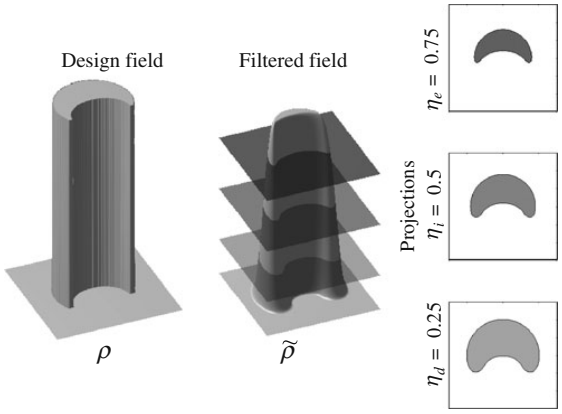

Fig. 6 Illustration of the threshold projections for different choices of the threshold value η

1. Initialize the design variable ρ. Set up the threshold value η and the maximum design variable change $\Delta\rho_{\max}$, the iteration counter $i = 0$, and $\beta = 1$.

[1] The difference between the present robust formulation and the one introduced in Sigmund (2009) is the representation of the intermediate design and the volume bound which is applied on the dilated structure instead of the intermediate. In Sigmund (2009) the intermediate design is simply the design variable field ρ. However, in the present approach the intermediate design has gone through the same density filtering as the dilated and eroded designs and it is obtained as the projection for $\eta = 0.5$. The modifications eliminate numerical artifacts associated with the old approach and result in much more stable convergence of the optimization problem.

[2] It is interesting to note that there are many similarities between the threshold projection schemes and the level-set approach to topology optimization (Allaire et al. 2004; Wang et al. 2003; Kawamoto et al. 2010). In the presented scheme the filtered density field $\tilde{\rho}$ correspond to the level-set function ϕ and the projections correspond to zero and $\pm\Delta\eta$ level curves. Hence it is obvious that the proposed robust optimization scheme can be implemented using a level-set approach as well.

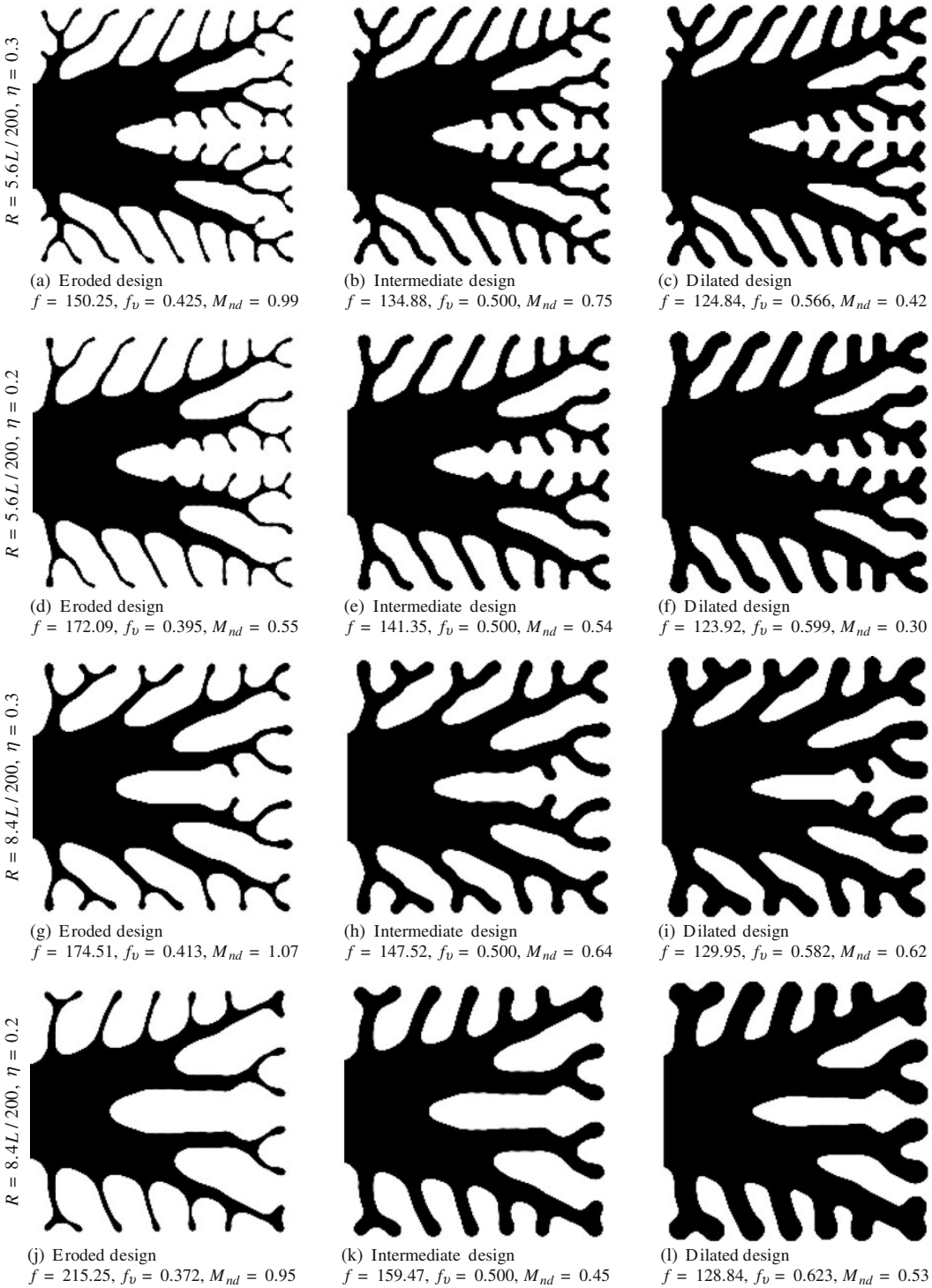

Fig. 7 Robust heat conduction design for different parameter sets

2. **while** $|\Delta\rho|_\infty \leq \Delta\rho_{\max}$ and $i \leq i_{\max}$ and $\beta \leq \beta_{\max}$ **do**
   - i = i + 1
   - Compute $\bar{\tilde{\rho}}^e$, $\bar{\tilde{\rho}}^i$ and $\bar{\tilde{\rho}}^d$ using (8).
   - Solve the three FEM problems $\mathbf{K}(\bar{\tilde{\rho}}^i)\mathbf{u}^i = \mathbf{f}$, $\mathbf{K}(\bar{\tilde{\rho}}^e)\mathbf{u}^e = \mathbf{f}$ and $\mathbf{K}(\bar{\tilde{\rho}}^d)\mathbf{u}^d = \mathbf{f}$.
   - Compute the sensitivities for the three designs using (7).
   - Update the design variables.
   - **if** [mod(i,20) =1] update the volume fraction of the dilated structure $V_d^* = \frac{V^*}{V_i} V_d$ such that the volume of the intermediate design V_i becomes equal to V^*.
   - **if** [mod(i,50) = 1 or $|\Delta\rho|_\infty \leq 0.01$] and [$\beta \leq \beta_{\max}$] **then** $\beta = 2\beta$

where V^* and V_i are the prescribed and the current volume fraction for the intermediate design, respectively. The design updates are performed using the method of moving asymptotes (MMA) by Svanberg (1987). Robust designs for the considered examples are demonstrated in Figs. 7, 8 and 9.

5.2 Heat conduction

Results obtained using the robust formulation, given by (14) for the heat conduction problem, are shown in Fig. 7. Two different filter radii are used in the simulation $R = 5.6L/200$ and $R = 8.4L/200$. The dilated and the eroded designs are obtained for $\eta = 0.2$ and $\eta = 0.3$. All designs possess high contrast with gray index indicator for almost

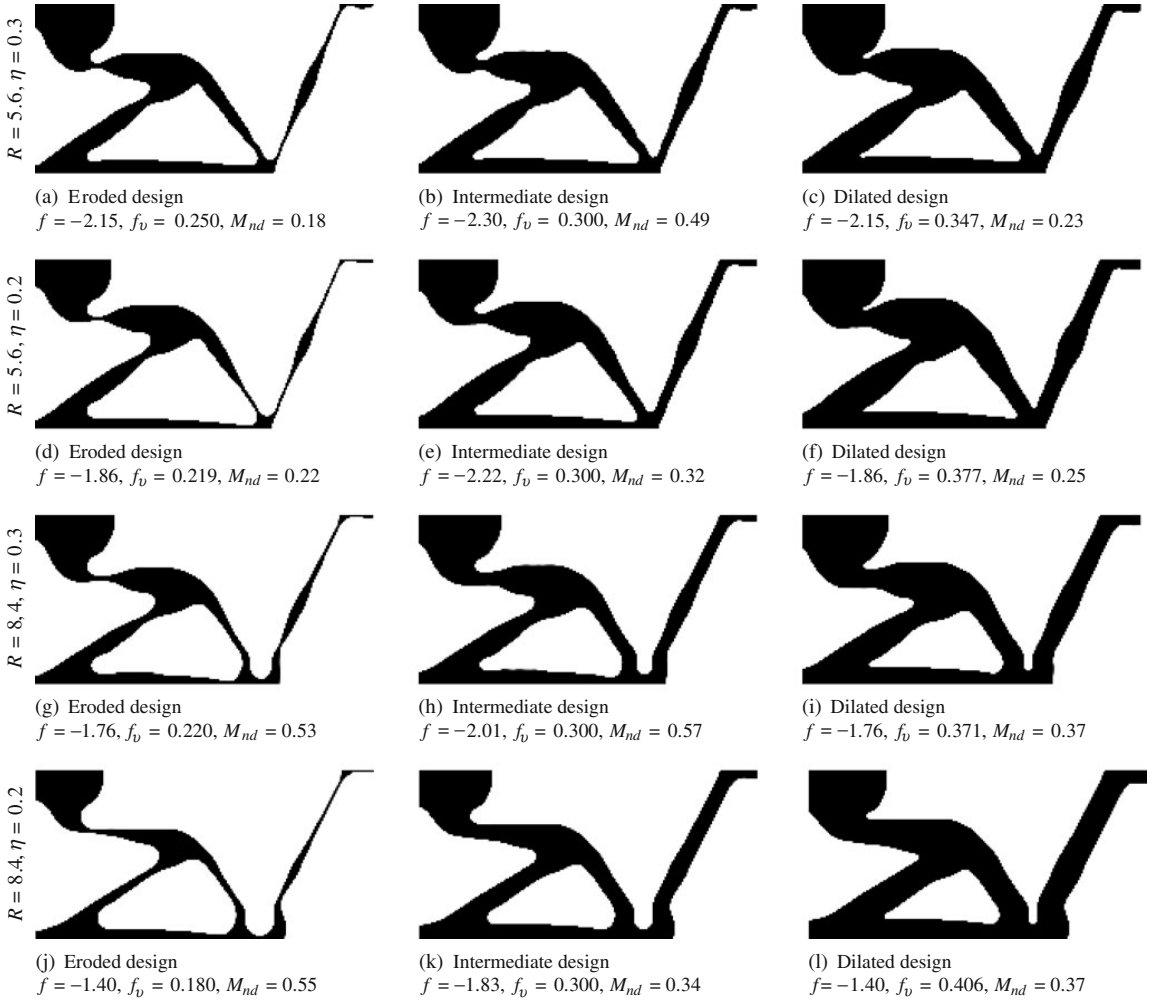

(a) Eroded design $f = -2.15$, $f_v = 0.250$, $M_{nd} = 0.18$
(b) Intermediate design $f = -2.30$, $f_v = 0.300$, $M_{nd} = 0.49$
(c) Dilated design $f = -2.15$, $f_v = 0.347$, $M_{nd} = 0.23$
(d) Eroded design $f = -1.86$, $f_v = 0.219$, $M_{nd} = 0.22$
(e) Intermediate design $f = -2.22$, $f_v = 0.300$, $M_{nd} = 0.32$
(f) Dilated design $f = -1.86$, $f_v = 0.377$, $M_{nd} = 0.25$
(g) Eroded design $f = -1.76$, $f_v = 0.220$, $M_{nd} = 0.53$
(h) Intermediate design $f = -2.01$, $f_v = 0.300$, $M_{nd} = 0.57$
(i) Dilated design $f = -1.76$, $f_v = 0.371$, $M_{nd} = 0.37$
(j) Eroded design $f = -1.40$, $f_v = 0.180$, $M_{nd} = 0.55$
(k) Intermediate design $f = -1.83$, $f_v = 0.300$, $M_{nd} = 0.34$
(l) Dilated design $f = -1.40$, $f_v = 0.406$, $M_{nd} = 0.37$

Fig. 8 Robust design of compliant inverter for different parameter sets

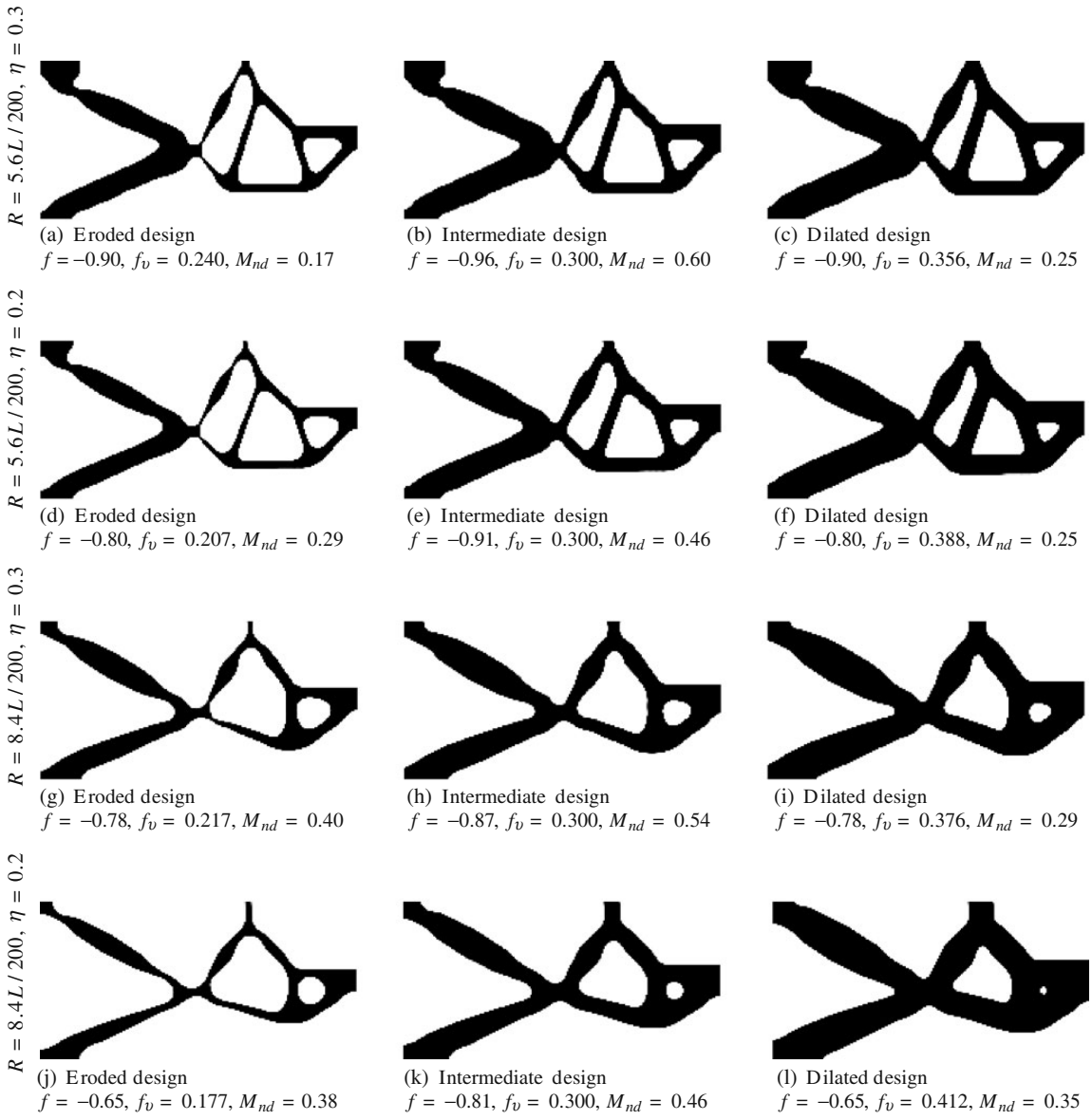

Fig. 9 Robust design of compliant gripper for different parameter sets

all of them less than 1%. As expected the eroded design consists of several solid features with very small thicknesses and the dilated design exhibits features with larger thicknesses. The intermediate design in all cases is between the eroded and the dilated. The topology for the eroded, intermediate and dilated designs is the same for all of the presented cases. The objective decreases from the eroded to the dilated design, because of the monotonous dependency on the volume fraction. Close inspection of the intermediate designs with the same filter radius and for $\eta = 0.3$ and $\eta = 0.2$, reveals that thin elements which appear in the case for $\eta = 0.3$ do not exist for $\eta = 0.2$. As demonstrated later in Section 6, the design obtained using $\eta = 0.2$ has larger minimum length scale than the design obtained with $\eta = 0.3$. The length scale increases with increasing distance between the intermediate threshold and η and depends on the filter radius as well. All edges in the intermediate designs are smooth.

After optimization, the intermediate design $\bar{\tilde{\rho}}^i$ defines the optimized blue-print design. This design is robust with respect to under- or over- etching which is very important for micro and nano-fabrication processes (e.g. Sardan et al. 2008; Borel et al. 2005). In addition, as we show in this paper, the intermediate blue-print design $\bar{\tilde{\boldsymbol{\rho}}}^i$ is in general a very good design with full control of minimum solid and void length scales.

5.3 Compliant mechanism design

Robust optimized topologies for the compliant inverter example are shown in Figs. 8 and 14. Two filter radii $R = 5.6L/200$ and $R = 8.4L/200$, and two different threshold values are utilized in the designs. In contrast to the standard formulation where zero length hinges can be observed in the design, all elements have finite thickness which is always larger than zero. Similar to the heat conduction problem the minimal feature thickness for the same filter radius increases with decreasing threshold value. The obtained designs posses high contrast. The topology in all of the presented cases does not change between the eroded, intermediate and dilated designs.

5.4 Compliant gripper design

Robust designs for the compliant gripper are shown in Fig. 9. The density filter radii and the thresholds are chosen to be the same as for the heat conduction and the compliant inverter design. For all four cases the topology does not change from the eroded to the dilated designs. The robust formulation prevents the appearance of zero length features, i.e. hinges, in the design. Sharp corners in the intermediate design do not appear which indicates that length scale is imposed on the void phase as well.

6 Minimum length scale definition

The examples given in the previous section clearly demonstrate that the proposed robust formulation imposes length scale on the 0/1 optimized design. The remaining question is how the choice of η can be linked with the imposed length scale? In order to provide an answer, first the filtering together with the projection processes are discussed in details and later based on the assumption of having the same topology for the eroded, intermediate and dilated designs, the length scale is estimated as a function of η. The obtained results are valid for 2D and 3D problems. In 2D the minimum length scale is defined by a circle dot and in 3D by a spherical dot with diameters equal to the length scale in 1D. The filter support domain $\mathbb{B}_R$ is an interval in 1D, a circle in 2D and a sphere in 3D with radius R. The analysis performed here is for normalized weighting function defined by (5), however similar analysis can be performed for any other weighting function.

The filtering process for 1D design is demonstrated in Fig. 10. First the original design variables ρ are smoothed by the density filter, and then, by selecting a threshold value, the filtered density $\tilde{\rho}$ is projected to 0/1 space. The width of the solid(left) or void(right) region is denoted with h. If $h \geq 2R$ the filtered value at point $x_{p,1}$ is equal to the value of the design field. For $h \leq 2R$ the filtered value $\tilde{\rho}_i(x_{p,1})$ is always smaller than or equal to $\rho(x_{p,1})$. A similar relation holds for the void phase - for $h \leq 2R$, $1 - \tilde{\rho}_i$ is always bigger or equal to $1 - \rho$. Plot of the filtered density $\tilde{\rho}_i$ and void phases $1-\tilde{\rho}_i$ as functions of $h/2R$ are shown in Fig. 11.

Applying Heaviside projection with threshold taken to be the maximum of the filtered solid phase, results in a point with length zero for all points lying on the solid line in Fig. 11, and on interval with length larger than zero for all points under the line. For all combinations of η and $h/2R$ above the solid curve the 0/1 projection results in void phase. For the void phase all points $(h/2R, \eta)$ lying on the dashed curve are projected to void points with length zero and all points above the dashed curve are projected into the void interval with length larger than zero. Based on the above discussion and on the examples in Section 4 it can be concluded that there is no length scale associated with the projected density $\bar{\tilde{\rho}}$, even though $\tilde{\rho}_i$ is mesh independent (Bourdin 2001) and the density filter imposes length scale for the filtered density field.

In the examples presented in Section 5 it can be clearly seen that the robust formulation given by (14), imposes minimum length scale on the design. Here the relation between

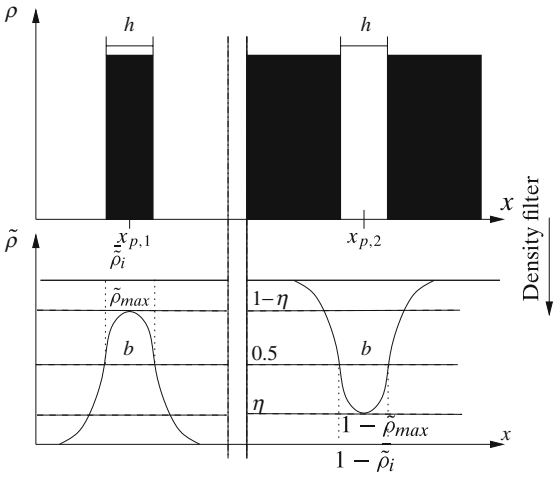

Fig. 10 Density filtering of solid and void phases and their Heaviside projections

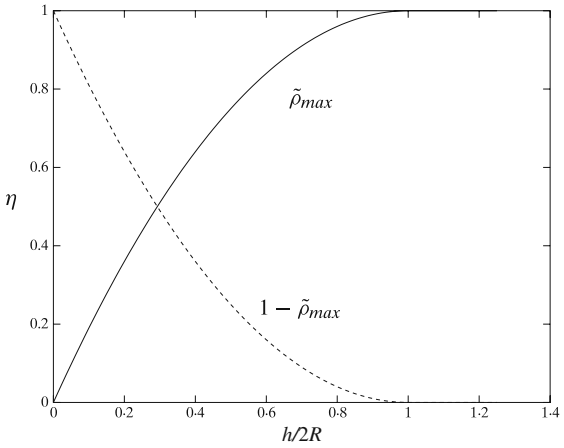

Fig. 11 Maximum/minimum of the filtered density of the solid/void phase as functions of the normalized width $h/2R$

the minimum length scale and the choice for the threshold value η is defined based on the assumption that the topology for all three cases η, 0.5 and $1-\eta$ is the same. A solid point with length zero in the eroded design is projected to a solid interval for the intermediate design with finite length larger than zero, e.g. Fig. 10. For the void, a point with length zero in the dilated design is projected to a void interval with finite length larger than zero in the intermediate design. Therefore, based on the assumption that the eroded, intermediate and dilated designs share the same topology, the choice of η determines uniquely the minimum length features which can appear in the solid and in the void phases in the projected 0/1 space. Relation between η and the minimum length scale in the 0/1 space for the solid and void can be obtained numerically by evaluating the maxima/minima

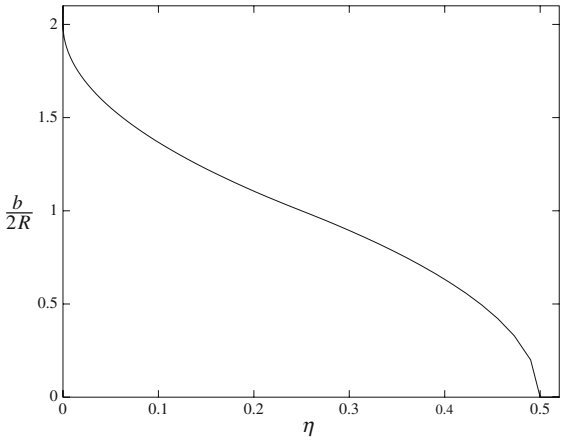

Fig. 12 Normalized length scale on the intermediate design as a function of the threshold η for the robust formulation

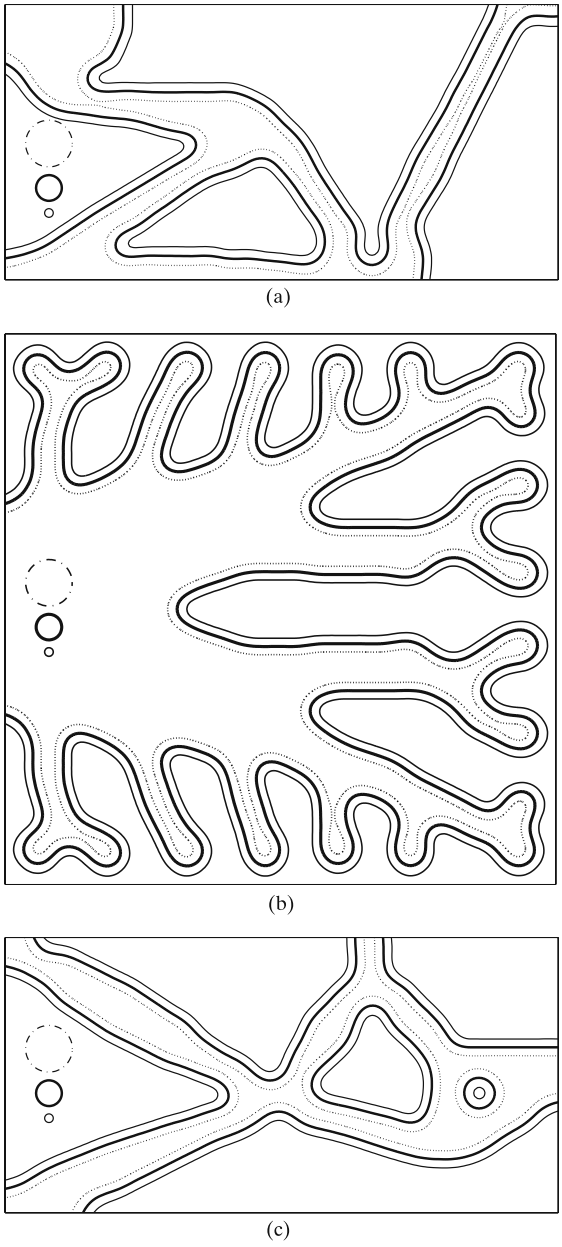

Fig. 13 Contours of different designs with $R = 8.4L/200$ and $\eta = 0.2$, The *thin solid lines* denote the contour of the dilated design, the *bold solid lines* denote the contour of the intermediate design, and the *dotted lines* denote the contour of the eroded design. The *dot-dashed circle* indicates the filter support domain, the *bold circle* indicates the minimal length scale on the intermediate design and the *small thin circle* indicates the minimum manufacturing tolerance between the eroded and intermediate designs or the intermediate and the dilated designs. **a** Compliant inverter. **b** Heat conduction. **c** Compliant gripper

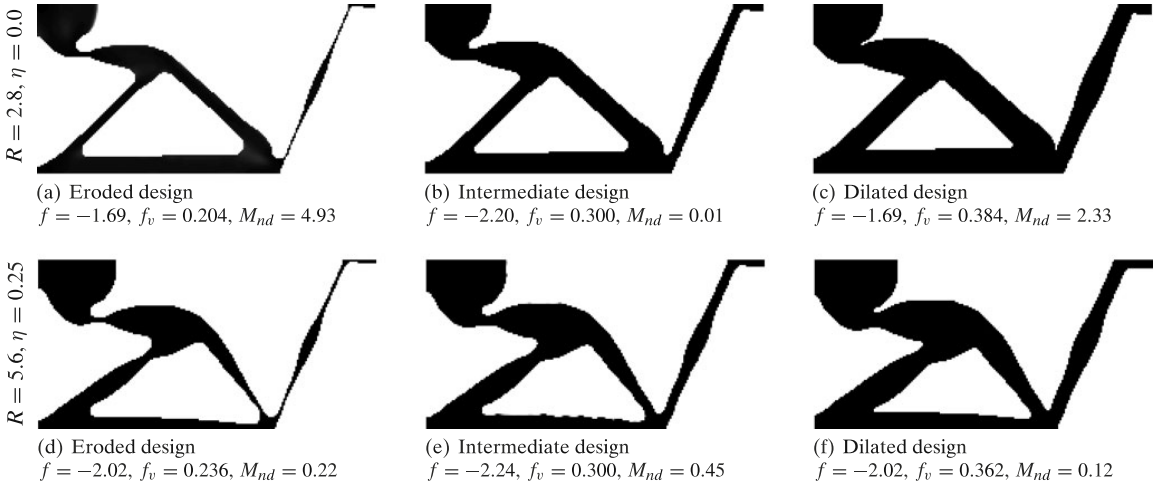

(a) Eroded design
$f = -1.69,\ f_v = 0.204,\ M_{nd} = 4.93$

(b) Intermediate design
$f = -2.20,\ f_v = 0.300,\ M_{nd} = 0.01$

(c) Dilated design
$f = -1.69,\ f_v = 0.384,\ M_{nd} = 2.33$

(d) Eroded design
$f = -2.02,\ f_v = 0.236,\ M_{nd} = 0.22$

(e) Intermediate design
$f = -2.24,\ f_v = 0.300,\ M_{nd} = 0.45$

(f) Dilated design
$f = -2.02,\ f_v = 0.362,\ M_{nd} = 0.12$

Fig. 14 Robust design of compliant inverter with different filter radius and same minimum length scale

and the interval length at level 0.5 bounded by the filtered design as shown in Fig. 10. Results for different values of the threshold η are shown in Fig. 12. Projecting point from the curve on the vertical and horizontal axes, gives the minimum length scale and the value of η which ensures it. For example if the minimum length scale is required to be $b = 0.092L$ and the filter radius is set $R = 8.4L/200$, the ratio $b/2R$ is equal to 1.1055. Using the graph shown in Fig. 12 for ratio $b/2R = 1.1055$ one can determine the value of $\eta = 0.2$. Selecting different filter radius will result in different value of η. The size of the filter determines the robustness of the design and is discussed later in this section. The relation between the minimum length scale and η can be generalized further by taking three independent thresholds for the dilated, intermediate and eroded design. This case is discussed shortly in Appendix.

6.1 Minimum length scale—examples

In order to validate the estimated minimum length scale, contours of the optimized designs for each problem shown in Fig. 2, the heat conduction, the compliant inverter and the compliant gripper, for $R = 8.4L/200$ and $\eta = 0.2$, are shown in Fig. 13. The estimated minimum length scale for the intermediate design is shown with a bold circle. The circle can be freely moved inside each of the phases, the solid and the void, without crossing the solid line which is the border of the intermediate design. For elements which are located on the borders of the design domain the minimum length scale is half of the estimation due to the symmetry in the boundary conditions. The eroded and the dilated designs are shown with dotted and thin solid lines respectively. They indicate the allowed error bounds for the design. Under-etching or over-etching the intermediate design with error outside the error bounds will violate the objective function for the robust formulation. The length scale imposed on the solid phase in the dilated design and on the void phase in the eroded design can be estimated in the same way as the minimum length scale. More details can be found in Appendix.

The minimum length scale depends on both the filter radius R and the threshold η. Different combination of

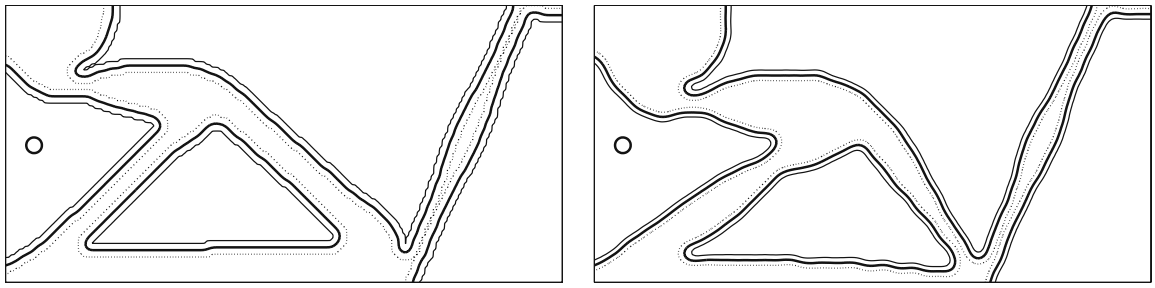

(a) $R = 2.8, \eta = 0.0$

(b) $R = 5.6, \eta = 0.25$

Fig. 15 Error tolerance and minimum length scale for the robust compliant inverter design

(R, η) can lead to the same minimum length scale. Examples for robust optimized designs for the compliant inverter with the same minimum length scale are shown in Fig. 14 and length scale verification is shown on Fig. 15. The topologies of the obtained intermediate designs differ even though the minimum length scale is the same for both of them. This is due to the different robustness of the designs. For $R = 2.8$ and $\eta = 0$ the error bounds are larger than for the design obtained with $R = 5.6$ and $\eta = 0.25$. Selecting smaller η provides a more robust optimized topology for the same minimum length scale.

7 Design of photonic crystal waveguide with tailored dispersion properties

In the previous section we discussed and showed how the proposed robust formulation provides a minimum length scale on both void and solid regions of the intermediate design. This finding assumes that the structure remains connected and that the eroded, intermediate and dilated structures share the same topology. In the examples considered so far these requirements have been fulfilled. A disconnected mechanical or thermal structure would not be able to transfer force or heat and hence these structures generally want to stay connected.

Examples where the structures do not necessarily want to stay connected are photonic crystal based waveguides and structures (Borel et al. 2005; Jensen and Sigmund 2005). Here, the material property (permittivity) of void regions is finite (equal to the vacuum permittivity) and the contrast in permittivity between solid and void regions is small (one order of magnitude). Hence, a topological change from connected to unconnected happens frequently during optimization.

As a specific example we consider the design of a photonic crystal based waveguide for slow light (small and constant group velocity) (Stainko and Sigmund 2007; Wang et al. 2010). These dispersion relations can be obtained by optimizing the dielectric material distribution in the supercell, the periodical cell of the photonic crystal waveguide. The robust design for slow light with group velocity of $v_g = 0.04c$ is shown in Fig. 16. Almost constant group velocity of $v_g = 0.04c$ is achieved for both the eroded, the intermediate and the dilated structures. However, there are topological changes between the eroded and the other two designs and isolated components show up in the eroded design. Hence, no strict definition of length scales can be proven for this kind of topology optimization problems. Nevertheless, the optimized design provides a robust solution which will diminish errors associated with etching uncertainties during the nano-fabrication process. For more details on the problem formulation and a description of a methodology for avoiding disconnected solid regions the reader is referred to Wang et al. (2010).

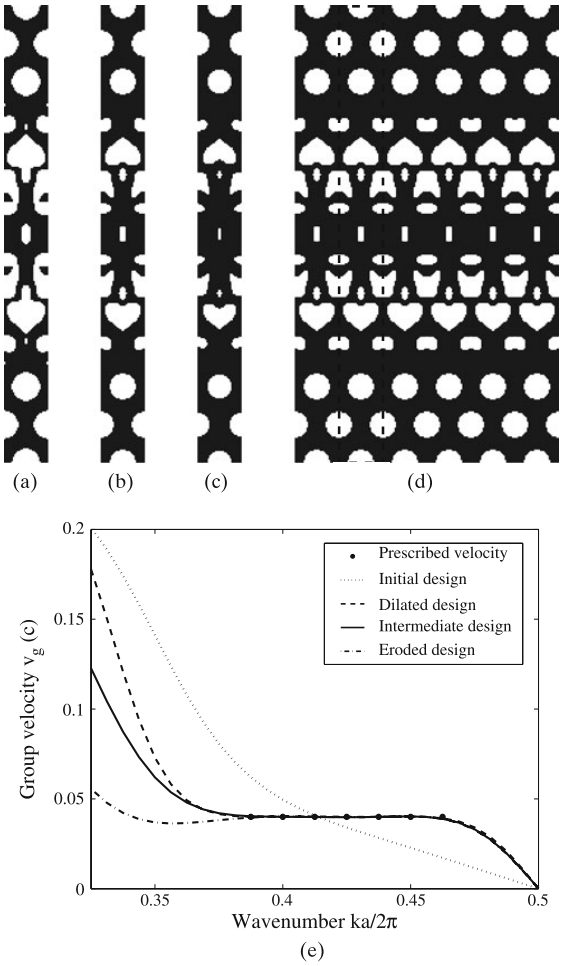

Fig. 16 Photonic crystal waveguide design for slow light. **a** Dilated design. **b** Intermediate design. **c** Eroded design. **d** The super cell from **b** is repeated five times. **e** Group velocity of different designs and the prescribed group velocity

8 Helmholtz filtering

Instead of using the explicit filter form (4), the density filter can be defined implicitly as a solution of the Helmholtz partial differential equation (Lazarov and Sigmund 2010) with homogeneous Neumann boundary conditions

$$-r^2\nabla^2\widetilde{\rho} + \widetilde{\rho} = \rho \tag{15}$$

$$\frac{\partial\widetilde{\rho}}{\partial\mathbf{n}} = 0 \tag{16}$$

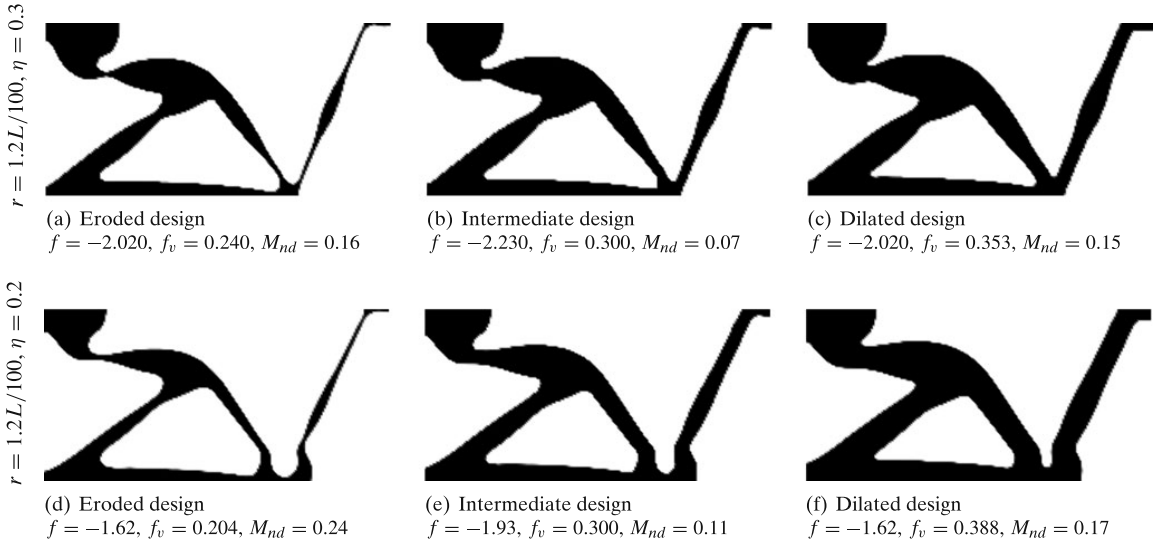

(a) Eroded design
$f = -2.020$, $f_v = 0.240$, $M_{nd} = 0.16$

(b) Intermediate design
$f = -2.230$, $f_v = 0.300$, $M_{nd} = 0.07$

(c) Dilated design
$f = -2.020$, $f_v = 0.353$, $M_{nd} = 0.15$

(d) Eroded design
$f = -1.62$, $f_v = 0.204$, $M_{nd} = 0.24$

(e) Intermediate design
$f = -1.93$, $f_v = 0.300$, $M_{nd} = 0.11$

(f) Dilated design
$f = -1.62$, $f_v = 0.388$, $M_{nd} = 0.17$

Fig. 17 Robust design of compliant inverter where the filter (4) has been substituted with the Helmholtz filters (15) and (16)

where ρ is the unfiltered density field, $\widetilde{\rho}$ is the filtered density field and Ω is the design domain. The parameter r in (15) plays a similar role as R in the original filter.

The solution of the PDE filter can be obtained by Finite Element discretization utilizing the mesh for the state problem. The sensitivities are obtained by using the chain rule (7). The cost of solving the PDE for a given mesh is proportional to the length parameter r, if an iterative method is employed. A relation between the length parameter r and the classical filter radius R can be obtained by equating the second moments of the weighting functions $r = R/2\sqrt{3}$.

The Helmholtz filter has been previously utilized as a sensitivity filter and density filter in topology optimization problems (Lazarov and Sigmund 2009, 2010), where some of its properties with respect to parallelization of the solution process have been discussed in details. Here only the main advantages with respect to memory usage and computational cost are highlighted. The classical filter requires information about the neighbor elements, which is obtained by a relatively expensive search. In case the search is performed only once as a preprocessing step and the information about the neighbors is stored, the memory consumption is proportional to R^2 in 2D and to R^3 in 3D. The computational complexity is proportional to the memory consumption. In contrast, the Helmholtz PDE utilizes the mesh used for performing the state analysis and does not require any additional information, which avoids excessive memory usage. Furthermore the computational cost depends linearly on the filter parameter. Therefore, for large filter radius the PDE filtering scheme should be the preferred choice.

Examples of optimized designs for the compliant force inverter obtained by using the Helmholtz filter and the robust formulation are shown in Fig. 17. The 0/1 projection utilizes the expression given by (9). The optimization process follows the algorithm presented in Section 5.1. The results are very similar to the ones obtained by using the classical filter. A finer mesh design is shown in Fig. 18. The design contours are much smoother due to the finer resolution. The main difference between the PDE and the classical filter is the size of the filter support domain. Due to the finite circular support domain, 0/1 projection with threshold

(a) Coarse mesh 20000 elements
$f = -1.93$, $f_v = 0.300$, $M_{nd} = 0.11$

(b) Fine mesh 125000 elements
$f = -1.89$, $f_v = 0.300$, $M_{nd} = 0.07$

Fig. 18 Robust design (intermediate) obtained with two different mesh sizes with the Helmholtz filter

0 or 1 for the classical filter introduces length scale for the solid or void regions respectively. The PDE filter support domain coincides with the design domain and projections with thresholds 0 or 1 must be avoided.

9 Conclusions

In this paper we have demonstrated that standard Heaviside projection filtering schemes used to ensure 0/1 designs in topology optimization cannot provide local length scale control. The original Heaviside projection method only provides a minimum length scale on solid regions, the modified Heaviside projection method only provides a length scale on void regions and the volume preserving projection method neither imposes length scale on solid nor on void regions. In order to alleviate this problem we propose a modified robust formulation that combines the three projections into a min-max problem that (1) ensures optimized designs that are robust towards under- or overetching, (2) ensures local length scale control on both solid and void regions of the intermediate design and (3) results in crisp black and white designs for moderate β values. The proposed method is very computationally stable and all examples in the paper have been run automatically with the same parameter settings. Disadvantages of the proposed method are the added computational cost of having to solve three separate finite element problems and large iteration numbers due to the β continuation strategy. The authors believe that the added computational cost can (or must) be tolerated when considering robust optimization formulations, however, time savings may be obtained by considering efficient re-analysis techniques (Amir et al. 2009; Kirsch 2008). Concerning the β continuation strategy further investigations on move-limit strategies and choice of other optimization parameters may make it possible to start with higher values of β and/or increase it in larger steps, hence lowering iterations counts.

Acknowledgments This work was financially supported by Villum Fonden (via the NATEC Centre of Excellence), a Eurohorcs/ESF European Young Investigator Award (EURYI), a Center of Advanced User Support (CAUS) grant from the Danish Center of Scientific Computing (DCSC), and by the Elite Research Prize from the Danish Minister of Research.

Appendix

The thresholds for the dilated and the eroded designs can be chosen independently, if different length scales need to be imposed on the void and the solid phases. The procedure for determining the minimum length scale is similar to the one presented in Section 6. The estimation is based on the assumption that the topology does not change between the

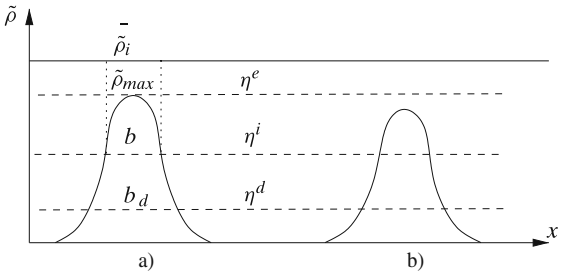

Fig. 19 Filtered density field and with 0/1 projection based on different thresholds

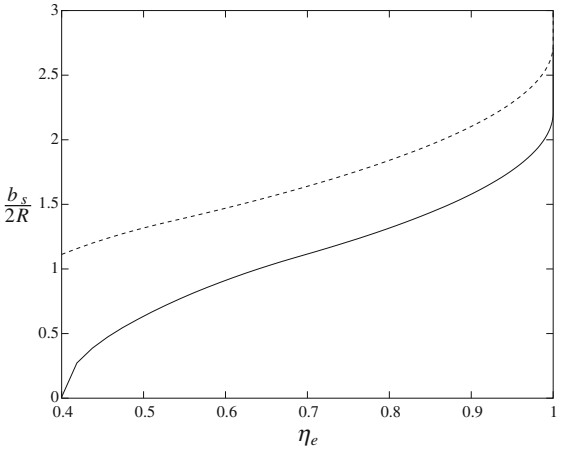

Fig. 20 Length scale of the solid phase as functions of the threshold for the eroded designs for $\eta_i = 0.4$. *Dashed line* shows the minimum length scale for the solid phase in the dilated design for $\eta_d = 0.2$

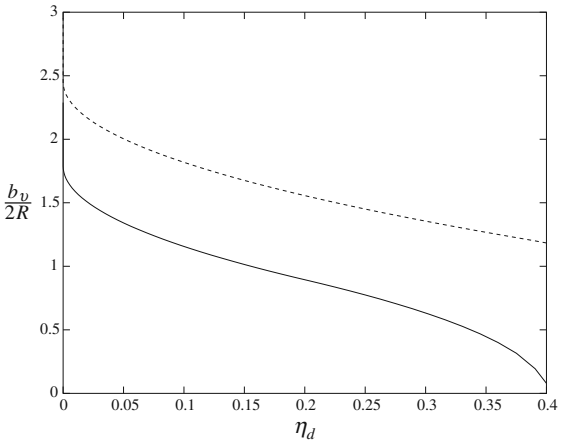

Fig. 21 Length scale of void phase as functions of the threshold for the dilated designs for $\eta_i = 0.4$. *Dotted line* shown the minimum length scale for the void phase in the eroded design for $\eta_e = 0.7$

three designs—the eroded, the intermediate and the dilated. Two cases for the filtered designs are shown in Fig. 19. In the first case, Fig. 19a, the maximum of the filtered design $\tilde{\bar{\rho}}$ is equal to the threshold for the eroded design and 0/1 projection with threshold η_e results in point with zero length scale. In the second case, Fig. 19b, the maximum of the filtered design is below η_e, and the projection with threshold η_e results in void phase. Therefore, even if the projections with thresholds η^i and η^d result in intervals with finite lengths, the topology for $\tilde{\bar{\rho}}^e$, $\tilde{\bar{\rho}}^i$ and $\tilde{\bar{\rho}}^d$ is different and the presented minimum length scale estimate is not valid for this case.

If the topologies are the same for all three thresholds η^e, η^i and η^d, $\tilde{\rho}_{\max}$ is always $\tilde{\rho}_{\max} \geq \eta_e$. Then the minimum length scale for the intermediate and the dilated designs can be estimated numerically by finding the lengths b and b^d of the intervals obtained by crossing the threshold lines with the filtered density. The length scale for the void phase can be estimated in a similar way. The difference between η^e and η^i determines the length scale in the solid phase and the difference between η^d and η^i determines the length scale in the void phase. Graphs for the normalized length scales of the solid and void phases as functions of the thresholds are shown in Figs. 20 and 21.

References

Allaire G, Jouve F, Toader AM (2004) Structural optimization using sensitivity analysis and a level-set method. J Comput Phys 194(1): 363–393

Ambrosio L, Buttazzo G (1993) An optimal design problem with perimeter penalization. Calc Var Partial Differ Equ 1:55–69

Amir O, Bendsoe MP, Sigmund O (2009) Approximate reanalysis in topology optimization. Int J Numer Methods Eng 78(12): 1474–1491

Bendsøe MP, Kikuchi N (1988) Generating optimal topologies in structural design using a homogenization method. Comput Methods Appl Mech Eng 71(2):197–224

Bendsøe MP, Sigmund O (2004) Topology optimization—theory, methods and applications. Springer, Berlin

Borel PI, Frandsen LH, Harpøth A, Kristensen M, Jensen JS, Sigmund O (2005) Topology optimised broadband photonic crystal Y-splitter. Electron Lett 41(2):69–71

Bourdin B (2001) Filters in topology optimization. Int J Numer Methods Eng 50(9):2143–2158

Bruns T, Tortorelli D (2001) Topology optimization of non-linear elastic structures and compliant mechanisms. Comput Methods Appl Mech Eng 190(26–27):3443–3459

Díaz A, Sigmund O (1995) Checkerboard patterns in layout optimization. Struct Multidisc Optim 10:40–45

Guest J (2009) Topology optimization with multiple phase projection. Comput Methods Appl Mech Eng 199(1–4):123–135. doi:10.1016/j.cma.2009.09.023

Guest J, Prevost J, Belytschko T (2004) Achieving minimum length scale in topology optimization using nodal design variables and projection functions. Int J Numer Methods Eng 61(2):238–254

Haber RB, Jog CS, Bendsøe MP (1996) A new approach to variable-topology shape design using a constraint on the perimeter. Struct Optim 11(1):1–11

Jensen JS, Sigmund O (2005) Topology optimization of photonic crystal structures: a high-bandwidth low-loss T-junction waveguide. J Opt Soc Am B Opt Phys 22(6):1191–1198

Jog CS, Haber RB (1996) Stability of finite element models for distributed-parameter optimization and topology design. Comput Methods Appl Mech Eng 130(3–4):203–226

Kawamoto A, Matsumori T, Yamasaki S, Nomura T, Kondoh T, Nishiwaki S (2010) Heaviside projection based topology optimization by a pde-filtered scalar function. Struct Multidisc Optim. doi:10.1007/s00158-010-0562-2

Kirsch U (2008) Reanalysis of structures. Springer, Berlin

Lazarov B, Sigmund O (2009) Sensitivity filters in topology optimisation as a solution to Helmholtz type differential equation. In: Proc. of the 8th world congress on structural and multidisciplinary optimization. Lisbon, Portugal

Lazarov B, Sigmund O (2010) Filters in topology optimizat ion based on Helmholtz type differential equations. Int J Numer Methods Eng. doi:10.1002/nme.3072

Luo J, Luo Z, Chen S, Tong L, Wang MY (2008) A new level set method for systematic design of hinge-free compliant mechanisms. Comput Methods Appl Mech Eng 198(2):318–331

Poulsen TA (2003) A new scheme for imposing a minimum length scale in topology optimization. Int J Numer Methods Eng 57(6): 741–760

Sardan Ö, Petersen DH, Mølhave K, Sigmund O, Bøggild P (2008) Topology optimized electrothermal polysilicon microgrippers. Microelectron Eng 85:1096–1099. doi:10.1016/j.mee.2008.01.049

Sigmund O (1997) On the design of compliant mechanisms using topology optimization. Mech Struct Mach 25(4):493–524

Sigmund O (2007) Morphology-based black and white filters for topology optimization. Struct Multidisc Optim 33(4–5):401–424

Sigmund O (2009) Manufacturing tolerant topology optimization. Acta Mech Sin 25(2):227–239. doi:10.1007/s10409-009-0240-z

Sigmund O, Petersson J (1998) Numerical instabilities in topology optimization: a survey on procedures dealing with checkerboards, mesh-dependencies and local minima. Struct Optim 16(1):68–75

Stainko R, Sigmund O (2007) Tailoring dispersion properties of photonic crystal waveguides by topology optimization. Waves Random Complex Media 17:477–489

Svanberg K (1987) The method of moving asymptotes—a new method for structural optimization. Int J Numer Methods Eng 24:359–373

Wang F, Jensen J, Sigmund O (2010) Robust topology optimization of photonic crystal waveguides with tailored dispersion properties (submitted)

Wang MY, Wang X, Guo D (2003) A level set method for structural topology optimization. Comput Methods Appl Mech Eng 192(1–2):227–246

Xu S, Cai Y, Cheng G (2010) Volume preserving nonlinear density filter based on heaviside funtions. Struct Multidisc Optim 41: 495–505

Yoon GH, Sigmund O (2008) A monolithic approach for topology optimization of electrostatically actuated devices. Comput Methods Appl Mech Eng 197:4062–4075. doi:10.1016/j.cma.2008.04.004

Publication [P3]

Robust topology optimization of photonic crystal waveguides with tailored dispersion properties

Robust topology optimization of photonic crystal waveguides with tailored dispersion properties

Fengwen Wang,* Jakob S. Jensen, and Ole Sigmund

Department of Mechanical Engineering, Technical University of Denmark, Nils Koppels Allé, Building 404, 2800 Kgs. Lyngby, Denmark
**Corresponding author: fwan@mek.dtu.dk*

Received August 16, 2010; revised December 9, 2010; accepted December 12, 2010; posted December 15, 2010 (Doc. ID 133488); published February 8, 2011

A robust topology optimization method is formulated to tailor dispersion properties of photonic crystal waveguides, with consideration of manufacturing uncertainties. Slightly dilated and eroded realizations are considered as well as the real structure, and by worst-case optimization, we also ensure a satisfactory performance in the case of an under- or overetching scenario in the manufacturing process. Two photonic crystal waveguides facilitating slow light with group indexes of $n_g = 25$ and $n_g = 100$ and bandwidths of $\Delta\omega/\omega = 2.3\%$ and 0.3%, respectively, are obtained through the proposed robust design procedure. In addition, a novel waveguide design with two different constant group index waveguide regions is demonstrated. The numerical examples illustrate the efficiency of the robust optimization formulation and indicate that the topology optimization procedure can provide a useful tool for designing waveguides that are robust to manufacturing uncertainties such as under or overetching.

OCIS codes: 000.4430, 130.5296, 230.7400.

1. INTRODUCTION

Slow-light waveguides have a great variety of applications, such as for compact optical delay lines, optical buffers, and enhanced light-matter interaction [1]. Photonic crystal waveguides (PhCWs), generated by missing air holes in a two-dimensional (2D) photonic crystal (PhC) slab, facilitate slow-light propagation within the bandgap of the PhC [2] through strong structural dispersion. The slow-light regime of PhCWs is usually located in the vicinity of the Brillouin zone edge, where the group index diverges to infinity. The slow-light bandwidth becomes narrower as the group index increases and large group-velocity dispersion (GVD) can be observed in the slow-light regime, which can severely distort the optical signal. Therefore, special attention has been paid to these issues [3–7].

The PhCW dispersion properties are strongly sensitive to structural details, and they can be tuned through the design of the supercell, the periodic cell of PhCWs. Previously, it was demonstrated that the dispersion curve can be tailored by different approaches. Slow light with low GVD has been achieved by chirping the waveguide properties [3,4], perturbing the diameters of the air holes [5] or the locations of air holes [6] adjacent to the central defect. However, slow-light propagation is very sensitive to geometrical parameters, and thus very careful experiments are necessary for observation and evaluation of the slow light [7]; manufacturing uncertainties may degrade or destroy the prescribed group velocity. Therefore, a systematic and robust design methodology is highly desirable for PhCW design.

A method that recently has been successfully applied to a range of PhC based structures and devices is the topology optimization method [8]. This method, which is based on repeated finite-element analyses and gradient-based optimization updates, was originally developed for mechanical problems, but has more recently been applied to PhC design in a number of papers [9–11]. A comprehensive review of topology optimization applied to nano-optical design can be found in Ref. [12]. Previously it was demonstrated that topology optimization can be applied to create novel waveguides with enhanced dispersion properties [13]. By maximizing the mode confinement for a prescribed frequency-wavenumber range, Stainko and Sigmund managed to achieve a constant group velocity within a 5% error interval. The present work addresses the dispersion control problem considered in [13] in a more rigorous manner and simultaneously tackles important manufacturability issues.

A main challenge in topology optimization is the manufacturability of the optimized designs, which includes imposing a minimum length scale on the designs and consideration of manufacturing uncertainties due to under or overetching in the manufacturing process. Different filter schemes have been introduced to control checkerboard instabilities and achieve minimum length scale [14–22]. In order to realize robustness in topology optimization, Sigmund [23] suggested a robust formulation based on dilated, intermediate, and eroded design realizations corresponding to under, normal, and overetching, respectively.

In this work, we focus on robust topology optimization of PhCWs with tailored dispersion properties. Manufacturing uncertainties are approximated by a threshold projection method with different thresholds [24]. Based on Floquet–Bloch type eigenvalue analysis of the supercell, we formulate the objective as the error between the actual group index and a prescribed group index for certain discrete wavenumbers. The robust formulation consists in minimizing the maximum error among the dilated, intermediate and eroded design realizations. Band constraints are introduced to avoid multiple modes and to isolate the designed propagation band.

This paper is organized as follows. In Section 2, we present the 2D model that is used to calculate the band structure of PhCWs and a numerical approximation of the group index. In Section 3, the formulation for robust topology optimization and the associated analytical sensitivities are given. Numerical examples are demonstrated in Section 4 and we summarize in Section 5

2. PHYSICAL PROBLEM

PhCWs can facilitate guided modes in the bandgap of PhCs. For a TE-polarized PhCW, the light propagation can be modeled by the Helmholtz equation in the frequency domain

$$\nabla \cdot \left(\frac{1}{\varepsilon_r}\nabla h\right) + \left(\frac{\omega}{c}\right)^2 h = 0, \tag{1}$$

where ε_r is the space-dependent relative permittivity, h is the magnetic field, ω is the wave frequency, and c is the speed of light in vacuum.

In this study, we focus on the triangular lattice PhCW based on a silicon membrane ($n_{\mathrm{Si}} = 3.476$, $\varepsilon_{\mathrm{Si}} = n_{\mathrm{Si}}^2$). As a starting point for our optimization study, we consider the initial waveguide structure illustrated in Fig. 1(a). The dimension of the supercell in the propagation direction is the lattice constant a. The line defect is surrounded by 5.5 layers of air holes and the dimension of the supercell perpendicular to the propagation direction is $b = 6\sqrt{3}a$. The diameter of the air holes is $d = 0.6a$. The calculation of the band structure of PhCWs can be formulated as an eigenvalue problem of the supercell with Floquet–Bloch wave boundary conditions. Based on the supercell in Fig. 1(a), the Floquet–Bloch wave boundary conditions can be stated as

$$h(x,a) = \exp(ika)h(x,0) \qquad h(0,y) = h(b,y), \tag{2}$$

where k is the Bloch-wavenumber in the propagation direction.

The discrete expression of Eq. (1) can be obtained using the finite-element method

$$(\mathbf{K}_k - \omega^2\mathbf{M})\mathbf{h} = 0, \tag{3}$$

where $\mathbf{K}_k$ is the global finite-element matrix stemming from the first term in Eq. (1), $\mathbf{h}$ is a vector of discretized nodal values of magnetic field h, and $\mathbf{M}$ is the global finite-element matrix from the second term in Eq. (1). The wavenumber dependency of $\mathbf{K}_k$ is introduced by the implementation of the boundary conditions in Eq. (2) through the penalty approach.

Figure 1(b) depicts the band structure of the supercell in Fig. 1(a). The gray regions indicate the slab mode region (modes in the crystal not confined to the line defect). The dotted curve denotes the light line $\omega = ck$, which represents the condition for light leaking in the out-of-plane direction. Beneath the light line, the higher index waveguide core pulls down discrete guided modes into the bandgap [2]. Because of the presence of a lateral symmetry, the guided modes can be classified as laterally even modes (solid curve) and laterally odd modes (dashed curve). In this paper, only even modes are considered for guided waves.

Figure 1(b) shows that the even band flattens out as it approaches the band edge and the group velocity of the guided mode decreases to zero. The group velocity v_g of a guided mode with frequency ω is defined as the band slope at frequency ω:

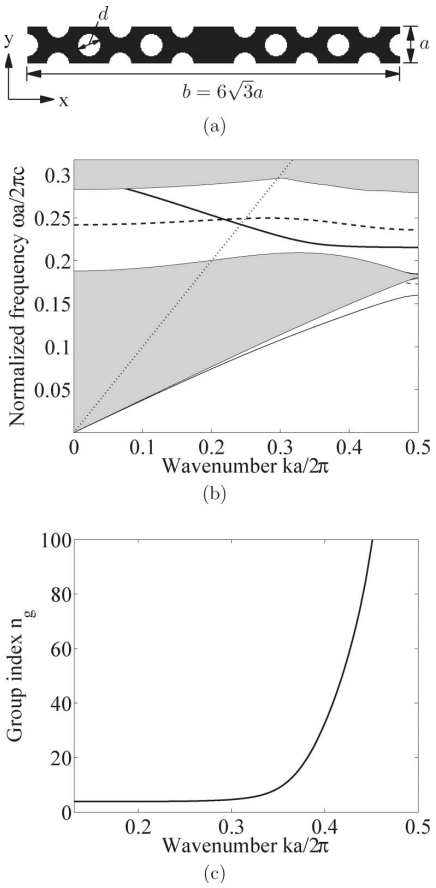

Fig. 1. (a) Schematic illustration of the supercell of a triangular lattice PhCW. (b) Corresponding band structure. Gray region indicates slab mode region, the dotted curve represents the light line, the solid curves denote the even guided modes, and the dashed curves denote the odd guided modes. (c) Group index of the even guided modes in the bandgap.

$$v_g = \frac{\partial\omega}{\partial k}. \tag{4}$$

The even band has a negative band slope and thus the group index n_g for the even guided mode is calculated by

$$n_g = -c\frac{\partial k}{\partial\omega}. \tag{5}$$

Numerically, we approximate the group index for frequency $\omega_n(k_i)$ by

$$n_g(\omega_n(k_i)) = \frac{c(k_i - k)}{\omega_n(k) - \omega_n(k_i)}, \tag{6}$$

where n is the band number of the designed band in order of increasing frequency and k is a wavenumber close to k_i. This method is sufficiently accurate if k is sufficiently close to k_i.

The group index plot [Fig. 1(c)] shows that the mode is index- guided in the fast light regime ($n_g \approx n_{\mathrm{Si}}$), whereas in the slow-light regime ($n_g \gg 1$), the mode is bandgap guided. The group index diverges near the band edge and the group index here is strongly dependent on the frequency. Thus a

$$\min_{\rho_j}\max_{q}\max_{k_i} f(\bar{\rho}^q)=\left(\frac{c(k_i-k_{i-1})}{\omega_n^q(k_{i-1})-\omega_n^q(k_i)}-n_g^*\right)^2 \quad \text{s.t.} \quad [\mathbf{K}_k^q-(\omega^q)^2\mathbf{M}^q]\mathbf{h}^q=0 \quad \max_{k_{ii}}\omega_{n-1}^q(k_{ii})\le a_1\min_{k_i}\omega_n^q(k_i)$$

$$\omega_n^q(0)\ge a_2\max_{k_i}\omega_n^q(k_i) \quad \min_{k_{ii}}\omega_{n+1}^q(k_{ii})\ge a_2\max_{k_i}\omega_n^q(k_i) \quad f_v=\frac{\sum_j\bar{\rho}_j^d v_j}{\sum_j v_j}\le f_v^*$$

$$0\le\rho_j\le 1 \quad j=1,\ldots,N, \quad i=2,\ldots,m, \quad a_1<1, \quad a_2>1, \quad q=\{d,i,e\} \tag{7}$$

large GVD is obtained (GVD $=c^{-1}\mathrm{d}n_g/\mathrm{d}\omega$), which distorts the waveform of optical signals and, moreover, the bandwidth becomes narrower for the slow light.

3. ROBUST TOPOLOGY OPTIMIZATION PROBLEM

A. Formulation of Robust Design

In many applications, it is highly desirable to reduce the GVD and extend the bandwidth for slow-light operation. This can be realized through a proper modification of the waveguide geometry. In topology optimization, the elementwise design variables ρ are introduced to represent the material distribution in the supercell. These design variables are used to control the dielectric permittivity in each element. The optimization problem can be formulated as minimizing the error between the actual group index and the prescribed group index for certain discrete wavenumbers k_i, in order to reduce the GVD and extend the bandwidth of the slow light (shown in Fig. 2). In order to realize the desired design robustness, the underetched structure (dilated design, $\bar{\rho}^d$), normal etched structure (intermediate design, $\bar{\rho}^i$) and overetched structure (eroded design, $\bar{\rho}^e$) in the manufacturing process can be considered with a min-max optimization formulation [23]. Robust topology optimization for tailoring dispersion properties is achieved by minimizing the maximum error for certain discrete wavenumbers for the three design realizations.

In order to avoid multimode interference for the tailored modes, band constraints are implemented. First, the lower and upper bands should be kept away from the design (slow light) band. Also, as Fig. 1(b) shows, there is interaction between guided odd and even bands. In order to keep the odd band away from the designed even modes, an additional constraint is implemented on the odd band for $k_i=0$ (shown in Fig. 2). The robust formulation can be stated as

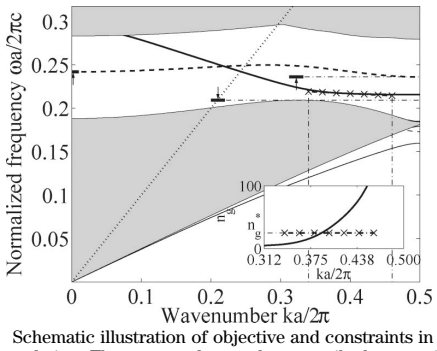

Fig. 2. Schematic illustration of objective and constraints in the robust formulation. The crosses denote the prescribed properties, upward arrow indicates pushing upward, downward arrow indicates pushing downward, and the inset shows the prescribed group index and actual group index versus wavenumber.

where ρ_j is the design variable for element j, The superscript q denotes the design type among the three different design realizations; $q=\{d,i,e\}$ indicates the dilated, intermediate, and eroded designs, respectively; $\bar{\rho}^q$ is the physical density vector of the structure q; k_i is the discrete design wavenumber; $\omega_n^q(k_i)$ is the nth order frequency corresponding to wavenumber k_i for the design q; n_g^* is the prescribed group index; k_{ii} is the discrete wavenumber for lower band ($\omega_{n-1}^q(k_{ii})$) and upper band ($\omega_{n+1}^q(k_{ii})$); a_1 and a_2 represent the band constraints; N is the total element number; v_j is the volume of element j; f_v is the actual volume fraction of the total material, f_v^* is the given volume fraction; and m is the total number of the design wavenumbers k_i. The volume constraint is implemented on the dilated design realization.

B. Numerical Approximation of Manufacturing Uncertainties

The basis for the approximation of under, normal, and overetching in the manufacturing process is the traditional density filter introduced by Bruns and Tortorelli [16] and Bourdin [17]

$$\tilde{\rho}_e=\frac{\sum_{j\in N_e} w(\mathbf{x}_j)v_j\rho_j}{\sum_{j\in N_e} w(\mathbf{x}_j)v_j}, \tag{8}$$

where $\tilde{\rho}_e$ is the filtered density of element e, $\mathbf{x}_j$ is the location of element j, N_e is the neighborhood of element e within a certain filter radius r specified by

$$N_e=\{j\,|\,\|\mathbf{x}_j-\mathbf{x}_e\|\le r\}, \tag{9}$$

and $w(\mathbf{x}_j)$ is the weighting factor defined as $w(\mathbf{x}_j)=r-\|\mathbf{x}_j-\mathbf{x}_e\|$.

Based on the filtered density, the under, normal, and overetching can be realized based on a threshold projection by choosing different thresholds. For a given threshold η, the

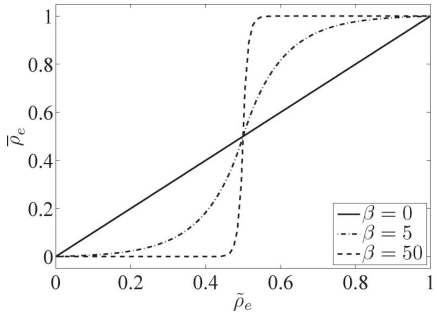

Fig. 3. Illustration of the smoothed threshold projection for $\eta=0.5$ and different values of β.

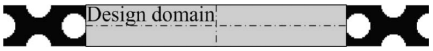

Fig. 4. Illustration of design domain. The dash-dot curves denote the symmetric axes of design domain.

physical density $\bar{\rho}_e$ can be approximated by a smooth function governed by the parameter β (shown in Fig. 3 for $\eta = 0.5$):

$$\bar{\rho}_e = \begin{cases} \eta\{\exp[-\beta(1-\tilde{\rho}_e/\eta)] - (1-\tilde{\rho}_e/\eta)\exp(-\beta)\} & 0 \le \tilde{\rho}_e \le \eta \\ (1-\eta)\{1-\exp[-\beta(\tilde{\rho}_e-\eta)/(1-\eta)] & \\ \quad +(\tilde{\rho}_e-\eta)/(1-\eta)\exp(-\beta)\} + \eta & \eta < \tilde{\rho}_e \le 1 \end{cases} \quad (10)$$

Three threshold values are chosen as η_d, η_i, and η_e corresponding to the dilated, intermediate, and eroded design. They satisfy $0 \le \eta_d < \eta_i < \eta_e \le 1$. By controlling the threshold values, we control the manufacturing tolerance between the dilated, intermediate, and eroded designs. More details can be found in [24].

C. Sensitivity Analysis

The interpolation of the relative permittivity of element e in the design domain is given by a linear function based on the inverse permittivity

$$\frac{1}{\varepsilon_e^q} = (1-\bar{\rho}_e^q)\frac{1}{\varepsilon_1} + \bar{\rho}_e^q \frac{1}{\varepsilon_2}, \quad (11)$$

where $\varepsilon_1 = 1$ is the relative permittivity of air and $\varepsilon_2 = \varepsilon_{Si}$ is the relative permittivity of silicon. The sensitivity of the objective and constraints can be calculated separately for each structure by the standard chain rule [20]

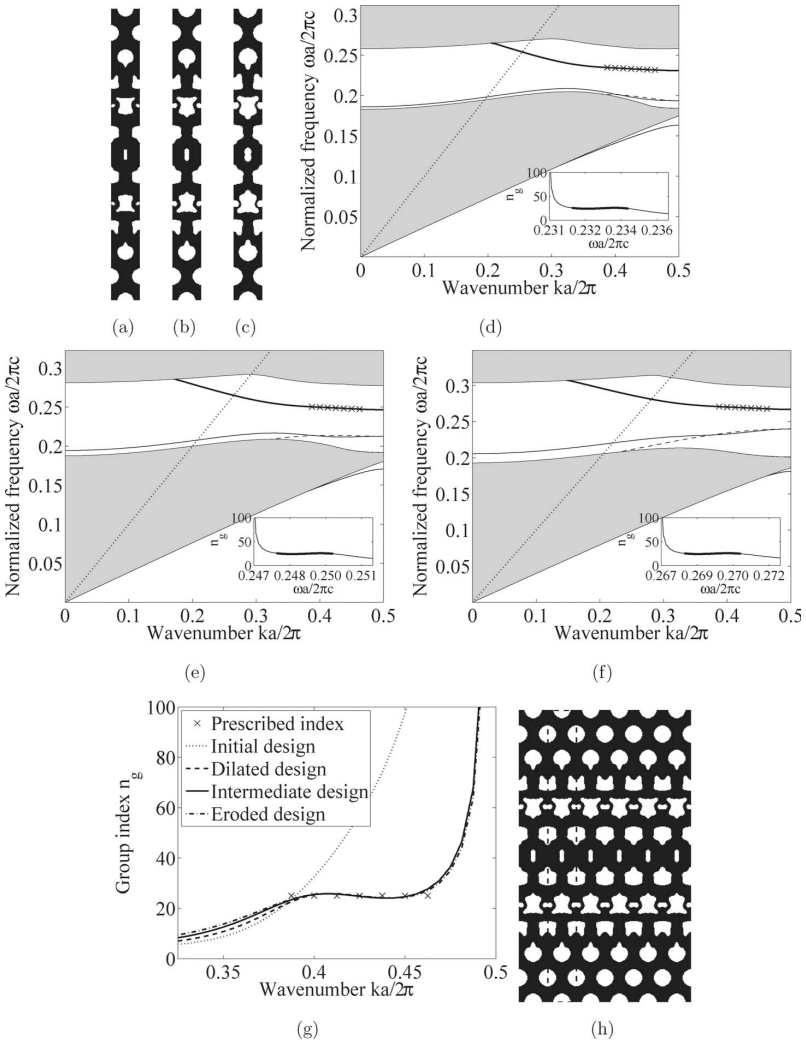

Fig. 5. Robust design of PhCWs. (a) Dilated design. (b) Intermediate design. (c) Eroded design. (d) Band structure of dilated design. The crosses indicate the design range and the bold curve in the inset denotes the bandwidth of prescribed group index. (e) Band structure of intermediate design. (f) Band structure of eroded design. (g) Group index of the different design realizations and prescribed group index. (h) PhCW constituted by intermediate design.

$$\frac{\partial F}{\partial \rho_j} = \sum_{e \in N_j} \frac{\partial F}{\partial \bar{\rho}_e^q} \frac{\partial \bar{\rho}_e^q}{\partial \tilde{\rho}_e} \frac{\partial \tilde{\rho}_e}{\partial \rho_j}, \tag{12}$$

where F denotes the objective f or constraints.

The sensitivity of the objective with respect to the physical density can be expressed as

$$\frac{\partial f(\bar{\rho}^q)}{\partial \bar{\rho}_e^q} = -2\left(\frac{c(k_i - k_{i-1})}{\omega_n^q(k_{i-1}) - \omega_n^q(k_i)} - n_g^*\right) \times \frac{c(k_i - k_{i-1})}{(\omega_n^q(k_{i-1}) - \omega_n^q(k_i))^2}\left(\frac{\partial \omega_n^q(k_{i-1})}{\partial \bar{\rho}_e^q} - \frac{\partial \omega_n^q(k_i)}{\partial \bar{\rho}_e^q}\right). \tag{13}$$

The sensitivity of the eigenvalues and also for multiple eigenvalues can be found in many papers, e.g., Seyranian *et al.* [25] and Pedersen and Nielsen [26]. Based on Eq. (10), the derivative of the physical density $\bar{\rho}_e^q$ with respect to the filtered density $\tilde{\rho}_e$ is

$$\frac{\partial \bar{\rho}_e^q}{\partial \tilde{\rho}_e} = \begin{cases} \beta \exp[-\beta(1 - \tilde{\rho}_e/\eta_q)] + \exp(-\beta) & 0 \le \tilde{\rho}_e \le \eta_q \\ \beta \exp[-\beta(\tilde{\rho}_e - \eta_q)/(1 - \eta_q)] + \exp(-\beta) & \eta_q < \tilde{\rho}_e \le 1 \end{cases}. \tag{14}$$

The sensitivity of the filtered density $\tilde{\rho}_e$ with respect to the design variable ρ_j can be calculated by

$$\frac{\partial \tilde{\rho}_e}{\partial \rho_j} = \frac{w(\mathbf{x}_j) v_j}{\sum_{i \in N_e} w(\mathbf{x}_i) v_i}. \tag{15}$$

D. Numerical Implementation

Since the supercell is the periodic cell of PhCWs, the neighborhood of element e, N_e includes the neighbor elements in the previous or next supercell in the density filter. Furthermore, in order to keep the smoothness between design domain and nondesign domain, the physical densities of the elements adjacent to the design domain are updated according to the design variables. The optimization problem is solved by the globally convergent version of the method of moving asymptotes (GCMMA) from Svanberg [27]. The full optimization procedure is as follows:

1. Set the design domain and choose the η set: η_d, η_i, and η_e.
2. Build the neighborhood **N** for changeable elements.
3. Initialize design variables ρ.
4. Compute the dilated ($\bar{\rho}^d$), intermediate ($\bar{\rho}^i$), and eroded ($\bar{\rho}^e$) design realizations based on the design variables.
5. Solve the eigenvalue problems based on the dilated, intermediate, and eroded designs.
6. Calculate objectives and constraints and corresponding sensitivities.
7. Update design variables ρ using GCMMA.
8. Calculate max design variable change $\Delta\rho$ and max objective change Δf.
9. For every fortieth iteration or if ($\{\Delta\rho < 1e-3$ or $\Delta f < 1e-3\}$ and $\beta < \beta_{\max}$), set $\beta = 1.3\beta$.
10. If ($\Delta\rho < 1e-4$ or $\Delta f < 1e-4$) and $\beta \ge \beta_{\max}$, terminate, else, goto 4.

Here the maximum value of β is $\beta_{\max} = 50$.

The optimization procedure is implemented in MATLAB and runs in parallel on a standard four-processor PC. The optimization converges in 400–500 GCMMA iterations, for which each GCMMA iteration includes three or four inner-iterations and takes 3–4 min for seven discrete wavenumbers.

4. RESULTS

It was shown in [5] that the first two rows of air holes adjacent to the waveguide core have a significant influence on the group index. Here we add one and one-quarter rows and set the first three and one-quarter rows adjacent to the waveguide core as the design domain. A symmetry condition is introduced to ensure symmetric designs (shown in Fig. 4). The initial design is illustrated in Fig. 1(a). The supercell is discretized with 40×408 quadrilateral four-node elements. The volume constraint is $f_v^* = 0.8$, the filter radius r is set as $1/8a$, and the threshold set is $\eta = \{0.35, 0.5, 0.65\}$. In order to measure the separation between the designed band and the other bands, we define the relative band distance: the relative band distance is defined as the band distance to mid-distance frequency ratio $\Delta\omega/\omega_m$, $\Delta\omega$ is the minimum of the minimal distance between upper band and lower band, and the distance between the minimal odd mode and lower band and ω_m is the frequency at the middle of the band distance.

A. Robust Design of PhWGs

In the first example, we try to design PhCWs with the constant group index of $n_g = 25$ in the wavenumber range $k \in [0.3875, 0.4625]2\pi/a$. The target wavenumbers k_i are set to seven equidistant points in above wavenumber range. The final robust design is shown in Fig. 5. Figures 5(a)–5(c) display the dilated, intermediate, and eroded design realization. The corresponding band structures [Figs. 5(d)–5(f)] show that the design regions are well isolated from other modes. By studying the band structures and the inset group index plots, we can see that the guided modes with almost constant group index are located at different frequency ranges for the three design realizations. This is an expected feature, since the frequency scales as $1/\sqrt{\varepsilon}$ in a medium of dielectric constant ε. The volume fraction of silicon decreases from the dilated design to the eroded design; therefore, the average dielectric constant decreases from the dilated design to the eroded design, and correspondingly, the location of the designed band should increase in frequency. Figure 5(g) shows the group index plot of all the designs versus wavenumber k. It can be seen that all the design realizations have equally good performance in the design region. Therefore, almost constant group velocity also is achieved when the design is slightly

Table 1. Performance of Different Designs in Fig. 5

Design	f_v	Band distance ($2\pi c/a$)	Bandwidth ($2\pi c/a$)	Error
Dilated	0.740	21.1% in [0.20866, 0.25802]	0.00250 in [0.23188, 0.23438]	3.6%
Intermediate	0.678	24.6% in [0.21670, 0.27749]	0.00250 in [0.24760, 0.25011]	3.7%
Eroded	0.613	21.5% in [0.24000, 0.29783]	0.00250 in [0.26800, 0.27050]	3.3%

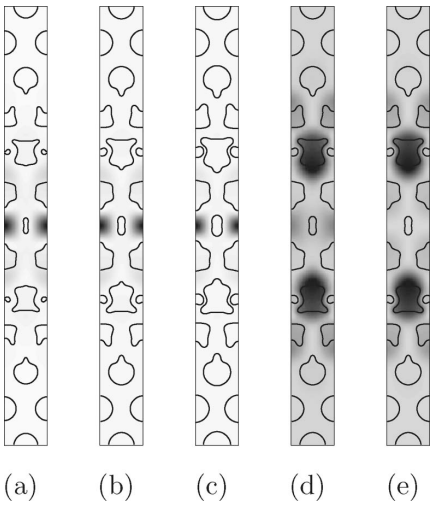

Fig. 6. Amplitudes of the magnetic field at $k_i = 0.425\ 2\pi/a$. (a) Amplitude of the magnetic field for dilated design. (b) Amplitude of the magnetic field for intermediate design. (c) Amplitude of the magnetic field for eroded design. (d) Amplitude of the lower odd magnetic mode for intermediate design. (e) Amplitude of the lower even mode for intermediate design.

under or overetched during the manufacturing process. A constant group velocity is achieved by all three design realizations in the wavenumber range $k \in [0.39375, 0.45625]2\pi/a$, which is smaller than the target wavenumber range. This is due to the numerical calculation of the group index based on finite differences [Eq. (6)], which causes the errors between actual group index and prescribed group index at the first and last wavenumbers to be much larger than for the other target wavenumbers.

Detailed properties of the three design realizations are shown in Table 1. Among the three design realizations, the dilated one has the smallest relative band distance. The same bandwidth of $\Delta\omega = 0.0025\ 2\pi c/a$ can be achieved by all three of the design realizations in different frequency ranges. The frequency ranges of the bandwidths reveal that the designed modes are located near the center of the corresponding distance. The maximum error of the constant group index is limited to 3.7%.

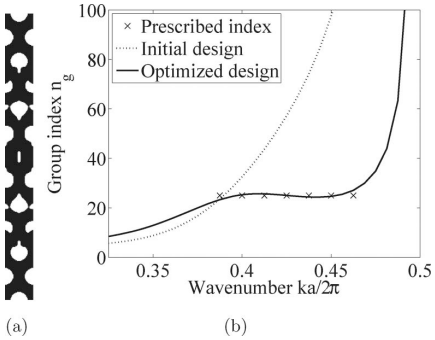

Fig. 7. Optimized design of PhCW without considering robustness for $\eta = 0.5$. (a) Optimized design. (b) Group index of different designs and prescribed group index.

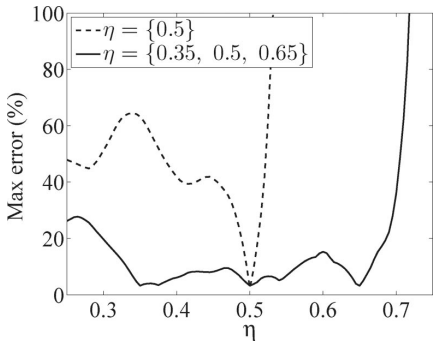

Fig. 8. Maximum error between actual group index and prescribed group index in the design wavenumber range versus η for normal and robust formulation.

The band structures of the robust design show that there are two other bands between the slab mode region and the designed band. These two bands interact and degenerate at the band edge. Whereas the designed mode is confined in the waveguide core for all the three design realizations (Fig. 6), the modes of the other two bands are confined in the design domain, but not in the waveguide core.

In order to compare normal nonrobust optimization and robust optimization, we perform a normal optimization for $\eta = 0.5$ with the same parameter set as in above case. The final design is shown in Fig. 7. Figure 8 depicts the maximum error between actual group index and the prescribed group index versus η for the normal design (Fig. 7) and the robust design (Fig. 5). The best performance is obtained by the structures corresponding to the design η, $\eta = 0.5$ for the normal design and $\eta = \{0.35, 0.5, 0.65\}$ for the robust design. Compared with the normal optimization, which degenerates for even very small etching errors, the performance of the PhCW has been improved significantly through the robust optimization approach. The robust optimization formulation ensures that the structure realizations corresponding to $\eta \in [\eta_d, \eta_e]$ preserve good performance, and the maximum error is limited within 15.3%. An even better performance could be obtained by considering more values of η in the interval of $[\eta_d, \eta_e]$, but at the expense of increased computation time.

B. Robust Design of PhWGs with Smaller GVD

In this example, we investigate the influence of the band constraints on the group index and aim to decrease the error of the constant group index. The band constraints are relaxed slightly, i.e., given a smaller relative band distance. The other parameters are kept exactly the same as in the first case. The final design is shown in Fig. 9 illustrating that the topology of the design is quite different in comparison to the first case. There are topological differences between the eroded and the other two design realizations and small isolated components show up in the eroded design realization. All of the conclusions about the frequency shift and confinement drawn from the first case still apply in this case: the frequency of the band shifts upwards from the dilated to the eroded design and the designed modes are confined to the waveguide core [shown in Figs. 9(e)–9(g)]. The group index plot [Fig. 9(i)] shows that a group index of $n_g = 25$ is achieved with negligible error by all three designs. The smallest bandwidth of $\Delta w = 0.0025\ 2\pi c/a$ can be achieved by all the three designs

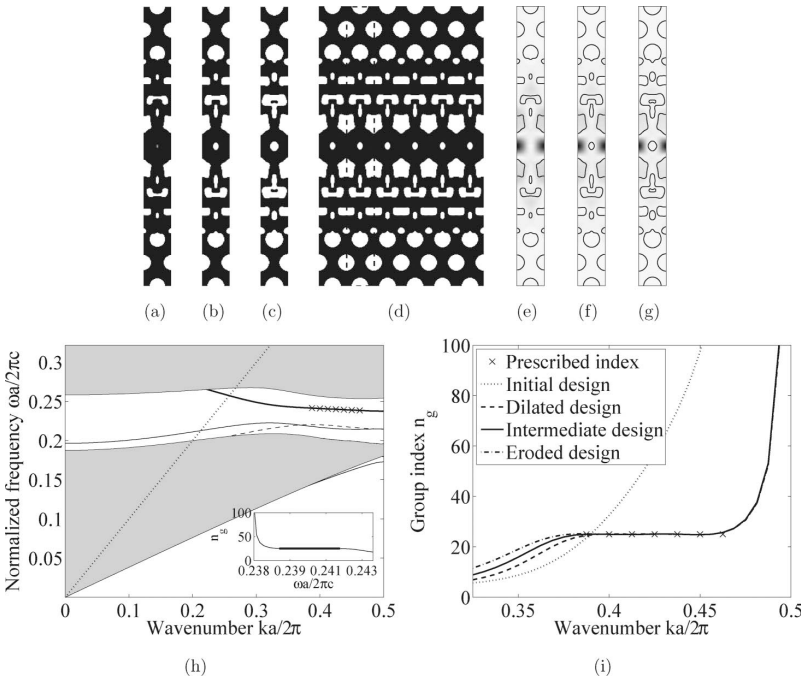

Fig. 9. Robust design of PhCWs with small GVD. (a) Dilated design. (b) Intermediate design. (c) Eroded design. (d) PhCW constituted by intermediate design. (e) Amplitude of the magnetic field at $k_i = 0.425\ 2\pi/a$ for dilated design. (f) Amplitude of the magnetic field at $k_i = 0.425\ 2\pi/a$ for intermediate design. (g) Amplitude of the magnetic field at $k_i = 0.425\ 2\pi/a$ for eroded design. (h) Band structure of intermediate design. (i) Groups indexes of the different design realizations and prescribed group index.

within an error of 0.8%. Comparison between the first example and this example reveals that the improvement of the dispersion properties can be obtained at the expense of the relative band distance (Table 2).

C. Extension of the Bandwidth

Two key parameters of slow light in PhCWs are the dispersion properties and the bandwidth. In the first two examples, we have demonstrated that the GVD of the slow-light regime can be reduced significantly, and a constant group velocity with very small error can be obtained for a certain bandwidth. In this example, we aim to design PhCWs with enlarged bandwidth of the constant group index. To achieve this, we extend the design wavenumber range to $k \in [0.3, 0.47]2\pi/a$ by setting 10 equidistant target wavenumber k_i in above range. The final design is presented in Fig. 10. It is seen that a broader bandwidth is obtained in this case. An almost constant group velocity of $v_g = 0.04c$ can be achieved for the wavenumber range $k \in [0.30625, 0.46250]2\pi/a$ by all the three design realizations.

Table 3 shows the properties of all of the design realizations. The smallest bandwidth of $\Delta\omega = 0.00625\ 2\pi c/a$ can be achieved by all design realizations with the maximum error of 2.6%. Compared to the previous example, the bandwidth is more than doubled, at the expense of a slightly increased error. Examining the guided frequency range and the design wavenumber range, we can see that the largest frequency of the eroded design is close to the light line, which indicates that this bandwidth is close to the largest bandwidth we can obtain.

D. Design of PhCWs with Different Constant Group Indexes

In this example, we explore the ability of the robust design formulation further by designing a PhCW, which exhibits two different constant group indexes over different frequency ranges. Our prescribed group indexes are $n_g^* = 20$ for five equidistant design wavenumbers in the wavenumber range of $k \in [0.32, 0.37]2\pi/a$ and $n_g^* = 25$ for five equidistant design wavenumbers in the wavenumber range of $k \in [0.41, 0.46]2\pi/a$.

The final design is presented in Fig. 11. The group index plot [Fig. 11(i)] shows two relatively flat parts corresponding to the group indexes of $n_g = 20$ and $n_g = 25$. The constant group index of $n_g = 20$ can be achieved in the wavenumber range of $k \in [0.32500, 0.36875]2\pi/a$ and the constant group

Table 2. Performance of Different Designs in Fig. 9

Design	f_v	Band distance ($2\pi c/a$)	Bandwidth ($2\pi c/a$)	Error
Dilated	0.761	11.2% in [0.21129, 0.23644]	0.00250 in [0.22243, 0.22493]	0.6%
Intermediate	0.695	13.0% in [0.22265, 0.25367]	0.00275 in [0.23881, 0.24156]	0.7%
Eroded	0.617	13.2% in [0.24338, 0.27796]	0.00325 in [0.26087, 0.26412]	0.8%

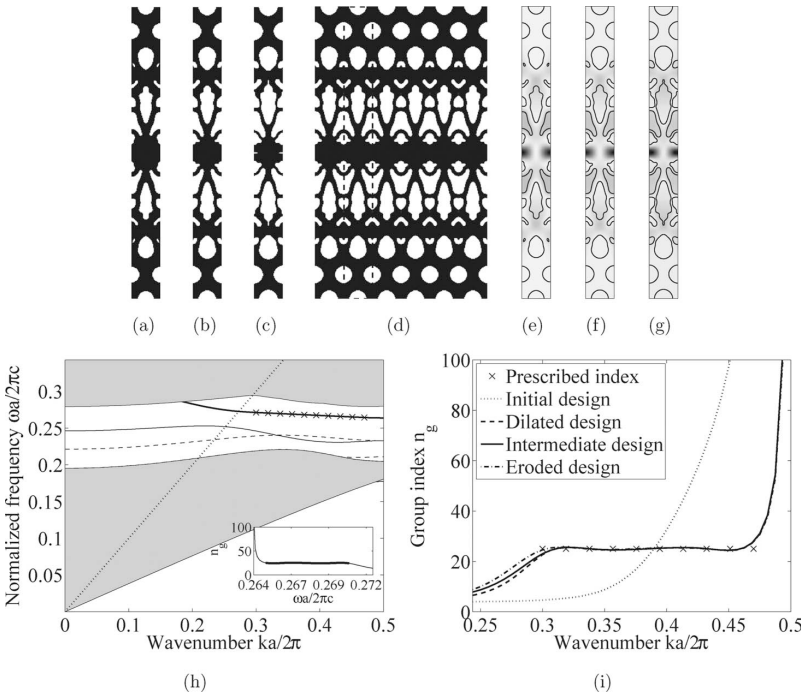

Fig. 10. Robust design of PhCWs with large bandwidth. (a) Dilated design. (b) Intermediate design. (c) Eroded design. (d) PhCW constituted by intermediate design. (e) Amplitude of the magnetic field at $k_i = 0.376\ 2\pi/a$ for dilated design. (f) Amplitude of the magnetic field at $k_i = 0.376\ 2\pi/a$ for intermediate design. (g) Amplitude of the magnetic field at $k_i = 0.376\ 2\pi/a$ for eroded design. (h) Band structure of intermediate design. (i) Groups indexes of the different design realizations and prescribed group index.

index of $n_g = 25$ can be achieved in the wavenumber range of $k \in [0.41250, 0.45625]2\pi/a$ by all the three design realizations.

The detailed properties of these three design realizations are listed in Tables 4 and 5. The bandwidth of $n_g = 20$ is $\Delta\omega = 0.0025\ 2\pi c/a$ with maximum error of 1.7% and the bandwidth of $n_g = 25$ is $\Delta\omega = 0.00175\ 2\pi c/a$ with maximum error of 1.8%. Among the three design realization, the eroded design exhibits the largest bandwidths for both group indexes.

E. Further Discussion

The isolated components, which show up in the eroded designs in the second and fourth examples, are not suitable for membrane waveguides. Therefore, further consideration should be given to prevent the isolated components during the optimization process. The isolated components cause the fundamental free mechanical vibration frequency of the supercell to be zero. Therefore, a fundamental mechanical vibration frequency constraint is added to the optimization formulation to prevent isolated components in the designs. The free mechanical vibration problem can be solved as an eigenvalue problem of the supercell under the following boundary conditions:

$$\mathbf{u}(x, a) = \mathbf{u}(x, 0) \qquad \mathbf{u}(0, y) = \mathbf{u}(b, y) = 0. \tag{16}$$

The mechanical properties are interpolated based on the SIMP model [8] as

$$\begin{aligned} E_e^q &= E_{\min} + (E_1 - E_{\min})(\bar{\rho}_e^q)^p, \\ m_e^q &= m_{\min} + (m_1 - m_{\min})\bar{\rho}_e^q, \end{aligned} \tag{17}$$

where E_e^q and m_e^q are the Young's modulus and mass density of element e in design q, respectively, and p is the exponential power of the SIMP model. The parameters in the SIMP model are set as: $E_{\min} = 10^{-9}E_1$, $m_{\min} = 10^{-9}m_1$, $p = 5$, and Poisson's ratio is $\nu = 0.3$.

Table 3. Performance of Different Designs in Fig. 10

Design	f_v	Band distance ($2\pi c/a$)	Bandwidth ($2\pi c/a$)	Error
Dilated	0.682	8.7% in [0.23711, 0.25878]	0.00625 in [0.24473, 0.25098]	2.6%
Intermediate	0.611	9.9% in [0.25299, 0.27942]	0.00625 in [0.26477, 0.27102]	2.6%
Eroded	0.537	8.3% in [0.27770, 0.30189]	0.00649 in [0.28665, 0.29314]	2.6%

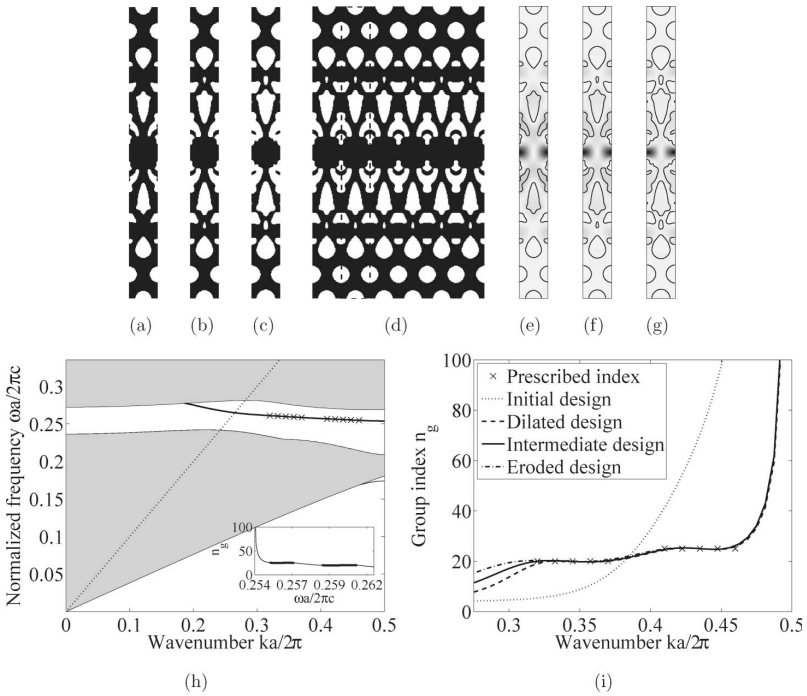

Fig. 11. Robust design of PhCWs with two constant group indexes. (a) Dilated design. (b) Intermediate design. (c) Eroded design. (d) PhCW constituted by intermediate design. (e) Amplitude of the magnetic field at $k_i = 0.345\ 2\pi/a$ for dilated design. (f) Amplitude of the magnetic field at $k_i = 0.345\ 2\pi/a$ for intermediate design. (g) Amplitude of the magnetic field at $k_i = 0.345\ 2\pi/a$ for eroded design. (h) Band structure of intermediate design (f) Groups indexes of the different design realizations and prescribed group index.

The entire robust formulation can thus be modified as

$$\min_{\rho_j} \max_{q} \max_{k_i} f(\bar{\rho}^q) = \left(\frac{c(k_i - k_{i-1})}{\omega_n^q(k_{i-1}) - \omega_n^q(k_i)} - n_g^*\right)^2 \quad \text{s.t.} \quad [\mathbf{K}_k^q - (\omega^q)^2\mathbf{M}^q]\mathbf{h}^q = 0 \quad (\tilde{\mathbf{K}}^q - \lambda_1^q\tilde{\mathbf{M}}^q)\mathbf{u}^q = 0$$

$$\max_{k_{ii}} \omega_{n-1}^q(k_{ii}) \le a_1 \min_{k_i} \omega_n^q(k_i) \qquad \omega_n^q(0) \ge a_2 \max_{k_i} \omega_n^q(k_i) \qquad \min_{k_{ii}} \omega_{n+1}^q(k_{ii}) \ge a_2 \max_{k_i} \omega_n^q(k_i) \qquad \frac{\lambda_1^q}{\lambda_0} \ge \delta, \qquad \lambda_0 = \frac{E_1}{m_1}$$

$$f_v = \frac{\sum_j \bar{\rho}_j^d v_j}{\sum_j v_j} \le f_v^* \qquad 0 \le \rho_j \le 1 \qquad j = 1, \ldots, N, \qquad i = 2, \ldots, m, \qquad a_1 < 1, \qquad a_2 > 1, \qquad q = \{d, i, e\}. \tag{18}$$

To illustrate the efficiency of this formulation, we optimize the second example with the same parameter set (shown in Fig. 12) and another example for $n_g^* = 100$ (shown in Fig. 13). The fundamental free vibration frequency constraint is set to $\delta = 0.00025$. The normalized bandwidths $\Delta\omega/\omega$ of these two examples are 1.24% and 0.33%, respectively with maximum error of 2%. The final designs show that this new formulation can prevent the isolated components effectively and also performs well for high group indexes. However, it should be noted that the algorithm is quite sensitive to the choice of the parameter δ.

Table 4. Performance of Different Designs in Fig. 11

Design	f_v	Band distance $(2\pi c/a)$	Bandwidth $(2\pi c/a)$ of $n_g = 20$	Error
Dilated	0.720	8.7% in [0.22847, 0.24939]	0.00250 in [0.23909, 0.24159]	1.7%
Intermediate	0.648	10.5% in [0.24210, 0.26892]	0.00250 in [0.25866, 0.26116]	1.3%
Eroded	0.565	11.5% in [0.26388, 0.29623]	0.00284 in [0.28553, 0.28834]	1.6%

Table 5. Performance of Different Designs in Fig. 11

Design	Band distance ($2\pi c/a$) of $n_g = 25$	Error
Dilated	0.00175 in [0.23741, 0.23566]	1.2%
Intermediate	0.00175 in [0.25495, 0.25670]	1.7%
Eroded	0.00200 in [0.28355, 0.28155]	1.8%

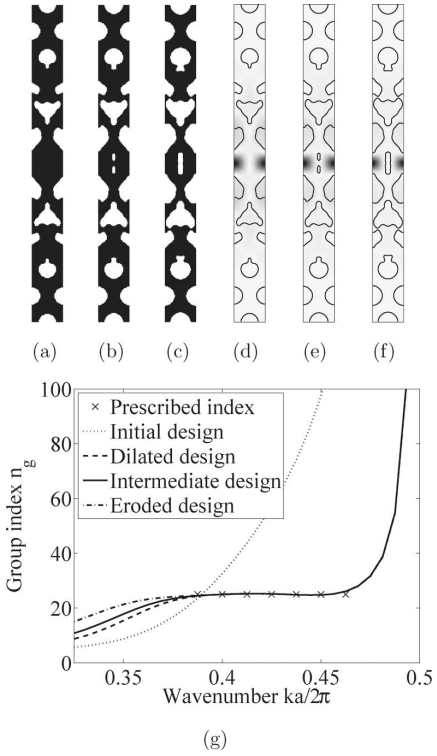

Fig. 12. Robust design of PhCWs with fundamental free vibration frequency constraint. (a) Dilated design. (b) Intermediate design. (c) Eroded design. (d) Amplitude of the magnetic field at $k_i = 0.425\ 2\pi/a$ for dilated design. (e) Amplitude of the magnetic field at $k_i = 0.425\ 2\pi/a$ for intermediate design. (f) Amplitude of the magnetic field at $k_i = 0.425\ 2\pi/a$ for eroded design. (g) Group indexes of the different design realizations and prescribed group index.

5. CONCLUSION

In this study, a robust topology optimization method to tailor the dispersion properties of PhCWs has been presented. The objective is formulated as a min-max optimization problem based on the errors between actual group indexes and a prescribed group index among the dilated, intermediate, and eroded designs, which mimic under, normal, and overetching in the manufacturing process. Band constraints are implemented to isolate the design modes from other modes. This formulation ensures that if the proposed design is slightly dilated or eroded during manufacturing, the PhCW still preserves the desired performance. The proposed robust formulation indirectly ensures a minimum length scale on important design features (the response of the optimized design is tolerant towards errors in the realization of smaller details). The minimum length scale can be controlled by proper selection of

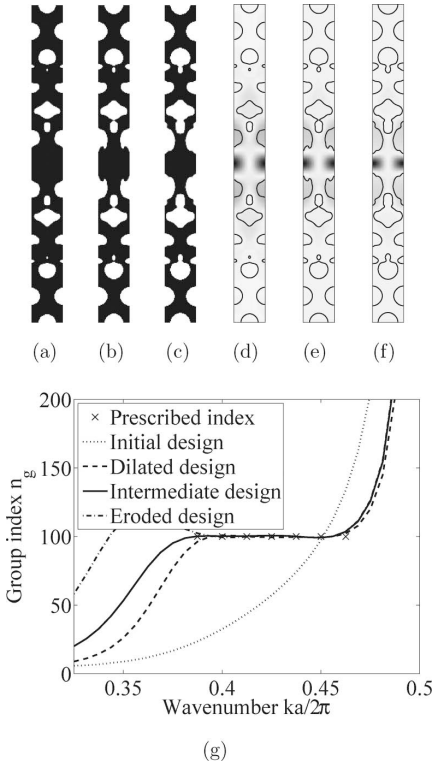

Fig. 13. Robust design of PhCWs with $n_g = 100$. (a) Dilated design. (b) Intermediate design. (c) Eroded design. (d) Amplitude of the magnetic field at $k_i = 0.425\ 2\pi/a$ for dilated design. (e) Amplitude of the magnetic field at $k_i = 0.425\ 2\pi/a$ for intermediate design. (f) Amplitude of the magnetic field at $k_i = 0.425\ 2\pi/a$ for eroded design. (g) Group indexes of the different design realizations and prescribed group index.

filter size and projection values (see [24] for more details). PhCWs with group index of $n_g = 25$ are demonstrated with very small GVD and the bandwidth of slow light of $n_g = 25$ can be increased to $0.00625\ 2\pi c/a$ through the robust design. The detailed properties of the PhCWs reveal that the reduction of the GVD and the extension of the bandwidth are at expense of the relative band distance. Another example shows that a slow-light PhCW with $n_g = 100$ can be achieved with a bandwidth of $0.00079\ 2\pi c/a$. Moreover, PhCWs with novel functionality, exhibiting two constant group index regions over different frequency ranges, can be created by the robust design formulation. The appearance of isolated components in the overetching are avoided by introducing a fundamental free mechanical vibration constraint. The proposed design method provides a systematic and robust method for tailoring the dispersion of PhCWs.

ACKNOWLEDGMENTS

This work was financially supported by Villum Fonden (via the NATEC Centre of Excellence), the Eurohorcs/ESF European Young Investigator Award (EURYI, www.esf.org/euryi), and the Danish Center for Scientific Computing (DCSC).

REFERENCES

1. T. Baba, "Slow light in photonic crystals," Nat. Photon. **2**, 465–473 (2008).
2. J. D. Joannopoulos, S. G. Johnson, J. N. Winn, and R. D. Meade, *Photonic Crystals—Molding the Flow of Light*, 2nd ed. (Princeton University Press, 2008).
3. D. Mori and T. Baba, "Wideband and low dispersion slow light by chirped photonic crystal coupled waveguide," Opt. Express **13**, 9398–9408 (2005).
4. D. Mori, S. Kubo, H. Sasaki, and T. Baba, "Experimental demonstration of wideband dispersion-compensated slow light by a chirped photonic crystal directional coupler," Opt. Express **15**, 5264–5270 (2007).
5. L. H. Frandsen, A. V. Lavrinenko, J. Fage-Pedersen, and P. I. Borel, "Photonic crystal waveguides with semi-slow light and tailored dispersion properties," Opt. Express **14**, 9444–9450 (2006).
6. J. Li, T. P. White, L. O'Faolain, A. Gomez-Iglesias, and T. F. Kraus, "Systematic design of flat band slow light in photonic crystal waveguides," Opt. Express **16**, 6227–6232 (2008).
7. S. Kubo, D. Mori, and T. Baba, "Low-group-velocity and low-dispersion slow light in photonic crystal waveguides," Opt. Lett. **32**, 2981–2983 (2007).
8. M. P. Bendsøe and O. Sigmund, *Topology Optimization—Theory, Methods and Applications* (Springer Verlag, 2004).
9. P. I. Borel, A. Harpøth, L. H. Frandsen, M. Kristensen, J. S. Jensen, P. Shi, and O. Sigmund, "Topology optimization and fabrication of photonic crystal structures," Opt. Express **12**, 1996–2001 (2004).
10. J. S. Jensen and O. Sigmund, "Systematic design of photonic crystal structures using topology optimization: low-loss waveguide bends," Appl. Phys. Lett. **84**, 2022–2024 (2004).
11. J. S. Jensen and O. Sigmund, "Topology optimization of photonic crystal structures: a high-bandwidth low-loss *T*-junction waveguide," J. Opt. Soc. Am. B **22**, 1191–1198 (2005).
12. J. S. Jensen and O. Sigmund, "Topology optimization for nano-photonics—a review," Laser Photon. Rev. (to be published).
13. R. Stainko and O. Sigmund, "Tailoring dispersion properties of photonic crystal waveguides by topology optimization," Waves in Random and Complex Media **17**, 477–489 (2007).
14. O. Sigmund, "On the design of compliant mechanisms using topology optimization," Mechan. Struct. Mach. **25**, 493–524 (1997).
15. O. Sigmund and J. Petersson, "Numerical instabilities in topology optimization: a survey on procedures dealing with checkerboards, mesh-dependencies and local minima," Struct. Opt. **16**, 68–75 (1998).
16. T. E. Bruns and D. A. Tortorelli, "Topology optimization of nonlinear elastic structures and compliant mechanisms," Comput. Methods Appl. Mech. Eng. **190**, 3443–3459 (2001).
17. B. Bourdin, "Filters in topology optimization," Int. J. Numer. Methods Eng. **50**, 2143–2158 (2001).
18. J. K. Guest, J. H. Prevost, and T. Belytschko, "Achieving minimum length scale in topology optimization using nodal design variables and projection functions," Int. J. Numer. Methods Eng. **61**, 238–254 (2004).
19. M. Y. Wang and S. Wang, "Bilateral filtering for structural topology optimization," Int. J. Numer. Methods Eng. **63**, 1911–1938 (2005).
20. O. Sigmund, "Morphology-based black and white filters," Struct. Multidisc. Optim. **33**, 401–424 (2007).
21. J. K. Guest, "Topology optimization with multiple phase projection," Comput. Methods Appl. Mech. Eng. **199**, 123–135 (2009).
22. S. Xu, Y. Cai, and G. Cheng, "Volume preserving nonlinear density filter based on heaviside functions," Struct. Multidisc. Optim. **41**, 495–505 (2009).
23. O. Sigmund, "Manufacturing tolerant topology optimization," Acta Mech. Sin. **25**, 227–239 (2009).
24. F. Wang, B. S. Lazarov, and O. Sigmund, "On projection methods, convergence and robust formulations in topology optimization," Struct. Multidisc. Optim. (to be published).
25. A. P. Seyranian, E. Lund, and N. Olhoff, "Multiple eigenvalues in structural optimization problems," Struct. Multidisc. Optim. **8**, 207–227 (1994).
26. N. L. Pedersen and A. K. Nielsen, "Optimization of practical trusses with constraints on eigenfrequencies, displacements," Struct. Multidisc. Optim. **25**, 436–445 (2003).
27. K. Svanberg, "A class of globally convergent optimization methods based on conservative convex separable approximations," SIAM J. Optim. **12**, 555–573 (2002).

Publication [P4]

High-performance slow light photonic crystal waveguides with topology optimized or circular-hole based material layouts

Available online at www.sciencedirect.com
SciVerse ScienceDirect
PHOTONICS AND NANOSTRUCTURES Fundamentals and Applications
Photonics and Nanostructures – Fundamentals and Applications xxx (2012) xxx–xxx
www.elsevier.com/locate/photonics

High-performance slow light photonic crystal waveguides with topology optimized or circular-hole based material layouts

Fengwen Wang *, Jakob S. Jensen, Ole Sigmund

Department of Mechanical Engineering, Solid Mechanics, Technical University of Denmark, Nils Koppels Allé, Building 404, 2800 Kgs., Lyngby, Denmark

Received 19 January 2012; received in revised form 12 April 2012; accepted 14 April 2012

Abstract

Photonic crystal waveguides are optimized for modal confinement and loss related to slow light with high group index. A detailed comparison between optimized circular-hole based waveguides and optimized waveguides with free topology is performed. Design robustness with respect to manufacturing imperfections is enforced by considering different design realizations generated from under-, standard- and over-etching processes in the optimization procedure. A constraint ensures a certain modal confinement, and loss related to slow light with high group index is indirectly treated by penalizing field energy located in air regions. It is demonstrated that slow light with a group index up to $n_g = 278$ can be achieved by topology optimized waveguides with promising modal confinement and restricted group-velocity-dispersion. All the topology optimized waveguides achieve a normalized group-index bandwidth of 0.48 or above. The comparisons between circular-hole based designs and topology optimized designs illustrate that the former can be efficient for dispersion engineering but that larger improvements are possible if irregular geometries are allowed.

Keywords: Slow light; Photonic crystal waveguide; Topology optimization; Robust design

1. Introduction

In recent years it has been demonstrated that photonic crystal waveguides (PhCWs), generated by introducing line defects in photonic crystals (PhC), can facilitate slow light propagation in the vicinity of the band edge [1,2]. Slow light in PhCWs has many potential applications, especially in telecommunication and optical data processing, e.g. for optical switching and nonlinear optics [3]. However, slow light in PhCWs is usually accompanied by high group-velocity-dispersion (GVD) that results in severe signal distortion and limits the available slow light bandwidth [4]. Also, poor modal confinement and high losses have been reported for slow light PhCWs [5,6].

Previous studies have demonstrated that the GVD of slow light can be suppressed through dispersion compensation and dispersion engineering. Dispersion compensation has been realized in photonic crystal coupled waveguides, where structural parameters (hole sizes) change gradually to generate wide-band and dispersion-compensated slow light [2,7]. The dispersion engineering methods have been carried out by parameter optimization, where the dispersion curve of PhCWs is tailored by changing radii and locations of air holes in PhCWs using geometrical perturbations. Slow

* Corresponding author. Tel.: +45 4525 4266.
E-mail address: fwan@mek.dtu.dk (F. Wang).

1569-4410/$ – see front matter © 2012 Elsevier B.V. All rights reserved.
http://dx.doi.org/10.1016/j.photonics.2012.04.004

light PhCWs with different group indexes from $n_g = 25$ to $n_g = 120$ have been obtained by geometrical perturbations [8–11]. More recently a group index as high as $n_g = 233$ is reported by location tuning and a corresponding design of $n_g = 44$ is numerically demonstrated to be robust under a location manufacturing tolerance of 1 nm [12]. A recent review of different geometrical perturbations and dispersion compensation results can be found in Schulz et al. [13].

In the last decade, numerical and experimental studies have shown that optical properties of PhC devices can be significantly improved by systematically redistributing material in the PhC devices, e.g. by using topology optimization [14,15]. A comprehensive review on the application of topology optimization in optical devices can be found in Jensen and Sigmund [16]. Topology optimization has been extended to design PhCWs with tailored dispersion properties [17], and recently a robust topology optimization formulation was proposed by the authors to ensure that devices perform satisfactorily also if they are slightly over- or under-etched due to manufacturing imperfections [18].

Previous work focused on designing PhCWs with constant high group index in a large wavenumber range thereby reducing the GVD. However, for applications such as in nonlinear devices, other properties may be of equal interest, for instance, modal confinement, losses and ultra high group index. In this paper the optimization procedure is extended to address these effects. Additionally, we propose an alternative parametrization using a material mask overlay strategy (MMOS) [19], which allows for creation of simpler optimized topologies consisting solely of circular holes which may sometimes be attractive for fabrication purposes. A comparison between the two parametrization methods is included to illustrate the potentials and limitations of regular circular-hole based PhCWs.

2. Physical model

We consider transverse electric (TE) modes in two-dimensional (2D) PhCWs, consisting of triangle patterned air holes in a dielectric material. The corresponding periodic supercell is shown in Fig. 1(a) with a lateral length of 12 rows of air holes and a lattice constant of a. With usually good accuracy TE-polarized light propagating in a 2D PhCW can be modeled by the scalar Helmholtz equation in the frequency domain:

$$\nabla \cdot \left(\frac{1}{\varepsilon}\nabla h\right) + \left(\frac{\omega}{c}\right)^2 h = 0 \tag{1}$$

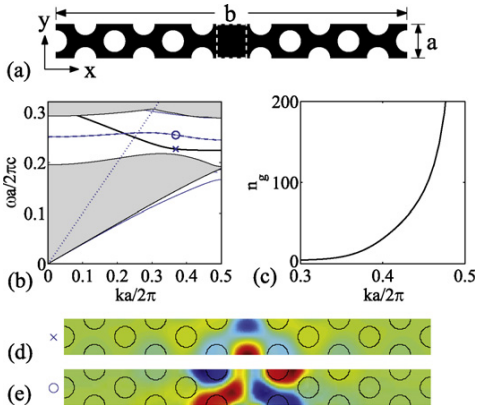

Fig. 1. Supercell in PhCWs and corresponding properties. (a) Geometry of the supercell; (b) band structure. Gray regions indicate slab mode regions, the dotted line represents the light line, the solid lines denote the even guided modes and the dashed lines denote the odd guided modes; (c) group index of the even modes versus wavenumber; (d) even modal profile; and (e) odd modal profile.

where ε is the relative permittivity, h is the out-of-plane component of the magnetic field, ω is the wave frequency and c is the speed of light in vacuum. The dispersion curve ($\omega(k)$) of PhCWs can be calculated by solving the eigenvalue problem of the supercell presented in Eq. (1) under Floquet–Bloch wave boundary conditions.

Based on the finite element method, the discrete expression of Eq. (1) can be written:

$$(\mathbf{K}_k - \omega^2\mathbf{M})\mathbf{h} = 0 \tag{2}$$

where $\mathbf{K}_k$ is the global finite element matrix from the first term in Eq. (1), the subscript k indicates the wavenumber in the waveguide direction, $\mathbf{h}$ is a vector of discretized nodal values of the magnetic field h and $\mathbf{M}$ is the global finite element matrix from the second term in Eq. (1). The wavenumber dependency of $\mathbf{K}_k$ is introduced by the implementation of the boundary conditions.

Fig. 1 (b) depicts the dispersion curve of the supercell in Fig. 1(a), with two guided bands within the band gap. According to the symmetry of the modal profiles along the waveguide direction, the guided bands can be classified into even bands (illustrated by solid lines) and odd bands (illustrated by dashed lines). The corresponding modal profiles are presented in Fig. 1(d)–(e). In this paper, we focus on the even band. The even mode exhibits slow light characteristics when approaching the band-edge. The group velocity of slow light at frequency ω is defined

Please cite this article in press as: F. Wang, et al., High-performance slow light photonic crystal waveguides with topology optimized or circular-hole based material layouts, Photon Nanostruct: Fundam Appl (2012), http://dx.doi.org/10.1016/j.photonics.2012.04.004

by the slope of the dispersion curve as

$$v_g = \frac{c}{n_g} = -\frac{\partial\omega}{\partial k} \tag{3}$$

where n_g is the group index of the guided mode and the minus sign only appears when the dispersion curve has a negative slope. The strong dependence of the group index on frequency, as illustrated in Fig. 1(c), leads to high GVD in the slow light regime. The GVD parameter is defined as:

$$\mathrm{GVD} = \frac{\partial^2 k}{\partial\omega^2} = -\frac{1}{v_g^3}\frac{\partial v_g}{\partial k} \tag{4}$$

In order to evaluate the capacity of slow light PhCWs, the normalized group-index bandwidth product (NGBP) is used to represent the trade-off between low group velocity and large bandwidth and has previously been employed as a key figure of merit to describe and compare different slow light PhCWs [13]. The NGBP is given as:

$$NGBP = \langle n_g \rangle \frac{\Delta\omega}{\omega_0} \tag{5}$$

here $\langle n_g \rangle$ is the average group index and $\Delta\omega$ is the bandwidth centered at ω_0, where the GVD is negligible. In practice, a relative group index error of $\pm 10\%$ is utilized to indicate the acceptable GVD region. In this paper, we also employ the $\pm 10\%$ criterion when calculating the NGBP of the optimized PhCWs.

Slow light modes generally penetrate deeper into the photonic crystal cladding compared to fast light modes [5,6,11]. Thus, a slow light mode is usually less confined to the waveguide core. In order to measure the modal confinement in the waveguide core, we define the modal confinement ratio r_{conf} as the energy ratio localized at the waveguide core with respect to the total field energy [17]:

$$r_{\mathrm{conf}} = \frac{\int_{\Omega_0} |h|^2 d\Omega}{\int_{\Omega} |h|^2 d\Omega} \tag{6}$$

For simplicity, we choose the center region with a size of $\sqrt{3}/2a \times a$ as the waveguide core, specified by the dashed rectangle in Fig. 1(a).

3. Optimization problem

In this section, we present the optimization problem for dispersion engineered slow light waveguides using topology optimization and circular-hole based parameter optimization.

3.1. Parameterization of geometrical model

The supercell geometry is in the following parameterized by two different methods: topology optimization using the density approach [14] and parameter optimization using a recently proposed material mask overlay strategy (MMOS) [19]. Common for the two methods we introduce a continuous element physical density $\overline{\rho}_e \in [0,\ 1]$ that is used to control the permittivity in element e in the supercell in the following way:

$$\frac{1}{\varepsilon_e} = \frac{1}{\varepsilon_1} + \overline{\rho}_e\left(\frac{1}{\varepsilon_2} - \frac{1}{\varepsilon_1}\right) \tag{7}$$

where ε_1 is the relative permittivity of air and ε_2 is the relative permittivity of dielectric material. In this paper, we consider InP as dielectric material ($\varepsilon_2 = 11.19$). The material in element e is dielectric material when $\overline{\rho}_e = 1$ and air when $\overline{\rho}_e = 0$. In the optimization procedure we allow $\overline{\rho}_e$ to take intermediate values between 0 and 1 so that we can apply a gradient-based optimization approach. However, for the final design we aim at a pure 0 and 1 solution corresponding to well defined material properties.

3.1.1. Topology optimization using the density approach

Here, the supercell geometry is modeled by a density approach. The supercell topology is represented by a threshold projection of the element-wise designs (ρ), given by:

$$\overline{\rho}_e = \begin{cases} \eta\{\exp[-\beta(1-\tilde{\rho}_e/\eta)] - (1-\tilde{\rho}_e/\eta)\exp(-\beta)\}, & 0 \le \tilde{\rho}_e \le \eta \\ (1-\eta)\{1-\exp[-\beta(\tilde{\rho}_e-\eta)/(1-\eta)] + (\tilde{\rho}_e-\eta)/(1-\eta)\exp(-\beta)\} + \eta, & \eta < \tilde{\rho}_e \le 1 \end{cases} \tag{8}$$

Here η is the chosen threshold, β is a regularization parameter and $\tilde{\rho}_e$ is the filtered density of element e. More details on this procedure can be found in Wang et al. [18].

3.1.2. Parameter optimization using MMOS

MMOS was introduced recently for structural optimization problems [19] and is adapted for photonic problems in this paper.

Please cite this article in press as: F. Wang, et al., High-performance slow light photonic crystal waveguides with topology optimized or circular-hole based material layouts, Photon Nanostruct: Fundam Appl (2012), http://dx.doi.org/10.1016/j.photonics.2012.04.004

The supercell topology is here represented by a set of circles using MMOS. We define the region within the circle to be occupied by air and the region outside to be occupied by dielectric material. The physical density of element e ($\overline{\rho}_e$) at the location $\mathbf{x}_e$ based on the ith circle can be formulated in terms of a Heaviside function as:

$$\overline{\rho}_e = H(\mathbf{x}_e, \mathbf{y}_i, r_i) = \begin{cases} 0 & \text{if } \dfrac{\|\mathbf{x}_e - \mathbf{y}_i\|^2}{r_i^2} - 1 < 0 \\ 1 & \text{if } \dfrac{\|\mathbf{x}_e - \mathbf{y}_i\|^2}{r_i^2} - 1 > 0 \end{cases} \tag{9}$$

Here $\mathbf{y}_i$ and r_i are the location and radius of ith circle. The Heaviside function is regularized with a parameter β

$$H(\mathbf{x}_e, \mathbf{y}_i, r_i) = \frac{1}{1 + \exp(-\beta((\|\mathbf{x}_e - \mathbf{y}_i\|^2 / r_i^2) - 1))} \tag{10}$$

The periodicity of the PhCW is enforced by considering each circle with three periods in the waveguide direction as $\mathbf{y}_i - \mathbf{a}$, $\mathbf{y}_i$ and $\mathbf{y}_i + \mathbf{a}$ with $\mathbf{a}$ being $[0, a]$. The final physical density $\overline{\rho}_e$ of element e generated from all M circles can be described by:

$$\overline{\rho}_e = \Pi_{i=1}^{M} H(\mathbf{x}_e, \mathbf{y}_i - \mathbf{a}, r_i) H(\mathbf{x}_e, \mathbf{y}_i, r_i) H(\mathbf{x}_e, \mathbf{y}_i + \mathbf{a}, r_i) \tag{11}$$

3.2. Optimization formulation

The robust formulation introduced in Wang et al. [18] is employed in this paper to reduce the influence of manufacturing imperfections on the performance of the final designs. Manufacturing imperfections are tackled by considering simulated under-, standard- and over-etching processes in the optimization procedure and the optimization problem is stated as to minimize the maximum error between actual group velocity $v_g(k_i)$ and a prescribed group velocity v_g^* in a certain wavenumber range $k_i \in [k_1,\ k_2]$ among different design realizations:

$$\min_{\mathbf{x}} \max_{q} \max_{k_i} f(\overline{\boldsymbol{\rho}}^q) = \left(\frac{v_g(\overline{\boldsymbol{\rho}}^q, k_i)}{v_g^*} - 1 \right)^2 \tag{12}$$

Here $\mathbf{x}$ denotes the design variables. In this unified formulation $\mathbf{x}$ represents element-wise design variables in topology optimization or the locations or radii of air holes in parameter optimization, and q denotes different design realizations from the manufacturing process. In topology optimization, these different design realizations are generated using different thresholds in the projection, Eq. (8), as $\eta \in [\eta_1, \eta_2]$. In parameter optimization, the design robustness is implemented by considering a small variation of the radii of air holes Δr. A variation of the hole position is neglected since the location can be controlled more accurately in the electron beam fabrication process [13]. In both methods, the standard design realization corresponds to the blueprint design for fabrication.

In order to avoid degenerated modes in the optimized designs, band separation constraints are implemented to push the bands above and below the design band away from the designed band. Furthermore a fundamental free vibration constraint is implemented on design realizations in the topology optimization formulation in order to avoid isolated components, but this is not an issue in the parameter optimization procedure due to constraints on the circle radii. More details on these constraints can be found in Ref. [18].

3.3. Sensitivity analysis

The group velocity can be calculated by finite differences and thus the sensitivity of the group velocity can be found directly from the sensitivity of the computed eigenvalues [18]. Here, we present an alternative approach where the finite difference approximation is circumvented by evaluating the analytical group velocity as:

$$v_g = -\frac{\partial \omega}{\partial k} = -\frac{1}{2\omega} \overline{\mathbf{h}}^T \frac{\partial \mathbf{K}_k}{\partial k} \mathbf{h} \tag{13}$$

The eigenvalues of the designed band are distinct due to the band separation constraints, so the sensitivity of the corresponding group velocity v_g with respect to a physical density $\overline{\rho}_e$ can be calculated in a straightforward manner using adjoint sensitivity analysis:

$$\frac{\partial v_g}{\partial \overline{\rho}_e} = 2\Re\left(\mathbf{u}^T \left(\frac{\partial \mathbf{K}_k}{\partial \overline{\rho}_e} - \lambda \frac{\partial \mathbf{M}}{\partial \overline{\rho}_e} \right) \mathbf{h} \right) + \upsilon \overline{\mathbf{h}}^T \frac{\partial \mathbf{M}}{\partial \overline{\rho}_e} \mathbf{h} - \frac{1}{2\omega} \overline{\mathbf{h}}^T \frac{\partial^2 \mathbf{K}_k}{\partial \overline{\rho}_e \partial k} \mathbf{h}, \tag{14}$$

$$\lambda = \omega^2$$

Here, $\Re(\cdot)$ indicates the real part of vectors, the superscript T denotes the transpose of vectors, the bar denotes the conjugate of vectors, $\mathbf{u}$ and υ are the adjoint variable vector and adjoint variable, obtained by solving the adjoint problem:

$$\begin{bmatrix} 2(\mathbf{K}_k - \lambda \mathbf{M}) & 2\mathbf{M}\mathbf{h} \\ 2\overline{\mathbf{h}}^T \mathbf{M} & 0 \end{bmatrix} \begin{bmatrix} \overline{\mathbf{u}} \\ \upsilon \end{bmatrix} = \begin{bmatrix} -\left(\dfrac{\partial v_g}{\partial \mathbf{h}^R} + i \dfrac{\partial v_g}{\partial \mathbf{h}^I} \right)^T \\ \dfrac{\partial v_g}{\partial \lambda} \end{bmatrix} \tag{15}$$

Please cite this article in press as: F. Wang, et al., High-performance slow light photonic crystal waveguides with topology optimized or circular-hole based material layouts, Photon Nanostruct: Fundam Appl (2012), http://dx.doi.org/10.1016/j.photonics.2012.04.004

where the superscripts R and I indicate the real and imaginary part of vectors, respectively.

The sensitivity of the band separation constraints and fundamental free vibration constraints is calculated using standard sensitivity analysis of eigenvalues [20,21].

Based on the above equations, the sensitivity of the objective and constraint function with respect to the design variable x is calculated using the chain rule [22]:

$$\frac{\partial F}{\partial x} = \sum_{i=1}^{M} \frac{\partial F}{\partial \overline{\rho}_e} \frac{\partial \overline{\rho}_e}{\partial x} \tag{16}$$

The sensitivity of the physical density $\overline{\rho}_e$ with respect to the design variable x is derived from Eqs. (8) and (11) for the two different parameterizations.

3.4. Numerical implementation

The optimized designs are iteratively generated using a gradient-based algorithm. The topology optimization problem is solved by the min-max algorithm with the Globally Convergent version of the Method of Moving Asymptotes (GCMMA) from Svanberg [23]. A continuation strategy is employed to update the regularization parameter β using $\beta = 1.3 \times \beta$ with the maximum value set to be $\beta_{\max} = 200$. A detailed description of the numerical implementation of topology optimization can be found in Wang et al. [18]. Since the parameter optimization problem involves only few design variables, the locations and radii of air holes are updated using FMINCON in MATLAB which we have found to be the most efficient algorithm in this case. Numerical studies show that the parameter optimization problem does not benefit from the continuation strategy of the regularization parameter β, hence, β is fixed to $\beta = 100$.

In order to avoid the non-differentiability of the objective in the min-max formulation in Eq. (12), we convert the problem to the bound formulation, i.e. a new variable $f_{\max}$ is introduced to represent the maximum value of the objectives. The objective is converted to:

$$\min_{\mathbf{x}} \quad f_{\max}, \qquad \text{s.t.} \quad \left(\frac{v_g(\overline{\boldsymbol{\rho}}^q, k_i)}{v_g^*} - 1 \right)^2 < f_{\max} \tag{17}$$

The topology optimization procedure is implemented in MATLAB and runs in parallel on a standard eight-processor PC. The optimization converges in 400–500 GCMMA iterations for 3-case robust design, for which each GCMMA iteration includes three or four inner-iterations and takes 2–3 min for eight design wavenumbers. The parameter optimization procedure can be completed within 400 function evaluations owning to the few design variables.

4. Results

In this section, we first employ topology optimization to design slow light PhCWs for high group index and we address the modal confinement and loss issues related to slow light with high group index. Moreover, we investigate the limits for slow light with restrictions on the modal confinement and GVD. Finally, we compare the performances of the circular-hole based PhCWs and topology optimized PhCWs.

The initial structure used as basis for the optimization procedures is a conventional PhCW with triangle patterned air holes of $r = 0.3a$ shown in Fig. 1. The supercell is discretized using 408×40 quadrilateral four-node elements. The design domains used for the two different parameterizations are illustrated in Fig. 2. The design domain in topology optimization is chosen to be the first three and a quarter rows of air holes adjacent to the waveguide core (shown in Fig. 2(a)). Here, the design robustness is enforced by considering the different design realizations generated using different thresholds as $\eta \in [0.35,\ 0.65]$ in Eq. (8) with a filter radius of $r = a/8$. The threshold interval is chosen to mimic an approximate etching variation of $\pm 0.02a$. The design variables for the parameter optimization are the locations and radii of the first two rows of air holes adjacent to the waveguide core and the radius of the remaining air holes as shown in Fig. 2(b). The design variables associated with the first row of air holes (C_1) are set to be relative lateral and vertical locations (x_1, y_1) with respect to the supercell center and radius r_1. The ones associated with the second row are set to be lateral and vertical locations (x_2, y_2) and radius r_2. We assign the same radius for the remaining rows of air holes (C_0) with the associated design variable set to be radius r_0. In order to realize the design robustness, a small radius variation Δr is introduced and different design realizations are generated using $\Delta r_i \in [-\Delta r,\ \Delta r]$.

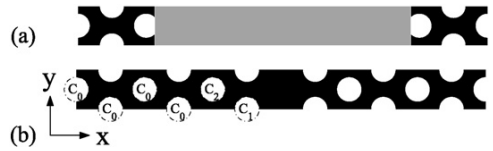

Fig. 2. Design domains in different parameterizations. (a) Design domain in topology optimization; and (b) design domain in parameter optimization.

Please cite this article in press as: F. Wang, et al., High-performance slow light photonic crystal waveguides with topology optimized or circular-hole based material layouts, Photon Nanostruct: Fundam Appl (2012), http://dx.doi.org/10.1016/j.photonics.2012.04.004

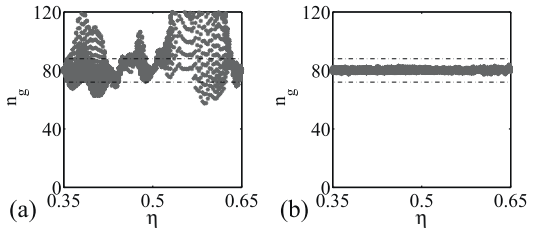

Fig. 3. Performance of the optimized designs for group index of $n_g^* = 80$. (a) Performance of 3-case robust design; and (b) performance of 51-case robust design.

4.1. Optimized PhCWs with reduction of GVD

As the first optimization example we design a PhCW for $n_g^* = 80$ with $n_g^* = c/v_g^*$, where the design symmetry is enforced along the waveguide direction. The target wavenumber range is set to be $k_i \in [0.34,\ 0.46]2\pi/a$ with 8 design wavenumbers. The optimization is first performed to design slow light PhCW considering three different realizations corresponding to $\eta = [0.35,\ 0.5,\ 0.65]$ as in Ref. [18]. The performance of the optimized design is depicted in Fig. 3(a) with respect to different manufacturing errors, where asterisks denote the group index of guided modes in design wavenumber range in 100 different design realizations. Here it is noted that 3 design realizations are not enough to ensure robustness. In between, very large response deviations are found. In order to ensure robustness, the number of design realizations considered in the optimization procedure is gradually increased to 51. The final design achieves good performance under different manufacturing errors as shown in Fig. 3(b). In the subsequent examples, the final optimized designs are obtained by considering 51 different design realizations to guarantee the design robustness. Alternatively, the design robustness can also been enhanced using a stochastic robust formulation [24,25].

The final optimized design for $n_g^* = 80$ and corresponding performances are depicted in Fig. 4. Fig. 4(a) illustrates the manufacturing errors considered in the optimization procedure with the bold line indicating the standard design realization corresponding to $\eta = 0.5$ and Fig. 4(b) shows the corresponding standard design realization, i.e. the blueprint for the fabrication process. Fig. 4(c) describes the designed band and the group index of the blueprint design as functions of normalized frequencies. Fig. 4(d) shows group indexes of the different design realizations where the gray region indicates the group index range of guided modes in 100 different design realizations. A

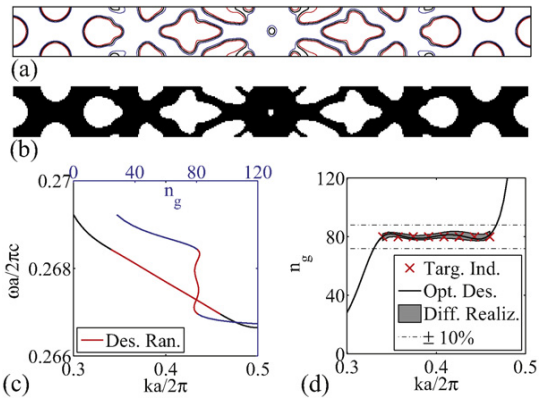

Fig. 4. Robust topology optimized design for group index of $n_g^* = 80$ and the corresponding performances. (a) Illustration of the manufacturing error considered; (b) optimized design; (c) performance of the optimized design. Black line represents the design band and the blue line represents the group index; and (d) group index versus wavenumber. Gray region indicates the group index range of 100 design realizations in the design wavenumber range. (For interpretation of the references to color in this figure legend, the reader is referred to the web version of the article.)

small group index variation is observed in the design wavenumber range with respect to the prescribed group index represented by crosses. The blueprint design achieves an NGBP of 0.50 centered at $\omega_0 = 0.2677\ 2\pi c/a$. It is observed that the actual wavenumber range for the constant group index is larger than prescribed when we use the $\pm 10\%$ criterion shown by dashed lines in Fig. 4.

4.2. Optimized PhCWs with enhanced modal confinement

The confinement plot of the different design realizations (seen in Fig. 5) illustrates that the guided modes may have low modal confinement. In the

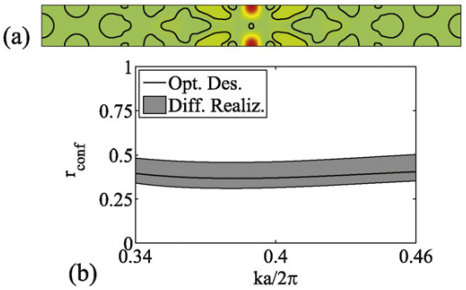

Fig. 5. Modal confinement of the optimized design from Fig. 4. (a) Field intensity profile of the optimized design at the center frequency of design wavenumber range; and (b) modal confinement ratio versus wavenumber.

Please cite this article in press as: F. Wang, et al., High-performance slow light photonic crystal waveguides with topology optimized or circular-hole based material layouts, Photon Nanostruct: Fundam Appl (2012), http://dx.doi.org/10.1016/j.photonics.2012.04.004

optimization procedure, the modal confinement can be enhanced by setting a lower bound r^*_{conf} on the modal confinement ratio:

$$r^*_{\text{conf}} - r_{\text{conf}}(k_i) \leq 0 \tag{18}$$

Here, the confinement constraint is implemented on the dilated design realization of $\eta = 0.35$ since it exhibits the lowest modal confinement among all the different realizations.

We have designed PhCWs for a set of prescribed group indexes and prescribed confinement ratios. The final designs and corresponding performances are summarized in Fig. 6. The first PhCW is designed for a prescribed group index of $n^*_g = 80$ with a minimum confinement ratio of $r^*_{\text{conf}} = 0.5$ (seen in Fig. 6(a)). With the same confinement ratio, the second PhCW is designed for a higher group index of $n^*_g = 150$ (seen in Fig. 6(b)). The last PhCW is designed for $n^*_g = 80$ with a confinement ratio of $r^*_{\text{conf}} = 0.6$ (seen in Fig. 6(c)). An increased group index variation can be observed when the prescribed group index increases from $n^*_g = 80$ to $n^*_g = 150$. A severe group index variation is observed for $r^*_{\text{conf}} = 0.6$, which indicates a significant distortion of the light pulse.

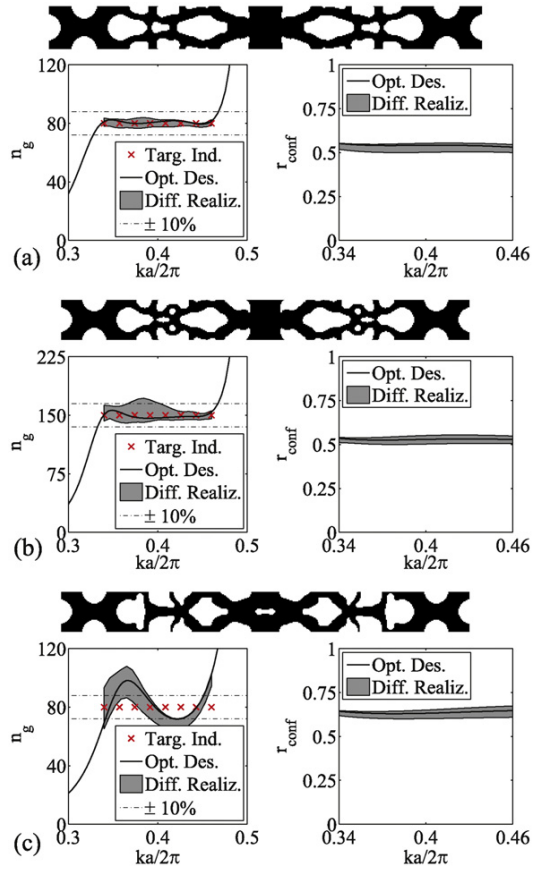

Fig. 6. Influence of the prescribed group index and prescribed confinement ratio. (a) Optimized design for $n^*_g = 80$ with $r^*_{\text{conf}} = 0.5$. Up: Optimized design. Left: Group index versus wavenumber. Right: Confinement ratio versus wavenumber; (b) optimized design for $n^*_g = 150$ with $r^*_{\text{conf}} = 0.5$; and (c) optimized design for $n^*_g = 80$ with $r^*_{\text{conf}} = 0.6$.

The three examples of optimized PhCWs show that the modal confinement of slow light is inherently restricted and that slow light with high group index and low GVD cannot achieve a very high modal confinement. Nevertheless, for a minimum confinement ratio of $r^*_{\text{conf}} = 0.5$, a good performance is achieved by the optimized PhCWs for both $n^*_g = 80$ and $n^*_g = 150$. The blueprint design for $n^*_g = 80$ achieves an NGBP of 0.50 centered at $\omega_0 = 0.2750\ 2\pi c/a$ and an NGBP of 0.49 centered at $\omega_0 = 0.2755\ 2\pi c/a$ for $n^*_g = 150$. Moreover, when compared to the optimized PhCW shown in Fig. 4, the modal confinement of the guided modes has been significantly enhanced by enforcing the lower bound.

4.3. Optimized PhCWs considering field losses

Fig. 7 depicts the energy fraction located in air regions of the optimized design in Fig. 6(a). More than 22% of the total energy of the guided mode is located in air regions for the blueprint design and an even higher energy fraction for other design realizations due to the higher fraction of air regions. This implies that the optimized designs may encounter high undesirable losses according to Ref. [6] where the loss in slow light waveguides is modeled to be proportional to the field energy on the sidewall of air holes. In the following example we aim at reducing the losses in PhCWs indirectly by penalizing the field energy located in air regions. The corresponding optimization formulation is

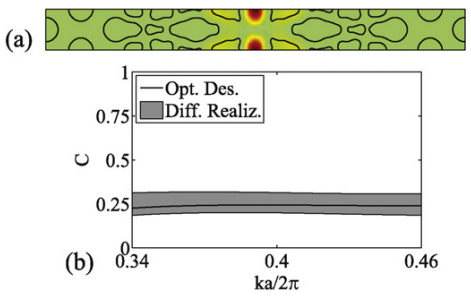

Fig. 7. Field energy fraction located in air regions in the topology optimized design in Fig. 6(a). (a) Field intensity profile; and (b) field energy fraction in air regions.

Please cite this article in press as: F. Wang, et al., High-performance slow light photonic crystal waveguides with topology optimized or circular-hole based material layouts, Photon Nanostruct: Fundam Appl (2012), http://dx.doi.org/10.1016/j.photonics.2012.04.004

modified accordingly:

$$\min_{\mathbf{x}} \quad \max_{q} \quad \max_{k_i} \quad \log\left(\left(\frac{v_g(\overline{\boldsymbol{\rho}}^q, k_i)}{v_g^*} - 1\right)^2 + 1\right) + \alpha \sum_{k_i} C(k_i) \tag{19}$$

Here, α is the corresponding penalty factor and C denotes the field energy located in air regions, calculated as:

$$C = \int_{\Omega_{design}} (1 - \overline{\rho}_e)^2 \overline{h} h \; dv \tag{20}$$

The penalty term is calculated using the design realization of $\eta = 0.65$. Fig. 8 shows the final design for group index of $n_g^* = 80$ with $\alpha = 50$. Compared to the design showed in Fig. 6(a), the energy located in air regions (Fig. 8(b)) has been significantly reduced. The field intensity profile indicates that the field energy located at sidewalls is efficiently reduced using the proposed method. Moreover no significant change can be observed on group index deviation. The blueprint design achieves an NGBP of 0.49 centered at $\omega_0 = 0.2723\ 2\pi c/a$.

The non-periodic perturbations due to manufacturing imperfections can also significantly influence propagation losses [26]. Numerically, the non-periodic perturbations can be represented by a supercell of several periods. The propagation losses, due to the back-scattering from non-periodic perturbations, can be modeled using a phenomenological approach [27]. In this approach, the losses are represented by an effective dissipation coefficient, i.e. an imaginary part of permittivity ε'' with $\varepsilon = \varepsilon' + i\varepsilon''$. The propagation loss can then be evaluated from the solution of the complex eigenvalue problem. Furthermore, using a large supercell, we can investigate the influence of non-periodic perturbations on the group indexes. This work is ongoing and will be presented in future studies.

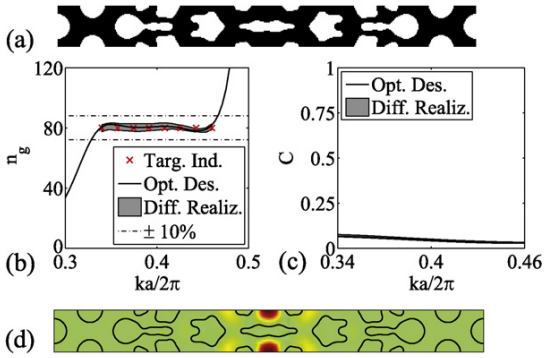

Fig. 8. Topology optimized design for group index of $n_g^* = 80$ considering losses. (a) Optimized design; (b) group index versus wavenumber; (c) field energy fraction in air regions; and (d) field intensity profile.

4.4. Limits of slow light

The results in Fig. 6 indicate that the objectives: modal confinement, group index and GVD act in opposite directions. Thus, a high prescribed group index and large prescribed modal confinement ratio results in a bigger GVD. A natural question that emerges is how much we can slow down light using dispersion engineered PhCWs while retaining a certain modal confinement and acceptable GVD. In this section, we propose a modified optimization formulation to investigate this problem.

The previous numerical results have shown that the modal confinement issue can be addressed using the confinement constraints and GVD can be represented by a relative error criterion. The modified optimization problem is formulated to maximize the product of confinement ratio and group index with limited GVD as

$$\begin{aligned} \min_{\mathbf{x}} \quad & \log\left(\frac{v_g^*}{r_{\text{conf}}^*}\right) \\ \text{s.t.} \quad & \log\left(\frac{v_g(\overline{\boldsymbol{\rho}}^q, k_i)}{v_g^*} - 1\right)^2 < \log((e_r^*)^2) \\ & r_{\text{conf}}(\overline{\boldsymbol{\rho}}^d, k_i) \geq r_{\text{conf}}^* \end{aligned} \tag{21}$$

Here v_g^* represents the average group velocity, r_{conf}^* represents the average modal confinement ratio, and e_r^* is the prescribed relative group velocity error, which directly indicates GVD of the final designs. The bounds for group velocity is set to be $1/300 \leq v_g^* \leq 1/40$ to ensure a practical slow light bandwidth. At the same time, a lower bound is set for the modal confinement to localize the guided mode to the waveguide core as $0.4 \leq r_{\text{conf}}^* \leq 1$. The optimization formulation is completed with the equilibrium equation and other constraints already described.

The whole optimization procedure can be described as follows: Eq. (21) is first employed to obtain the target group index n_g^* and minimum confinement ratio r_{conf}^* using three different realizations; then Eqs. (17) and (18) are utilized to further enhance the design robustness by considering 51 different design realizations for the target group index and confinement ratio.

Please cite this article in press as: F. Wang, et al., High-performance slow light photonic crystal waveguides with topology optimized or circular-hole based material layouts, Photon Nanostruct: Fundam Appl (2012), http://dx.doi.org/10.1016/j.photonics.2012.04.004

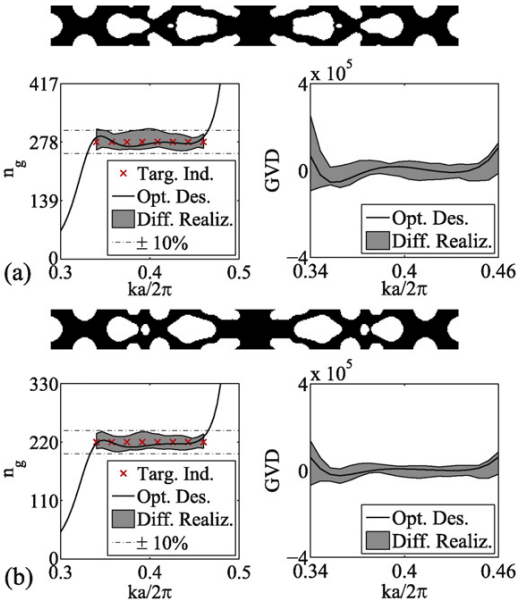

Fig. 9. Influence of the relative group velocity error on the optimized PhCWs. (a) Optimized design for $e_r^* = 0.03$. Top: Optimized design. Left: Group index versus wavenumber. Right: GVD parameter plot; and (b) optimized design for $e_r^* = 0.02$.

Two optimizations are performed corresponding to the relative group velocity errors of $e_r^* = 0.03$ and $e_r^* = 0.02$, respectively. The final designs and corresponding properties are depicted in Fig. 9. Under $e_r^* = 0.03$, a target group index of $n_g^* = 278$ can be achieved with $r_{\text{conf}}^* = 0.43$. An NGBP of 0.48 is reached by the blueprint design, which corresponds to a bandwidth of 2.7 nm centered at $\lambda_0 = 1550$ nm. For $e_r^* = 0.02$, a target group index of $n_g^* = 220$ can be reached with $r_{\text{conf}}^* = 0.43$. The corresponding GVD parameter of different design realizations is reduced to be half of the one of $e_r^* = 0.03$. The bandwidth of the blueprint design is around 3.4 nm with an NGBP of 0.49.

4.5. Comparison between circular-hole based PhCWs and topology optimized PhCWs

Variations of circular-hole based PhCWs have been extensively studied to reduce the GVD of slow light. In this section, we compare the performances of the topology optimized PhCWs and circular-hole based PhCWs created using an efficient parameter optimization scheme, as discussed in Section 3. In the following examples, we aim to reduce the GVD of slow light in the circular-hole based PhCWs.

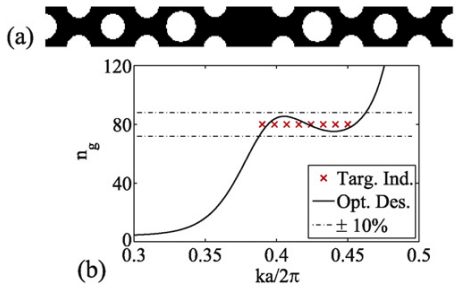

Fig. 10. Final design for $n_g^* = 80$ from radii tuning. (a) Optimized design; and (b) group index versus wavenumber.

In order to evaluate the circular-hole based optimization, we first perform several parameter optimizations with the design variables as the radii of the first two rows of air holes in the supercell. The design wavenumber range is set to be $k_i \in [0.39, 0.45]2\pi/a$ with 8 target wavenumbers. Different prescribed group indexes are chosen as $n_g^* \in [40, 100]$. Fig. 10 depicts the final design and corresponding performance for $n_g^* = 80$. The group index variation is barely within $\pm 10\%$ in the design wavenumber range. The optimized design achieves an NGBP of 0.32 centered at $\omega_0 = 0.2267\ 2\pi c/a$ and the corresponding average group index is $\langle n_g \rangle = 80.2$.

The final design parameters for different prescribed group indexes and corresponding performances are summarized in Table 1. The radii of both rows of air holes increase as the prescribed group index increases. Compared to the initial guess, the radius of the second row of air holes is increased and the one of the first row is decreased in order to obtain a flat dispersion curve with constant slope. The tendency resembles the one from geometrical perturbations considered earlier [8]. The optimized design for $n_g^* = 40$ possesses a slightly higher group index than prescribed whereas the remaining designs match the prescribed group indexes. All the optimized designs achieve an NGBP of 0.31, which is bigger than the one obtained by manually perturbing the radii of the first two rows of air holes [8].

Table 1
Parameters and characteristics of the designs from radii tuning.

n_g^*	Design (r_1, r_2)	ω_0	NGBP	$\langle n_g \rangle$
40	(0.2272, 0.3518)	0.2207	0.35	42.0
50	(0.2373, 0.3543)	0.2216	0.34	50.0
60	(0.2547, 0.3584)	0.2234	0.31	59.9
70	(0.2661, 0.3619)	0.2251	0.32	70.0
80	(0.2821, 0.3652)	0.2267	0.32	80.2
90	(0.2855, 0.3672)	0.2276	0.32	89.9
100	(0.2879, 0.3688)	0.2282	0.32	100.1

Please cite this article in press as: F. Wang, et al., High-performance slow light photonic crystal waveguides with topology optimized or circular-hole based material layouts, Photon Nanostruct: Fundam Appl (2012), http://dx.doi.org/10.1016/j.photonics.2012.04.004

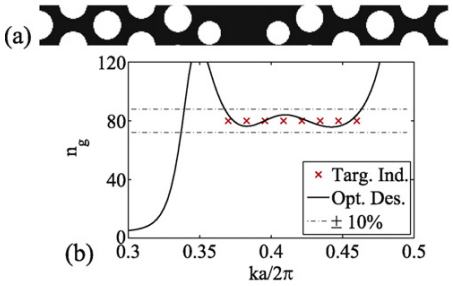

Fig. 11. Final design for $n_g^* = 80$ from radii tuning. (a) Optimized design; and (b) group index versus wavenumber.

A further fine tuning is performed by including the locations of the first two rows of air holes and the radius of the remaining air holes as additional design variables. The optimized design for $n_g^* = 80$ achieves an NGBP of 0.41 centered at $\omega_0 = 0.2317\ 2\pi c/a$ (seen in Fig. 11), which is better than any results obtained by geometrical perturbations in the literature.

In order to enhance the design robustness, a radius variation is introduced as $\Delta r = 0.02a$ which corresponds to a manufacturing error equivalent to the one considered for the topology optimization examples. The design wavenumber range is set to be $k_i \in [0.39, 0.45]2\pi/a$. The final design for $n_g^* = 80$ is shown in Fig. 12. The blueprint design achieves an average group index of $\langle n_g \rangle = 83.5$ with an NGBP of 0.27 centered at $\omega = 0.2627\ 2\pi c/a$ shown in Fig. 12(b). It should be noted that the group index variation of different design realizations (shown in Fig. 12(c)) is slightly out of the range of ±10%. Nevertheless, the limited group index error ensures that distortions of signals are restricted in the designed slow light PhCW.

Comparisons between the optimized designs in Figs. 4 and 12 show that the NGBP of the topology optimized design is 1.85 times the one of the circular-hole optimized

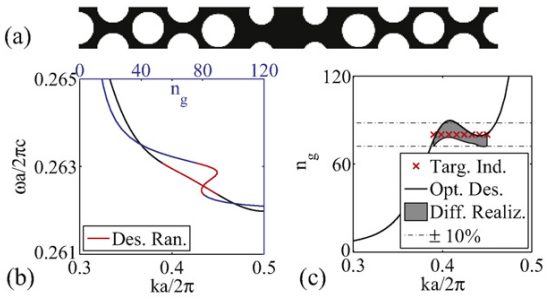

Fig. 12. Robust parameter design of $n_g^* = 80$ and corresponding performances. (a) Optimized design; (b) performance of the optimized design; and (c) group index versus wavenumber.

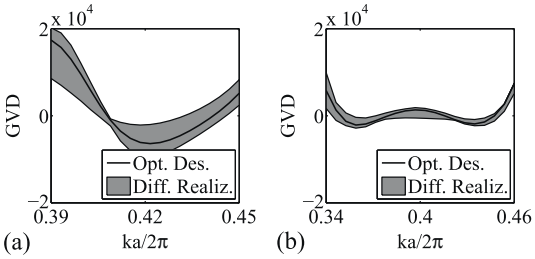

Fig. 13. Comparison of the performances between different optimized designs. (a) GVD parameter of the robust parameter design in Fig. 12; and (b) GVD parameter of the robust topology optimized design in Fig. 4.

design. Furthermore, the GVD of topology optimized design is much smaller than the one of the circular-hole based design, as shown in Fig. 13.

5. Conclusion

In this paper, we have addressed the modal confinement and loss issues related to slow light with high group index in the topology optimization procedure and investigated the limits for slow light using dispersion engineered slow light PhCWs while constraining the modal confinement and GVD. Furthermore, we have investigated the potentials and limitation of using the circular-hole based PhCWs by using a parameter optimization procedure.

The design robustness in topology optimization has been realized by considering different design realizations generated by a threshold projection. The modal confinement issue has been solved by setting a low bound on the confinement ratios of guided modes at the waveguide core. The losses related to slow light have been tackled by penalizing field energy located in the air regions in the supercell. Additionally, a new optimization problem has been proposed to study how much light can be delayed in a dispersion engineered PhCWs without sacrificing modal confinement and GVD. The corresponding numerical results illustrate that a group index of $n_g = 278$ can been achieved with negligible GVD and promising modal confinement. An NGBP of 0.48 has been achieved by all the optimized designs.

In the circular-hole based PhCWs, a material mask overlay strategy (MMOS) has been utilized to parameterize the geometry of the periodic supercell. An NGBP of 0.41 can be achieved by the optimized design for $n_g^* = 80$ from a fine tuning. Moreover, the design robustness with respect to manufacturing imperfections has been enforced by considering the different design realizations generated by a small radius variation on air

Please cite this article in press as: F. Wang, et al., High-performance slow light photonic crystal waveguides with topology optimized or circular-hole based material layouts, Photon Nanostruct: Fundam Appl (2012), http://dx.doi.org/10.1016/j.photonics.2012.04.004

holes in the supercell. An NGBP of 0.27 has been achieved by the robust design for $n_g^* = 80$.

The comparison between topology optimized PhCWs and circular-hole based PhCWs illustrates that slow light PhCWs obtained by the latter can be designed to have a very good performance but also that larger improvements of the NGBP can be achieved when irregular (but still manufacturing tolerant) geometries are allowed.

The presented algorithm can be directly applied in the optimization of 3D waveguides. However, the extra dimension will add considerably to the CPU-time and will also create challenges regarding efficient large scale eigenvalue solvers. CPU-time may be reduced considerably by using optimized 2D waveguide designs as staring guesses.

Acknowledgements

This work was financially supported by Villum Fonden (via the NATEC Centre of Excellence) and by the Danish Center for Scientific Computing (DCSC).

References

[1] M. Notomi, K. Yamada, A. Shinya, J. Takahashi, C. Takahashi, I. Yokohama, Physical Review Letters 85 (2001).
[2] D. Mori, T. Baba, Applied Physics Letters 85 (2004) 1101–1103.
[3] T.F. Krauss, Nature Photonics 2 (2008) 448–450.
[4] R.J.P. Engelen, Y. Sugimoto, Y. Watanabe, J.P. Korterik, N. Ikeda, N.F. van Hulst, K. Asakawa, L. Kuipers, Optics Express 14 (2006) 1658–1672.
[5] H. Kurt, K. Ustun, L. Ayas, Optics Express 18 (2010) 26965–26977.
[6] L. O'Faolain, S.A. Schulz, D.M. Beggs, T.P. White, M. Spasenovic, L. Kuipers, F. Morichetti, A. Melloni, S. Mazoyer, J.P. Hugonin, P. Lalanne, T.F. Krauss, Optics Express 18 (2010) 27627–27638.
[7] D. Mori, S. Kubo, H. Sasaki, T. Baba, Optics Express 15 (2007) 5264–5270.
[8] L.H. Frandsen, A.V. Lavrinenko, J. Fage-Pedersen, P.I. Borel, Optics Express 14 (2006) 9444–9450.
[9] J. Li, T.P. White, L. O'Faolain, A. Gomez-Iglesias, T.F. Krauss, Optics Express 16 (2008) 6227–6232.
[10] R. Hao, E. Cassan, X. Le Roux, D.S. Gao, V. Do Khanh, L. Vivien, D. Marris-Morini, X.L. Zhang, Optics Express 8 (2010) 16309–16319.
[11] R. Hao, E. Cassan, H. Kurt, J. Hou, X. Le Roux, D. Marris-Morini, L. Vivien, D.S. Gao, Z.P. Zhou, X.L. Zhang, IEEE Photonics Technology Letters 22 (2010) 844–846.
[12] J. Liang, L.Y. Ren, M.J. Yun, X. Han, X.J. Wang, Journal of Applied Physics 110 (2011) 063103.
[13] S.A. Schulz, L. O'Faolain, D.M. Beggs, T.P. White, A. Melloni, T.F. Krauss, Journal of Optics 12 (2010).
[14] M.P. Bendsøe, O. Sigmund, Topology Optimization/Theory, Methods and Applications, Springer, Berlin, 2003.
[15] J.S. Jensen, O. Sigmund, Applied Physics Letters 84 (2004) 2022–2024.
[16] J.S. Jensen, O. Sigmund, Laser and Photonics Reviews 5 (2011) 308–321.
[17] R. Stainko, O. Sigmund, Waves in Random and Complex Media 17 (2007) 477–489.
[18] F. Wang, J.S. Jensen, O. Sigmund, Journal of the Optical Society of America B 28 (2011) 387–397.
[19] A. Saxena, Journal of Mechanical Design 133 (2011) 011001.
[20] A.P. Seyranian, E. Lund, N. Olhoff, Structural Optimization 8 (1994) 207–227.
[21] N.L. Pedersen, A. Nielsen, Structural and Multidisciplinary Optimization 25 (2003) 436–445.
[22] O. Sigmund, Structural and Multidisciplinary Optimization 33 (2007) 401–424.
[23] K. Svanberg, Siam Journal on Optimization 12 (2001) 555–573.
[24] Y. Elesin, B.S. Lazarov, J.S. Jensen, O. Sigmund, Photonics and Nanostructures: Fundamentals and Applications 10 (2012) 153–165.
[25] B.S. Lazarov, M. Schevenels, O. Sigmund, Mechanical Sciences 2 (2011) 175–182.
[26] M. Patterson, S. Hughes, S. Schulz, D.M. Beggs, T.P. White, L. O'Faolain, T.F. Krauss, Physical Review B 80 (2009) 195305.
[27] R. Ferrini, D. Leuenberger, R. Houdre, H. Benisty, M. Kamp, A. Forchel, Optics Letters 31 (2006) 1426–1428.

Please cite this article in press as: F. Wang, et al., High-performance slow light photonic crystal waveguides with topology optimized or circular-hole based material layouts, Photon Nanostruct: Fundam Appl (2012), http://dx.doi.org/10.1016/j.photonics.2012.04.004

Publication [P5]

Systematic design of loss engineered slow light waveguides

Systematic design of loss engineered slow light waveguides

Fengwen Wang,[1,*] Jakob Søndergaard Jensen,[1] Jesper Mørk,[2] and Ole Sigmund,[1]

[1] *Department of Mechanical Engineering, Technical University of Denmark, Nils Koppels Allé Building 404, 2800, Kgs. Lyngby, Denmark*

[2] *Department of Photonics Engineering, Technical University of Denmark, Ørsteds Plads, Building 345, 2800, Kgs. Lyngby, Denmark*

[*] *Corresponding author: fwan@mek.dtu.dk*

This paper employs topology optimization to systematically design free-topology loss engineered slow light waveguides with enlarged group index bandwidth product (GBP). The propagation losses of guided modes are evaluated by the imaginary part of eigenvalues in complex band structure calculations, where the scattering losses due to manufacturing imperfections are represented by an edge-related effective dissipation. The loss engineering of slow light waveguides is realized by minimizing the propagation losses of design modes. Numerical examples illustrate that the propagation losses of free-topology dispersion engineered waveguides can be significantly suppressed by loss engineering. Comparisons between fixed- and free-topology loss engineered waveguides demonstrate that the GBP can be enhanced significantly by the free-topology loss engineered waveguides with a small increase of the propagation losses.

OCIS codes: 000.4430, 130.5296, 230.7390.

1. Introduction

In the past decade, photonic crystal waveguides (PhCWs), i.e. photonic crystals (PhCs) with line defects, have attained extensive interest due to their capability in manipulating light propagation. Approaching the band edge, the group refractive index increases and slow light propagation effects prevail, with a number of possible applications, e.g. for tunable delays [1, 2], enhanced light-matter interaction, optical switching [3], nonlinear optics [4, 5]

and mode-locked lasers [6]. It has been reported that both material loss and material gain in the PhCWs restrict the attainable group index and degrade slow light effects [7,8]. Moreover, the benefits of slow light are typically compromised by significant group velocity dispersion (GVD) [9] and concomitant propagation losses [10, 11].

Several approaches have been investigated numerically and experimentally to engineer the dispersion of slow light modes and optimize the group index bandwidth products (GBP), namely, dispersion compensation in the coupled photonic crystal waveguides [12, 13] and dispersion curve engineering [14–16]. Dispersion compensation has been realized in photonic crystal coupled waveguides through adiabatic geometry change and a GBP of 0.38 has been experimentally achieved [17]. Dispersion curve engineering was initially performed using trial-and-error methods guided by physical intuition [14–16], i.e. changing radii and locations of air holes and recently, a material mask overlay strategy (MMOS) was used by some of the authors to optimize fixed-topology waveguides (circular-hole based waveguides) using a gradient-based algorithm [18]. Through distributing dielectric material in the periodic supercell, a GBP of 0.47 for group index above 200 can be achieved by free-topology waveguides using topology optimization [19,20], and furthermore the robustness of waveguides has been enhanced with respect to manufacturing imperfections through a robust optimization approach [20, 21].

The propagation losses in PhCWs are critical for the application of slow light waveguides and have received growing interest. Even though slow light propagation in PhCWs is intrinsically lossless below the light line, fabricated waveguides display significant extrinsic losses due to manufacturing imperfections. The manufacturing disorders, i.e. variations of vertical wall, surface roughness, cause significant out-of-plane radiation [22,23] and back-scattering [24,25], hence lead to large propagation losses, especially for slow light. The out-of-plane radiation has been reported to follow a n_g-scaling [26]. With a theoretical model based on Green function tensor (GFT), the back-scattering was found to follow a n_g^2-scaling [10,24,27], which has been experimentally confirmed [11]. More recently, Petrov et al have numerically demonstrated that the propagation losses vary in different designs due to the different field intensity on the interfaces between air and dielectric material [28]. This observation has been experimentally verified [25]. These very first studies have opened up new prospects in the loss engineering of slow light waveguides.

In this paper, we explore the use of a systematic (inverse) method for designing waveguides with minimum propagation loss due to fabrication-related disorder effects. While the disorder-induced losses originate from random variations between the unit-cells of the waveguide, we here assume that those losses will be minimized if the optical intensity overlap with the hole edges is minimized [28]. We thus, phenomenologically, introduce an edge loss to represent the scattering losses, modeled by an imaginary part of the permittivity [22,23,29]. The

propagation losses in the waveguides are directly evaluated by the solution of the complex band structure of the waveguide supercell. We use the MMOS and the density approach to parameterize the periodic supercell and design both fixed- and free-topology waveguides. We demonstrate that the propagation losses in the free-topology waveguides can be significantly reduced while retaining the enlarged GBP. Compared to the fixed-topology loss engineered waveguides, the enhancement of GBP in the free-topology loss engineered waveguides induces an acceptable increase of the propagation losses.

The paper is organized as follows. In Sec. 2, we introduce the governing equations for the complex band structure calculation and corresponding finite element formulation. We then discuss the optimization formulations for waveguide engineering including dispersion engineering and loss engineering based on two different parameterizations of the periodic supercell. In Sec. 3, we investigate the propagation losses of different waveguides and design fixed- and free-topology loss engineered waveguides for different group indices. We summarize our studies in Sec. 4.

2. Optimization problems of slow light waveguides

2.A. Complex band structure calculation

Assuming TE-polarized light in a two dimensional (2D) PhCW, the time harmonic modal profile with time dependence as $\exp(i\omega t)$ obeys the scalar Helmholtz equation

$$\nabla \cdot \left(\varepsilon_r^{-1} \nabla h\right) + (\omega/c)^2 \mu_r h = 0 \tag{1}$$

Here h is the magnetic field in the out-of-plane direction, ε_r is the relative permittivity, ω is the angular wave frequency, c is the speed of light in vacuum and $\mu_r = 1$ is the relative permeability. In order to tackle the losses encountered by slow light in waveguides we employ a phenomenological approach [22] and represent the losses using an effective dissipation by including an imaginary part of the permittivity [7], i.e. $\varepsilon_r = \varepsilon_r' + i\varepsilon_r''$.

In a periodic medium, $\varepsilon_r(\mathbf{r} + \mathbf{a}) = \varepsilon_r(\mathbf{r})$ with $\mathbf{r} = [x_1,\ x_2]$ being the position vector and $\mathbf{a}$ as the periodic vector, the solution of the above equation can be expressed in terms of the wave vector $\mathbf{k}$ following Bloch's theorem, $h(\mathbf{r}) = u(\mathbf{r}) \exp(i\mathbf{k} \cdot \mathbf{r})$. This leads to

$$(\nabla + i\mathbf{k}) \cdot \varepsilon_r^{-1} (\nabla + i\mathbf{k}) u + (\omega/c)^2 \mu_r u = 0 \tag{2}$$

with the periodic boundary conditions, $u(\mathbf{k}, \mathbf{r} + \mathbf{a}) = u(\mathbf{k}, \mathbf{r})$.

Using the finite element method (FEM) discretization procedure, Eq. (2) results in a quadratic eigenvalue equation in the longitudinal wavenumber k,

$$\left(\mathbf{K}_0 - \omega^2 \mathbf{M}\right) \mathbf{u} + \mathbf{K}_1 k \mathbf{u} + \mathbf{K}_2 k^2 \mathbf{u} = 0 \tag{3}$$

The element-wise quantities in Eq. (3) are calculated by

$$\begin{aligned}
\mathbf{K}_0 &= \sum_e \varepsilon_r^{-1} \int_e \left(\frac{\partial \mathbf{N}^T}{\partial x_1} \frac{\partial \mathbf{N}}{\partial x_1} + \frac{\partial \mathbf{N}^T}{\partial x_2} \frac{\partial \mathbf{N}}{\partial x_2} \right) dV \\
\mathbf{M} &= \sum_e \mu_r / c^2 \int_e \left(\mathbf{N}^T \mathbf{N} \right) dV \\
\mathbf{K}_1 &= \sum_e \varepsilon_r^{-1} i \int_e \left(\mathbf{N}^T \frac{\partial \mathbf{N}}{\partial x_2} - \frac{\partial \mathbf{N}^T}{\partial x_2} \mathbf{N} \right) dV \\
\mathbf{K}_2 &= \sum_e \varepsilon_r^{-1} \int_e \left(\mathbf{N}^T \mathbf{N} \right) dV
\end{aligned} \tag{4}$$

with $\mathbf{N}$ being the standard finite element shape functions and the waveguide being directed along x_2.

Eq. (3) can be solved for the eigenfrequencies ω for a given wavenumber k, named as $\omega\,(k)$-formulation, which corresponds to a linear eigenvalue problem for ω^2. Alternatively, this equation can also be solved for wavenumbers k for a given frequency ω, which results in a quadratic eigenvalue problem for k, named as $k\,(\omega)$-formulation. The detailed comparison between these two methods can be found in [30]. Here, we focus on the $k(\omega)$-formulation because of the straightforward way in which it can handle material dispersion and attenuation.

In the $k\,(\omega)$-formulation, Eq. (3) is solved by reformulating the equation into a linear eigenvalue problem in terms of k,

$$\left(\mathbf{K}_l - k \mathbf{M}_l \right) \mathbf{U} = \mathbf{0} \tag{5}$$

with

$$\begin{aligned}
\mathbf{K}_l &= \begin{bmatrix} -\mathbf{K}_1 & -\left(\mathbf{K}_0 - \omega^2 \mathbf{M} \right) \\ \mathbf{I} & \mathbf{0} \end{bmatrix}, \\
\mathbf{M}_l &= \begin{bmatrix} \mathbf{K}_2 & \mathbf{0} \\ \mathbf{0} & \mathbf{I} \end{bmatrix}, \qquad \mathbf{U} = \begin{bmatrix} k\mathbf{u} \\ \mathbf{u} \end{bmatrix}
\end{aligned} \tag{6}$$

The eigenvalues k found from Eq. (5) are complex-valued with the real part of the eigenvalue, $\Re(k)$, being the propagation constant and the imaginary part of the eigenvalue, $\Im(k)$, representing the spatial attenuation of the wave at the given frequency.

Fig. 1 (b) depicts the band structure of a PhCW with triangular patterned air holes of $r = 0.3a$ in Silicon (Si) (seen in Fig. 1 (a)). The left panel shows in solid lines the band structure calculated using the $\omega\,(k)$-formulation while the markers show the calculated band structure based on the $k\,(\omega)$-formulation. The right panel shows the propagation loss of eigenmodes in the $k\,(\omega)$-formulation. Different from the $\omega\,(k)$-formulation, many other modes are detected with the $k\,(\omega)$-formulation. According to the characteristics of the eigenmodes,

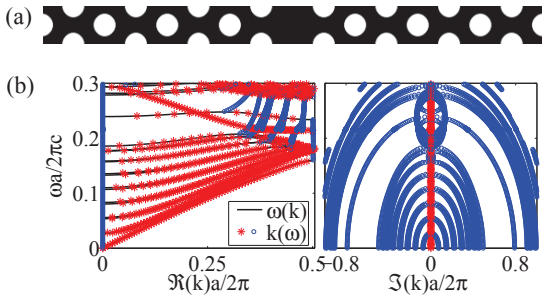

Fig. 1. Band structure calculations. (a) Supercell. (b) Complex band structure, the solid lines represent the band structure calculated using the $\omega\,(k)$-formulation, and the markers represent the band structure calculated using the $k\,(\omega)$-formulation, where the asterisks denote the guided modes and the circles denote the evanescent modes.

they can be classified into two catalogs: guided modes represented by asterisks and evanescent modes in circles connecting the inflection points ($v_g = 0$) in different bands. The evanescent and guided modes can be easily identified according to their propagation loss since the evanescent modes exhibit much larger propagation loss than the guided ones.

2.B. Influence of material loss/gain on the slow light waveguides

The group index of the gap-guided modes is defined as:

$$n_g = \frac{c}{v_g} = \Re\left(\frac{\partial k}{\partial \omega}\right) \tag{7}$$

where n_g is the group index of the guided modes, v_g is the group velocity of the guided modes and $\Re(\cdot)$ indicates the real part of the value.

Numerically, the derivative of eigenvalue k with respect to ω can be calculated by

$$\frac{\partial k}{\partial \omega} = \left(\mathbf{U}_0'\left(\frac{\partial \mathbf{K}_l}{\partial \omega} - k\frac{\partial \mathbf{M}_l}{\partial \omega}\right)\mathbf{U}\right) \tag{8}$$

where the prime denotes the conjugate transpose and $\mathbf{U}_0'$ is the left eigenvector of the eigenvalue problem in Eq. (5) obtained by solving

$$\left(\mathbf{K}_l' - k'\mathbf{M}_l'\right)\mathbf{U}_0 = \mathbf{0} \tag{9}$$

The left eigenvector $\mathbf{U}_0'$ and the right eigenvector $\mathbf{U}$ are normalized with respect to $\mathbf{M}_l$,

$$\mathbf{U}_0'\mathbf{M}_l\mathbf{U} = 1 \tag{10}$$

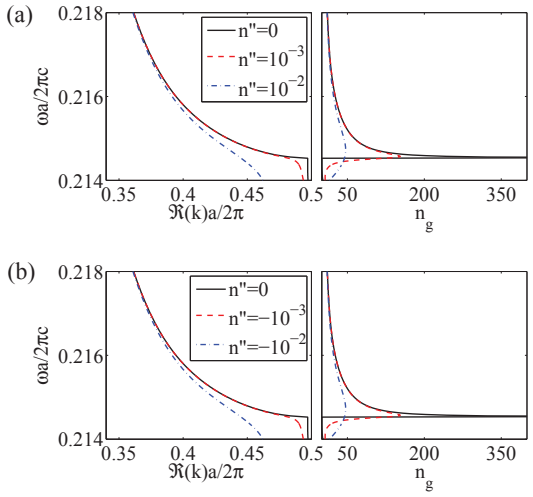

Fig. 2. Influence of material loss/gain on the performance of waveguides. (a) Influence of material loss, the solid line represents the guided band of the lossless waveguide, the dashed line shows the guided band when considering material loss of $n'' = 10^{-3}$ and the dash-dot line shows the guided band of $n'' = 10^{-2}$. (b) Influence of material gain, the solid line shows the guided band of the lossless waveguide, the dashed line represents the guided band of the waveguide with the material gain of $n'' = -10^{-3}$, and the dash-dot line denotes the guided band when considering the material gain of $n'' = -10^{-2}$.

Fig. 2 (a) shows the gap-guided bands and corresponding group indices in the presence of different amounts of material loss ($\varepsilon_{\mathrm{Si}} = (n + in'')^2$). The material loss causes the guided band to deviate from a parabolic shape, as in the lossless case when approaching the band-edge, and hence restricts the achievable group index [7]. Furthermore, a redshift is observed in the gap-guided band due to material loss.

It should be noted that material gain ($n'' < 0$) (shown in Fig. 2 (b)) exhibits the same influence on the achievable group index of waveguides as the corresponding loss, i.e. only the magnitude of n'' matters [8]. This conclusion can be deduced simply from Eq. (3). If we consider the same amount of material gain as material loss, all the matrices in Eq. (3) are conjugate transposes of the ones for material loss since

$$\begin{aligned} \mathbf{K}_0(\bar{\varepsilon}_r) &= \mathbf{K}_0'(\varepsilon_r), \qquad & \mathbf{M}(\bar{\varepsilon}_r) &= \mathbf{M}'(\varepsilon_r), \\ \mathbf{K}_1(\bar{\varepsilon}_r) &= \mathbf{K}_1'(\varepsilon_r), \qquad & \mathbf{K}_2(\bar{\varepsilon}_r) &= \mathbf{K}_2'(\varepsilon_r) \end{aligned} \tag{11}$$

The eigenvalue problem considering material gain is identical to the adjoint eigenvalue

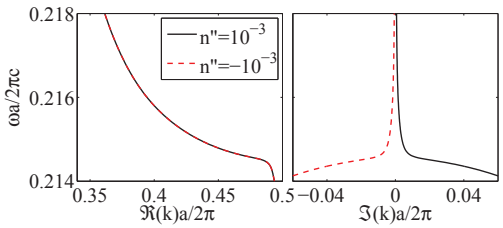

Fig. 3. Characteristics of guided bands considering material loss or gain. The solid lines show the characteristics of the guided band in the waveguide with material loss, and the dashed lines show the characteristics of the guided band in the waveguide with the same amount of material gain.

problem stated in Eq. (9) when considering material loss. Hence the eigen wavenumbers of the guided modes when considering material gain are the conjugates of the corresponding eigen wavenumbers for material loss as shown in Fig 3, and the reduction of the group index thus only depends on the magnitude of the imaginary part. This phenomenon can be explained by the amplitude mismatch in multiply scattered light due to material loss/gain, which results in an interference pattern and causes the group index to stay finite [31].

2.C. Design parameterization

A set of design variables $\mathbf{x}$ is now introduced to control and optimize the geometry of the waveguide.

Using both the MMOS approach and the free-topology density approach, we employ $\mathbf{x}$ indirectly to control element-wise physical densities $\overline{\rho}$ that govern the dielectric constant in each element according to:

$$\varepsilon_e = \varepsilon_1 + \overline{\rho}_e\left(\mathbf{x}\right)\left(\varepsilon_2 - \varepsilon_1\right) \tag{12}$$

Here, ε_e denotes the permittivity of a element, e, $\varepsilon_2 = (3.467)^2$ denotes the permittivity of Si, $\varepsilon_1 = 1$ denotes the permittivity of air.

The physical density of element e is found from a threshold projection based on an intermediate element variable $\widetilde{\rho}_e$ [20, 21]:

$$\overline{\rho}_e = \frac{\tanh\left(\beta\eta\right) + \tanh\left(\beta\left(\widetilde{\rho}_e - \eta\right)\right)}{\tanh\left(\beta\eta\right) + \tanh\left(\beta\left(1 - \eta\right)\right)}. \tag{13}$$

where η is the threshold and β is a regularization parameter. The variable $\widetilde{\rho}_e$ is computed as a filtered value

$$\widetilde{\rho}_e = \frac{\sum_{j\in Ne} w\left(\mathbf{r}_j\right) v_j \rho_j}{\sum_{j\in Ne} w\left(\mathbf{r}_j\right) v_j}. \tag{14}$$

where $\mathbf{r}_j$ and v_j is the centroid and the volume of element j, N_e is the neighborhood of element e within a certain filter radius r specified by

$$N_e = \{j \mid \|\mathbf{r}_j - \mathbf{r}_e\| \leq r\}. \tag{15}$$

$w(\mathbf{r}_j)$ is the weight factor of element j, calculated by $w(\mathbf{r}_j) = r - \|\mathbf{r}_j - \mathbf{r}_e\|$.

With the free-topology density approach the variable ρ_e that appears in Eq. (14) is used directly as the element design variable x_e. However in MMOS, the element-wise quantities are projected using a set of circles, where ρ_e=0 when element e is within circles and ρ_e=1 when e is outside of circles. Here, radii and locations of the circles are used as design variables. The detailed mathematical description of MMOS can be found in [18].

Backscattering induced by manufacturing imperfections has been reported to be the dominant loss mechanism in the slow light regime and has to be taken into account in the design procedure. In order to mimic the loss induced by surface roughness, we introduce an edge-related dissipation based on a normalized element-wise quantity ν_e that represents the interface between dielectric material and air. Based on Eq. (13) we compute ν_e as the normalized derivative of the physical density with respect to the filter density, given by $\nu_e = 1 - (\tanh(\beta(\widetilde{\rho} - \eta)))^2$, and the interface lies where $\nu_e > 0$.

The final element-wise permittivity is now interpolated by modifying Eq. (12) as

$$\varepsilon_e = \varepsilon_1 + \overline{\rho}_e(\varepsilon_2 - \varepsilon_1) + i{\nu_e}^p \varepsilon_0'' \tag{16}$$

with $p = 0.5$ and $\varepsilon_0'' = 0.1$. It must be pointed out here that the value $\varepsilon'' = 0.1$ is chosen arbitrarily to quantify the propagation attenuation in different PhCWs for comparisons and the magnitude of ε_0'' does not affect the optimized designs and the conclusions in the paper.

2.D. Optimization formulations

In addition to loss engineering of the waveguides, we study waveguides that are optimized with respect to dispersion to realize a prescribed dispersion function. Here we focus on dispersion engineered slow light waveguides with a prescribed group index. The optimization problem for the dispersion engineering is described in detail in [20] and can be formulated as

$$\min_{\mathbf{x}} \quad \max_{\omega_i} \quad f(\overline{\rho}, \omega_i) = \left(n_g(\overline{\rho}, \omega_i)/n_g^* - 1\right)^2 \tag{17}$$

here $\omega_i \in [\omega_1,\ \omega_2]$ is the target frequency with $[\omega_1,\ \omega_2]$ being the design frequency range, $n_g(\overline{\rho}, \omega_i)$ is the actual group index, n_g^* is the prescribed group index, and $\mathbf{x}$ denotes the set of the design variables considered.

Previous studies have illustrated that the propagation losses of slow light modes can be engineered through changing the field intensity profiles [25,28]. In the $k(\omega)$-formulation, the

propagation losses are represented by the imaginary part of the wavenumber, hence the $k(\omega)$-formulation enables loss engineering of slow light waveguides by minimizing either the average propagation loss of the designed modes or by minimizing the maximal propagation loss of the designed modes. The first approach emphasizes the average behavior in the designed frequency range while the latter one with the emphasis on the largest propagation loss within the designed frequency range. In the present work we employ the first variant and formulate the optimization problem as:

$$\begin{aligned} \min_{\mathbf{x}} \quad f(\overline{\rho}) &= \sum_{\omega_i} \left(\Im\left(k\left(\overline{\rho}, \omega_i\right)\right)\right) \\ s.t. \quad & \left(n_g\left(\overline{\rho}, \omega_i\right)/n_g^* - 1\right)^2 < e_r^2 \end{aligned} \tag{18}$$

Here, $0 \leq e_r \leq 1$ is the relative group index error, indicating the allowed GVD.

For both optimization problems, the presence of multiple guided modes at a given frequency may result in intermodal scattering [11, 20]. In order to avoid this, an additional band separation constraint is added to the optimization problems. It is problematic to classify bands in the order of increasing frequency with the $k(\omega)$-formulation and therefore the band separation constraints are implemented using the $\omega(k)$-formulation:

$$\Re\left(\omega_{n-1}\left(k_{ii}\right)\right) \leq a_1 \ \min\left(\omega_i\right), \quad \Re\left(\omega_{n+1}\left(k_{ii}\right)\right) \geq a_2 \ \max\left(\omega_i\right) \tag{19}$$

here k_{ii} is the specified wavenumber in the range $[0, \ \pi/a]$, n is the order of the designed band, and a_1 and a_2 are prescribed numbers defining how far the designed band is separated from the other bands. However, this implies that in the case of loss engineering both an $k(\omega)$ and an $\omega(k)$ eigenvalue problem need to be solved.

2.E. Sensitivity analysis

In order to apply gradient based optimizations, we need to compute the sensitivities of the group index $n_g\left(\overline{\rho}, \omega_i\right)$ and of the loss $\Im\left(k\left(\overline{\rho}, \omega_i\right)\right)$.

Although we can use adjoint sensitivity analysis to compute the sensitivity of n_g directly, this will be quite costly. Instead we compute the group index by the finite difference method given by

$$n_g = \frac{\Delta k}{\Delta \omega} = \frac{\Re(k(\omega_i)) - \Re(k(\omega))}{\omega_i - \omega} \tag{20}$$

which is accurate when ω is sufficiently close to ω_i. The corresponding sensitivity of the group index is then obtained using Eq. (8):

$$\frac{\partial n_g}{\partial \overline{\rho}_e} = \left(\Re\left(\frac{\partial k(\omega_i)}{\partial \overline{\rho}_e}\right) - \Re\left(\frac{\partial k(\omega)}{\partial \overline{\rho}_e}\right)\right) / \left(\omega_i - \omega\right) \tag{21}$$

The sensitivity of the propagation losses $\Im(k)$ with respect to the physical density $\overline{\rho}_e$ is calculated by:

$$\frac{\partial \Im(k)}{\partial \overline{\rho}_e} = \Im\left(\frac{\partial k}{\partial \overline{\rho}_e}\right) \tag{22}$$

The sensitivity of eigenvalues from the $\omega(k)$-formulation is calculated following the same procedure as in Eq. (8) when the eigenvalue is distinct, and the sensitivity of multiple eigenvalues is derived following [32].

Finally, the sensitivity of objective and constraints with respect to the design variable x_e is obtained using the chain rule [33]:

$$\frac{\partial f}{\partial x_e} = \frac{\partial f}{\partial \overline{\rho}_e}\frac{\partial \overline{\rho}_e}{\partial x_e} \tag{23}$$

Here $\partial \overline{\rho}_e / \partial x_e$ can be easily derived in the two different parameterizations.

Based on sensitivity analysis, the design is iteratively updated using a gradient-based algorithm, the Globally Convergent version of the Method of Moving Asymptotes (GCMMA) from Svanberg [34]. A detailed account of optimization procedure can be found in [21]. In the optimization procedure, the regularization parameter β is fixed and set to $\beta = 16$.

3. Results

In this section, we first investigate the loss mechanism by studying the propagation losses in fixed-topology waveguides and then evaluate the feasibility of loss engineering in the waveguides, comparing the cases of fixed- and free-topology using two parameterizations. Furthermore, we design free-topology loss engineered slow light waveguides with enlarged GBP for different group indices and compare them with corresponding fixed-topology loss engineered waveguides.

3.A. Propagation losses of fixed-topology waveguides

We first investigate the propagation loss in several fixed-topology dispersion engineered waveguides designed for $n_g^* = 50$ when subject to the edge-related dissipation discussed above. We consider designs obtained using dispersion engineering with an $\omega(k)$-formulation in absence of dissipation and with a fixed group index $n_g^* = 50$ [18]. The design variables are radii, lateral (normal to the waveguide direction) and longitudinal (along the waveguide direction) locations of the first two rows of air holes using MMOS, with an initial design as in Fig. 1. In this paper, we focus on symmetrical waveguides, where the symmetry along the waveguide direction is enforced by setting same design variables in the symmetrical locations in the optimization procedure. However, asymmetrical waveguides can also be engineered to reduce GVD of slow light [35, 36].

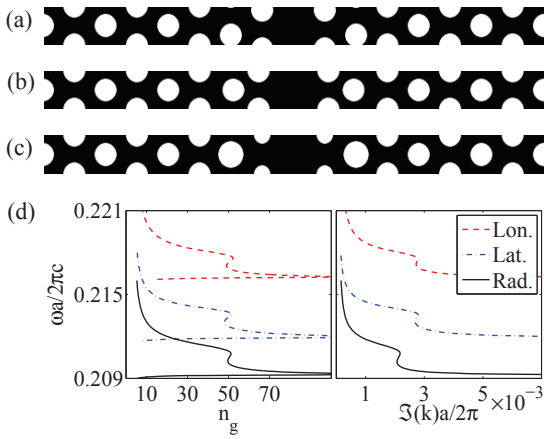

Fig. 4. Fixed-topology dispersion engineered waveguides for $n_g^* = 50$. (a) Longitudinal location tuned waveguide. (b) Lateral location tuned waveguide. (c) Radius tuned waveguide. (d) Performance of different waveguides. Left panel: Group index versus frequency. Right panel: Propagation loss versus frequency. The dashed lines represent the performance of the longitudinal location tuned waveguide, the dash-dot lines represent the performance of the lateral location tuned waveguide and the solid lines represent the performance of the radius tuned waveguide.

Fig. 4 (a) – (c) shows the designs obtained from radius, lateral and longitudinal location tuning. The performance of the waveguides is listed in Fig. 4 (d), in terms of group index and propagation loss. For each waveguide, the propagation loss variation versus frequency coincides with the group index variation versus frequency. Thus, a high group index seems to be intrinsically linked to high propagation losses.

We employ the group index bandwidth product (GBP) and the average propagation loss ($\langle \Im(k) \rangle$) as figures of merit to evaluate the performance of different waveguides. The GBP is defined by:

$$GBP = \Delta\omega \, \langle n_g \rangle / \omega_0 \tag{24}$$

where $\Delta\omega$ is the frequency range where the GVD is negligible, $\langle n_g \rangle$ and ω_0 are the corresponding average group index and the center frequency. In practice, a relative group index error of $\pm 10\%$ is utilized to indicate the negligible GVD region.

The detailed performances of the waveguides are summarized in Table 1. Under $\pm 10\%$ criterion, all the waveguides achieve a GBP of 0.29 or above. The average propagation losses differ for the different waveguides and the radius tuned waveguide exhibits the lowest average

Table 1. Performance comparison of fixed-topology waveguides. The first row represents the longitudinal (along the waveguide direction) location tuned waveguide, the second row represents the lateral (normal to the waveguide direction) location tuned waveguide, and the third row represents the radius tuned waveguide.

Des.	$\omega_0 a/2\pi c$	$\langle n_g \rangle$	GBP	$\langle \Im(k) \rangle\, a/2\pi(10^{-3})$
Lon.	0.2172	50.54	0.29	2.78
Lat.	0.2131	49.77	0.31	2.75
Rad.	0.2104	50.50	0.33	2.12

propagation loss among them.

In order to further study the loss mechanism, we employ the concepts of energy density $\mathbf{I}_s$ and dissipative energy density $\mathbf{I}_d$ [37], given by:

$$\mathbf{I}_s = \frac{1}{2}\varepsilon_0 \varepsilon_r' \left|\mathbf{E}\right|^2, \qquad \mathbf{I}_d = \frac{1}{2}\varepsilon_0 \varepsilon_r'' \left|\mathbf{E}\right|^2 \tag{25}$$

here $\mathbf{E}$ is the electric field calculated by $\mathbf{E} = 1/\left(i\omega\varepsilon_0\varepsilon_r\right)\nabla \times \mathbf{H}$ with $\mathbf{H} = [0\ 0\ h]$, and ε_0 is the permittivity in vacuum.

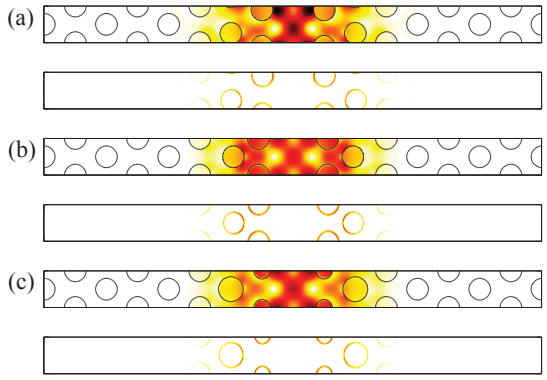

Fig. 5. Energy density and dissipative energy density of slow light modes with $n_g \approx 50$ in fixed-topology dispersion engineered waveguides. (a) Longitudinal location tuned waveguide. Top: Energy density. Bottom: Dissipative energy density. (b) Lateral location tuned waveguide. (c) Radius tuned waveguide.

Fig. 5 shows the energy density, $\mathbf{I}_s$, and dissipative energy density, $\mathbf{I}_d$, of slow light modes

with $n_g \approx 50$ in different waveguides. Compared to the radius tuned waveguide, the longitudinal location tuned waveguide has a smaller waveguide core, and hence exhibits a stronger field intensity at the waveguide core, which results in larger propagation losses on the interface of the first row of air holes. Despite a similar size of waveguide core as the radius tuned waveguide, stronger field intensity originating from the second row of air holes can be observed in the lateral location tuned waveguide, hence causing more propagation losses on the second row of air holes. Furthermore, the radius tuned waveguide has the shortest interface among all the designs, which also results in a smaller fraction of field available for scattering at imperfections. The detailed studies on the energy density and dissipative energy density illustrate that the smallest propagation loss is found with the smallest fraction of field intensity involved in scattering at imperfections. This is in agreement with recent theoretical and experimental studies [25, 28] and supports our phenomenological representation of disorder induced scattering losses by the edge-related dissipation.

3.B. Loss engineered slow light waveguides

From the conducted studies it is apparent that it is possible to manipulate the loss while maintaining high values for n_g and GBP, and in this section we study the feasibility of loss engineering slow light waveguides by minimizing the average propagation losses of the designed slow light modes using the optimization formulation presented in Eq. (18). The initial waveguide is the radius tuned waveguide with $n_g^* = 50$. The design frequency range is set to be $\omega_i \in [0.2097,\ 0.2112]\, 2\pi c/a$ with 16 design frequencies. In order to ensure that the average group index of the optimized waveguide is equal to or larger than n_g^* in the design frequency range, a constraint on the average group index is implemented as $\langle n_g \rangle \geq n_g^*$.

Fig. 6. Initial design and the design domain. The gray dashed rectangle indicates the design domain with a symmetry along the waveguide direction.

The free-topology loss engineered waveguides are obtained using the density approach with the design domain being the first three and a half rows of air holes adjacent to the waveguide core, shown in Fig. 6. The fixed-topology loss engineered waveguides are obtained using MMOS with the design variables as locations and radii of the first two rows of air holes.

The free-topology loss engineered waveguides for relative group index errors of $e_r = 10\%$ and $e_r = 5\%$ are shown in Fig. 7 (a) and (b), respectively. Fig. 7 (c) depicts the fixed-topology loss engineered waveguide for $e_r = 5\%$. The performances of the different waveguides are

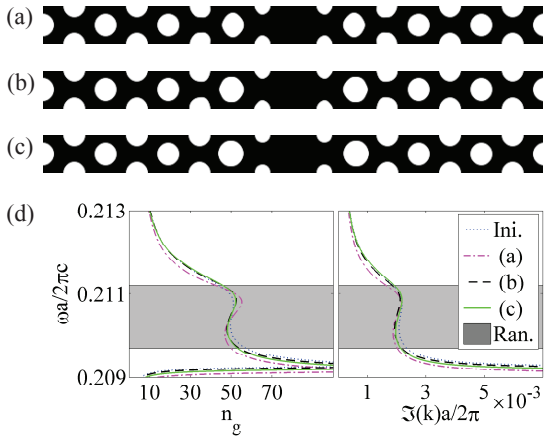

Fig. 7. Loss engineered slow light waveguides for $n_g^* = 50$. (a) Free-topology loss engineered waveguide for $e_r = 10\%$. (b) Free-topology loss engineered waveguide with $e_r = 5\%$. (c) Fixed-topology loss engineered waveguide for $e_r = 5\%$. (d) Performances of different waveguides. The dotted lines show the performance of the initial waveguide, the dash-dot lines show the performance of the free-topology loss engineered waveguide for $e_r = 10\%$, the dashed lines show the performance of the free-topology loss engineered waveguide $e_r = 5\%$, the solid lines show the performances of the fixed-topology loss engineered waveguides, and the gray regions indicate the design range.

depicted in Fig. 7 (d). As expected, the group index variation in the free-topology loss engineered waveguide of $e_r = 10\%$ is much larger than the one in the other waveguides including the initial design. Under the same relative group index error of $e_r = 5\%$, the free- and fixed-topology loss engineered waveguides deviate slightly from each other and achieve equivalent performances in terms of group index variation and propagation losses. Compared to the initial design shown in Fig. 4 (c), a noticable improvement of the propagation losses can be observed in both waveguides.

The detailed performances of different waveguides are summarized in Table 2. Compared with the initial waveguide, the loss engineered designs achieve observable lower average propagation losses. For the same group index, the free-topology loss engineered waveguide achieves a slightly smaller propagation loss than the fixed-topology loss engineered waveguide and the average propagation loss can be further reduced by allowing larger GVD. The energy density and dissipative energy density of slow light modes of $n_g \approx 50$ in different waveguides (shown in Fig. 8) illustrate that the reduction of the propagation loss is attributed to the

Table 2. Performance comparison of loss engineered waveguides with $n_g^* = 50$. The first row shows the performance of the free-topology loss engineered waveguide of $e_r = 10\%$, the second row shows the performance of the free-topology loss engineered waveguide of $e_r = 5\%$, and the third row shows the performance of the fixed-topology loss engineered waveguide of $e_r = 5\%$.

Des.	$\omega_0 a/2\pi c$	$\langle n_g \rangle$	GBP	$\langle \Im(k) \rangle\, a/2\pi(10^{-3})$
Fre. Top. 10%	0.2102	49.95	0.37	1.98
Fre. Top. 5%	0.2103	50.06	0.35	2.01
Fix. Top. 5%	0.2103	50.16	0.36	2.05

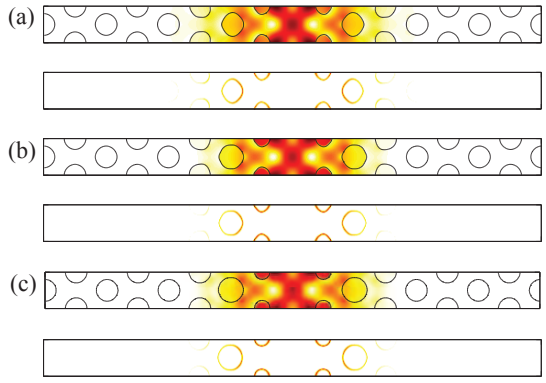

Fig. 8. Energy density and dissipative energy density of slow light modes with $n_g \approx 50$ in the optimized waveguides. (a) Free-topology loss engineered waveguide for $e_r = 10\%$. (b) Free-topology loss engineered waveguide for $e_r = 5\%$. (c) Fixed-topology loss engineered waveguide for $e_r = 5\%$.

smaller field intensity at the interface for the free-topology loss engineered waveguide with $e_r = 10\%$ and the reduction of the propagation loss in the loss engineered waveguides for $e_r = 5\%$ is mainly attributed to a smaller interface between air and Si in the first row. However, due to the fact that the modal profiles are dominated by the group index, i.e. the higher group index, the larger modal profile, the improvement of the propagation losses is restricted.

3.C. Loss engineered slow light waveguides with enlarged GBP

The capacity of slow light waveguides, i.e. GBP, is crucial for the applications. Previous studies have illustrated free-topology dispersion engineered waveguides can achieve significantly larger GBP compared with fixed-topology dispersion engineered waveguides [18]. In this section, we design free-topology loss engineered waveguides with an enlarged GBP. The optimization procedure is accomplished in two steps. The dispersion engineering is firstly performed to enhance the GBP using the optimization formulation presented in Eq. (17). Using the dispersion engineered slow light waveguide as an initial design, we further perform loss engineering to reduce the average propagation loss of the designed slow light modes under a relative group index error of $e_r = 5\%$.

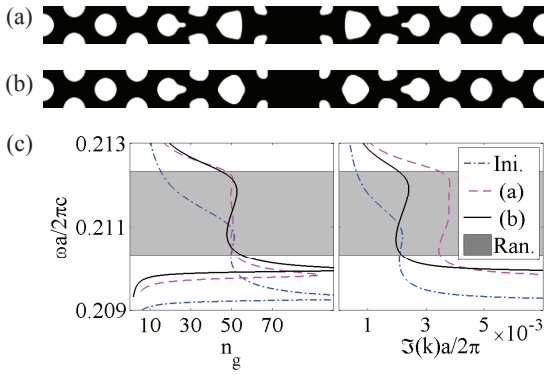

Fig. 9. Free-topology optimized slow light waveguides with an enlarged GBP for n_g^*=50. (a) Free-topology dispersion engineered waveguide. (b) Free-topology loss engineered waveguide. (c) Group index and loss of different waveguides. The dash-dot lines represent the performance of the initial design, the dashed lines represent the performances of the dispersion engineered waveguide, the solid lines represent the performance of the loss engineered waveguides, and the gray regions indicate the design range.

As the first example, we aim at designing a slow light waveguide for $n_g^* = 50$ in the frequency range of $\omega_i \in [0.2103,\ 0.2123]\, 2\pi c/a$. The frequency range is chosen to ensure a GBP of 0.45 for the optimized waveguides. The initial design is chosen as the radius tuned waveguide shown in Fig. 6. The dispersion engineered waveguide and loss engineered waveguide are shown in Fig. 9 (a) and (b), respectively. Fig. 9 (c) depicts the performance of the optimized waveguides. Compared with the radius tuned waveguide, the free-topology optimized waveguides achieve a much larger GBP. However, the dispersion engineered waveguide encounters significantly higher propagation losses due to the sharp features in the waveguide

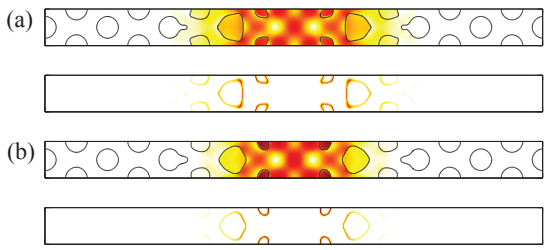

Fig. 10. Energy density and dissipative energy density of slow light modes with $n_g \approx 50$ in different waveguides. (a) Dispersion engineered waveguide of $n_g^* = 50$. (b) Loss engineered waveguide of $n_g^* = 50$.

shown in Fig. 9 (a) and the bigger modal size shown in Fig. 10 (a). Thus, a significant dissipation energy density can be observed on the third rows of air holes in the dispersion engineered design. In contrast to the dispersion engineered slow light waveguide, the loss engineered slow light waveguide has a smooth interface between air and dielectric material and the corresponding modal size is relatively small. Hence the propagation losses have been significantly reduced in the loss engineered waveguide and are equivalent to the ones in the radius tuned slow light waveguide (see Fig. 9 (c)).

Table 3. Performance comparison of the optimized waveguides with $n_g^* = 50$ and enlarged GBP. The first row shows the performance of the dispersion engineered waveguide, and the second row depicts the performance of the loss engineered waveguide.

Des.	$\omega_0 a/2\pi c$	$\langle n_g \rangle$	GBP	$\langle \Im(k) \rangle\, a/2\pi$ (10^{-3})
Dis.	0.2111	50.27	0.50	3.62
Los.	0.2112	49.82	0.47	2.13

The characteristics of the dispersion engineered waveguide and loss engineered waveguide are summarized in Table 3. The GPB of the waveguides has been improved by a factor of 1.42 or above compared to the initial design. Furthermore, through loss engineering, the free-topology engineered slow light waveguide can achieve an equally good performance in terms of propagation losses with the radius tuned waveguide. Compared with the loss engineered waveguides presented in the previous subsection, the GBP of the slow light waveguides has been improved by a factor of 1.27 with an acceptable sacrifice of the propagation losses.

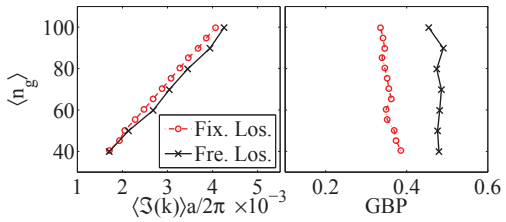

Fig. 11. Comparison between fixed- and free-topology loss engineered waveguides for different group indices. Left panel: Average group index versus average propagation loss. Right panel: Average group index versus GBP. The red dash-dot lines represent the performance of the fixed-topology loss engineered waveguides with circles indicating different designs considered. The black solid lines represent the performance of the loss engineered slow light waveguides with crosses indicating different design considered.

In order to further compare the fixed-topology loss engineered waveguides and free-topology loss engineered waveguides, we design loss engineered waveguides for different group indices in the interval of $n_g^* \in [40,\ 100]$. The same initial design, i.e. that of Fig. 6, is chosen for all the target group indices. The target frequency ranges of free-topology loss engineered waveguides are chosen to ensure a GBP of 0.45 with a starting frequency of $\omega_1 = 0.2103\ 2\pi c/a$, and the target frequency ranges of fixed-topology loss engineered waveguides are chosen to ensure a GBP of 0.33 with the same starting frequency.

Fig. 11 shows the characteristics of the fixed-topology loss engineered waveguides and the free-topology loss engineered waveguides in terms of average propagation losses and GBP. All the fixed-topology loss engineered waveguides achieve a GBP of 0.33 or above, and all the free-topology loss engineered waveguides can achieve a GBP of 0.45 or above. For the same target group index, the free-topology loss engineered waveguide displays higher average propagation loss than the fixed-topology loss engineered waveguides. Hence the enhancement of GBP is at the cost of the average propagation loss. It is noted that the average propagation loss increases with the target group index in both cases, which indicates at the light-slow down in itself is a dominant factor in determining the resulting losses.

Fig. 12 depicts the characteristics of the fixed- and free-topology loss engineered waveguides for $n_g^* = 90$. It is seen that at low frequencies, the slow light modes in the free-topology loss engineered waveguide exhibit equivalent propagation losses as the ones in the fixed-topology loss engineered waveguide, and at high frequencies, the slow light modes exhibit much higher propagation losses than encountered in the fixed-topology loss engineered waveguides. Hence the large average propagation loss in the free-topology loss engineered waveguide is attributed

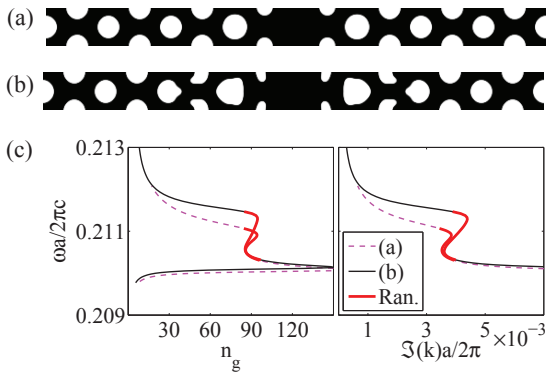

Fig. 12. Loss engineered waveguides for $n_g^* = 90$. (a) Fixed-topology loss engineered waveguide. (b) Free-topology loss engineered waveguide. (c) Performances of different waveguides. The dashed lines represent the performances of the fixed-topology loss engineered waveguide, the solid lines represent the free-topology loss engineered waveguides, and the red lines represent the design ranges.

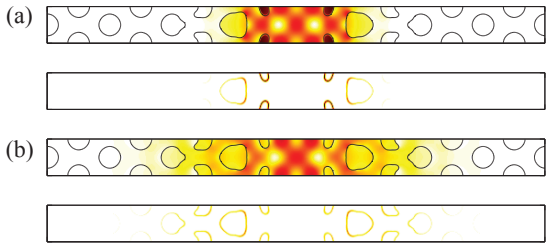

Fig. 13. Energy density and dissipative energy density of slow light modes with $n_g \approx 94$ at different frequencies in the free-topology loss engineered waveguide for $n_g^* = 90$. (a) $\omega a/2\pi = 0.21034$. (b) $\omega a/2\pi = 0.21123$.

to the large propagation losses of slow light modes with high frequencies. The energy densities of two design slow light modes with $n_g \approx 94$ in the free-topology loss engineered waveguide (seen in Fig. 13) reveal that the slow light mode with high frequency has much larger modal size compared to the other slow light mode. This leads to a significant increase in the propagation loss.

In order to further evaluate the performance of the loss engineered waveguides, we calculate the transmission (T) of the engineered waveguides of $n_g^* = 90$ in the presence of the

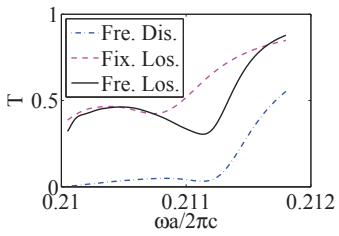

Fig. 14. Transmission spectra of the loss engineered waveguides of 20 periods in the presence of the edge-related loss. The dash-dot line represents the transmission spectrum of the free-topology dispersion engineered waveguide, the dashed line represents the one of the fixed-topology loss engineered waveguide and the solid line represent the one of the free-topology loss engineered waveguide.

edge-related loss, consisting of 20 periods of supercells. The transmission is found from the time-averaged Poynting vector, i.e. the component in the waveguide direction [38]. The transmission is normalized with respect to the transmission of the corresponding ideal waveguides. The normalized transmission spectra of the free-topology dispersion engineered waveguide, the fixed- and the free-topology loss engineered waveguides are shown in Fig. 14. As illustrated by the complex band structure, the transmission has been significantly enhanced through the loss engineering. A significant drop can be observed at high frequency in the transmission spectrum of the free-topology loss engineered waveguide. This observation supports the propagation losses evaluated from the $k\,(\omega)$-formulation.

4. Conclusions

In this study, systematic loss engineering has been performed to reduce the propagation losses of slow light waveguides. In order to mimic scattering losses induced by manufacturing imperfections, we have utilized the concept of the effective dissipation, where the scattering losses have been represented by an edge-related dissipation. The propagation losses of slow light modes have been evaluated by the imaginary part of eigenvalues in the complex band structure calculation and was supported by transmission computations for a finite waveguide.

Numerical studies on the propagation losses of circular-hole based waveguides obtained by radius and location tuning have shown that loss engineering can be realized by reducing the fraction of field available for scattering. Two parameterizations have been utilized to describe the supercell, i.e. the material mask overlay strategy for the fixed-topology waveguides and the density approach for the free-topology waveguides. By minimizing the average propaga-

tion losses, the loss engineered waveguides from these two parameterizations have achieved smaller propagation losses while maintaining equivalent performance in terms of GVD and GBP as the initial design. However, the improvement of the propagation losses is inherently restricted due to the limited freedom on the manipulation of the modal profiles for a given group index.

Loss engineered slow light waveguides with enlarged GPB have been designed in two steps. Firstly the dispersion engineering has been performed to enhance the GBP and then the loss engineering has been employed to reduce the propagation losses of the dispersion engineered waveguides caused by the sharp features in the design or/and the large modal size. Numerical examples for $n_g^* = 50$ have illustrated that the propagation losses can be significantly reduced in the free-topology engineered waveguides by the loss engineering. Detailed comparisons between fixed- and free-topology loss engineered waveguides for different target group indices, have illustrated that the enhancement of GBP in the free-topology loss engineered waveguides have been realized at the expense of propagation losses. Further studies on the free-topology loss engineered waveguide have revealed that the larger propagation losses in the free-topology loss engineered waveguides are due to the large propagation losses of slow light modes with high frequencies. The proper trade-off between propagation losses and GBP will depend on the specific application.

The presented approach can be extended in a straightforward way to the loss engineering of 3D waveguides, where 2D loss engineered waveguides will be good starting points. The out-of-plane radiation can be taken into account in the 3D loss engineered waveguides by using a proper boundary condition in the additional direction. However, increased dimensionality will increase the computing time significantly and introduce challenges regarding efficient large scale eigenvalue solvers.

Acknowledgments

This work was financially supported by Villum Fonden (via the NATEC Centre of Excellence) and by the Danish Center for Scientific Computing (DCSC). The authors would like to thank Vincent Laude for helpful discussions on the formulation of the $k(\omega)$ eigenvalue problem and fruitful discussions with members of the TopOpt-group(www.topopt.dtu.dk) and Department of Photonics Engineering in DTU are gratefully acknowledged.

References

1. T. F. Krauss, "Why do we need slow light?" Nature Photon. **2**, 448–450 (2008).
2. T. Baba, "Slow light in photonic crystals," Nature Photon. **2**, 465–473 (2008).
3. D. M. Beggs, T. P. White, L. O'Faolain, and T. F. Krauss, "Ultracompact and low-power optical switch based on silicon photonic crystals," Opt. Lett. **33**, 147–149 (2008).

4. J. E. McMillan, X. D. Yang, N. C. Panoiu, R. M. Osgood, and C. W. Wong, "Enhanced stimulated raman scattering in slow-light photonic crystal waveguides," Opt. Lett. **31**, 1235–1237 (2006).
5. B. Corcoran, C. Monat, C. Grillet, D. J. Moss, B. J. Eggleton, T. P. White, L. O'Faolain, and T. F. Krauss, "Green light emission in silicon through slow-light enhanced third-harmonic generation in photonic-crystal waveguides," Nature Photon. **3**, 206–210 (2009).
6. M. Heuck, S. Blaaberg, and J. Mork, "Theory of passively mode-locked photonic crystal semiconductor lasers," Opt. Express **18**, 18003–18014 (2010).
7. J. G. Pedersen, S. S. Xiao, and N. A. Mortensen, "Limits of slow light in photonic crystals," Phys. Rev. B **78**, 153101 (2008).
8. J. Grgić, J. R. Ott, F. Wang, O. Sigmund, A.-P. Jauho, J. Mørk, and N. A. Mortensen, "Fundamental limitations to gain enhancement in periodic media and waveguides," Phys. Rev. Lett. **108**, 183903 (2012).
9. R. J. P. Engelen, Y. Sugimoto, Y. Watanabe, J. P. Korterik, N. Ikeda, N. F. van Hulst, K. Asakawa, and L. Kuipers, "The effect of higher-order dispersion on slow light propagation in photonic crystal waveguides," Opt. Express **14**, 1658–1672 (2006).
10. S. Hughes, L. Ramunno, J. F. Young, and J. E. Sipe, "Extrinsic optical scattering loss in photonic crystal waveguides: Role of fabrication disorder and photon group velocity," Phys. Rev. Lett. **94**, 033903 (2005).
11. E. Kuramochi, M. Notomi, S. Hughes, A. Shinya, T. Watanabe, and L. Ramunno, "Disorder-induced scattering loss of line-defect waveguides in photonic crystal slabs," Phys. Rev. B **72**, 161318 (2005).
12. D. Mori and T. Baba, "Dispersion-controlled optical group delay device by chirped photonic crystal waveguides," Appl. Phys. Lett. **85**, 1101–1103 (2004).
13. D. Mori, S. Kubo, H. Sasaki, and T. Baba, "Experimental demonstration of wideband dispersion-compensated slow light by a chirped photonic crystal directional coupler," Opt. Express **15**, 5264–5270 (2007).
14. L. H. Frandsen, A. V. Lavrinenko, J. Fage-Pedersen, and P. I. Borel, "Photonic crystal waveguides with semi-slow light and tailored dispersion properties," Opt. Express **14**, 9444–9450 (2006).
15. J. Li, T. P. White, L. O'Faolain, A. Gomez-Iglesias, and T. F. Krauss, "Systematic design of flat band slow light in photonic crystal waveguides," Opt. Express **16**, 6227–6232 (2008).
16. S. A. Schulz, L. O'Faolain, D. M. Beggs, T. P. White, A. Melloni, and T. F. Krauss, "Dispersion engineered slow light in photonic crystals: a comparison," J. Opt.**12** (2010).
17. T. Kawasaki, D. Mori, and T. Baba, "Experimental observation of slow light in photonic crystal coupled waveguides," Opt. Express **15**, 10274–10281 (2007).

18. F. Wang, J. S. Jensen, and O. Sigmund, "High-performance slow light photonic crystal waveguides with topology optimized or circular-hole based material layouts," Phot. Nano. Fund. Appl. http://dx.doi.org/10.1016/j.photonics.2012.04.004 (2012).
19. R. Stainko and O. Sigmund, "Tailoring dispersion properties of photonic crystal waveguides by topology optimization," Waves In Random and Complex Media **17**, 477–489 (2007).
20. F. Wang, J. S. Jensen, and O. Sigmund, "Robust topology optimization of photonic crystal waveguides with tailored dispersion properties," J. Opt. Soc. Am. B **28**, 387–397 (2011).
21. F. Wang, B. S. Lazarov, and O. Sigmund, "On projection methods, convergence and robust formulations in topology optimization," Struct. Multidisc. Optim. **43**, 767–784 (2011).
22. H. Benisty, D. Labilloy, C. Weisbuch, C. J. M. Smith, T. F. Krauss, D. Cassagne, A. Beraud, and C. Jouanin, "Radiation losses of waveguide-based two-dimensional photonic crystals: Positive role of the substrate," Appl. Phys. Lett. **76**, 532–534 (2000).
23. R. Ferrini, R. Houdre, H. Benisty, M. Qiu, and J. Moosburger, "Radiation losses in planar photonic crystals: two-dimensional representation of hole depth and shape by an imaginary dielectric constant," J. Opt. Soc. Am. B **20**, 469–478 (2003).
24. M. Patterson, S. Hughes, S. Schulz, D. M. Beggs, T. P. White, L. O'Faolain, and T. F. Krauss, "Disorder-induced incoherent scattering losses in photonic crystal waveguides: Bloch mode reshaping, multiple scattering, and breakdown of the beer-lambert law," Phys. Rev. B **80**, 195305 (2009).
25. L. O'Faolain, S. A. Schulz, D. M. Beggs, T. P. White, M. Spasenovic, L. Kuipers, F. Morichetti, A. Melloni, S. Mazoyer, J. P. Hugonin, P. Lalanne, and T. F. Krauss, "Loss engineered slow light waveguides," Opt. Express **18**, 27627–27638 (2010).
26. L. C. Andreani and D. Gerace, "Light-matter interaction in photonic crystal slabs," Phys. Status Solidi B **244**, 3528–3539 (2007).
27. M. Patterson and S. Hughes, "Theory of disorder-induced coherent scattering and light localization in slow-light photonic crystal waveguides," J. Opt. **12**, 104013 (2010).
28. A. Petrov, M. Krause, and M. Eich, "Backscattering and disorder limits in slow light photonic crystal waveguides," Opt. Express **17**, 8676–8684 (2009).
29. R. Ferrini, D. Leuenberger, R. Houdre, H. Benisty, M. Kamp, and A. Forchel, "Disorder-induced losses in planar photonic crystals," Opt. Lett. **31**, 1426–1428 (2006).
30. K. C. Huang, E. Lidorikis, X. Y. Jiang, J. D. Joannopoulos, K. A. Nelson, P. Bienstman, and S. H. Fan, "Nature of lossy bloch states in polaritonic photonic crystals," Phys. Rev. B **69**, 195111 (2004).
31. T. F. Krauss, "Slow light in photonic crystal waveguides," J. Phys. D **40**, 2666–2670

(2007).

32. A. P. Seyranian, E. Lund, and N. Olhoff, "Multiple eigenvalues in structural optimization problems," Struct. Optim. **8**, 207227 (1994).
33. O. Sigmund, "Morphology-based black and white filters for topology optimization," Struct. Multidisc. Optim. **33**, 401–424 (2007).
34. K. Svanberg, "A class of globally convergent optimization methods based on conservative convex separable approximations," SIAM J. Optim. **12**, 555–573 (2001).
35. J. Ma and C. Jiang, "Demonstration of ultraslow modes in asymmetric line-defect photonic crystal waveguides," IEEE Photon. Tech. Lett. **20**, 1237–1239 (2008).
36. P. Colman, S. Combri, G. Lehoucq, and A. De Rossi, "Control of dispersion in photonic crystal waveguides using group symmetry theory," Opt. Express **20**, 13108–13114 (2012).
37. F. D. Nunes, T. C. Vasconcelos, M. Bezerra, and J. Weiner, "Electromagnetic energy density in dispersive and dissipative media," J. Opt. Soc. Am. B **28**, 1544–1552 (2011).
38. J. S. Jensen and O. Sigmund, "Topology optimization of photonic crystal structures: a high-bandwidth low-loss T-junction waveguide," J. Opt. Soc. Am. B **22**, 1191–1198 (2005).

Publication [P6]

Systematic design of plasmonic slow light waveguides with tailored dispersion

Systematic design of plasmonic slow light waveguides with tailored dispersion

Fengwen Wang,[1,*] **Jakob S. Jensen,**[1] **Boyan S. Lazarov,**[1]
N. Asger Mortensen,[2] **and Ole Sigmund**[1]

[1] *Department of Mechanical Engineering, Technical University of Denmark, Nils Koppels Allé, 2800, Kgs. Lyngby, Denmark*

[2] *Department of Photonics Engineering, Technical University of Denmark, Ørsteds Plads, 2800, Kgs. Lyngby, Denmark*

[*] *fwan@mek.dtu.dk*

Abstract: This paper develops a methodology to systematically design periodic plasmonic waveguides with tailored dispersion, and further studies the loss compensation of plasmonic slow light propagation by incorporating gain media. The dispersion relations of plasmonic waveguides are obtained using complex band structure calculations, where the propagation loss is evaluated by complex eigen wavenumbers. Through parameterizing plasmonic waveguides using a set of superellipses, an optimization formulation is presented to alleviate group velocity dispersion of plasmonic slow light propagation. Numerical examples illustrate that the dispersionless slow light plasmonic waveguides are achieved using the presented approach. Further study reveals that the propagation loss of the designed slow light modes can be significantly suppressed or canceled by integrating gain media while retaining negligible group velocity dispersion.

References and links

1. W. L. Barnes, A. Dereux, and T. W. Ebbesen, "Surface plasmon subwavelength optics," Nature **424**, 824–830 (2003).
2. D. K. Gramotnev and S. I. Bozhevolnyi, "Plasmonics beyond the diffraction limit," Nature Photonics **4**, 83–91 (2010).
3. J. N. Anker, W. P. Hall, O. Lyandres, N. C. Shah, J. Zhao, and R. P. Van Duyne, "Biosensing with plasmonic nanosensors," Nature Materials **7**, 442–453 (2008).
4. T. W. Ebbesen, C. Genet, and S. I. Bozhevolnyi, "Surface-plasmon circuitry," Physics Today **61**, 44–50 (2008).
5. P. Berini and I. De Leon, "Surface plasmon-polariton amplifiers and lasers," Nature Photonics **6**, 16–24 (2012).
6. A. Karalis, E. Lidorikis, M. Ibanescu, J. D. Joannopoulos, and M. Soljacic, "Surface-plasmon-assisted guiding of broadband slow and subwavelength light in air," Physical Review Letters **95**, 063901 (2005).
7. Q. Q. Gan, Z. Fu, Y. J. Ding, and F. J. Bartoli, "Ultrawide-bandwidth slow-light system based on THz plasmonic graded metallic grating structures," Physical Review Letters **100**, 256803 (2008).
8. L. Chen, G. P. Wang, X. Li, W. Li, Y. Shen, J. Lai, and S. Chen, "Broadband slow-light in graded-grating-loaded plasmonic waveguides at telecom frequencies," Applied Physics B **104**, 653–657 (2011).
9. E. P. Fitrakis, T. Kamalakis, and T. Sphicopoulos, "Slow light in insulator-metal-insulator plasmonic waveguides," Journal of the Optical Society of America B **28**, 2159–2164 (2011).
10. L. Yang, C. J. Min, and G. Veronis, "Guided subwavelength slow-light mode supported by a plasmonic waveguide system," Optics Letters **35**, 4184–4186 (2010).
11. Y. Huang, C. J. Min, and G. Veronis, "Subwavelength slow-light waveguides based on a plasmonic analogue of electromagnetically induced transparency," Applied Physics Letters **99**, 143117 (2011).
12. M. Miyata and J. Takahara, "Field enhancement by longitudinal compression of plasmonic slow light," Journal of Applied Physics **111**, 053102 (2012).
13. A. A. Govyadinov and V. A. Podolskiy, "Gain-assisted slow to superluminal group velocity manipulation in nanowaveguides," Physical Review Letters **97**, 223902 (2006).

14. Z. F. Yu, G. Veronis, S. H. Fan, and M. L. Brongersma, "Gain-induced switching in metal-dielectric-metal plasmonic waveguides," Applied Physics Letters **92**, 041117 (2008).
15. E. N. Economou, "Surface plasmons in thin films," Physical Review **182**, 539–554 (1969).
16. B. Tang, L. Dai, and C. Jiang, "Electromagnetically induced transparency in hybrid plasmonic-dielectric system," Optics Express **19**, 628–637 (2011).
17. A. Ishikawa, R. F. Oulton, T. Zentgraf, and X. Zhang, "Slow-light dispersion by transparent waveguide plasmon polaritons," Physical Review B **85**, 155108 (2012).
18. J. J. Chen, Z. Li, S. Yue, J. H. Xiao, and Q. H. Gong, "Plasmon-induced transparency in asymmetric T-shape single slit," Nano Letters **12**, 2494–2498 (2012).
19. H. Lu, X. M. Liu, and D. Mao, "Plasmonic analog of electromagnetically induced transparency in multi-nanoresonator-coupled waveguide systems," Physical Review A **85**, 053803 (2012).
20. M. A. Noginov, V. A. Podolskiy, G. Zhu, M. Mayy, M. Bahoura, J. A. Adegoke, B. A. Ritzo, and K. Reynolds, "Compensation of loss in propagating surface plasmon polariton by gain in adjacent dielectric medium," Optics Express **16**, 1385–1392 (2008).
21. I. De Leon and P. Berini, "Modeling surface plasmon-polariton gain in planar metallic structures," Optics Express **17**, 20191–20202 (2009).
22. V. Kuzmiak, A. A. Maradudin, and F. Pincemin, "Photonic band structures of 2-dimensional systems containing metallic components," Physical Review B **50**, 16835–16844 (1994).
23. M. Davanco, Y. Urzhumov, and G. Shvets, "The complex Bloch bands of a 2D plasmonic crystal displaying isotropic negative refraction," Optics Express **15**, 9681–9691 (2007).
24. C. Engstroem, C. Hafner, and K. Schmidt, "Computations of lossy Bloch waves in two-dimensional photonic crystals," Journal of Computational and Theoretical Nanoscience **6**, 775–783 (2009).
25. K. Schmidt and R. Kappeler, "Efficient computation of photonic crystal waveguide modes with dispersive material," Optics Express **18**, 7307–7322 (2010).
26. C. Fietz, Y. Urzhumov, and G. Shvets, "Complex k band diagrams of 3D metamaterial/photonic crystals," Optics Express **19**, 19027–19041 (2011).
27. R. P. Moiseyenko and V. Laude, "Material loss influence on the complex band structure and group velocity in phononic crystals," Physical Review B **83**, 064301 (2011).
28. J. P. Berenger, "A perfectly matched layer for the absorption of electromagnetic-waves," Journal of Computational Physics **114**, 185–200 (1994).
29. S. A. Maier, *Plasmonics: Fundamentals and Applications* (Springer, Bath, 2007).
30. R. Cook, D. Malkus, and M. Plesha, *Concepts and Applications of Finite Element Analysis* (Wiley, New York, N.Y., 2002).
31. K. C. Huang, E. Lidorikis, X. Y. Jiang, J. D. Joannopoulos, K. A. Nelson, P. Bienstman, and S. H. Fan, "Nature of lossy Bloch states in polaritonic photonic crystals," Physical Review B **69**, 195111 (2004).
32. P. B. Johnson and R. W. Christy, "Optical-constants of noble-metals," Physical Review B **6**, 4370–4379 (1972).
33. A. Saxena, "A material-mask overlay strategy for continuum topology optimization of compliant mechanisms using honeycomb discretization," Journal of Mechanical Design **130** (2008).
34. S. A. Schulz, L. O'Faolain, D. M. Beggs, T. P. White, A. Melloni, and T. F. Krauss, "Dispersion engineered slow light in photonic crystals: a comparison," Journal of Optics **12**, 104004 (2010).
35. J. G. Pedersen, S. S. Xiao, and N. A. Mortensen, "Limits of slow light in photonic crystals," Physical Review B **78**, 153101 (2008).
36. J. Grgic, J. G. Pedersen, S. Xiao, and N. A. Mortensen, "Group index limitations in slow-light photonic crystals," Photonics and Nanostructures: Fundamentals and Applications **8**, 56–61 (2010).
37. F. Wang, J. S. Jensen, J. Mørk, and O. Sigmund, "Loss engineered slow light waveguides," Submitted .
38. M. P. Nezhad, K. Tetz, and Y. Fainman, "Gain assisted propagation of surface plasmon polaritons on planar metallic waveguides," Optics Express **12**, 4072–4079 (2004).
39. S. A. Maier, "Gain-assisted propagation of electromagnetic energy in subwavelength surface plasmon polariton gap waveguides," Optics Communications **258**, 295–299 (2006).

1. Introduction

Surface-plasmon polaritons, TM polarized waves trapped at the interface between metal and isolators/dielectric materials, offer a powerful means to squeeze and manipulate light over the diffraction limit [1, 2], and have attained extensive interest for decades. The strong field enhancement induced by the localized plasmons is favorable in all the nonlinear optical applications, and has provided plasmonic waveguides unique opportunities for nanoscale miniaturization in the integrated optical devices [1, 3, 4, 5].

Recently, slow surface plasmon propagation has been demonstrated in diverse plasmonic waveguides [6, 7, 8, 9, 10, 11, 12]. The plasmonic slow light displays the characteristics of

both surface plasmons and slow light, and leads to strongly localized fields [5]. Among different plasmonic slow light waveguides, the metal-dielectric-metal (MDM) plasmonic waveguides are of particular interest due to their capability to integrate gain media [13, 14] and to support surface plasmon propagation over a very wide frequency range [15]. By utilizing a plasmonic analogue of electromagnetically induced transparency (EIT), plasmonic slow light propagation has been reported in various MDM plasmonic waveguide configurations with coupled resonators [11, 16, 17, 18, 19].

Slow light propagation in MDM plasmonic waveguides encounters two major challenges, i.e. high group velocity dispersion (GVD) and large metal-induced propagation loss. The high GVD induces severe signal distortions and restricts the attainable bandwidth, while the large propagation loss limits the effective propagation length of signals. To alleviate high GVD, it has been shown that the dispersion curve of the MDM plasmonic waveguides can be tailored by changing the side-coupled resonators [11, 19]. To mitigate propagation loss, the incorporation of gain media in the MDM plasmonic waveguides has been anticipated to be an efficient approach [13, 14, 20, 21]. However, no systematic study has been performed neither on the dispersion engineering of the MDM plasmonic waveguides nor on the loss compensation of the slow light propagation, because the material dispersion in metal raises the complexity of the band structure calculations of plasmonic waveguides [22, 23].

In this paper, we adapt the complex band structure calculations presented in [23, 24, 25, 26, 27] to detect the dispersion relations of plasmonic waveguides. The perfectly matched layers (PMLs) [28] are employed normal to the waveguide direction to truncate the computational domain , thus deliberately neglecting radiation losses while still allowing calculation to account for the Ohmic losses in the metal. Based on the band structure calculations, the dispersion engineering in MDM plasmonic waveguides with coupled resonators is systematically performed by formulating it as an optimization problem, where the waveguides are numerically parameterized by a set of superellipses. Furthermore, the loss compensation of the designed slow light modes is investigated by embedding material gain in the dielectric material.

2. Methods

2.1. Complex band structure calculations

Only H_z surface plasmonic modes are guided in the infinite planar plasmonic waveguides [29]. By assuming a harmonic time dependence $H_z(\mathbf{r},t) = H_z(\mathbf{r})\, e^{i\omega t}$ with $\mathbf{r} = (x,\, y)$ being a position vector, the surface plasmonic modes follow a scalar Helmholtz equation

$$\nabla \cdot \left(\varepsilon_r^{-1} \nabla H_z(\mathbf{r})\right) + (\omega/c)^2 \mu_r H_z(\mathbf{r}) = 0 \tag{1}$$

where ε_r is the relative permittivity, ω is the wave frequency, c is the light speed in vacuum, μ_r is the relative permeability and $\mu_r = 1$ for non-magnetic materials.

Following Bloch–Floquet theorem, surface plasmonic modes in a periodic structure take the form of $H_z(\mathbf{r}) = U(\mathbf{r})\, e^{i\mathbf{k}\cdot\mathbf{r}}$ with $\mathbf{k}$ being the wave vector and U being the envelope function. Hence, the guided plasmonic modes can be obtained by solving the eigenvalue problem in terms of wave vector $\mathbf{k}$, given by

$$(\nabla + i\mathbf{k}) \cdot \varepsilon_r^{-1} (\nabla + i\mathbf{k}) U + (\omega/c)^2 \mu_r U = 0 \tag{2}$$

Based on the finite element discretization [30], the eigenvalue problem can be written as

$$\left(\mathbf{K}_0 - \omega^2 \mathbf{M}\right) \mathbf{U} + \mathbf{K}_1 k \mathbf{U} + \mathbf{K}_2 k^2 \mathbf{U} = 0 \tag{3}$$

where k is the wavenumber in the direction considered, $\mathbf{U}$ is the nodal value vector of U, and $\mathbf{K}_0$, $\mathbf{M}$, $\mathbf{K}_1$ and $\mathbf{K}_2$ are finite element matrices [23, 24, 25]. The eigen wavenumber k can be

solved by reformulating Eq. (3) as

$$(\mathbf{K}_l - k\mathbf{M}_l)\,\mathbf{V} = \mathbf{0} \tag{4}$$

with

$$\mathbf{K}_l = \begin{bmatrix} -\mathbf{K}_1 & -\left(\mathbf{K}_0 - \omega^2\mathbf{M}\right) \\ \mathbf{I} & \mathbf{0} \end{bmatrix}, \qquad \mathbf{M}_l = \begin{bmatrix} \mathbf{K}_2 & \mathbf{0} \\ \mathbf{0} & \mathbf{I} \end{bmatrix}, \qquad \mathbf{V} = \begin{bmatrix} k\mathbf{U} \\ \mathbf{U} \end{bmatrix} \tag{5}$$

Proper boundary conditions need to be implemented in Eq. (3) to detect the eigenmodes. Normal to the waveguide direction, the periodic supercell is embedded in the PMLs in order to truncate the open boundary, and in the waveguide direction, the periodic condition is implemented as $U(0,y) = U(a,y)$ with the waveguide direction along x direction and a as the lattice constant. The computational model is sketched in Fig. 1 (a).

The eigen wavenumber k is complex valued with the real part ($\Re(k)$) representing the propagation constant and the imaginary part ($\Im(k)$) representing the corresponding propagation loss. Beside the guided modes, many evanescent modes with large propagation loss can be detected in this approach. But the guided plasmomic modes can be directly identified, according to the characteristic of the plasmonic modes, i.e. the high confinement at interface between metal and surrounding materials. Compared to the conventional band structure calculations, where Eq. (3) is solved for frequencies, ω, for given wave vectors, the complex band structure calculations outperform in handling material dispersion and direct measurement of propagation loss [31].

Based on the dispersion relations, the group index of a guided mode is defined by the slope of the dispersion curve, calculated by

$$n_g(\omega_i) = \frac{c}{v_g(\omega_i)} = \Re\left(\frac{\partial k}{\partial \omega}\right) \approx \frac{\Delta k}{\Delta \omega} = \frac{\Re(k(\omega_i)) - \Re(k(\omega))}{\omega_i - \omega} \tag{6}$$

here n_g and v_g are the group index and velocity of the guided mode at ω_i. This calculation is accurate when ω is sufficiently close to ω_i.

In order to evaluate the feasibility of the complex band structure calculations in the plasmonic waveguides, we calculate the dispersion relations of a single interface plasmonic waveguide consisting of Silver (Ag) and air, see Fig. 1 (a). The dispersion relations of such a waveguide can be calculated analytically by $k = \omega\sqrt{\varepsilon_{\text{air}}\varepsilon_{\text{Ag}}/\left(\varepsilon_{\text{air}} + \varepsilon_{\text{Ag}}\right)}$ [29]. In this study, the permittivity of Ag is modeled using the Drude-Lorentz model [32]. Fig. 1 (b) shows the propagation characteristics of the guided modes obtained from the analytical calculation and the numerical simulation. The dispersion curve folds back due to the structural periodicity. This leads to a negative dispersion slope and results in a negative group index according to Eq. (6). Moreover, the propagation loss in this band is characterized by a negative $\Im(k)$ due to the backward propagation. In order to avoid confusion and keep consistency, in the rest paper, we present the propagation loss coinciding with the form of $H_z(\mathbf{r}) = U(\mathbf{r})\,e^{i\mathbf{k}\cdot\mathbf{r}}$, i.e. $\Im(k) > 0$ indicating a modal loss and $\Im(k) < 0$ representing a modal gain. In addition, we ignore the sign on group index. The dispersion relations in the left panel in Fig. 1 (b) demonstrate that the dispersion curves of the plasmonic waveguide can be precisely detected using the complex band structure calculations. However, a big deviation is observed in the propagation loss at high wavelengths, see the right panel. The field intensities in Fig. 1 (c) illustrate that the inaccuracy in the propagation loss is attributed to the large modal size. The field penetration into PMLs results in inaccurate propagation loss. Hence, the inaccuracy of the propagation loss at high wavelengths can be resolved by enlarging the computational domain. Nevertheless, there is no observable difference in the propagation loss for the plasmonic modes highly confined at the interface.

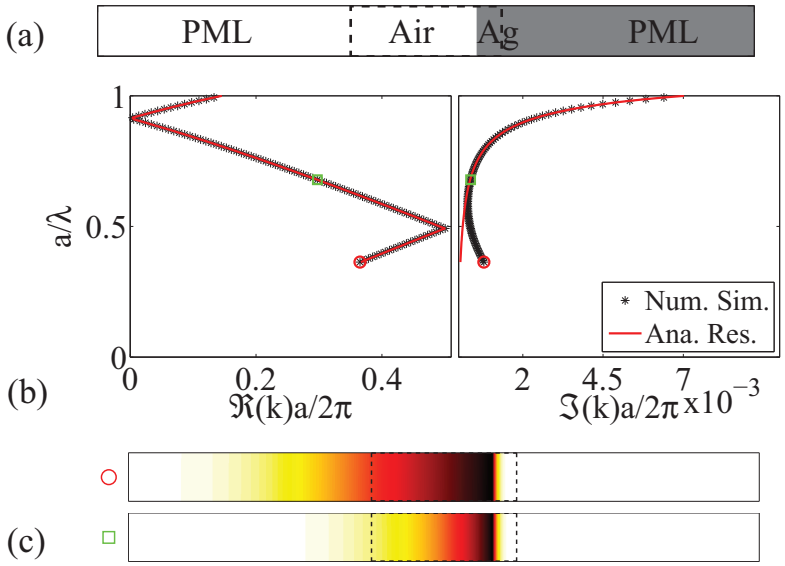

Fig. 1. Dispersion relations of the single interface plasmonic waveguide cconsisting of Ag and air. (a) Computational model of the supercell. PMLs indicate the regions for perfectly matched layers. The dashed rectangle shows the periodic supercell with the gray region indicating Ag and the white region indicating air. (b) Propagation characteristics of the guided modes. Left panel: Dispersion relations. Right panel: Propagation loss versus frequency. The red lines represent the analytical results and the asterisks show the numerical results. (c) Field intensity of the different modes marked in (b).

2.2. Optimization formulations for dispersion engineering

Recently, a planar MDM palsmonic waveguide, consisting of a periodic array of two stub resonators side-coupled to a MDM waveguide (see in Fig. 3 (b)), has been reported to support slow surface modes based on a plasmonic analogue of EIT [11]. Superior to the simple periodic grating plasmonic waveguides, the group velocity and bandwidth of the plasmonic slow light propagation in such a plasmonic waveguide can be tuned by changing the side-coupled resonators. In this section, we present an optimization formulation to systematically design plasmonic slow light waveguides.

Based on finite element discretization, we introduce an elemental quantity, ρ_e, to describe the material property in element e centered at (x_e, y_e). The element is occupied by the dielectric material when $\rho_e = 0$ and by metal when $\rho_e = 1$. Correspondingly, the elemental permittivity is modeled as

$$\varepsilon_e = \varepsilon_{\mathrm{d}} + \rho_e \left(\varepsilon_{\mathrm{m}} - \varepsilon_{\mathrm{d}}\right) \tag{7}$$

where ε_e is the relative permittivity of element e, ε_{d} is the relative permittivity of the dielectric material, and ε_{m} is the relative permittivity of the metal.

Inspired by the material mask overlay strategy [33], the periodic supercell in the plasmonic waveguide with coupled resonators can be parameterized using a set of superellipses, where the regions inside the superellipses are occupied by dielectric material and the regions outside of superellipses are occupied by metal, as illustrated in Fig. 2 (b). The elemental quantity, ρ_e, generated from by the ith superellipse is calculated using the following representation of the

Heaviside function,

$$\rho_e = H(x_i, y_i, a_i, b_i, n_i) = \frac{1}{1+\exp\left(-\beta\left(\frac{|x_i-x_e|^{n_i}}{a_i^{n_i}} + \frac{|y_i-y_e|^{n_i}}{b_i^{n_i}} - 1\right)\right)}. \tag{8}$$

Here (x_i, y_i) are the center of the ith superellipse, a_i, b_i and n_i are the corresponding semi-diameters and curvature (see Fig. 2 (a)), β is the regularization parameter and is set to be $\beta = 50$. The final elemental quantity $\overline{\rho}_e$ projected using all the M superellipses is obtained by

$$\rho_e = \prod_{i=1}^{M} H(x_i, y_i, a_i, b_i, n_i)\, H(x_i - a, y_i, a_i, b_i, n_i)\, H(x_i + a, y_i, a_i, b_i, n_i) \tag{9}$$

Here, three periods of the superellipses as $(x_i - a, y_i)$, (x_i, y_i) and $(x_i + a, y_i)$ are utilized to ensure the periodicity of the waveguide along the waveguide direction.

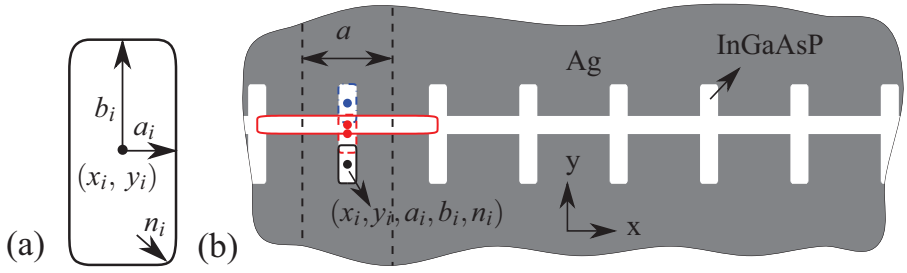

Fig. 2. Parameterization of the MDM plasmonic waveguide with side-coupled resonators. (a) Sketch of a superellipse. (b) Illustration of the parameterization of the plasmonic waveguide.

Fig. 2 (b) sketches the parameterization of the planar MDM plasmonic waveguide consisting of Ag and InGaAsP using the presented approach. For an illustration, we employ one superellipse to represent the waveguide core and three superellipses to describe the side-coupled resonators. The detailed structural parameters are as follows: the waveguide has a dielectric core of 60 nm and the side-coupled resonators have a total size of 60 nm $\times$ 330 nm with a downward shift of 50 nm along y direction. The dimension of the supercell is 300 nm $\times$ 1000 nm with the waveguide direction along x direction. In this paper, we ignore the material dispersion in InGaAsP and model its relative permittivity as $\varepsilon_d = 11.38$.

Fig. 3 (a) shows the propagation characteristics of the guided modes (solid lines) obtained from the complex band structure calculations presented above. It is noted that there are three guided bands and the band gaps are occupied by evanescent modes (dashed lines). The modes on the third band are higher order modes with one more node in the longitudinal direction, compared to the modes on the other two bands, see Fig. 3 (b). The third band corresponds to the wavelength range of $\lambda \in [1440,\ 1640]$ nm and is the focus of this study. The detailed propagation characteristics of the third band are depicted in Fig. 3 (c). It is observed that this MDM plasmonic waveguide supports slow light propagation with an average group index of $\langle n_g \rangle = 13$ centering at $\lambda_0 = 1524$ nm . The bandwidth of the slow light propagation is $\Delta\lambda = 94$ nm that corresponds to a group index bandwidth product (GBP) of 0.80 when using $\pm 10\%$ criterion to indicate a negligible GVD [34]. When approaching the band edges, the achievable group index in the waveguide is circumscribed by the loss in metal [35, 36].

With the locations, semi-diameters and curvatures of the superellipses as design variables, the MDM plasmonic waveguides can be designed for a prescribed group index, n_g^*, by formulating

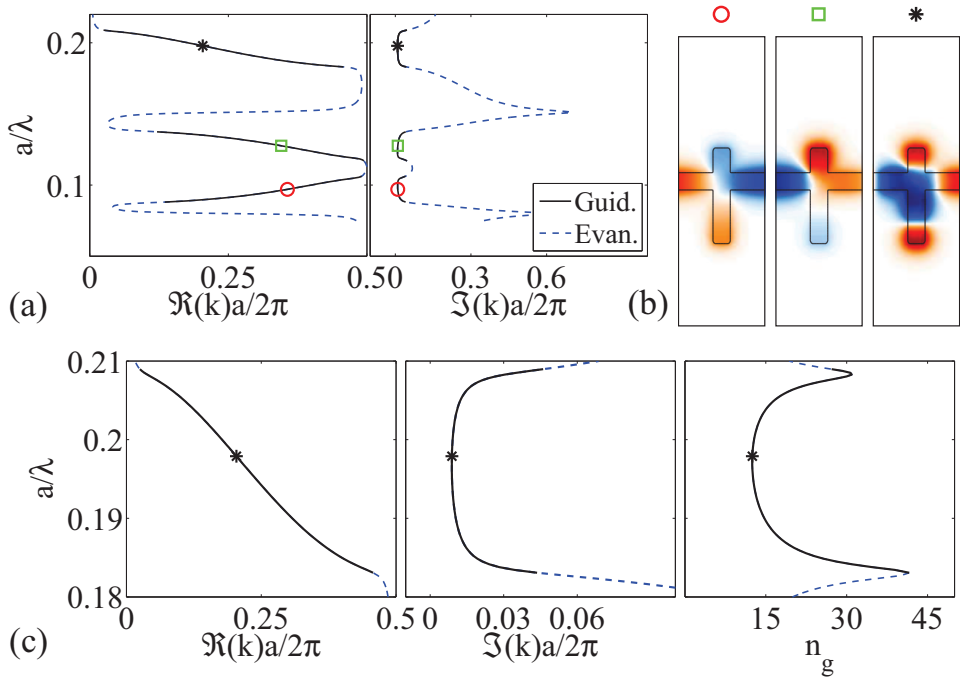

Fig. 3. Dispersion relations of the MDM plasmonic waveguide with side-coupled resonators. (a) Dispersion relations of the plasmonic waveguide. The solid and dashed lines depict the guided and evanescent modes, respectively. (b) Modal profiles of the guided modes in different bands marked in (a). (c) The detailed propagation characteristics of the third band. Left panel: Dispersion curve. Middle panel: Propagation loss. Right panel: Group index plot.

the dispersion engineering as an optimization problem,

$$\min_{\mathbf{x}} \qquad f\left(\rho\left(\mathbf{x}\right),\lambda_i\right)=\sum_{\lambda_i}\left(n_g\left(\rho\left(\mathbf{x}\right),\lambda_i\right)-n_g^*\right)^2 \tag{10}$$

where $\mathbf{x}$ represents the design variable vector, $\lambda_i \in [\lambda_1,\ \lambda_2]$ is the prescribed wavelength with $[\lambda_1,\ \lambda_2]$ indicating the designed wavelength range.

In order to ensure the designed modes are guided, a constraint is implemented to restrict the average propagation loss, $\langle \Im(k(\rho(\mathbf{x}),\lambda_i))\rangle$, in the designed wavelength range. Besides, additional constraints are implemented to force the designed modes away from the band edges. All the constraints are listed as follows

$$\langle \Im(k(\rho(\mathbf{x}),\lambda_i))\rangle < a_{11} \qquad \Re(k(\rho(\mathbf{x}),\lambda_i)) > k_{11} \qquad \Re(k(\rho(\mathbf{x}),\lambda_i)) < k_{22} \tag{11}$$

here a_{11} is the constant number indicating allowed propagation loss for the designed modes, k_{11} and k_{22} are the constant numbers to ensure the designed modes away from the band edges.

Based on the sensitivity analysis of the objective and constraints using adjoint sensitivity analysis, the supercell is iteratively updated by a gradient-based optimization algorithm, namely FMINCON in MATLAB. The detailed sensitivity analysis of the objective and constraints can be found in [37].

3. Results

In this section, slow light MDM plasmonic waveguides are designed for different target group indices n_g^* using the optimization formulation above. Moreover, the loss compensation of the

designed slow light propagation is studied by incorporating gain media.

3.1. Dispersion engineered MDM plasmonic waveguides

As the first example, we aim at designing a slow light MDM plasmonic waveguide for $n_g^* = 30$ over a wavelength range of $\lambda_i \in [1530,\ 1570]$ nm . The initial design is chosen the MDM plasmonic waveguides shown in Fig. 2. Different numbers of superellipses are chosen to parameterize the MDM plasmonic waveguide. One of them is employed to represent the waveguide core. The rest $M-1$ superellipses are employed to represent the coupled resonators, with locations, semi-diameters and curvatures as design variables.

Fig. 4 shows the final optimized design using 2 superellipses to parameterize the waveguide. In the designed wavelength range indicated by the bold lines in Fig. 4 (b), the group index variation is barely within $\pm 10\%$ in the designed wavelength range. It is noted that the achievable group index in the optimized waveguide is located at the designed wavelength range. The optimized waveguide facilitates slow light propapagation of $\langle n_g \rangle = 28.6$ centering at $\lambda_0 = 1552$ nm. The available bandwidth of the slow light propagation is around $\Delta\lambda = 48$ nm, which corresponds to a GBP of 0.88. The modal profile in Fig. 4 (c) illustrates that the designed mode displays the same nodes in the longitudinal direction as the initial guess.

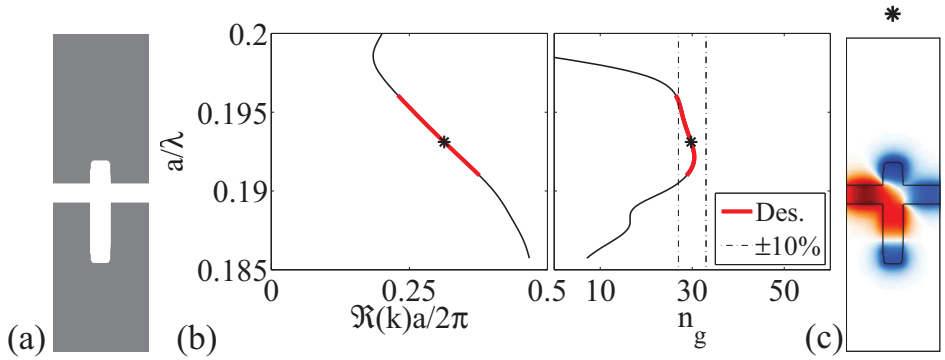

Fig. 4. Performances of the dispersion engineered plasmonic waveguide parameterized using 2 superellipses for $n_g^* = 30$. (a) Optimized plasmonic waveguide. (b) Dispersion curve and group index plot. Left panel: Dispersion curve. Right panel: Group index plot. The bold lines represent the designed wavelength range and the dashed lines show the $\pm 10\%$ range of the target group index. (c) Modal profile of the designed mode marked in (b).

Fig. 5 (a) and (b) present the final optimized plasmonic waveguides for $n_g^* = 30$ when employing 4 and 5 superellipses to parameterize the waveguide. For both plasmonic waveguides, a plateau is observed at the target group index of $n_g = 30$ in the designed wavelength range. Different to the previous case, the achievable group index in both waveguides is higher than the target group index. Slow light propagation of $\langle n_g \rangle = 30.0$ is achieved over a bandwidth of $\Delta\lambda = 62.8$ nm in the optimized waveguide in Fig. 5 (a). This corresponds to a GBP of 1.21. The optimized plasmonic waveguide in Fig. 5 (b) supports slow light propagation of $\langle n_g \rangle = 30.0$ over a bandwidth of slow light propagation is $\Delta\lambda = 62.0$ nm.

The studies above demonstrate that the bandwidth of the slow light propagation in the optimized waveguides is enhanced by a factor of 1.36 when allowing more complex geometries in the plasmonic waveguides. The detailed comparisons among the optimized plasmonic waveguides are presented in Fig. 6. It is seen that group index variation is significantly suppressed in the last two designs. Moreover, the corresponding designed slow light modes display smaller propagation loss, compared to the first designs. The performance of the last two optimized plasmonic waveguides is almost identical in terms of group index and propagation loss. This

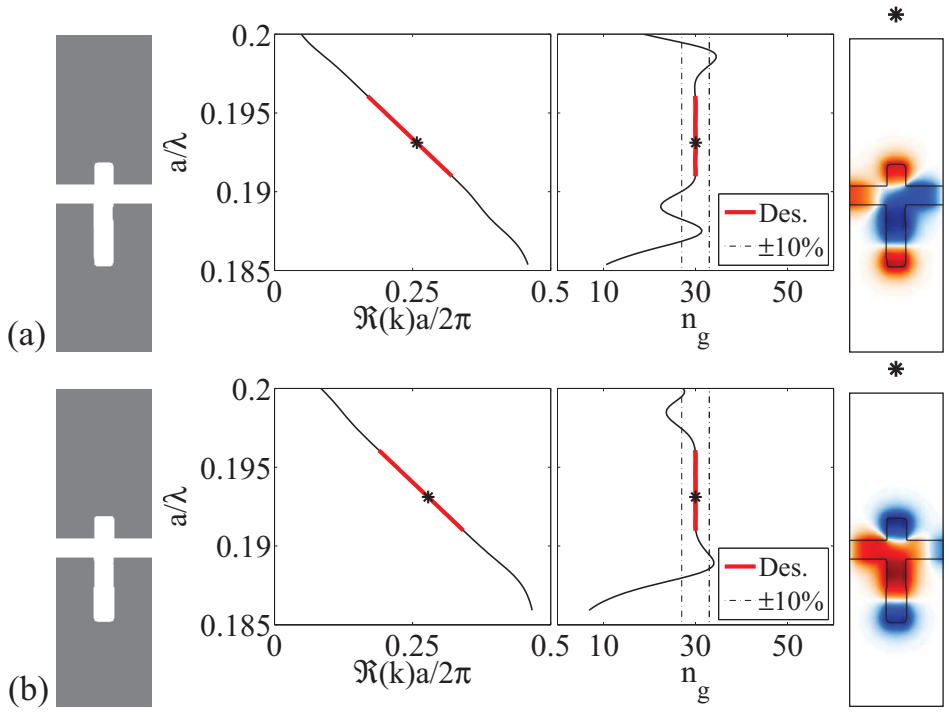

Fig. 5. Performances of the dispersion engineered plasmonic waveguide parameterized using different superellipses for $n_g^* = 30$. (a) Optimized plasmonic waveguide using 4 superellipses. (b) Optimized plasmonic waveguide using 5 superellipses.

reveals that different plasmonic waveguide configurations can achieve equivalently good performances. This is because that the optimized design is a local minimal of the optimization problem and depends on the parameterizations.

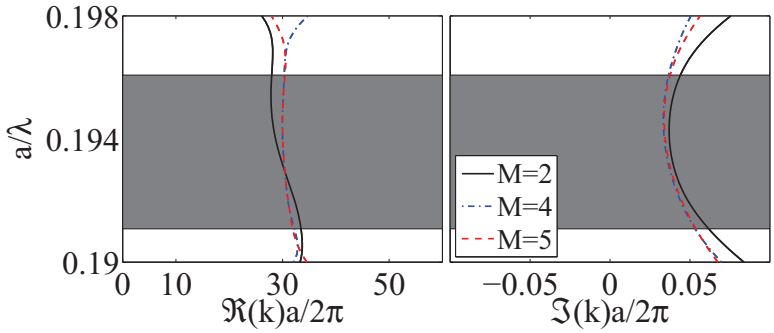

Fig. 6. Comparisons among the optimized designs parameterized using different numbers of superellipses. Left panel: Group index plot. Right panel: Propagation loss.

In the following example, a slow light plasmonic waveguide is designed for $n_g^* = 40$ with a target bandwidth of $\Delta\lambda = 30$ nm centering at $\lambda_0 = 1550$ nm. Fig. 7 (a) presents the final design using 5 superellipses. Fig. 7 (b) shows the dispersion curve and the group index plot of the optimized waveguide. Same as in the previous case, a plateau on the group index is located at the target group index of $n_g = 40$ in the designed wavelength range. Slow light propagation of $\langle n_g \rangle = 39.6$ is achieved over a bandwidth of $\Delta\lambda = 56$ nm by the optimized waveguide. It is noted that the achievable group index in the optimized MDM plasmonic waveguide is the target

group index due to the material loss in metal.

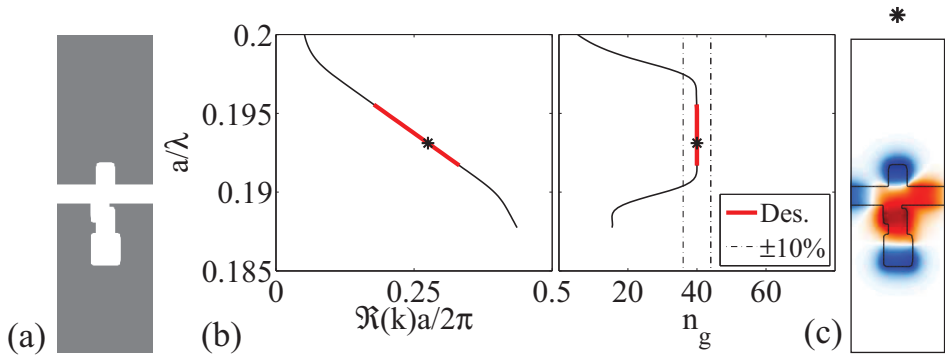

Fig. 7. Performances of the dispersion engineered plasmonic waveguide for $n_g^* = 40$. (a) Optimized plasmonic waveguide. (b) Dispersion curve and corresponding group index. (c) Modal profile of the designed mode marked in (b).

It needs to be pointed out here that loss in metal restricts the achievable group index of slow light propagation in MDM plasmonic waveguides. An average group index above 40 is difficult to achieve in the passive plasmonic waveguide, while keeping similar GBP as in the previous cases.

3.2. Gain-assisted dispersion engineered MDM plasmonic waveguides

It is well known that the detrimental loss in metal in MDM plasmonic waveguides leads to diminishing propagation length, which strongly restricts the potential application scope of MDM plasmonic waveguides. To compensate loss, integration of gain media in MDM plasmonic waveguides has been suggested to be an effective approach for various applications [14, 20, 38, 39]. Based on the optimized waveguides obtained from 5 superellipses, we investigate the loss compensation in the dispersion engineered MDM plasmonic waveguides, and further explore the influence of material gain on the GVD of the designed slow light modes. To simplify the problem, we assume uniform gain in InGaAsP [14, 21], and model the material gain by adding a small imaginary part, ε'', to the dielectric constant as $\varepsilon_d = 11.38 - i\varepsilon''$. The magnitude of ε'' depends on the pumping power.

Fig. 8 (a) presents the detailed performances of the optimized MDM plasmonic waveguide for $n_g^* = 30$ in the presence of material gain. Fig. 8 (b) shows the characteristics of the optimized MDM plasmonic waveguide for $n_g^* = 40$. It is noted that in both cases the propagation loss of the designed modes varies in the designed wavelength range indicated by the gray regions. This is attributed to the field variations between different designed modes. The integration of a gain medium significantly suppresses or even cancels the propagation loss of the guided modes. The propagation loss of the guided modes decreases monotonically as the material gain rises. The detailed observations show that some guided modes in the designed wavelength range are slightly amplified when incorporating material gain of $\varepsilon'' = 0.15$, indicated by $\Im(k) < 0$. However, the incorporation of the material gain tilts the dispersion curve and leads to high group indices in the designed slow light modes. It is apparent that the incorporation of the material gain upgrades the average group index of the designed slow light propagation. Moreover, the group index variation in the designed wavelength range is enlarged by the material gain, and a big group index variation can be observed in the gain-assisted MDM plasmonic waveguides with $\varepsilon'' = 0.15$. The amplification of the group index variation is again explained by the field variations between the designed slow light modes.

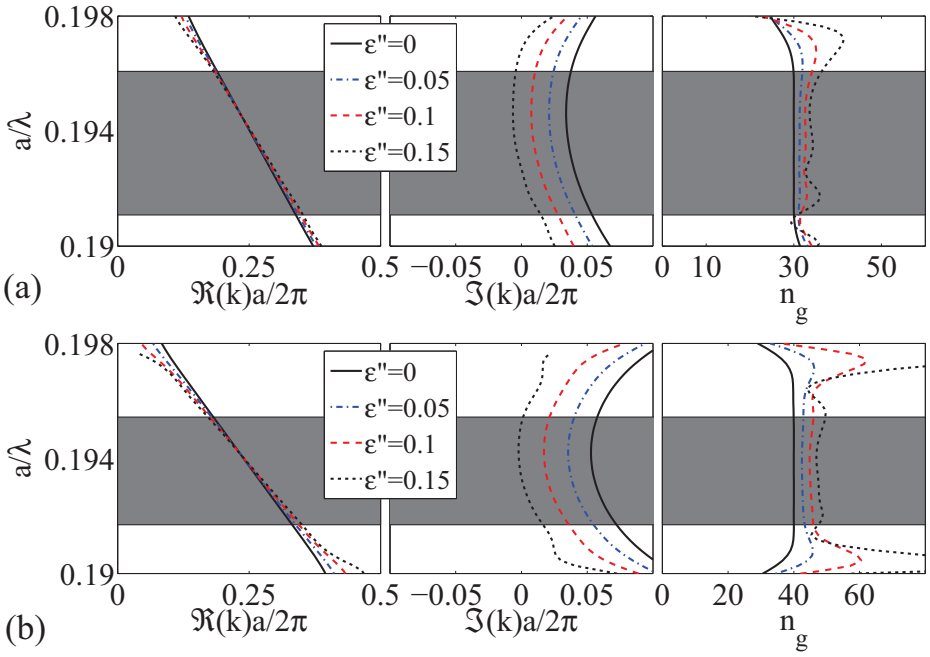

Fig. 8. Performance of the optimized MDM plasmonic waveguides with different amounts of material gain. (a) The optimized MDM plasmonic waveguide for $n_g^* = 30$. (b) The optimized MDM plasmonic waveguide for $n_g^* = 40$.

Under the $\pm 10\%$ criterion, we quantitively evaluate the slow light propagation in the designed waveguides in terms of the GBP and the average propagation loss. The detailed characteristics of the gain-assisted MDM plasmonic waveguide for $n_g^* = 30$ are listed in Tab. 1. It is seen that the average group index, $\langle n_g \rangle$, increases monotonically with the material gain, while the corresponding average propagation loss, $\langle \Im(k) \rangle$, reduces. With a material gain of $\varepsilon'' = 0.15$, the designed slow light modes are slightly amplified, indicated by the negative average propagation loss. The different gain-assisted MDM plasmonic waveguides achieve a GBP of 1.20 or above when integrating material gain of $\varepsilon'' \leq 0.1$. However, due to strong amplification of the group index variation in the case of $\varepsilon'' = 0.15$, the GBP of the slow light propagation is reduced to 0.89.

Table 1. Detailed characteristics of the gain-assisted MDM plasmonic waveguide for $n_g^* = 30$.

ε''	λ_0 (nm)	$\langle n_g \rangle$	GBP	$\langle \Im(k) \rangle a/2\pi$
0	1552	30.0	1.20	0.044
0.05	1550	31.5	1.25	0.031
0.1	1550	33.0	1.32	0.017
0.15	1549	34.2	0.89	-0.001

Tab. 2 summarizes the detailed performances of the optimized MDM plasmonic waveguide for $n_g^* = 40$. All the MDM plasmonic waveguides can achieve a GBP of 1.28 or above. With a same amount of material gain, the plasmonic waveguide for $n_g^* = 40$ displays larger average propagation loss, compared to the one for $n_g^* = 30$. When integrating material gain of $\varepsilon'' = 0.15$, slow light propagation up to $\langle n_g \rangle = 47.5$ can be supported in the gain-assisted plasmonic waveguide, while a small average propagation attenuation is observed in the slow light

propagation. Fig. 8 (b) illustrates that the propagation attenuation is induced by the slow light propagation located at the higher wavelengths. Larger material gain has to be added in order to fully compensate the propagation loss in the slow light propagation.

Table 2. Detailed performances of the gain-assisted slow light MDM plasmonic waveguide for $n_g^* = 40$.

ε''	λ_0 (nm)	$\langle n_g \rangle$	GBP	$\langle \Im(k) \rangle a/2\pi$
0	1547	39.6	1.43	0.067
0.05	1547	43.4	1.65	0.051
0.1	1547	45.7	1.28	0.025
0.15	1547	47.5	1.37	0.006

4. Conclusion

In conclusion, we present a systematic approach for dispersion engineering in slow light MDM plasmonic waveguides. Through parameterizing the MDM plasmonic waveguide with side-coupled resonators using a set of superellipses, the dispersion engineering is formulated as an optimization problem based on the complex band structure calculations. Numerical results show the dispersionless slow light MDM plasmonic waveguides are achieved for prescribed group indices using the presented approach. By assuming uniform gain in the semiconductor, we further study the loss compensation of the designed slow light modes by incorporating gain media. The results suggest that the lossless propagation can be realized in the gain-assisted slow light MDM plasmonic waveguides and the integration of material gain upgrades the average group index in the designed wavelength range. However, the incorporation of gain media magnifies the signal distortions. The trade-off between GVD and propagation loss depends on the applications.

Acknowledgment

This work was financially supported by Villum Fonden (via the NATEC Centre of Excellence) and by the Danish Center for Scientific Computing (DCSC). The authors would like to thank Sanshui Xiao for helpful discussions and fruitful discussions with members of the TopOpt-group(www.topopt.dtu.dk) and Department of Photonics Engineering in DTU are gratefully acknowledged.

DTU Mechanical Engineering
Section of Solid Mechanics
Technical University of Denmark

Nils Koppels Allé, Bld. 404
DK- 2800 Kgs. Lyngby
Denmark
Phone (+45) 4525 4250
Fax (+45) 4593 1475
www.mek.dtu.dk
ISBN: 978-87-90416-85-0

DCAMM
Danish Center for Applied Mathematics and Mechanics

Nils Koppels Allé, Bld. 404
DK-2800 Kgs. Lyngby
Denmark
Phone (+45) 4525 4250
Fax (+45) 4593 1475
www.dcamm.dk
ISSN: 0903-1685